



Scientific Technical Report

ISSN 1610-0956



Barbara Heuer

Lithospheric and upper mantle structure beneath the western Bohemian Massif obtained from teleseismic P and S receiver functions

Scientific Technical Report STR06/12

Gutachter:

Prof. Dr. Rainer Kind (GeoForschungsZentrum Potsdam, Freie Universität Berlin)

Prof. Dr. Serge Shapiro (Freie Universität Berlin)

Tag der Disputation: 21. Juli 2006

Impressum

GeoForschungsZentrum Potsdam
in der Helmholtz-Gemeinschaft
Telegrafenberg
D-14473 Potsdam

e-mail: postmaster@gfz-potsdam.de
www: <http://www.gfz-potsdam.de>

Gedruckt in Potsdam
August 2006

ISSN 1610-0956

Die vorliegende Arbeit ist in elektronischer Form erhältlich unter:
<http://www.gfz-potsdam.de/bib/zbstr.htm>

Barbara Heuer

**Lithospheric and
upper mantle structure beneath the
western Bohemian Massif obtained
from teleseismic P and S
receiver functions**

Dissertation

zur Erlangung des akademischen Grades

Doktor der Naturwissenschaften

am Fachbereich Geowissenschaften

der Freien Universität Berlin

Scientific Technical Report STR06/12

Abstract

The Bohemian Massif is the largest coherent surface outcrop of the Variscan basement in central Europe. The investigation area of this study, the western Bohemian Massif, is situated at the junction of three Variscan structural units: the Saxothuringian in the north, the Teplá-Barrandian and Moldanubian units in the south. The Palaeozoic suture between the Saxothuringian and Teplá-Barrandian/Moldanubian units has been reactivated since the Upper Cretaceous/Tertiary as part of the European Cenozoic Rift System. This led to the evolution of the 300 km long and 50 km wide ENE-WSW trending Eger (Ohře) Rift. The western part of the Eger Rift is known for geophysical and geological phenomena such as the occurrence of earthquake swarms, CO₂ dominated free gas emanations of subcontinental lithospheric mantle signature in mineral springs and mofettes, Tertiary/Quaternary volcanism and neotectonic crustal movements.

To explain the observed phenomena, several possible scenarios have been suggested: a small-scale mantle plume, lithospheric thinning beneath the Eger Rift, and presently ongoing magmatic processes near the crust-mantle boundary, including magmatic underplating.

This thesis focuses on the seismic structure of the lithosphere and upper mantle beneath the western Eger Rift area with the aim of investigating deep-lying possible causes of the phenomena observed at surface.

For the investigation, data of the international passive seismic experiment BOHEMA carried out in 2002/2003 was used. The BOHEMA network consisted of 61 permanent and 84 temporary stations and was centred on the western Eger Rift. The resulting large data set allowed a high resolution *P* and *S* receiver function study using *P*-to-*S* and *S*-to-*P* converted waves, respectively, to map seismic discontinuities in the lithosphere and upper mantle. Data from an earlier passive seismic experiment was additionally used to complement the BOHEMA data set. The results of the analysis are described in this thesis ‘from top to bottom’.

A high resolution Moho depth map of the investigated area could be obtained from more than 5000 *P* receiver function traces. It shows crustal thicknesses of 27 to 31 km in the Saxothuringian unit, 30 to 33 km in the Teplá-Barrandian and 34 to 39 km in the Moldanubian unit east of the Bavarian Shear Zone, which generally agrees with earlier results from seismic studies. A dominant feature in the Moho depth map is an area of thin crust of about 26 to 28 km beneath the western Eger Rift with irregular internal geometry. This apparent Moho updoming was already observed with less resolution in a previous receiver function study. It corresponds well with the area of CO₂ degassing fields, the region of earthquake swarm occurrence and the location of Quaternary volcanoes at surface. The Moho depth values have an estimated uncertainty of ± 2 km.

Furthermore, the first map of average crustal v_p/v_s ratios is presented for the investigated area. The mean values associated with structural units of the Variscan orogen vary between 1.69 and 1.75. For individual locations the variations are larger (between 1.66 and 1.81).

In the area of Moho updoming and CO₂ gas emanations, additional phases were observed in the *P* receiver function data: a positive phase at about 6 s delay time, followed by a strong negative phase at about 7 to 8 s. A mapping of the occurrence of these additional phases showed that they form a coherent structure centred on the western Eger Rift. The phases can be modelled by a discontinuity at 50 km suggested by results of seismic reflection and refraction investigations and a velocity decrease at 65 km depth. The velocity decrease might perhaps be explained by local asthenospheric updoming and/or a confined body of partial melt.

S receiver functions were used to investigate the base of the lithosphere as a second, independent method. If the velocity reduction observed at 8 to 14 s delay time is interpreted as the lithosphere-asthenosphere transition, the data show lithospheric thickness of 80 to 90 km beneath the Saxothuringian and the northern Teplá-Barrandian unit. Towards the south, the thickness strongly increases in the Moldanubian unit to 115 to 135 km, which corresponds well with results of previous studies. The data of the transition from the thinner Saxothuringian/Teplá-Barrandian lithosphere to the thicker Moldanubian lithosphere show a doubling or broadening of the negative signal, which could point to either an abrupt increase of lithospheric thickness, or a very steep slope, or possibly even a structure from palaeosubduction within the lithosphere of this part of the investigated area. However, asthenospheric updoming beneath the contact of the Saxothuringian and Moldanubian units, centred beneath the western Eger Rift as suggested in *P* receiver function data, cannot be stated from *S* receiver functions. Two scenarios are suggested to explain the occurrence of the negative phase in the *P* and *S* receiver functions at different depths: **(1)** The negative phases in the *P* and *S* receiver functions represent two distinct velocity reductions. A thin low velocity layer is detected by *P* receiver functions in the lithospheric mantle at approximately 65 km depth that cannot be resolved by *S* receiver functions. The velocity reduction observed in *S* receiver function data might be interpreted as the lithosphere-asthenosphere transition. **(2)** The negative phases in the *P* and *S* receiver functions represent in principle the same negative velocity gradient (the lithosphere-asthenosphere transition), but strongly influenced by the different frequency contents of the *P* and *S* waves and by the possible nature of the transition from high to low velocities with increasing depth. Both scenarios imply a thin region of strongly decreased seismic velocity at about 65 km depth which might be associated with the occurrence of partial melt in this depth range.

The *P*-to-*S* converted waves from the discontinuities of the mantle transition zone at 410 and 660 km depth show slightly increased delay times compared to the *IASP91* global reference model. However, the thickness of the mantle transition zone is not affected and thus points to normal temperatures in the mantle transition zone and increased v_p/v_s ratio somewhere in the upper mantle above the mantle transition zone. Furthermore, a coherent converted phase is observed in *P* receiver functions that might be attributed to the discontinuity at 520 km depth.

Zusammenfassung

Das Böhmisches Massiv bildet das größte zusammenhängende Gebiet anstehenden variskischen Grundgebirges in Mitteleuropa. Das Untersuchungsgebiet dieser Arbeit, das westliche Böhmisches Massiv, befindet sich an der Nahtstelle dreier variskischer Struktureinheiten: dem Saxothuringikum im Norden, und dem Teplá-Barrandium und Moldanubikum im Süden. Die paläozoische Suture zwischen Saxothuringikum und Teplá-Barrandium/Moldanubikum wurde durch das Europäische Känozoische Riftsystem seit der Oberkreide/Tertiär reaktiviert. Dies führte zur Entstehung des 300 km langen und 50 km breiten, ENE-WSW streichenden Eger (Ohře) Rifts. Der westliche Teil des Eger Rifts ist bekannt für geologische und geophysikalische Phänomene wie das Auftreten von Erdbebenschwärmen, CO₂-dominierte Gasaustritte aus Mineralquellen und Mofetten mit subkontinentaler lithosphärischer Mantelsignatur, tertiären/quartären Vulkanismus und neotektonische Krustenbewegungen.

Um die beobachteten Phänomene zu erklären, wurden verschiedene Szenarien vorgeschlagen: ein kleinräumiger Mantelplume, verringerte Lithosphärenmächtigkeit unter dem Eger Rift und gegenwärtig aktive magmatische Prozesse nahe der Kruste-Mantel-Grenze einschliesslich magmatischem *underplating*.

Die vorliegende Arbeit befasst sich mit der seismischen Struktur der Lithosphäre und des oberen Erdmantels unter dem westlichen Eger Rift. Ziel ist die Untersuchung möglicher tiefliegender Ursachen der an der Oberfläche beobachteten Phänomene.

Dafür wurden Daten des internationalen passiven seismischen Experiments BOHEMA genutzt, welches 2002-2003 durchgeführt wurde. Das BOHEMA-Stationsnetz bestand aus 61 Permanent- und 84 Mobilstationen, die im und um das westliche Eger Rift zentriert lagen. Der daraus hervorgehende große Datensatz erlaubte eine hochauflösende *P* und *S Receiver Function* Analyse, um seismische Diskontinuitäten in der Lithosphäre und im oberen Erdmantel mittels *P*-zu-*S* bzw. *S*-zu-*P* konvertierter Wellen zu kartieren. Zur Ergänzung konnten Daten eines früheren passiven seismischen Experiments genutzt werden. Die Ergebnisse der Untersuchung werden in der vorliegenden Arbeit "von oben nach unten" beschrieben.

Eine hoch aufgelöste Mohotiefen-Karte des Untersuchungsgebietes wurde aus der Bearbeitung von mehr als 5000 Einzelspuren abgeleitet. Sie zeigt im Saxothuringikum Krustenmächtigkeiten von 27 bis 31 km, im Teplá-Barrandium 30 bis 33 km, und im Moldanubikum östlich des Bayrischen Pfahls 34 bis 39 km. Das stimmt generell gut mit bisherigen Ergebnissen seismischer Untersuchungen überein. In der Mohotiefen-Karte fällt ein Bereich dünner Erdkruste (26 bis 28 km) unter dem westlichen Eger Rift mit asymmetrischer Struktur auf. Diese sich andeutende Mohoaufwölbung wurde bereits mit geringerer Auflösung in einer früheren *Receiver Function* Untersuchung beobachtet. Das Gebiet der Mohoaufwölbung stimmt gut mit dem Gebiet der CO₂ Entgasungsfelder, Erdbebenschwärme und dem Auftreten zweier quartärer Vulkane an der Erdoberfläche überein. Die ermittelten Werte für die Mohotiefe haben eine Unsicherheit von ± 2 km.

Des weiteren wurde die erste Karte durchschnittlicher krustaler v_p/v_s -Verhältnisse des Untersuchungsgebietes erstellt. Die Durchschnittswerte für Struktureinheiten des

variskischen Orogens variieren zwischen 1,69 und 1,75, Einzelwerte variieren stärker (zwischen 1,66 und 1,81).

Im Gebiet der Mohoaufwölbung und CO₂ Gasaustritte wurden zusätzliche Phasen in den *P Receiver Functions* beobachtet: eine positive Phase bei etwa 6 s Verzögerungszeit, gefolgt von einer starken negativen Phase bei 7 bis 8 s Verzögerungszeit. Diese zusätzlichen Phasen treten in einem zusammenhängenden Bereich des Untersuchungsgebietes auf, der sein Zentrum wiederum unter dem westlichen Eger Rift hat. Die Phasen können durch eine Diskontinuität in 50 km Tiefe, die in früheren seismischen Untersuchungen beobachtet wurde, und eine Geschwindigkeitsabnahme in 65 km Tiefe modelliert werden. Die Geschwindigkeitsabnahme könnte durch eine lokale Aufwölbung der Asthenosphäre und/oder das Auftreten partieller Schmelzen erklärt werden.

Um die Dicke der Lithosphäre mit einer zweiten, unabhängigen Methode zu untersuchen, wurden *S Receiver Functions* analysiert. Dabei wurde bei 8 bis 14 s Verzögerungszeit eine Geschwindigkeitsreduktion beobachtet, die als Lithosphären-Asthenosphärengrenze interpretiert werden kann. Die Lithosphärenmächtigkeit beträgt demnach unter dem Saxothuringikum und dem nördlichen Teplá-Barrandium 80 bis 90 km. Nach Süden nimmt die Lithosphärenmächtigkeit stark zu und beträgt unter dem Moldanubikum 115 bis 135 km, was generell gut mit den Ergebnissen früherer Arbeiten übereinstimmt. Die Daten am Übergang von der dünneren Saxothuringischen/Teplá-Barrandischen zur dickeren Moldanubischen Lithosphäre zeigen eine Verdopplung bzw. Verbreiterung des negativen Signals. Das könnte entweder auf einen stufenartigen oder sehr steilen Anstieg der Lithosphärendicke oder möglicherweise auf eine Paläosubduktionsstruktur hinweisen. Allerdings konnte in den *S Receiver Functions* keine Aufwölbung der Asthenosphäre unter dem westlichen Eger Rift, wie sie in *P Receiver Functions* vermutet wurde, beobachtet werden. Zwei Szenarien könnten das beobachtete Auftreten einer negativen Phase in *P* und *S Receiver Functions* in unterschiedlichen Tiefen erklären: **(1)** Die negativen Phasen in *P* und *S Receiver Functions* bilden zwei unterschiedliche Geschwindigkeitsverringerungen ab. Eine dünne Niedriggeschwindigkeitsschicht in etwa 65 km Tiefe wird von den *P Receiver Functions* aufgelöst, während sie von *S Receiver Functions* nicht aufgelöst werden kann. Die Geschwindigkeitsverringerung, die in den *S Receiver Functions* abgebildet wird, wird dagegen als Lithosphären-Asthenosphärengrenze interpretiert. **(2)** Die negativen Phasen in *P* und *S Receiver Functions* bilden im Prinzip die gleiche Geschwindigkeitsverringerung ab (die Lithosphären-Asthenosphärengrenze), allerdings beeinflusst von den Eigenschaften dieser Zone und dem unterschiedlichen Frequenzgehalt von *P*- und *S*-Wellen. Auch in diesem Fall müsste es einen dünnen Bereich mit starkem negativen Geschwindigkeitsgradienten in 65 km Tiefe geben, in dem auch partielle Schmelzen auftreten könnten.

Die *P*-zu-*S* konvertierten Wellen von den Diskontinuitäten der Mantelübergangszone in 410 und 660 km Tiefe zeigen leicht erhöhte Verzögerungszeiten im Vergleich zum *IASP91* Standard-Erdmodell. Die Dicke der Mantelübergangszone ist allerdings unverändert und weist daher auf normale Temperaturen in der Mantelübergangszone und ein erhöhtes v_p/v_s Verhältnis in einer Schicht oberhalb der Mantelübergangszone hin. Weiterhin wurden Anzeichen für die Existenz einer Diskontinuität in 520 km Tiefe beobachtet.

Contents

1	Geological and tectonic setting	1
1.1	Regional overview	1
1.2	Geological setting of the western Bohemian Massif	3
1.2.1	Variscan structural units	3
1.2.2	Tectonomagmatic structures	5
2	Results of previous geophysical, geochemical and petrological research	7
2.1	Seismicity of the Vogtland/NW-Bohemia swarm earthquake region	7
2.2	The crust and crust-mantle boundary in seismic studies	10
2.3	Lithospheric and upper mantle structure	12
2.4	CO ₂ emanations and fluid investigations	15
2.5	Xenolith investigations	16
2.6	Thermal structure	16
2.7	Further models of the investigation area	17
3	Data	19
3.1	The passive seismic experiment BOHEMA	19
3.2	Data set for <i>P</i> receiver function analysis	21
3.3	Data set for <i>S</i> receiver function analysis	22
4	Methods	23
4.1	<i>P</i> receiver function method	23
4.2	<i>S</i> receiver function method	25
5	Moho depths and crustal v_p/v_s ratios	29
5.1	Nature of the Moho	29
5.2	Data examples	29
5.3	Observations	29
5.3.1	<i>Ps</i> delay times of the Moho discontinuity	29
5.3.2	Crustal v_p/v_s ratios	36

5.4	Discussion	38
5.4.1	Map of crustal v_p/v_s ratios	38
5.4.2	Depth map of the Moho discontinuity	42
5.4.3	Comparison with seismic refraction profile CEL09	45
6	Structure and thickness of the lithospheric mantle	47
6.1	Nature of the lithosphere and lithosphere-asthenosphere transition	47
6.2	Additional phases observed in P receiver function data	49
6.3	Discussion: Structures within the lithospheric mantle	50
6.4	Observations in S receiver function data	54
6.4.1	S receiver functions obtained at the seismic stations	54
6.4.2	Dividing the data into local “boxes”	56
6.5	Discussion	60
6.5.1	Lithospheric thickness beneath the western Bohemian Massif	60
6.5.2	N-S and E-W profiles	63
7	Discontinuities of the mantle transition zone	71
7.1	Nature of the mantle transition zone	71
7.2	Observation of the upper mantle discontinuities in the study area	73
7.3	Discussion	78
8	Summary and Conclusions	85
8.1	Moho depths and crustal v_p/v_s ratios beneath the western Bohemian Massif	85
8.2	Structure and thickness of the lithospheric mantle	88
8.3	Upper mantle discontinuities at 410 and 660 km depth	90
8.4	Model of the lithosphere and upper mantle beneath the western Bohemian Massif	91
8.5	Open questions/ Outlook	93
	Acknowledgements	97
	References	99

Appendices	111
A.1 Station parameters of the BOHEMA experiment	111
A.2 Station parameters of the experiment by <i>Geissler et al.</i>	114
A.3 Members of the BOHEMA working group	115
B.1 Teleseismic events used for <i>P</i> receiver function analysis (BOHEMA stations)	116
B.2 Teleseismic events used for <i>P</i> receiver function analysis (stations by <i>Geissler et al.</i> , 2005)	121
B.3 Teleseismic events used for <i>S</i> receiver function analysis	135
C.1 Moho depths and v_p/v_s ratios (<i>Zhu and Kanamori</i> method)	140
C.2 Moho depths and v_p/v_s ratios from <i>Ps</i> and <i>PpPs</i>	146

List of Figures

1.1	Structural sketch map of the Variscan Belt in central and eastern Europe	2
1.2	Structural map of the northwestern Bohemian Massif	5
2.1	Distribution of earthquakes in Western Bohemia/Vogtland	8
2.2	Depth map of the Moho discontinuity in central Europe	10
2.3	Schematic tectonic model along profile CEL09	11
2.4	Model of lithospheric thickness beneath central Europe	12
2.5	Anisotropic structures in the lithosphere of the Bohemian Massif	13
2.6	Small-scale mantle fingers beneath the European lithosphere	14
2.7	Distribution of $^3\text{He}/^4\text{He}$ ratios in the gas escape centres of the Eger Rift	16
2.8	Model of the lithosphere beneath the western Eger Rift	17
2.9	Tectonic situation in the western Bohemian Massif	18
3.1	Distribution of seismic stations of the BOHEMA experiment	20
3.2	Enlarged detail of the central part of Figure 3.1	21
3.3	Distribution of teleseismic events used for P receiver function analysis	22
3.4	Distribution of teleseismic events used for S receiver function analysis	22
4.1	Sketch of P -to- S converted waves	23
4.2	Ray paths of Sp and Ps converted phases	25
4.3	Rotation from Z-N-E system into Z-R-T system	27
5.1	Data examples for P receiver functions	30
5.2	Sum traces of P receiver functions of all BOHEMA stations	34
5.3	Delay times of the Ps conversion from the Moho discontinuity	35
5.4	Sum traces of 34 stations used for inversion of Moho depth and v_p/v_s	36
5.5	Inversion results of Moho depth and v_p/v_s for stations BG10 and BG24	37
5.6	v_p/v_s ratios obtained with grid search method by <i>Zhu and Kanamori</i>	37
5.7	Map of v_p/v_s ratios	38
5.8	Moho depth values at each station and piercing points	43
5.9	Simplified Moho depth map	44
5.10	Receiver functions along seismic refraction profile CEL09	46
6.1	Occurrence of a negative phase near 7.5 s delay time	50
6.2	Sum traces of all boxes containing at least 10 individual traces	52
6.3	Sum traces of the boxes along two profiles	53
6.4	Test of the distance moveout of the additional phases near 6 and 7.5 s	53
6.5	Modelling of the observed additional phases	54
6.6	S receiver functions at permanent stations GRA1 and WET	55
6.7	S receiver functions at temporary stations B09 and BG04	55
6.8	Piercing points of P and S rays at 80 km depth	56
6.9	Data examples of S receiver functions obtained for six boxes	57
6.10	Comparison of stacked L and Q components for all boxes	59

6.11	Boxes with a clear negative phase	60
6.12	Map of the depth origin of the negative phase	62
6.13	N-S profiles of <i>S</i> receiver functions between 12°-13°E	64
6.14	N-S profiles of <i>S</i> receiver functions between 13°-14°E	65
6.15	N-S profiles of <i>S</i> receiver functions between 14°-15°E	65
6.16	E-W profiles of <i>S</i> receiver functions between 49.5°-50.0°N	66
6.17	E-W profiles of <i>S</i> receiver functions between 50.0°-50.5°N	66
6.18	E-W profiles of <i>S</i> receiver functions 50.5°-51.0°N	67
6.19	Location of the N-S profile between 12°-13°E	68
6.20	Comparison of <i>P</i> and <i>S</i> receiver functions along the profile	68
6.21	Superimposed traces of <i>P</i> and <i>S</i> receiver functions along the profile	69
7.1	Schematic depiction of the mantle transition zone	72
7.2	Piercing points of <i>P_s</i> rays at 410 km and 660 km depth	74
7.3	Data examples Box 19	75
7.4	Data examples Box 08	76
7.5	Stacked receiver functions sorted by piercing points at 410 km depth	76
7.6	Stacked receiver functions sorted by piercing points at 660 km depth	77
7.7	Difference between measured and theoretical delay time for the ‘410’	79
7.8	Difference between measured and theoretical delay time for the ‘660’	81
7.9	Difference of the delay times of the ‘660’ and ‘410’	82
8.1	Sum traces of <i>P</i> receiver functions of all BOHEMA stations	87
8.2	Cartoon of the seismic discontinuities beneath the western Bohemian Massif ..	92

List of Tables

5.1	Moho depths and v_p/v_s ratios obtained with method by <i>Zhu and Kanamori</i>	40
5.2	Comparison of v_p/v_s ratios obtained by <i>Geissler et al.</i> and this study	42
5.3	Moho depths obtained in previous receiver function investigations	45
6.1	Delay time of the <i>S_p</i> conversion from the LAB and corresponding depth	61
7.1	Delay times of <i>P_s</i> conversions from the ‘410’ and ‘660’	77

Chapter 1

Geological and tectonic setting

1.1 Regional overview

The Bohemian Massif is the largest coherent surface exposure of basement rocks in central Europe. It shows records of at least two orogenic phases: The Cadomian cycle spanned the period from Neoproterozoic to Cambrian. The Variscan collage and orogeny was active from Silurian to Permian times. It shaped a belt which extended from the Appalachian Mountains and Morocco/Northern Algeria via Western-, Central-, Southern Europe and Asia Minor to the Ural before the opening of the Atlantic ocean. It is now established that the Variscan belt resulted from the collision of two main continents – Gondwana to the south and Laurentia-Baltica to the north (*Matte, 1986*). Between these two continents, small microplates, separated by oceanic basins, drifted during the early Palaeozoic. Two main microplates have been defined as Avalonia and Armorica. Geological studies allow smaller microplates to be defined within Armorica (*Matte, 1991; Franke, 2000*). Between Avalonia and the Armorica microplate, the Rheic ocean was situated (*Matte, 2001*). Its closure led to the Variscan orogeny by collision of Avalonia plus Armorica with Gondwana.

During the period of plate convergence, each of the active margins developed into a separate band of the orogenic belt. Most of these separate bands can be traced across Europe. In central Europe, this led to a regional tectonic subdivision into the following zones from north to south (Figure 1.1): the Rhenohercynian, the Saxothuringian (subdivided into the Mid-German Crystalline High in the north and the Saxothuringian basin in the south), the Moldanubian including the unmetamorphosed sequences of the Teplá-Barrandian unit and the Moravo-Silesian. The main phase of folding, combined with metamorphism, granite intrusions and uplift took place in the Carboniferous. While the outer parts of the Variscan orogen are mostly not or only weakly metamorphic, the central parts were stronger or highly metamorphosed.

Later phases of the collisional history were characterized by extensive intrusions of granites, followed by Late Carboniferous to Permian volcanism and renewed extension. The Variscan orogens had been leveled down by erosion already in Late Carboniferous/Permian times, and were subsequently covered by Permo-Mesozoic sediments.

In Mesozoic and Cenozoic times, the Bohemian Massif formed the northern foreland of the Alpine orogen. Alpine compression led to inversion tectonics and thrusting of

basement blocks on top of Mesozoic strata (e.g. along the Frankonian lineament, Figure 1.2). Thus, large parts of the Bohemian Massif were uplifted during late Cretaceous reverse faulting (Dallmeyer *et al.*, 1995; Zulauf, 2005).

In Cenozoic times the European Cenozoic Rift System pervaded the lithosphere of western and central Europe over large distances (Ziegler, 1992; Prodehl *et al.*, 1995; Dèzes *et al.*, 2004). The widespread rifting and alkaline volcanism is often explained by effects of the Atlantic opening and Alpine orogeny. In the Bohemian Massif, the Variscan shear zones were reactivated during Cenozoic extension. This holds particularly for the Lower Carboniferous North Bohemian shear zone. Reactive extensional slip along this shear zone led to the evolution of the Eger Rift (Figure 1.2), which is characterized by elevated heat flow, alkaline volcanism, active tectonics and recent escape of mantle-derived gas.

To the west, the Bohemian Massif is bounded by the Frankonian lineament (Figure 1.2), a NW trending, deep reaching system of reverse faults of late- to post-Variscan origin which was repeatedly reactivated until recently by Alpine Foreland deformation (Wagner *et al.*, 1997). Its continuation in the Moldanubian is a more extended fault system comprising mainly the Bavarian Pfahl and Donaurandbruch faults. Southwest of the Frankonian lineament, Permo-Mesozoic sediments cover the basement. The insufficiently

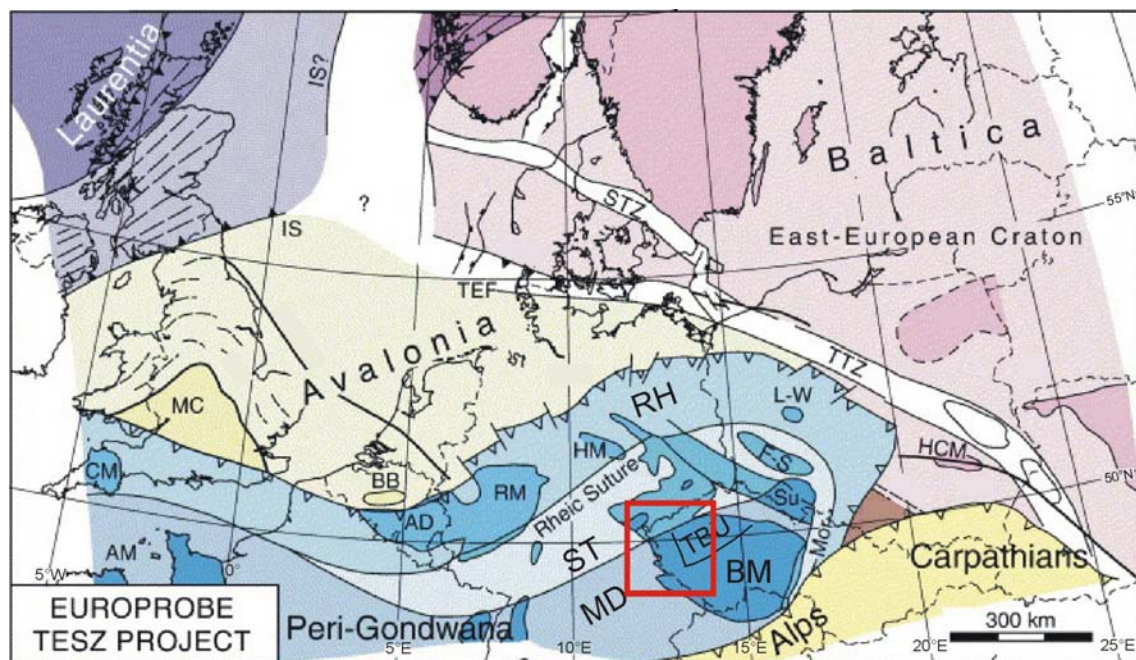


Figure 1.1: Structural sketch map of the northern Variscan Belt in central and eastern Europe and Palaeozoic terranes/continents, slightly modified from Shomali *et al.* (2006). The red rectangle shows the investigation area of this study. Key: AM – Armorican Massif, BB – Brabant Massif, BM – Bohemian Massif, CM – Cornubian Massif, F-S – Fore Sudetic Block, HM – Harz Mountains, HCM – Holy Cross Mountains, IS – Iapetus Suture (Avalonia-Laurentia), IS? – uncertain location of Laurentia-Baltica Suture, L-W – Leszno-Wolsztyn Basement High, MD – Moldanubian Variscan structural unit, MC – Midlands microcraton, Mor – Moravia, RH – Rhenohercynian Variscan structural unit, RM – Rhenish Massif, ST – Saxothuringian Variscan structural unit, STZ – Sorgenfrei-Tornquist Zone, Su – Sudetes Mountains, TBU – Teplá-Barrandian Variscan structural unit, TEF – Trans-European Fault Zone, TTZ – Tornquist-Tetseyre Zone.

constrained fault throw is estimated for different parts of the lineament between several 100 m to a few kilometres (*Franke, 1989; Freudenberger, 1996*). To the southeast, the Moldanubian region is bounded by the Moldanubian overthrust.

To explain the present thin overall lithospheric thickness beneath the Bohemian Massif, *Willner et al. (2002)* relate the fast exhumation of large volumes of high-pressure rocks from the crustal root after the closure of oceans to delamination and complete detachment of the lithospheric mantle. According to *Schott and Schmeling (1998)*, subduction of the Rheic ocean between Avalonia and Gondwana in pre-Variscan time could have had enriched the subduction zones and the upper mantle involved in the Variscan orogeny with a significant amount of water. This might have led to weakening of parts of the Variscan orogenic root, propelling the delamination and detachment of the lithospheric root. *Zulauf (1997)* also uses the concept of lithospheric thickening and delamination in the Moldanubian area to explain the large amounts of plutons (partly derived from mantle melt) along the shear zones in the Moldanubian region. However, *Babuška and Plomerová (2001)* argue against large-scale detachment of the crust from the mantle lithosphere on the basis of their observations of the different orientations of the fabrics in the subcrustal lithosphere of the Saxothuringian and the Moldanubian, as well as the consistency of the fabric within each unit.

1.2 Geological setting of the western Bohemian Massif

1.2.1 Variscan structural units

The area of this study is situated at the junction of three Variscan structural units: the Saxothuringian in the north, the Teplá-Barrandian and the Moldanubian in the south (Figures 1.1 and 1.2).

The Saxothuringian unit consists of Variscan folded Palaeozoic sediments and a variety of Precambrian rocks that are discordantly overlain by unfolded Permo-Carboniferous sedimentary rocks (*Walter, 1995*). The Münchberg Gneiss massif, traditionally interpreted as part of the Saxothuringian zone, is now considered as Teplá-Barrandian allochthonous nappe complex (*Behrmann and Tanner, 1997*). The Eibenstock, Fichtelgebirge and Karlovy Vary plutons are Variscan granitic intrusions into the upper Saxothuringian crust.

The Teplá-Barrandian unit consists of a Cadomic basement overlain by Late Cambrian to Devonian sediments and volcanic rocks (*Franke, 2000*). It forms a largely supracrustal complex which, in contrast to the surrounding Moldanubian and Saxothuringian high-grade units, was not affected by Carboniferous high-temperature/low-pressure metamorphism (*Dörr et al., 2002*).

The contact between the Teplá-Barrandian upper crustal complex and adjacent lower crustal rocks of Moldanubia and Saxothuringia is formed by the Bohemian Shear Zone, a crustal-scale ductile shear zone that is characterised by sharp (up to 90 degrees) bends at the surface (*Zulauf et al., 2002a*). These deflections of the Bohemian Shear Zone in map view (see Figure 1.2) are unusual and have led to a subdivision of the zone into the North Bohemian shear zone (the later Eger Graben and Eger Rift) (*Zulauf et al., 2002b*), West Bohemian shear zone (the later Bohemian quartz lode) (*Zulauf et al., 2002a*), Hoher-Bogen shear zone (*Bues et al., 2002*) and the Central Bohemian shear zone (*Scheuven and*

Zulauf, 2000). All these shear zones are characterised by a mylonite belt, dip-slip or oblique-slip normal movements and retrograde metamorphism during shearing (Zulauf *et al.*, 2002a; Zulauf, 1994). In former times, the Teplá-Barrandian unit was considered to be a superposition of the Moldanubian unit. Nowadays, the hypothesis that both units were originally spatially separated and that the Teplá-Barrandian might be closer related to the Saxothuringian unit is preferred. Thus, the contact between both units is considered to be a tectonic contact (Schönenberg and Neugebauer, 1997).

The term “Moldanubian” is used with two different meanings: the Moldanubian s.str. (*sensu stricto*) which is the largest unit within the Bohemian Massif, and the Moldanubian s.l. (*sensu lato*) as a zone of the regional tectonic subdivision of the Variscan belt of central Europe (see Figure 1.1). In the following, the term is generally used in the meaning “*sensu stricto*”.

The Moldanubian is a complex association of rocks whose protolith ages are mostly unknown. The structure of the Moldanubian is dominated by large scale, thrust-related inversion of metamorphic facies, which has emplaced high pressure rocks (Gföhl Assemblage) over the paraautochthonous Drosendorf Assemblage (Franke, 2000; Tollmann, 1982). The Gföhl unit consists of various metaigneous and metasedimentary rocks, which include granulites, eclogites, and peridotites. The Drosendorf unit consists essentially of fairly monotonous metasedimentary sequences which include quartzites, graphitic quartzites, and carbonates.

1.2.2 Tectonomagmatic structures

The approximately 300 km long and 50 km wide ENE-WSW striking Eger (Ohře) Rift (Figure 1.2) is a tectonomagmatic active intracontinental rift with predominantly vertical movements (Kopecký, 1978). It is part of the European Cenozoic Rift System. The Eger Rift evolved at the Upper Cretaceous/Tertiary and reactivates the Variscan Saxothuringian-Moldanubian suture zone. Its tectonomagmatic evolution comprises several phases (e.g. Ulrych and Pivec, 1997; Kämpf *et al.*, 1999; Špičáková *et al.*, 2000; Bräuer *et al.*, 2005). The main rifting phase took place at 42-9 Ma, with beginning graben formation and intraplate alkaline volcanism. The Eger Rift is characterized by Miocene sedimentation and some basaltic flows. It showed volcanic activity mainly in the Tertiary and with low intensity in the Quaternary until about 0.3-0.5 Ma ago (Wagner *et al.*, 2002). During the Tertiary the small Cheb Basin developed at the western end of the Eger Rift (see Figure 1.2). The basin was initiated by reactivation of basement faults. It covers granites and Lower Palaeozoic series. The asymmetric basin is deepening towards east and limited there by the Mariánské Lázně fault, at the other sides Tertiary sediments overlap basement series (Bankwitz *et al.*, 2003).

At present, the rifting process is still active, which results in further formation of the Cheb basin, accompanied by CO₂ emanations at the surface in NW-Bohemia, southern Vogtland and eastern Fichtelgebirge area, neotectonic uplift in some southern parts of the rift flank and earthquake swarm activity in the Vogtland/NW-Bohemia area.

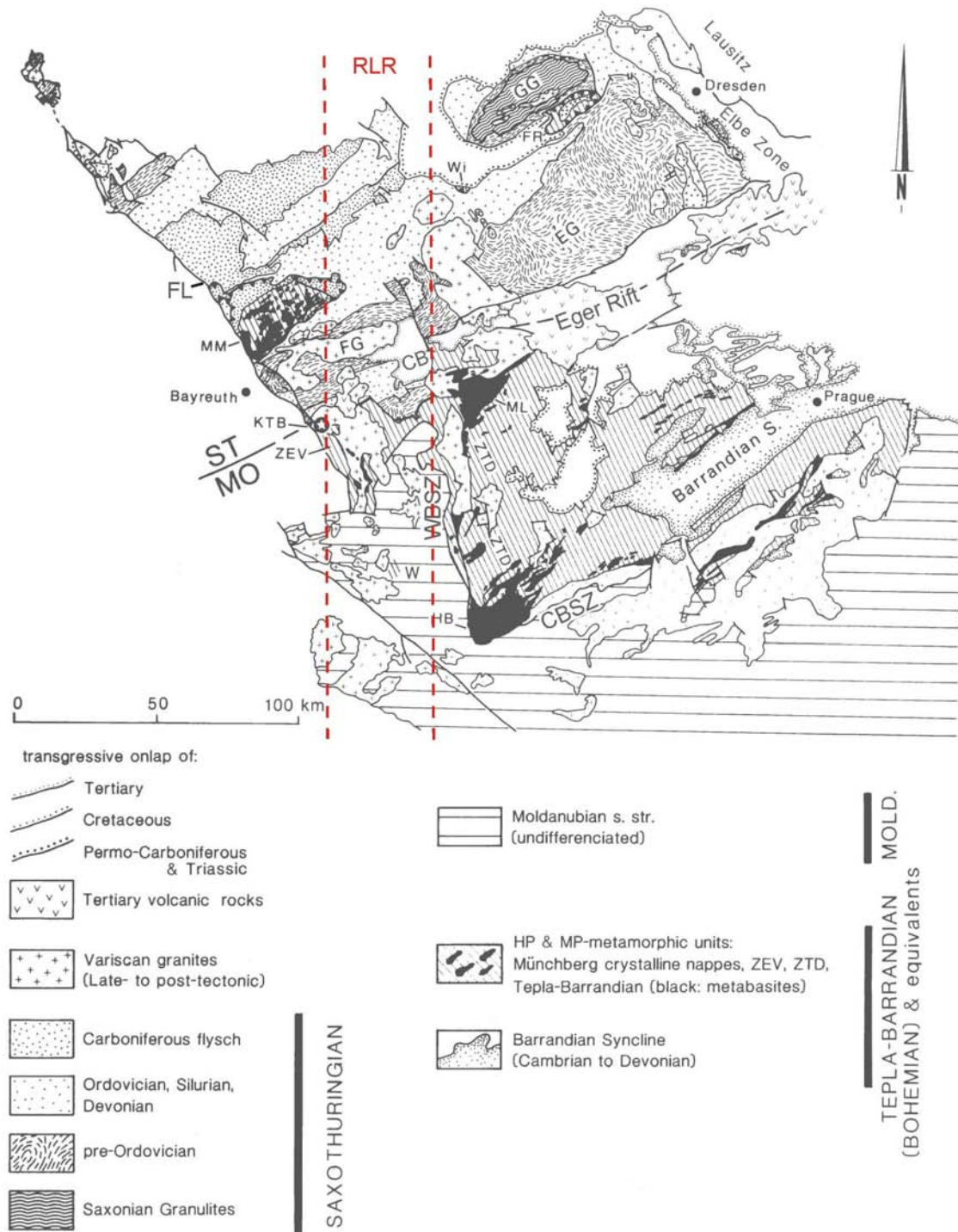


Figure 1.2: Structural map of the northwestern Bohemian Massif (slightly modified from *Franke et al.*, 1995). Abbreviations: ST Saxothuringian; MO Moldanubian region; FL Frankonian Lineament; WBSZ West Bohemian Shear Zone; CBSZ Central Bohemian Shear Zone; GG Saxonian Granulite Complex; MM, Wi, FR metamorphic klippe of Münchberg, Wildenfels, and Frankenberg, and underlying low-grade allochthons; EP, KP Eibenstock and Karlovy Vary plutons, CB Cheb basin, FG, EG antiform of the Fichtelgebirge and Erzgebirge; KTB Continental Deep Drilling Site; ZEV zone of Erbenhof/Vohenstrauß; ZTD zone of Teplá/Domazlice; W high-grade metabasites near Winklarn; ML Mariánské Lázně ophiolite; HB Hoher Bogen (Neukirchen-Kdyně) igneous complex; RLR (red) Regensburg-Leipzig-Rostock zone after *Bankwitz et al.* (2003).

The Regensburg-Leipzig-Rostock zone (Figure 1.2) is described by *Bankwitz et al.* (2003) as one of several prominent sinistral N-S running faulting zones within a belt between the French Massif Central and the northern part of the Bohemian Massif. It was defined on the basis of observations within satellite images (*Bankwitz et al.*, 2003). The Regensburg-Leipzig-Rostock zone is seismically active in its middle part (about 150 km between Cheb and Leipzig), where it consists of a set of subparallel faults. Its intersection area with the Eger Rift is known for geophysical and geological phenomena such as the occurrence of earthquake swarms, mineral springs and mofettes (dry gas outbursts), mantle-derived CO₂ emissions, increased heat flow, a steep gravity gradient, and Tertiary/Quaternary volcanism.

Two Quaternary volcanoes, Komorní Hůrka and Železná Hůrka, are located only 15 and 25 km away from the main epicentral zone at Nový Kostel. A detailed overview about Cenozoic volcanism in western and central Europe is given by *Wilson and Downes* (1991, 1992) and for the western Bohemian Massif by *Ulrych et al.* (2003).

Chapter 2

Results of previous geophysical, geochemical and petrological research

2.1 Seismicity of the Vogtland/NW-Bohemia swarm earthquake region

The Vogtland/NW-Bohemia region is known for the periodic occurrence of intraplate seismic earthquake swarms of mostly $M_L < 3.5$ earthquakes. The general swarm-like character of seismicity has been observed in historical macroseismic reports since 1552 (Grünthal, 1989). Primarily, earthquake swarms are a peculiarity of volcanic regions and of mid-ocean ridges. Swarms in intraplate regions and without active volcanism are unusual. However, they may occur in intracontinental regions of increased geodynamic activity such as continental rifts, as shown by Ibs-von Seht *et al.* (2006). They compared the swarm earthquake areas of the Rio Grande, Kenya, and Eger rifts and found major similarities regarding magnitudes and b -values as well as the fact that in all three rifts the main swarm activity occurred at graben sections intersected by large-scale fracture zones.

The German expression *Schwarmbeben* ('swarm earthquake') was first used with regard to the Vogtland/NW-Bohemia region by Knett (1899) and Credner (1900). The term earthquake swarm denotes a group of seismic events strongly clustering in time and space. Earthquake swarms differ from typical mainshock-aftershock sequences mainly by a missing dominant mainshock, and the b -value of their magnitude-frequency distribution is usually larger than that of aftershock sequences at plate boundaries (Lay and Wallace, 1995).

The swarm earthquake activity in the Vogtland/NW-Bohemia region is generally attributed to the combined influences of tectonic stress, fluid migration and magmatic/volcanic activity (e.g. Weinlich *et al.*, 1999; Špičák *et al.*, 1999; Špičák, 2000; Parotidis *et al.*, 2003, 2005; Bräuer *et al.*, 2003, 2005; Geissler *et al.*, 2005). According to Špičák and Horálek (2001), many earthquake swarm regions are characterized by Quaternary volcanism, indicating that ascending magmatic fluids trigger earthquakes. They also stress the similarity between the fault plane solutions for the earthquake swarms in the Vogtland/NW-Bohemia region and the KTB borehole, ~50 km away, where fluid injections were carried out (Zoback and Harjes, 1997; Rothert *et al.*, 2003). Until recently, the Mariánské Lázně fault was considered to be seismically most active in the region under

study. However, *Bankwitz et al.* (2003) propose that in the Cheb basin the N-S trending newly found sinistral Počátky-Plesná zone is identical with the main earthquake line. According to their investigations, evidence from the relocated hypocentres indicate that the Mariánské Lázně fault is seismically inactive.

Fischer and Horálek (2003) classify three types of earthquake activity in the Vogtland/NW-Bohemia region: swarms, micro-swarms and solitary events. *Horálek et al.* (2000a) distinguish seven main epicentral areas (Figure 2.1). The strongest seismic activity is observed in the Nový Kostel focal zone (area 1). Apart from the anomalous deep micro-swarm in February 2004, focal depths in the Nový Kostel area do not exceed 12 km, whereas the focal depths in the whole Vogtland/NW Bohemia region reach up to 23 km (*Horálek et al.*, 2000a). The northernmost earthquake swarm in this region was detected

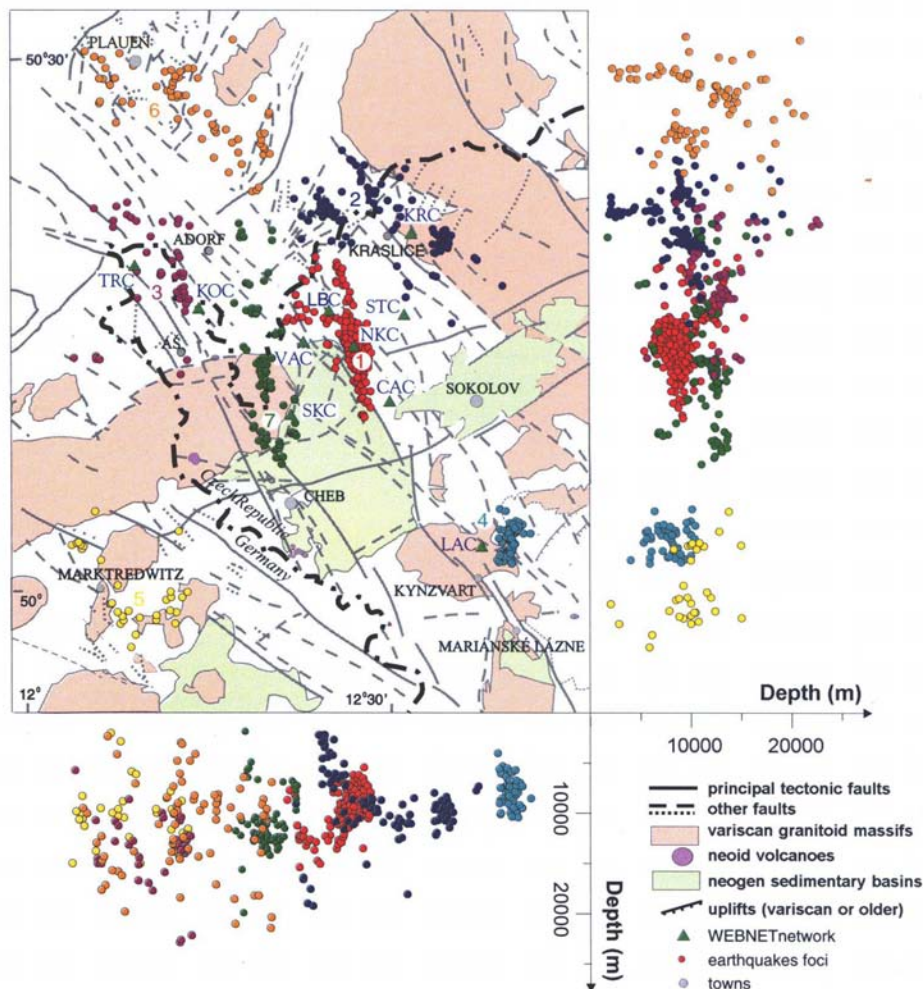


Figure 2.1: Distribution of micro-earthquake foci for the period 1991-1999 in western Bohemia/Vogtland (upper left: map of epicentres, upper right: N-S depth cross-section, lower left: E-W depth cross-section) and positions of WEBNET seismic stations operated by the Geophysical Institute, Academy of Sciences of the Czech Republic, Prague (*Horálek et al.*, 2000a). The colours of earthquake foci represent the seven main epicentral areas distinguished by *Horálek et al.* (2000a). The black dash-dot line marks the state boundary between the Czech Republic (SE) and Germany (NW).

1997/1998 in West Saxony, near Werdau (*Hemmann et al.*, 2003). The hypocenters were located in the area of intersection of the Regensburg-Leipzig-Rostock zone (*Bankwitz et al.*, 2003) and the Gera-Jachimov fault zone. No active fluid processes like in the Vogtland/NW-Bohemia region are known for the area around Werdau, only hints from drillings and geological mapping towards sub-recent upper mantle fluid activity.

Since the start of digital recording of earthquakes, the most prominent swarm in the Nový Kostel focal area occurred in 1985/86 with more than 8000 recorded events, the strongest of which reached the maximum magnitude $M_{Lmax}=4.5$. Further swarms occurred in January 1992 ($M_{Lmax}=2.0$), December 1994 ($M_{Lmax}=2.2$), January 1997 ($M_{Lmax}=3.0$) and August to December 2000 ($M_{Lmax}=3.4$, more than 10 000 microearthquakes recorded) (*Fischer*, 2003; *Fischer and Horálek*, 2003). Clusters in the Nový Kostel zone show relatively large b -values, yet the b -value of nearby clusters may vary remarkably (*Neunhöfer and Meier*, 2004; *Neunhöfer and Hemmann*, 2005). While epicentres of swarms are confined to a few subregions, non-swarmlike events are distributed over a larger region.

There exist several models to explain the origin of earthquake swarms:

Mogi (1963) suggested stress concentration in unusually heterogeneous rock and mentioned magma intrusions as one possible cause for the stress accumulation. *Hill* (1977) explained earthquake swarms in volcanic areas by assuming magmatic intrusions in brittle country rock. He also suggests fluid migration as a reason for increased stress difference $\sigma_1 - \sigma_3$ which may cause an earthquake swarm. *Yamashita* (1999) proposed that the increase of pore volume due to rupture allows fluids to migrate from high pressure reservoirs into this volume located in the fault zone. A high rate of pore volume increase thus causes a high seismic b -value, which corresponds to observations of volcanic earthquake swarms. *Hainzl* (2003) showed that the temporal clustering and magnitude-frequency distribution of swarms can be simulated also without the presence of active fluids but instead with self-organization within the swarm due to local stress transfer and viscous coupling. *Parotidis et al.* (2005) hypothesize that ascending magmatic fluids trigger the Vogtland/NW-Bohemian swarm earthquakes by causing pore pressure perturbations which propagate according to the diffusion equation. They propose that pore pressure diffusion is the main triggering mechanism. *Fischer and Horálek* (2005) investigated space-time relations between consecutive events of the West Bohemian earthquake swarm in 2000 and found indications for a triggering effect of prior earthquakes upon subsequent events. Furthermore, they showed that subsequent events are preferably triggered in the slip direction indicated by the focal mechanisms.

The stress field in the Vogtland/NW-Bohemia does not differ substantially from the known overall SE-NW directed stress field in western and central Europe (*Plenefisch and Klinge*, 2003). The determination of focal mechanisms indicates the presence of an isotropic component in the moment tensors of some of the events, inferring possible fluid activity during the faulting process (*Dahm et al.*, 2000; *Horálek et al.*, 2000b; *Vavryčuk*, 2001, 2002). Many of the swarm events display a multiplet character. Likewise, similar focal mechanisms of the events were found by *Horálek et al.* (2000b) and *Wirth et al.* (2000).

Zoback and Harjes (1997) presented evidence for fluid injection-induced micro-earthquakes at 9 km depth in the nearby KTB deep drilling site. They demonstrated that a relatively small pore pressure perturbation (<1% of the normal) was able to trigger local

microseismicity. *Shapiro et al.* (2006) also showed that very weak pore pressure perturbations triggered seismicity at the seismic SE2 reflector during recent hydraulic experiments at the KTB.

2.2 The crust and crust-mantle boundary in seismic studies

From the compilation of results of seismic experiments, *Giese* (1995) created a contour map of crustal thickness in central Europe. It shows crustal thicknesses of 28 to 32 km beneath the Saxothuringian unit and a maximum crustal thickness of 36 km in the central part of the Bohemian Massif. A European Moho map was compiled from several sources by *Dèzes and Ziegler* (2001) (see Figure 2.2) which also shows Moho depths in the range of 28 to more than 36 km in the investigation area. Taken altogether, crustal thickness appears mainly to reflect post-Variscan processes such as Permo-Carboniferous extension and Cenozoic rifting.

Geissler et al. (2005) carried out a receiver function study in the western Bohemian Massif which was one of the initial studies to lead to the passive seismic experiment BOHEMA, the data of which is analysed in this thesis. *Geissler et al.* (2005) observed clear *P*-to-*S* converted phases from the Moho with delay times between 3 and 4.5 s. The calculated crustal thicknesses vary between 27 and 38 km and the v_p/v_s ratios between 1.63 and 1.81. In general, the Moho depth increases from northwest (31 km) to southeast (38

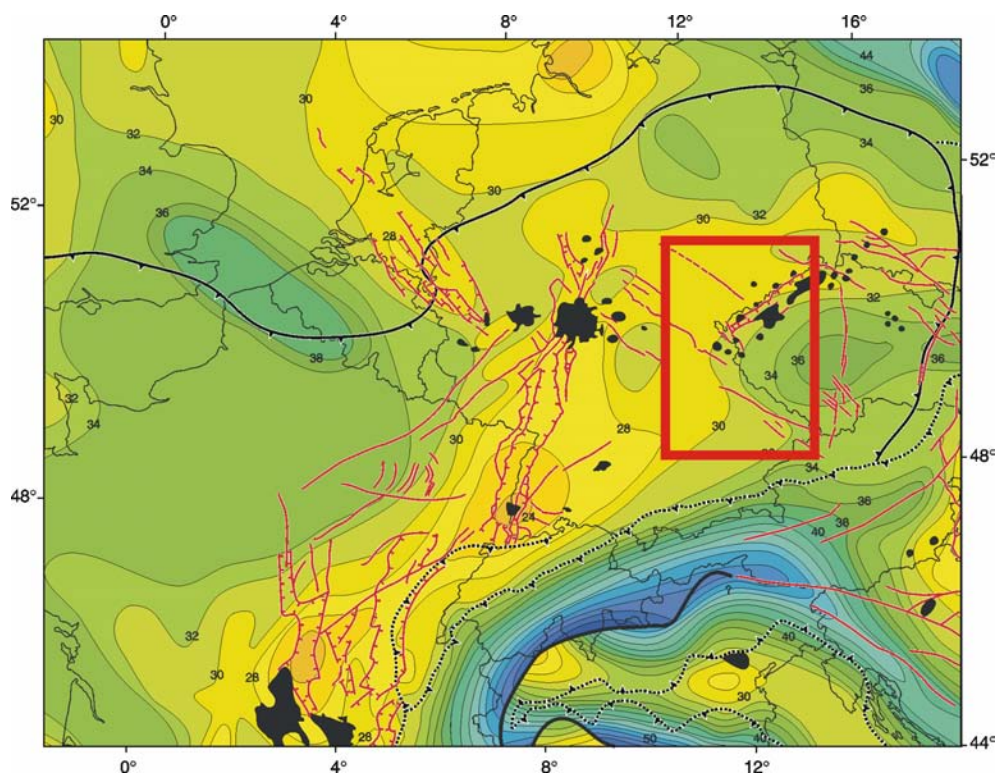


Figure 2.2: Depth map of the Moho discontinuity in central Europe, contour interval 2 km (*Dèzes and Ziegler*, 2001) with major fault systems and graben structures (red lines,) volcanic centres (black fields) and Variscan deformation front (solid black line). The investigation area of this study is marked by a red rectangle. The Moho depth beneath the study area ranges from about 28 to more than 36 km.

km). Beneath the western Eger Rift they found indications of a local Moho updoming up to 27 km with a diameter of approximately 40 km. The area coincides with the location of centres of CO₂ emanations at the surface. At some stations in the area of updoming, the signal from the Moho discontinuity is weak or disappears. In a receiver function study carried out by *Kind et al.* (1995), the Moho at station GRA1 of the Gräfenberg array (also used in this study) is 32 km deep. However, the strongest signal resulted from the bottom of the very low-velocity Mesozoic sedimentary rocks. At station Wettzell, which is also used here, *Kind et al.* (1995) found a weak and very broad Moho conversion, indicating a smooth transition between the lower crust and mantle at approximately 34 km.

Hrubcová et al. (2005) analysed profile CEL09 of the seismic refraction experiment CELEBRATION 2000. They determined two types of crust-mantle transition in the northwestern and central Bohemian Massif, respectively (Figure 2.3): (1) The Saxothuringian has a highly reflective lower crustal layer above the Moho with a strong velocity contrast at the top of the lower crustal layer. This reflective laminated lower crust is located at depths of 26-35 km and was also indicated by data of the deep reflection profile MVE90 as part of the DEKORP investigation (*DEKORP Research Group*, 1994; *Bleibinhaus et al.*, 2003) and the seismic refraction experiment GRANU'95 (*Enderle et al.*, 1998). Such a highly reflective lower crust is a phenomenon frequently observed in Caledonian and Variscan areas (*Warner*, 1990). The Moho in the model by *Hrubcová et al.* (2005) is represented by a thin (about 1 km) gradient zone at 34-35 km depth, which is deeper than in case of GRANU'95 and MVE 90 (30 and 33 km, respectively); (2) The Moldanubian in the central part of profile CEL09 is characterized by the deepest (39 km) and the most pronounced Moho within the whole Bohemian Massif with a strong velocity

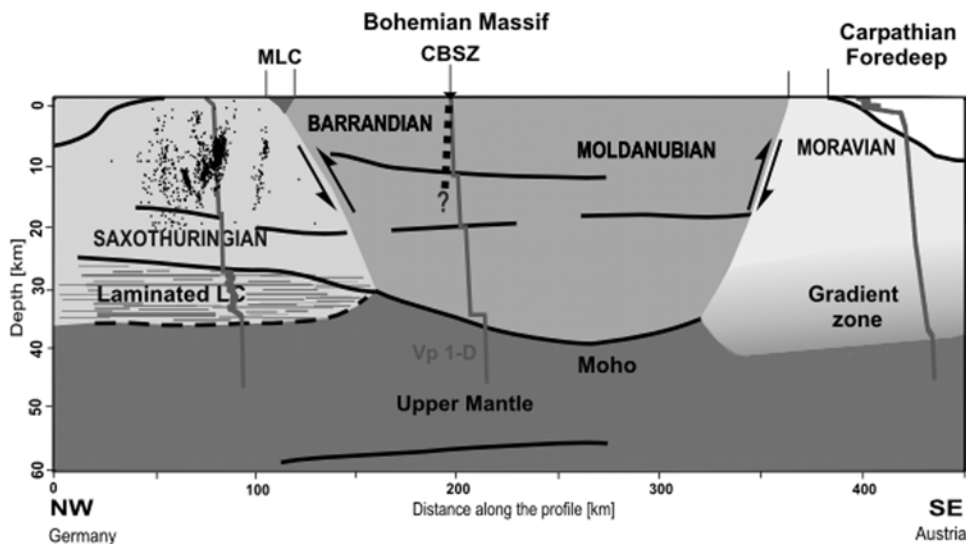


Figure 2.3: Schematic tectonic representation along profile CEL09 (*Hrubcová et al.*, 2005). Dots show locations of hypocentres of the earthquake swarms in the Vogtland/West Bohemia area. Superimposed are 1-D velocity characteristics showing differentiation in the lower crust for different parts of the Bohemian Massif: the Saxothuringian with laminated lower crust dipping southeast; high velocity contrast at the Moho in the Moldanubian; the Moravian with whole-crustal gradient zone. Arrows indicate relative movement along contact zones. MLC – Mariánské Lázně Complex, CBSZ – Central Bohemian Shear Zone. Vertical exaggeration is 1:3.

contrast. In general, *Hrubcová et al.* (2005) found that the average overall compressional velocity of the crust in the Bohemian Massif is about 6.3 km/s.

They furthermore observed reflectors in the middle crust at 7-12 km depth in the Barrandian and partly Moldanubian units, at 17-20 km depth almost throughout the whole model and in the upper mantle at 55-58 km depth in the central part of the Bohemian Massif (Figure 2.3). The latter reflector dips slightly northwest and probably corresponds to a locally sharp reflector found at 56 km depth in the reflection seismic profile 9HR by *Tomek et al.* (1997).

Wilde-Piórko et al. (2005) carried out a receiver function investigation at permanent seismic stations in the Bohemian Massif and surroundings which confirms that the structure of the crust and uppermost mantle differs significantly for the northwestern and southeastern parts of the Bohemian Massif. The crust and upper mantle in the southeastern (~Moldanubian) part have a “normal” structure, without low velocity zones. The crust is 35 to 40 km thick. The crust of the northwestern (~Saxothuringian) part is much thinner (28 to 32 km). Low *S* wave velocities were modelled from receiver functions in the middle crust and in the lower lithosphere. The authors conclude that these features together with recent micro-seismic activity and CO₂ emanation are related to tectonic and magmatic activity in the Eger Rift.

2.3 Lithospheric and upper mantle structure

Lithospheric thickness is a critical parameter in the development of continents. In this study, the seismic definition of the high-velocity Earth's crust and uppermost mantle overlying the low-velocity zone in the upper mantle (asthenosphere) is used for the lithosphere. According to *Babuška and Plomerová* (1992), the lithospheric thickness in the Variscan belt of central Europe varies between about 60 and 150 km with typical values of 100-120 km (Figure 2.4). These depth values were obtained by tomographic studies based on the investigation of relative *P*-wave residuals computed at networks of seismological stations. *Babuška and Plomerová* (1992) furthermore observed a regional thinning of the

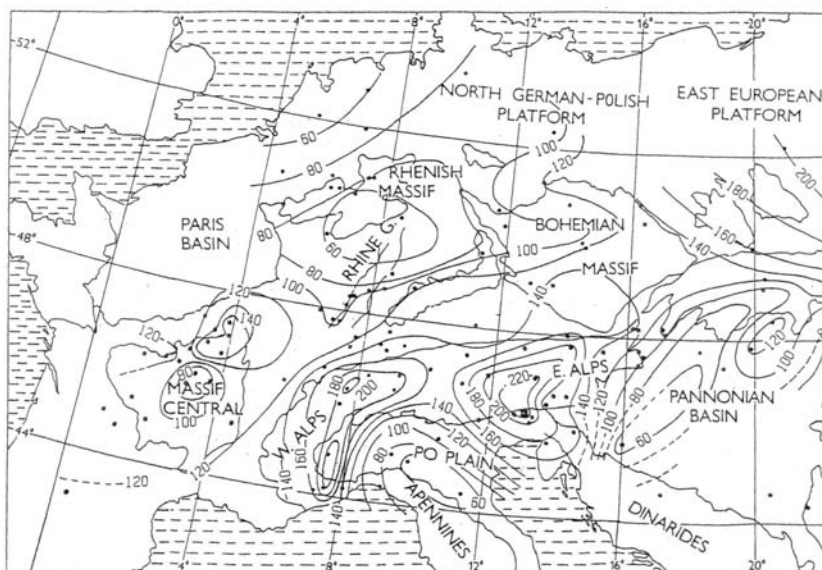


Figure 2.4: Model of lithospheric thickness (isothickness contours in km) beneath central Europe derived from *P*-wave residuals at individual seismological stations (dots) (*Babuška and Plomerová*, 1992).

lithosphere up to about 60-80 km beneath regions of active Tertiary-Quaternary volcanism like the French Massif Central and Rhenish Massif in the Variscan belt of central and western Europe. *Babuška and Plomerová* (2001) introduced a model of thickness and anisotropy of the subcrustal lithosphere of the Bohemian Massif which combines variations of *P*-wave residuals and shear-wave splitting observations (Figure 2.5). In this model the lithosphere is thinning to 80-90 km beneath the contact of the Moldanubian and Saxothuringian units from 90-120 km in the Saxothuringian and 120-140 km in the Moldanubian unit. The model corresponds very well to a model of lithospheric thickness derived from heat flow measurements by *Čermák* (1994). Asthenospheric upwelling beneath the western Eger Rift is also indicated by e.g. *Faber et al.* (1986), *Plomerová and Babuška* (1988), *Passier and Snieder* (1996), and *Plomerová et al.* (1998).

By joint analysis of *P*-wave residuals and shear wave splitting parameters, *Babuška and Plomerová* (1992, 2001) observed large-scale anisotropic structures in the subcrustal lithosphere which are oriented northwestwards in the Saxothuringian and southeastwards in the Moldanubian (Figure 2.5). The authors suggest that the anisotropic structures may represent remnants of successive palaeosubductions of the ancient oceanic lithosphere “frozen” in the subcrustal lithosphere of both units a long time before their Variscan collision. *Babuška and Plomerová* (2001) relate the distinct change in anisotropy to the deep suture which cuts the whole lithosphere thickness and separates the Saxothuringian and Moldanubian units. The observed mixture of anisotropic characteristics within the lower lithosphere south of the surface trace of the Saxothuringian/Moldanubian contact is suggested to reflect underthrusting of a part of the Saxothuringian subcrustal lithosphere beneath the Moldanubian. Alternatively, it could represent a hypothetical remnant of the Early Palaeozoic oceanic lithosphere subducted to the south during collision of the Saxothuringian and Moldanubian units.

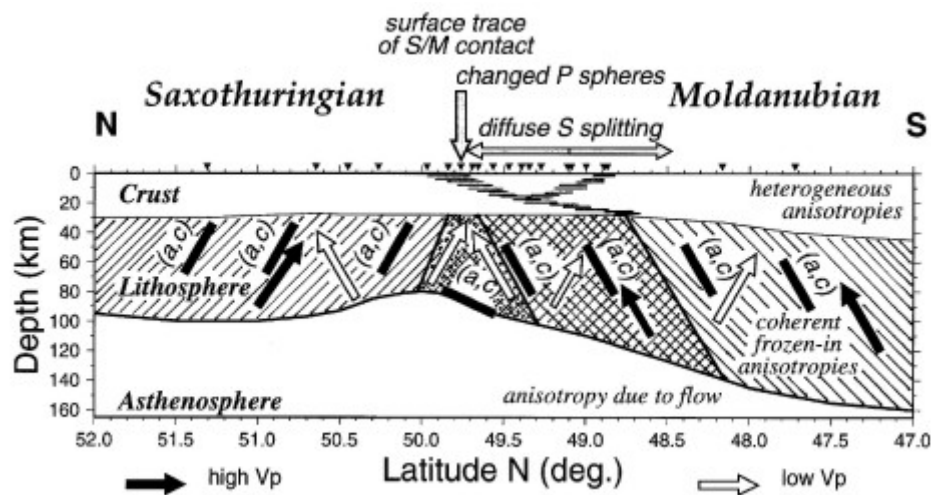


Figure 2.5: Cartoon by *Babuška and Plomerová* (2001) showing a summary of the body-wave observations of anisotropy and their interpretation in terms of large-scale fabric. The regions of “mixed” subcrustal lithospheres of both tectonic units is cross-hatched. A region of lower velocities beneath the surface trace of the Saxothuringian/Moldanubian (S/M) contact is stippled. Thick bars indicate the dipping (a/c) foliation planes of the model peridotite aggregate. DEKORP 4 crustal reflections are schematically shown by dense hatching.

In the receiver function study by *Geissler et al.* (2005) in the western Bohemian Massif, a phase near 6 s delay time was locally observed underneath the region of earthquake swarms and CO₂ degassing which may originate from a discontinuity in approx. 50 to 60 km depth or from a structure within the crust. The authors propose that in the uppermost mantle isolated active magma/fluid reservoirs exist in the depth range of 60 to 30 km (magmatic underplating) (see Figure 2.8).

In two other regions of Variscan origin, namely the French Massif Central and the Eifel (Rhenish Massif), the existence of active mantle fingers was suggested by *Granet et al.* (1995) and *Ritter et al.* (2001), respectively, from seismic tomography studies. *Granet et al.* (1995) suggested that the European Cenozoic Rift System may have a common source of a “plume-like” volcanism in the mantle and predicted the existence of a similar diapiric mantle upwelling also for the Bohemian Massif (Figure 2.6). Active mantle fingers might furthermore be related to release of gas that ascends to the surface. In the French Massif Central, Eifel and western Bohemian Massif, the isotope (He, C, N) composition of ascending gases points clearly to an origin in the European subcontinental mantle. However, structural indications for the existence of a plume beneath the western Bohemian Massif have not yet been clearly observed. Recently, *Achauer et al.* (2005) found indications for an updoming of the asthenosphere beneath the western Eger Rift by teleseismic *P* wave tomography.

Passier and Snieder (1996) obtained a three-dimensional *S* velocity distribution beneath central and southern Germany. It shows low velocities in the uppermost mantle beneath the Eger Rift (80-120 km), the Naab-Pritzwalk-Rostock lineament (80-200 km) and the volcanic Eifel (80-200 km). They suggest the creation of magma in the asthenosphere or at the base of the lithosphere beneath this region.

The upper mantle discontinuity at 410 km depth beneath the western Bohemian Massif was investigated in a receiver function study by *Geissler* (2004). He observed an apparent

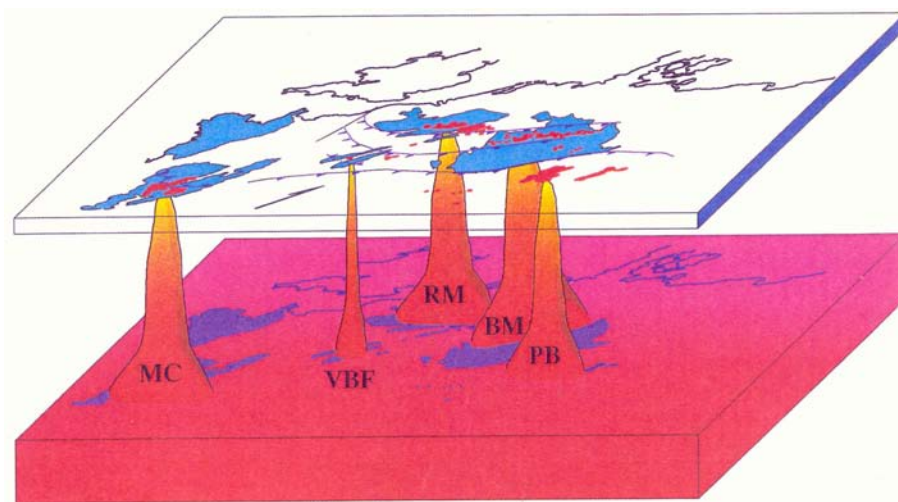


Figure 2.6: Schematic cartoon by *Granet et al.* (1995) showing the upwelling of small-scale mantle fingers beneath the European lithosphere from a thermally and geochemically anomalous layer at ca. 400 km depth. The upper surface of the block shows the distribution of uplifted Variscan basement massifs and Tertiary-Quaternary volcanic fields.

deepening of the 410 km discontinuity, which might be the result of lower seismic velocities in the upper mantle compared to the *IASP91* reference model (Kennett, 1991; Kennet and Engdahl, 1991). However, a real deepening could not be excluded by his study. Another receiver function study by Grunewald *et al.* (2001) focuses on the Eifel volcanic region in the Rhenish massif of western Germany. They observed a 150 km wide and 20 km deep depression of the 410-km discontinuity in the upper mantle beneath the Eifel region. Their data set extends to the western Bohemian Massif for the discontinuities of the mantle transition zone at 410 and 660 km depth. However, they do not observe any anomaly of the discontinuities of the mantle transition zone in this region.

2.4 CO₂ emanations and fluid investigations

From investigation of the mantle-related CO₂-dominated gas flux in the area of the Cheb basin, Weinlich *et al.* (1999) claimed the existence of a magmatic body in the subcontinental mantle. The fluid activity connected with this body is discussed as a probable trigger mechanism for the earthquake swarms. Evidence for CO₂ degassing from fluid reservoirs in the subcontinental lithospheric mantle was found in three areas of magmatic activity within the European Cenozoic Rift system: the French Massif Central (Matthews *et al.*, 1987), the Eifel volcanic fields (Griesshaber *et al.*, 1992; May, 2002) and the western Eger Rift (O’Nions *et al.*, 1989; Weinlich *et al.*, 1999, 2003; Bräuer *et al.*, 2004).

The permeable upper crust beneath the area under investigation enables high permanent CO₂ transport through the upper crust. Hydrological, geochemical and isotope investigations at springs and mofettes in the Vogtland/NW-Bohemia region give evidence of a fluidal response to the seismogenic processes in the swarm earthquake area of Nový Kostel (e.g. Heinicke and Koch, 2000; Bräuer *et al.*, 2003; Koch *et al.*, 2003). An increased CO₂ emission is assumed to be responsible for different phenomena such as anomalous behaviour of groundwater level, hydrostatic pressure, free gas flow and radon emission (Heinicke and Koch, 2000; Koch *et al.*, 2003).

Weinlich *et al.* (1999) and Bräuer *et al.* (2005) classify three gas escape centres (Figure 2.7): 1. Cheb basin/Františkovy Lázně, 2. Mariánské Lázně and 3. Karlovy Vary. From the independent behaviour of the ³He/⁴He ratios in the three gas escape centres, Bräuer *et al.* (2005) conclude that there might be small isolated magmatic reservoirs present (not a continuous magma body as suggested by Weinlich *et al.* (1999)). The observed increase of the ³He/⁴He ratio beneath the Cheb basin degassing centre during the past decade points to an increased magmatic activity and an intrusion of fresh magma into the lower crust and might thus be an indicator of ongoing magmatic processes in this area (Bräuer *et al.*, 2005).

Beneath the presently non-volcanic Mammoth mountain in eastern California, magmatic unrest was detected with similar symptoms as in Vogtland/NW Bohemia, like swarm earthquakes, ground deformation, emission of magmatic CO₂ and fumarole gases with elevated ³He/⁴He ratios (Hill and Prejean, 2005). The authors suggest that the unrest is caused by the episodic release of a volume of CO₂-rich hydrous magmatic fluid derived from magmatic intrusions at mid-crustal depths.

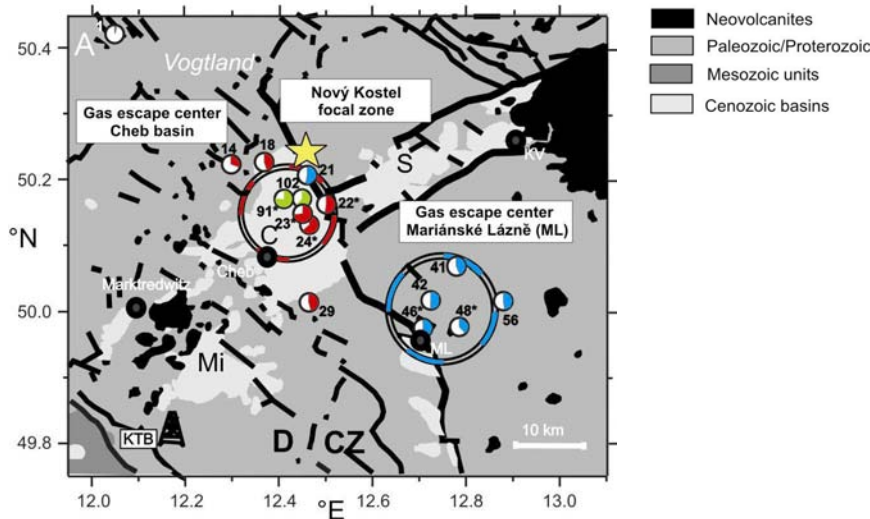


Figure 2.7: Distribution of $^3\text{He}/^4\text{He}$ ratios in the gas escape centres of the Eger Rift. The locations where $^3\text{He}/^4\text{He}$ ratios have increased since 1992/93 are shown in red, those with nearly equal values in blue, and two locations which were studied for the first time in green. Symbols and abbreviations: KTB position of the German Continental Deep Drilling site, KV Karlovy Vary, D Germany, CZ Czech Republic, Mi Mitterteich basin, C Cheb basin, S Sokolov basin (Bräuer *et al.*, 2005).

2.5 Xenolith investigations

In a thermobarometric and geochemical study, Geissler *et al.* (2006) analysed upper mantle and lower crustal xenoliths from a Quaternary tephra deposit in Mýtina (age 0.3 to 0.5 Ma) near the Quaternary scoria cone Železná Hůrka. The upper-mantle xenoliths are dominated by wehrlites, clinopyroxenites, and hornblendites, while crustal xenoliths are dominated by rock types similar to crystalline country rock in the surroundings. Only one lower-crustal sample was found. Most of the analysed samples are cumulates of alkaline melts, fragments of pegmatitic veins, or rocks from a metasomatic upper mantle. The metasomatized samples from subcrustal regions give evidence for a lithospheric mantle strongly altered and depth-structured by magmatic/fluid processes. This metasomatism can cause slower than typical uppermost-mantle seismic velocities in a greater area and might help to explain observed seismic anomalies.

2.6 Thermal structure

Relatively low heat flow values of about $50\text{--}60\text{ mW/m}^2$ were observed in the southeastern and central parts of the Bohemian Massif, i.e. in areas where crustal thickness attains its maximum close to 40 km (Čermák, 1994). Relatively high heat flow values ($70\text{--}80\text{ mW/m}^2$, locally as high as 90 mW/m^2) observed in the Eger Rift are explained by an increased heat supply from below the crust associated with deep seated processes of rejuvenation during the Alpine-Carpathian orogenesis. However, the radiogenic heat of Late Variscan granitic plutons probably contributes here to the observed high heat flow by

up to 30-40 mW/m² (Čermák, 1994). Therefore it is difficult to extrapolate the regional surface heat flow data to depth and to estimate the regional Moho heat flow and temperatures (Förster and Förster, 2000).

The heat flow value measured at the KTB superdeep borehole corresponds well to the average background value of about 80 mW/m² in southern Germany. However, a considerably higher than expected geothermal gradient was observed. The data show that heat production is controlled by lithology, and there is only a slight overall decrease of heat production with depth (Emmertmann and Lauterjung, 1997).

In the thermobarometric and geochemical study by Geissler *et al.* (2006), p-T estimates for xenoliths from the Quaternary tephra deposit in Mýtina near the Quaternary scoria cone Železná Hůrka also indicate higher temperatures within crust and uppermost mantle than proposed by regional geotherms by Čermák (1994).

2.7 Further models of the investigation area

From receiver function studies, xenolith studies and a compilation of previous studies, Geissler *et al.* (2005) and Geissler *et al.* (2006) developed a model of the present lithosphere for the NW Bohemian Massif (Figure 2.8). It describes the lithosphere-asthenosphere interaction beneath the western Eger Rift with reflectors in the lower crust, fluid reservoirs at subcrustal and possibly lower crustal depth, metasomatic upper mantle, assumed updoming of the asthenosphere and CO₂ channels. According to the model, the crust-mantle boundary is overprinted by magmatic and tectonic processes. A shear wave velocity model is proposed for the western Eger rift area based on receiver function

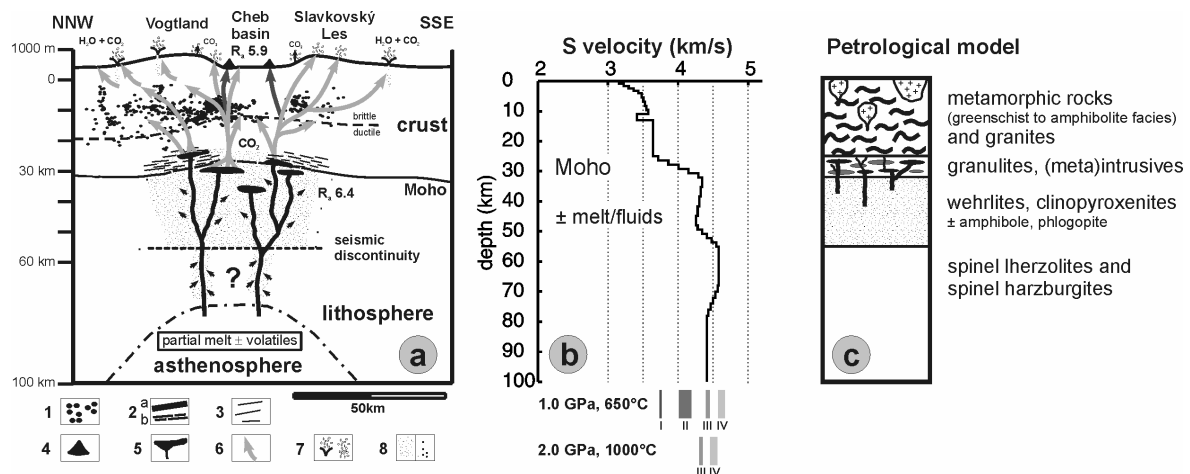


Figure 2.8: Model of the lithosphere beneath the western Eger Rift (Geissler *et al.*, 2006). **(a)** Cartoon illustrating the asthenosphere-lithosphere interaction in the Vogtland/NW-Bohemia region. Legend: 1 - seismogenic zones, 2 – a: Moho, b: disrupted Moho, 3 – reflectors in the lower crust, 4 – scoria cone, 5 – fluid/magma reservoirs, 6 – CO₂ channels, 7 – mineral springs and mofettes, 8 – metasomatic upper mantle. **(b)** Proposed present-day shear wave velocity model beneath the western Eger Rift where an additional phase at 6 s delay time occurs in the receiver function data. Also shown are the ranges of shear wave velocities for different (ultra-)mafic rock types at different temperature-pressure conditions. **(c)** Petrological crustal section derived from the xenolith study and local surface geology.

observations and seismic velocities of the investigated xenoliths. Furthermore, the xenolith study combined with local surface geology led to a petrological crustal and lithospheric model.

Another model was proposed by *Babuška et al.*, 2003 (Figure 2.9) demonstrating the complexity of assumed crustal and upper mantle structures, including the suggestion of traces of palaeosubduction zones.

Further models of the region regarding mechanisms of gas emanation were provided by e.g. *Weinlich et al.* (1999) and *Bräuer et al.* (2003).

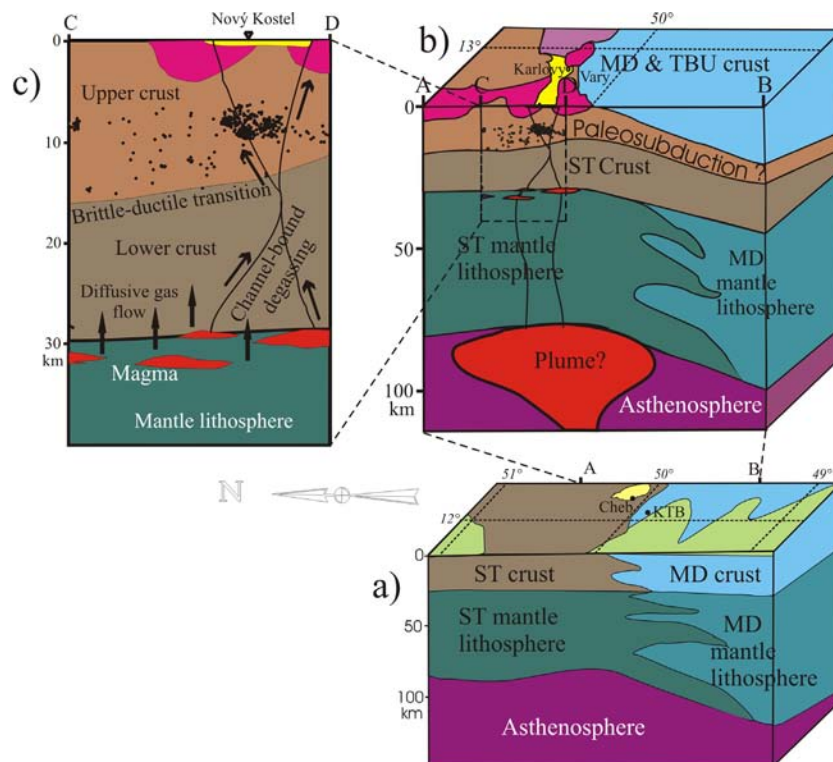


Figure 2.9: Schematic diagrams showing the tectonic situation in the western Bohemian Massif (*Babuška et al.*, 2003). **(a)** N-S section of the deep structure of the Saxothuringian-Moldanubian contact based on observations of seismic anisotropy. **(b)** Close-up of the rear of the lower diagram shows a hypothetical plume head beneath the western Eger Rift, and a hypothetical palaeosubduction of Saxothuringian crust beneath the Moldanubian and Teplá-Barrandian. Granite massifs (red) are also schematically shown. **(c)** Close-up of the distribution of foci of earthquake swarms in Nový Kostel-Kraslice region, as shown in panel (b). Gas flow from the mantle may play an important role in triggering earthquake swarms.

Chapter 3

Data

3.1 The passive seismic experiment BOHEMA

Between October 2001 and February 2004, the international passive seismic experiment BOHEMA (Bohemian Massif Heterogeneity and Anisotropy) was carried out, with its main period of recordings in 2002 (*Plomerová et al.*, 2003; *Babuška et al.*, 2003). It was an initiative of Czech, French and German Scientists from 10 institutions who form the BOHEMA Working Group (see Appendix A.3). The project was aimed at studying the structure and dynamics of the lithosphere and upper mantle with different seismic techniques (high resolution tomography, 3D anisotropy, receiver function analysis) as well as xenolith investigations. Altogether, 61 permanent seismic stations in the region together with 84 temporary stations deployed for time spans between 5 months up to two years could be used. Figures 3.1 and 3.2 show the station distribution of the BOHEMA experiment, Appendix A.1 gives the corresponding station parameters. The array of seismological stations forming the BOHEMA network covered a territory of approximately 270 km in N-S and 150 km in E-W direction. The aperture of the array resulted from demands of tomographic research of the crust and upper mantle down to 250 km. The network was centred on the geodynamically active part of the western part of the Bohemian Massif, around the intersection of the Eger Rift with the Mariánské Lázně Fault. The experiment was oriented with its long axis perpendicular to the strike of major tectonic units and to the Eger Rift. Three-component short-period stations represent about 1/3 of the network, while broad-band stations constitute the remaining 2/3. Average spacing of stations was about 30 km or less, especially in the central part of the array, where the station spacing was between 10 and 15 km. The stations provided continuous recordings with exception of local permanent networks (e.g. WEBNET, KRASNET) focused primarily on monitoring local seismic activity in the Vogtland/West Bohemia region. While the data quality of permanent Czech and German stations was generally high, data quality of the temporary stations varied considerably. The data amount or quality of seven temporary stations was not sufficient for further analysis. However, the BOHEMA data set as a whole provides a very large amount of good quality seismic data for investigation of the northwestern Bohemian Massif.

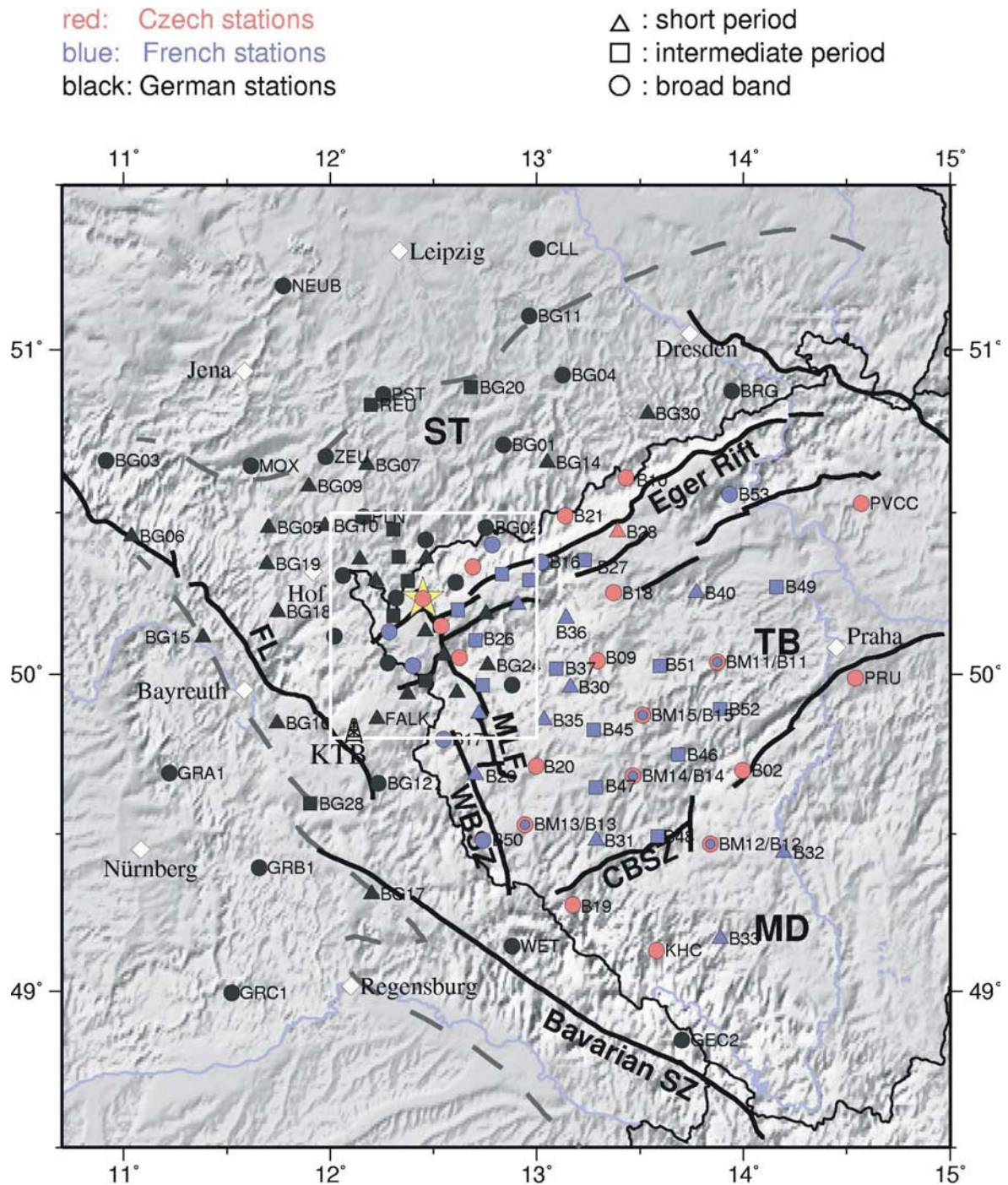


Figure 3.1: Distribution of seismic stations of the BOHEMA experiment used for receiver function analysis. The area within the white rectangle is shown again in an enlarged map in Figure 3.2. Also shown are the major tectonometamorphic units of the Bohemian Massif: Saxothuringian (ST), Moldanubian (MD) and Teplá-Barrandian (TB) block. Major faults are the Eger Rift faults, Mariánské Lázně fault (MLF), West Bohemian Shear Zone (WBSZ), Central Bohemian Shear Zone (CBSZ), Frankonian Lineament (FL) and Bavarian Shear Zone. Grey dashed line: outline of the Bohemian Massif; yellow star: main earthquake swarm area; KTB: German Continental Deep Drilling boreholes.

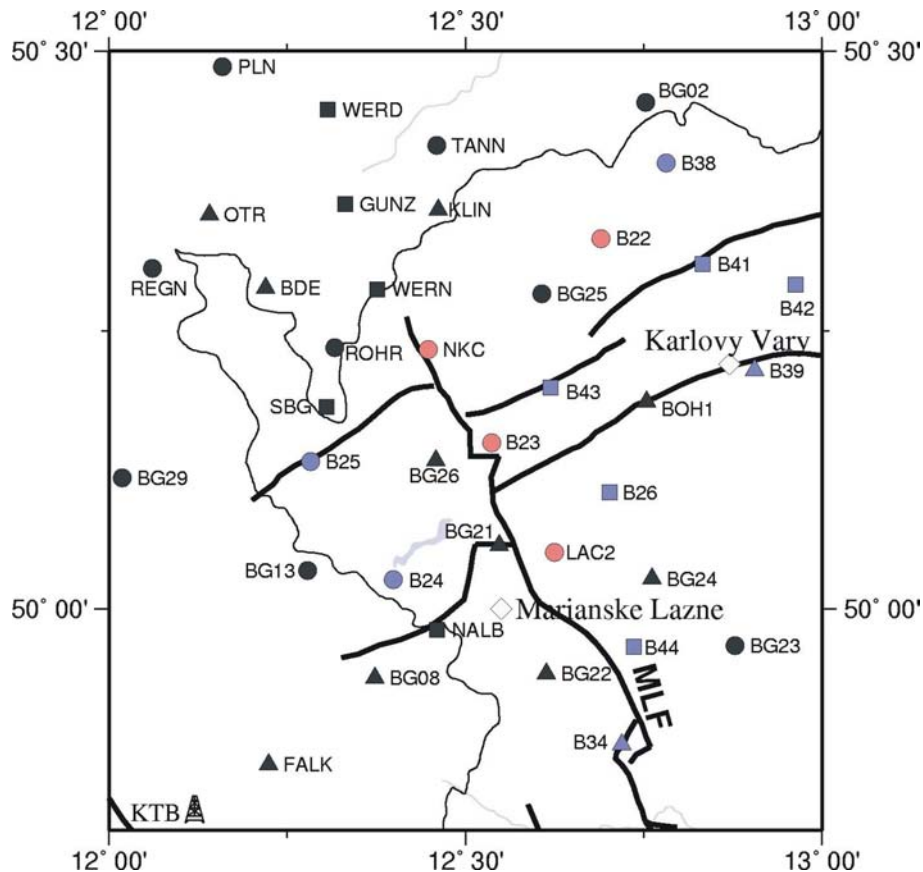


Figure 3.2: Enlarged detail of Figure 3.1 showing the BOHEMA stations used for receiver function analysis in the central part of the investigated region.

29 of the temporary stations were provided by the Geophysical Instrument Pool Potsdam (GIPP). Apart from deploying and maintaining the seismic stations, the storage discs had to be exchanged regularly, the data had to be converted into an uniform *miniseed* format and archived in the GEOFON data archive at GFZ Potsdam¹.

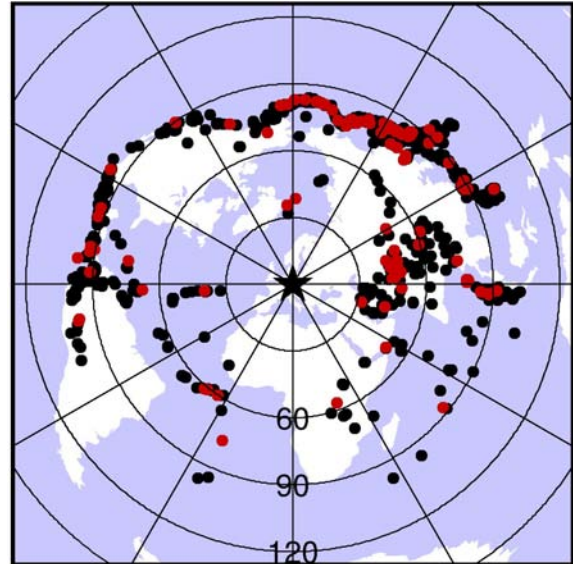
3.2 Data set for *P* receiver function analysis

For *P* receiver function analysis, the stations shown in Figures 3.1 and 3.2 were used. The selected teleseismic events have epicentral distances between 30°-95°, magnitudes larger than 5.3 for temporary stations and larger than 6.0 for permanent stations (due to the longer available recording time span) and a clear *P* onset with a high signal-to-noise ratio. The selected events are listed in Appendix B.1; their epicentre distribution is shown in Figure 3.3. A total number of 254 teleseismic earthquakes recorded by 110 broad band and short period BOHEMA stations have been used to estimate lithospheric and upper mantle structure of the western Bohemian Massif using the *P* receiver function technique, which led to more than 5000 *P* receiver function traces. Additionally, approx. 3500 receiver

¹ The GEOFON Data Center at GFZ Potsdam permits access to a large unified archive of permanent and temporary seismic network data via the internet (<http://www.gfz-potsdam.de/geofon>).

function traces obtained by *Geissler et al.* (2005) were used for investigation of the mantle transition zone (Chapter 7) to complement the BOHEMA data set (for station parameters and event list see Appendices A.2 and B.2, respectively).

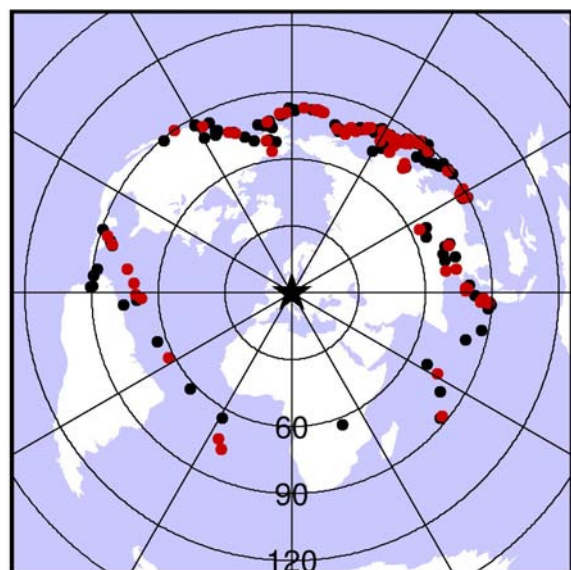
Figure 3.3: Distribution of teleseismic events used for *P* receiver function analysis in this study. Coordinates and origin times are listed in Appendices B.1 and B.2. The black star marks the location of the investigation area. Events that occurred within the recording time span of the BOHEMA experiment are shown by red dots. Events that occurred before and after that time span are coloured black and were recorded by permanent stations and/or by stations of the experiment of *Geissler et al.* (2005), whose data were used for investigation of the mantle transition zone. Due to the very long time span included by *Geissler et al.* (2005), many of the black coloured events were only recorded by few stations that operated during that time span.



3.3 Data set for *S* receiver function analysis

For *S* receiver function analysis, the selected events lie within an epicentral distance range of 60° – 85° and have magnitudes of 5.7 and higher (Figure 3.4, Appendix B.3). A clear *S* onset with high signal-to-noise ratio was a further criterion to select events. A total number of 264 teleseismic earthquakes has been utilized to investigate the lithosphere–asthenosphere boundary (Chapter 6) in the western Bohemian Massif. Additionally, data obtained by *Geissler et al.* (2005) were used to complement the BOHEMA data set. Both data sets together result in a total number of approximately 5700 *S* receiver function traces.

Figure 3.4: Distribution of teleseismic events used for *S* receiver function analysis in this study. Coordinates and origin times are listed in Appendix B.3. The black star marks the location of the investigation area. Events that occurred within the recording time span of the BOHEMA experiment are shown by red dots. Events that occurred before and after that time span are coloured black and were recorded by permanent stations and/or by stations of the experiment of *Geissler et al.* (2005).



Chapter 4

Methods

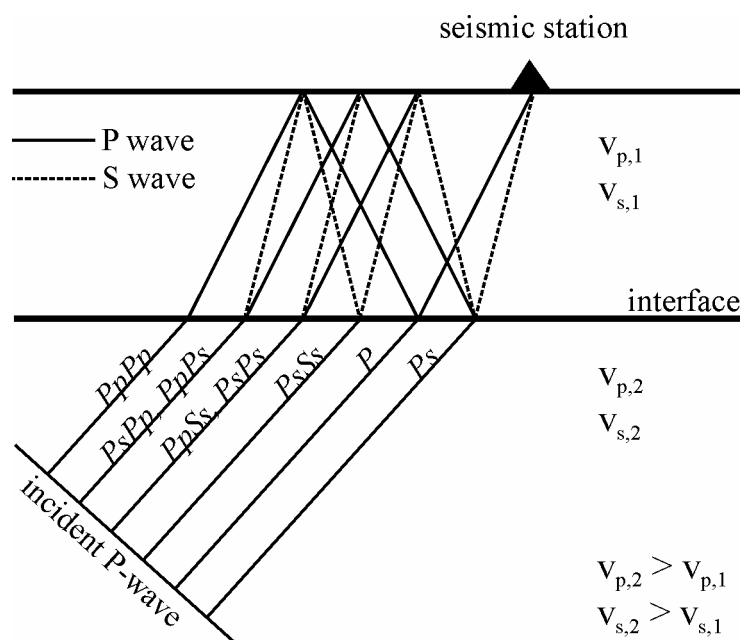
4.1 *P receiver function method*

Seismic phases converted from *P* to *S* underneath the receiver are particularly useful in studies of the crust and mantle (Figure 4.1). Due to the lower velocity of *S* waves in comparison to *P* waves, the converted *S* waves arrive after the onset of the direct *P* wave within the *P* wave coda. By extracting the small *P*-to-*S* (*Ps*) converted energy from the large *P* wave and measuring the time delay between the two phases it is possible to “map” seismic discontinuities beneath stations.

The frequency band of teleseismic body waves covers the range of one to several seconds and thus lies between controlled source methods (several Hertz) and surface-wave methods (many seconds).

The theoretical background of the technique was described e.g. by *Vinnik (1977)*, *Burdick and Langston (1977)*, *Langston (1979)*, *Owens et al. (1984)*, *Kind and Vinnik (1988)*, *Kosarev et al. (1993)*, and *Zandt et al. (1995)*.

Figure 4.1: Sketch of a model with a horizontal layer over a half space. A plane *P* wave is incident upon the interface from below and generates *P*-to-*S* converted waves and many reverberations between the free surface and the interface.



The essential points in processing the observed data are:

1. If data from different types of seismic sensors and/or short-period seismic stations with different frequency responses are used, as is the case in the present investigation, it is necessary to reconstitute the broad-band ground displacement in order to make the signals better comparable. However, restoring longer periods from short period instruments is only possible for large magnitudes and depends on the transfer function of the sensor and the sampling rate. Furthermore, long period noise is also increased by restitution. The main frequencies of teleseismic body waves lie between 1 Hz and 0.1 Hz. High-pass filtering may be necessary after restitution to suppress long period noise.
2. Rotation of the original Z , NS and EW components of the P -wave group into the ray coordinate system L , Q and T . L contains mainly P -energy, Q mainly SV -energy, and T mainly SH -energy. The theoretical back azimuth is used to determine the radial component, and the angle of incidence is determined from the radial-vertical covariance matrix of the P -signal of the original data. The Q -component contains the information of main interest for this investigation: the P -to- SV converted energy. This energy depends mainly on the S -velocity distribution underneath the station (*Kind et al.*, 1995).
3. Deconvolution of the Q - and T -components with the P -signal on the L -component in the time domain. Deconvolution is used as a source-equalization procedure because it excludes effects of the rupture process and of the ray-path below the converting interfaces. Differences in the source durations and magnitudes are equalized, permitting the summation of many different events. Amplitude ratios are preserved by this procedure. The P waveform on the L -component is used to generate the time-domain wave shaping deconvolution filter. After deconvolution, all components are normalized to the maximum of L (*Kind et al.*, 1995).
4. Summation of many events from a large distance and azimuth range. Before summation, the data are corrected for distance move-out for direct P -to- S conversions using the *IASP91* reference model (*Kennett*, 1991; *Kennett and Engdahl*, 1991) and a standard slowness of 6.4 s per degree, corresponding to a reference epicentral distance of 67° (*Yuan et al.*, 1997). Thus, summation of records from different distances is possible in order to improve the signal-to-noise ratio and therefore the stability and reliability of the observations.

The processed receiver functions are usually filtered in order to enhance signals and to suppress noise. The choice of an inappropriate filter can heavily influence the information contained in the recorded data. Since the recorded signals have to be assumed to be mixed-phase, the processing of the data avoids pre-filtering of the data.

The receiver function technique has been successfully applied in numerous studies to investigate the crustal and upper mantle structure at regional scale, e.g. in central Europe (*Kind et al.*, 1995; *Grunewald et al.* 2001; *Wilde- Piórko et al.*, 2005), in Tibet (*Yuan et al.*, 1997; *Kosarev et al.*, 1999, *Kind et al.*, 2002), in North America (e.g. *Ramesh et al.*, 2002; *Rychert et al.*, 2005)), in the Middle East and North Africa (*Sandvol et al.*, 1998; *Hofstetter and Bock*, 2004), for the Hawaiian and other oceanic mantle plumes (*Li et al.*, 2000; *Li et al.*, 2003a) and in the Andes (*Yuan et al.*, 2000, 2002).

The classic receiver function technique used in the present study neglects indications of anisotropy of the earth medium. Signals in the T (transverse) component of the receiver function are usually explained by lateral heterogeneity of the isotropic medium, in particular, by dipping layers (*Langston*, 1979; *Savage*, 1998). By stacking receiver

functions from different distances and directions, effects of lateral structural variation are suppressed, and an average crustal model is obtained.

If a crustal velocity model is known for the investigated area, crustal thickness can be calculated from the measured delay times of the Moho P_s conversion. However, the crustal thickness estimated only from the delay time of the Moho P -to- S converted phase trades off strongly with the crustal v_p/v_s ratio. The ambiguity can be reduced significantly by incorporating the later multiple converted phases, namely, the $PpPs$ and $PpSs+PsPs$ (Zandt *et al.*, 1995, Zhu and Kanamori, 2000) (see Figure 4.1). In this thesis, the method of Zhu and Kanamori (2000) was used to calculate the depth of the Moho and the average crustal v_p/v_s ratio. In their grid search algorithm, the best estimations of crustal thickness and v_p/v_s ratio are found when the three phases are stacked coherently and thus reach the maximum-stacked amplitude. In this study, the grid search was carried out for Moho depths between 20 to 60 km and v_p/v_s ratios between 1.5 and 2.0. The direct P_s conversion from the Moho was weighted 0.5, the multiple conversions $PpPs$ and $PpSs+PsPs$ were each weighted 0.25 following the suggestions of Zhu and Kanamori (2000).

However, direct conversions and multiples sample different paths within the crust. The direct Moho conversions sample the Moho about 5-10 km away from the station, whereas the crustal multiples sample the Moho over a distance of 5-30 km from the station (Zandt *et al.*, 1995). By using average values over all back azimuths at single stations, a spatial low pass filter effect is obtained. Thus we get average crustal thicknesses beneath the stations.

4.2 S receiver function method

While the receiver function method analysing P -to- S conversions (P receiver function method) has been used successfully for quite a long time to investigate the crust and mantle structures, the study of S -to- P (Sp) conversions (Figure 4.2) is not a routine method yet. Although there are early works using S -to- P conversions (e.g. Båth and Stefánsson, 1966; Burdick and Langston, 1977; Sacks and Snoke, 1977; Bock and Kind, 1991), the use of these phases has only recently become more popular after receiver function analysis, meaning coordinate rotation and deconvolution, was also applied to the S waves in order to isolate the S -to- P converted phases from the incident S phases (Farra and Vinnik, 2000;

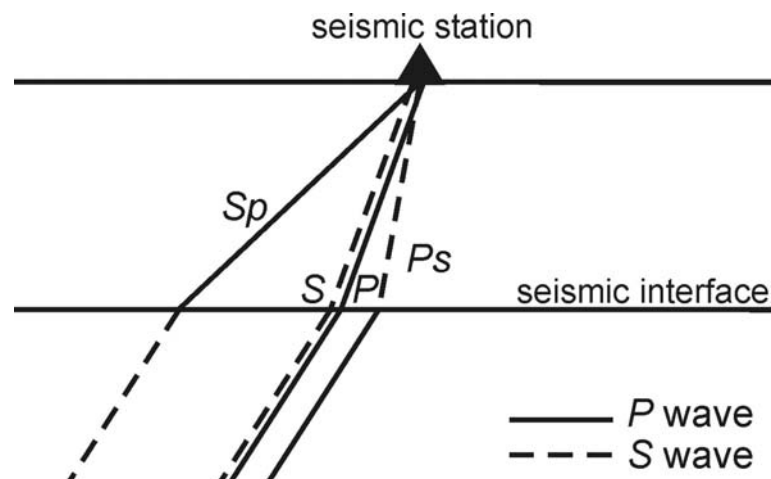


Figure 4.2: Ray paths of Sp and Ps converted phases.

Vinnik and Farra, 2002; Vinnik *et al.*, 2003; Vinnik *et al.*, 2004). Hence, this method is called *S* receiver function method. It was applied by Li *et al.* (2004), Wittlinger *et al.*, 2004; Kumar *et al.* (2005a, 2005b, 2006), and Sodoudi *et al.* (2006a, b) for mapping particularly the lithosphere-asthenosphere transition. A comprehensive overview about the *S* receiver function method applied to synthetic seismograms is given by Yuan *et al.* (2006).

As the converted *P* leg of the ray travels with a higher wave velocity than the direct *S* leg, *S*-to-*P* converted phases arrive at the receiver prior to the *S* wave onset, while the multiple reverberations appear after the *S* onset. Boundaries such as the lithosphere-asthenosphere transition, which are often obscured in the *P* receiver functions by crustal multiple reverberations arriving in the same time interval, can thus be better observed in the *S* receiver functions.

However, due to the ray geometry, the use of the *S* receiver functions has some limitations. Converted *Sp* phases from the lithosphere-asthenosphere boundary are best observed at epicentral distances between 60 - 85° (Faber and Müller, 1980; Yuan *et al.*, 2006). Beyond 85°, *SKS* waves arrive in front of *S*. *S* receiver functions are much noisier than *P* receiver functions, primarily because they arrive after the *P* wave. *S* waves have a lower frequency content, hence a lower spatial resolution than *P* waves.

The conversion coefficients of the Moho for *Sp* conversions are negative and of the lithosphere-asthenosphere transition positive, i.e. the sign of amplitudes is opposite to those of *Ps* conversions. The sign of amplitudes depends on the definition of *Z* components (downward positive), the sign of the velocity contrast at the discontinuities (downward positive at Moho, downward negative at lithosphere-asthenosphere transition) and the polarity of the triggering phase. The absolute conversion coefficients of *Sp* phases decrease with increasing epicentral distance (Yuan *et al.*, 2006). For epicentral distances of 60 - 85°, the conversion coefficient of the Moho varies between -0.165 and -0.12, and that of the lithosphere-asthenosphere transition between 0.043 and 0.024 (Yuan *et al.*, 2006).

In this study, *S* receiver functions were obtained from waveforms of *S* waves in order to investigate the lithosphere-asthenosphere transition. Initially, the broad-band ground displacement was restituted for the different seismic sensors.

The rotation into the ray coordinate system was performed in two steps. First, the seismograms in the *Z-N-E* System were rotated into the *Z-R-T* system using the theoretical back azimuth of the station-event combination. After this step a visual quality check was carried out: if the *R* component which contains most of the *SV* energy of the event showed *SV* energy at the time of the *S*-onset with a high signal-to-noise ratio, the event was chosen for further processing. If no *SV* energy was visible on the *R* component, the event was omitted (Figure 4.3). In the second step, the *Z* and *R* components of the mantle *S* phase are rotated into the ray coordinate system *L* and *Q* components, which contain the *P* and *SV* wave energy, respectively. The incidence angle for the rotation was determined by minimizing the amplitudes of *L* components at *S* arrivals.

Time domain wave shaping deconvolution of the *L* component with the signal on the *Q* component is then used for source equalisation and elimination of travel path effects. The resulting *L* component, which contains only *S*-to-*P* converted phases, is named *S* receiver function. Thus, 1043 traces of *S* receiver functions have been obtained in this study.

Since Sp conversions are generally weak, we need the summation of many individual records. Before stacking of the data, moveout correction is applied to the obtained S receiver functions to correct for the time dependence with epicentral distance. A reference slowness of $6.4 \text{ s}/^\circ$ and the IASP91 reference model (*Kennet and Engdahl, 1991*) are used. The time axis and sign of amplitudes are reversed so that the S -to- P conversions have positive arrival times and can be compared to the results of P receiver function analysis.

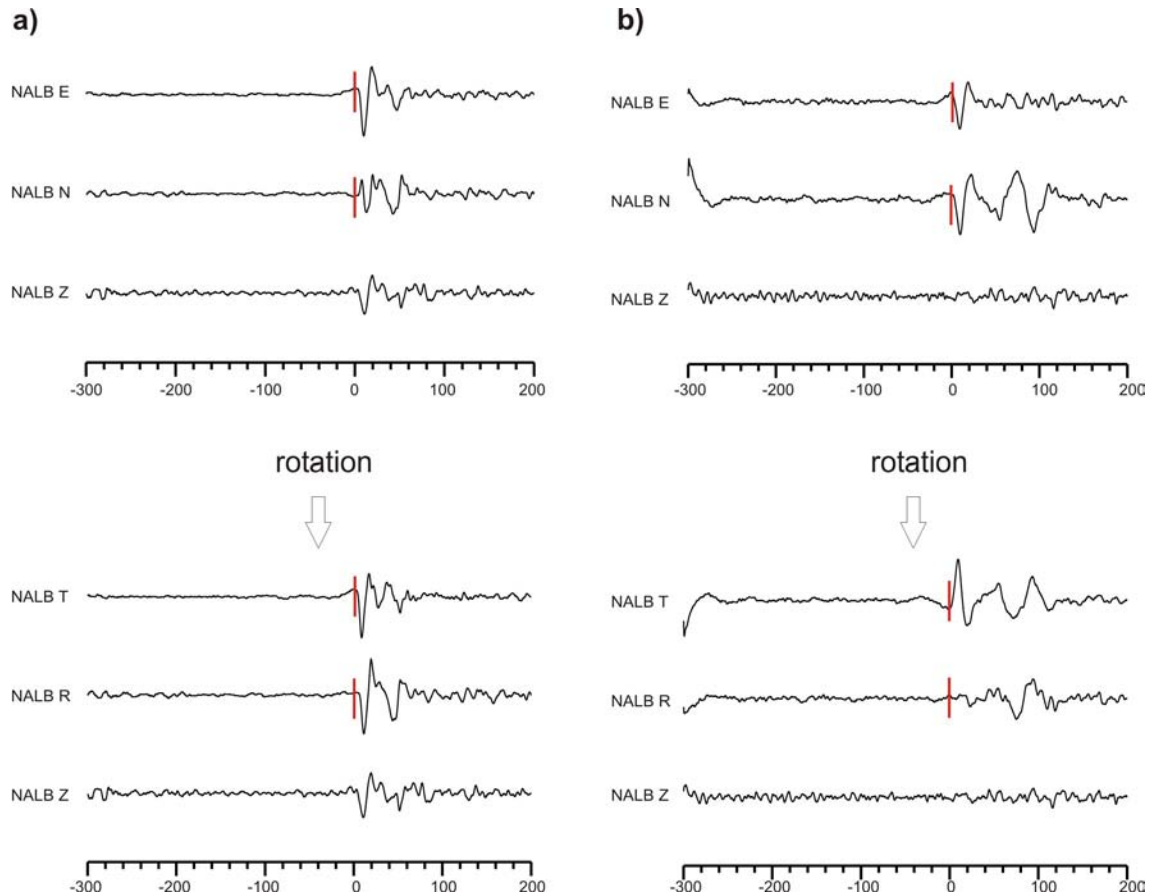


Figure 4.3: Rotation from the Z-N-E system into the Z-R-T system by theoretical back azimuth. After this step, a quality check of the data was carried out regarding the signal-to-noise ratio of SV energy on the R component. The time axis is set to zero at the time of the S onset. **a)** strong SV signal on R component at the time of the S onset, therefore the event is chosen for further processing. **b)** weak SV energy on the R component, event is omitted.

Chapter 5

Moho depths and crustal v_p/v_s ratios

5.1 Nature of the Moho

In the Earth's crust, P wave velocities are approx. 6 to 7 km/s. Below the Mohorovičić discontinuity (Moho), the P wave velocity abruptly increases to 8 km/s, which is an indication for a very sharp boundary between crustal rocks (in continental crust mainly granitic rocks and gabbro) and mantle rocks (peridotite). The Moho comprises major changes in chemical, rheological and seismic properties of the rocks. It was discovered by Andrija Mohorovičić in 1909 (*Mohorovičić*, 1910). Underneath continents, the Moho is usually between 30 and 50 km deep. The depth of Moho is an important parameter to characterize the overall structure of the crust and can often be related to geology and tectonic evolution of the region.

5.2 Data examples

Figure 5.1 shows data examples of P receiver functions recorded at stations near the intersection area of Eger Rift and Regensburg-Leipzig-Rostock zone (stations NALB, B24, NKC) as well as in the Saxothuringian unit (station BG07), Teplá-Barrandian (station B09) and Moldanubian unit (station B12/BM12). A strong positive signal is visible in the data of all stations at 3.0 to 4.5 s delay time, which is interpreted as the P -to- S converted signal from the Moho discontinuity. Accordingly, the positive signal at 11 to 13 s delay time and the negative signal at 15 to 17 s are interpreted as multiple reverberations within the crust (phases $PpPs$ and $PsPs+PpSs$, respectively).

5.3 Observations

5.3.1 Ps delay times of the Moho discontinuity

The delay time of the P -to- S converted phase of the Moho discontinuity was read from the sum trace of each station of the BOHEMA passive seismic experiment (Figures 5.2 and 5.3). The obtained delay times vary between 3.0 and 4.5. The Moho delay times are displayed together with the piercing points of the individual rays at an interface at 30 km

depth to visualize where the obtained information originates. The piercing points have a horizontal distance to the recording station of 5-10 km.

The obtained delay times of the Moho *Ps* conversion reveal rather clear structures:

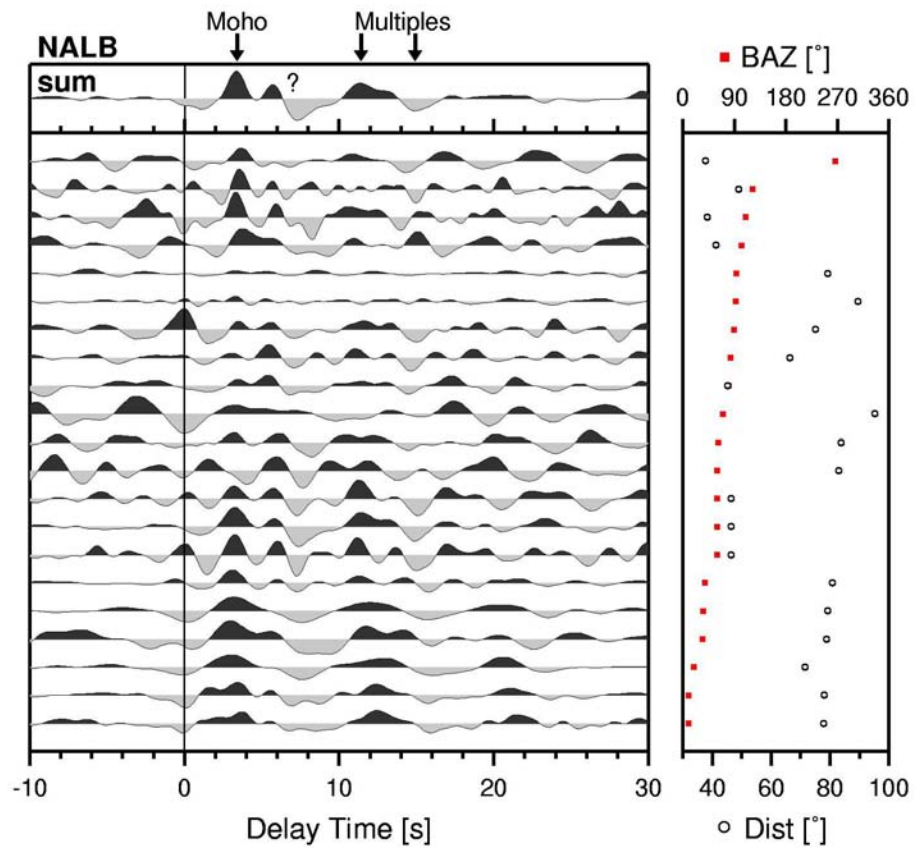
- In the Saxothuringian unit, delay times vary between 3.3 and 4.1 s. However, the majority of stations shows values around 3.5 to 3.6 s.
- In the Teplá-Barrandian unit, values increase from 3.4 s in the NW to 4.1 s in the SE.
- Beneath the western Eger Rift, delay time values clearly decrease up to approx. 3.0 s as was already indicated by *Geissler et al.* (2005).
- In the Moldanubian unit between the Central Bohemian and Bavarian Shear Zone, the delay time strongly increases to values of 4.3 to 4.5 s.

Along the Eger Rift towards ENE, unfortunately there is not enough data to investigate crustal thickness beneath the rift. However, the existing sparse data shows that there are no indications for an anomaly along the Eger Rift comparable to the delay time anomaly beneath the westernmost part of the rift.

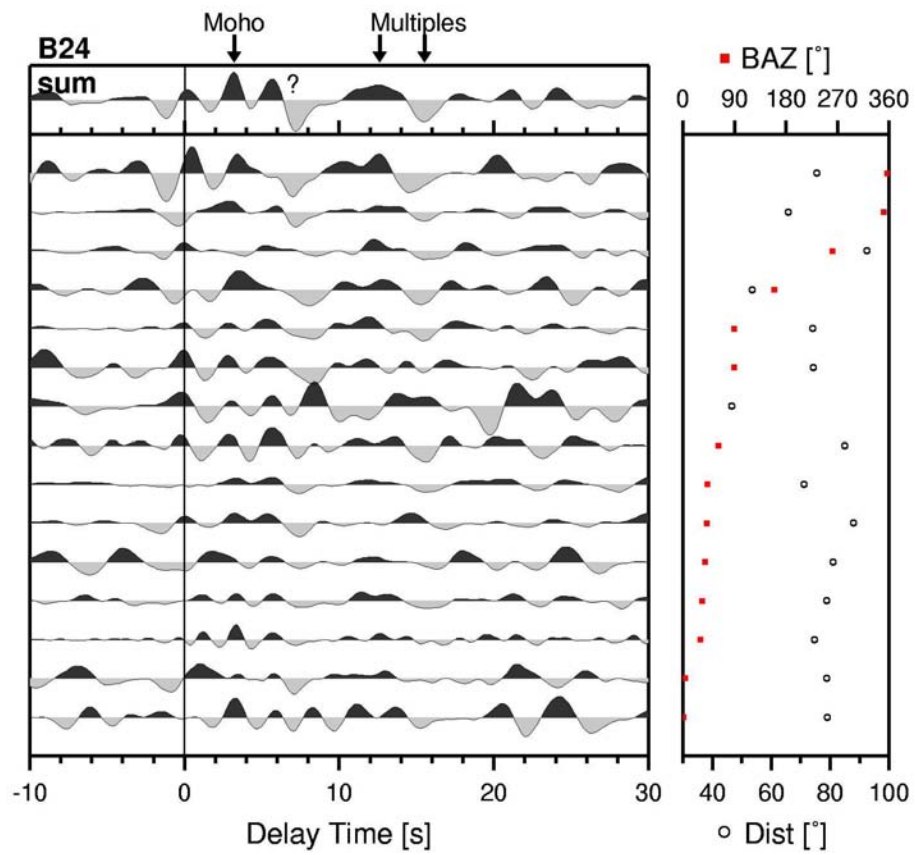
Figure 5.1 a to f (next pages): *P* receiver functions recorded at temporary and permanent stations of the BOHEMA network. On the left of each figure, individual receiver functions are displayed in the time domain. The time axis shows the delay time of the *P*-to-*S* converted phases with respect to the *P* onset (time=0). The single traces are sorted according to their back azimuths, the latter of which are shown in the right box of each figure by red squares. Furthermore, the box on the right gives the epicentral distance of the corresponding event. The individual traces are filtered between 1 and 12 s and corrected for distance moveout for a reference epicentral distance of 67°. On top of the individual traces, the summation trace is shown.

- Temporary station NALB (21 traces). Delay time of the Moho *Ps* conversion in the sum trace is 3.4 s, crustal multiples follow at 11.4 and 14.9 s. At 5.7 s appears a positive phase and at 7.3 s a strong negative phase which will be discussed in more detail in Chapter 6.2. In the individual traces, the amplitude of the converted signals varies strongly.
- Temporary station B24 (15 traces). Delay time of the Moho *Ps* conversion in the sum trace is 3.2 s, crustal multiples follow at 12.6 and 15.5 s. Like at station NALB, at 5.7 s appears a positive phase and at 7.2 s a strong negative phase which will be discussed in more detail in Chapter 6.2.
- Permanent station NKC (121 traces). Delay time of the Moho *Ps* conversion in the sum trace is 3.4 s, crustal multiples follow at 12.4 and 15.6 s. A positive signal after the Moho signal like at stations NALB and B24 is visible for eastern and western back azimuths, but not in the summation trace.
- Temporary station BG07 (31 traces). Delay time of the Moho *Ps* conversion in the sum trace is 3.6 s, crustal multiples follow at 12.8 and 16.0 s. A positive and negative signal after the Moho signal also exist at 7.6 and 9.2 s, respectively, which is approximately 2 s later than at stations NALB and B24 (see a and b above).
- Temporary station B09 (83 traces). Delay time of the Moho *Ps* conversion in the sum trace is 3.6 s, crustal multiples follow at 12.8 and 16.5 s.
- Temporary station B12/BM12 (20 traces). Delay time of the Moho *Ps* conversion in the sum trace is 4.4 s, crustal multiples follow at 15.2 and 19.2 s.

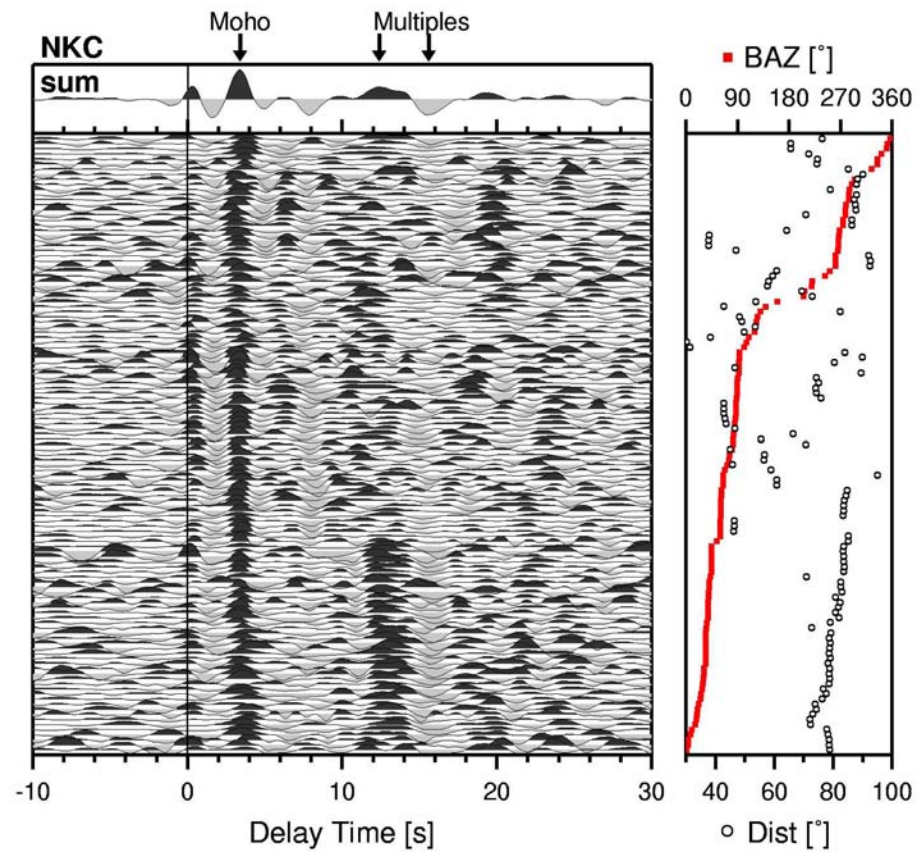
a)



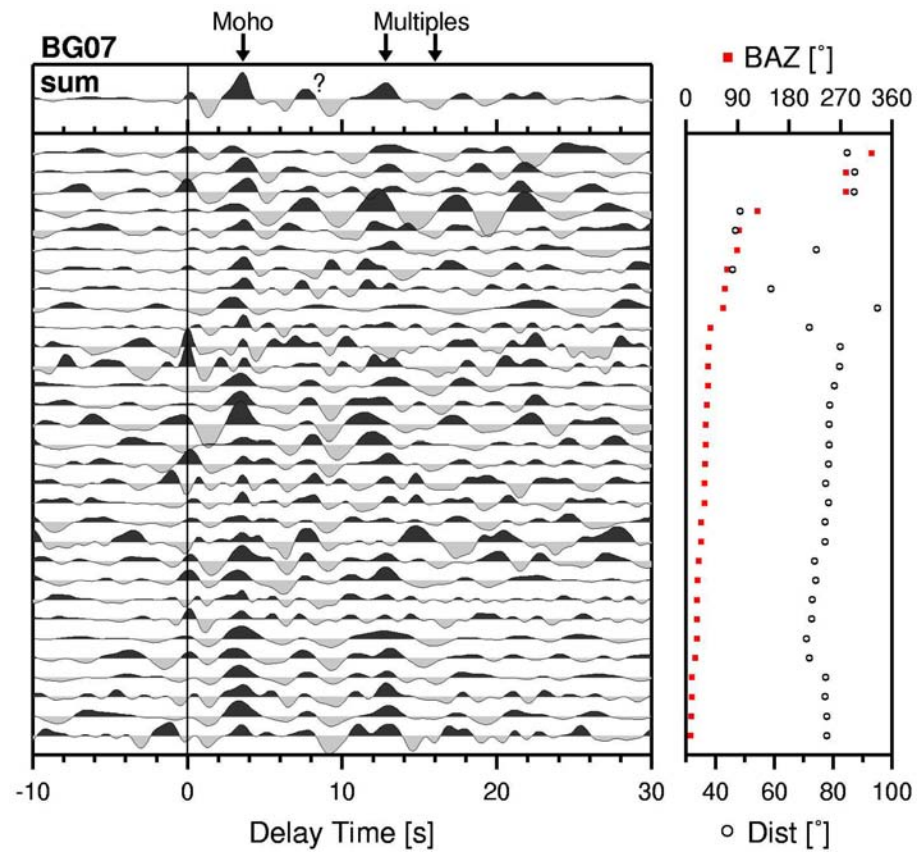
b)



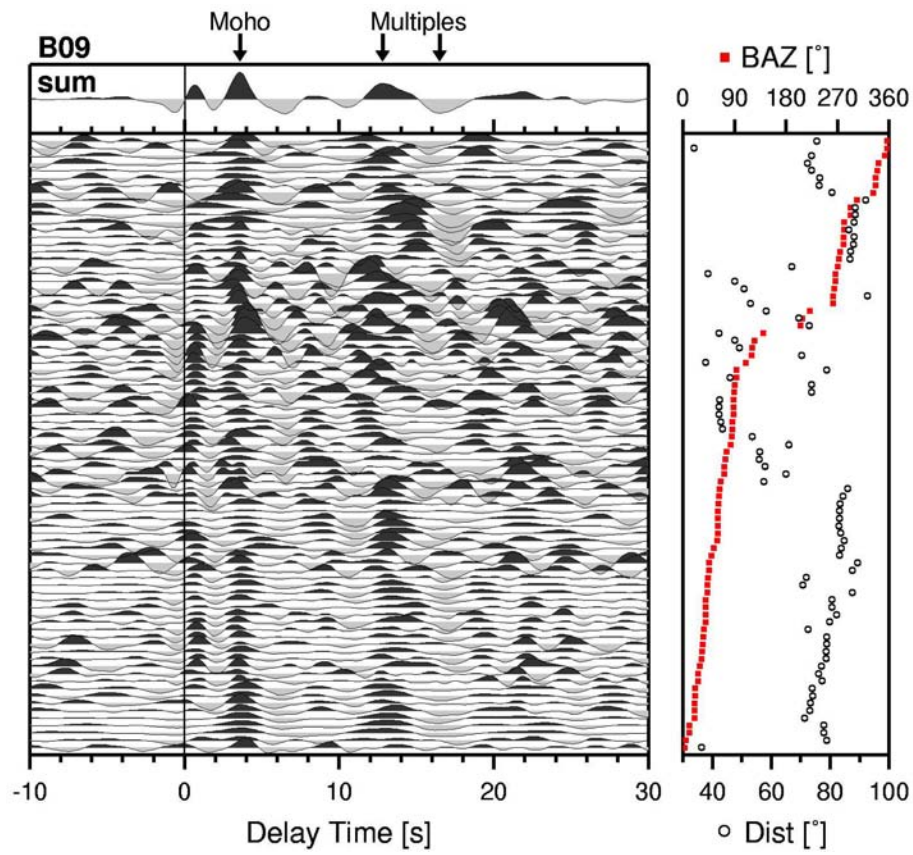
c)



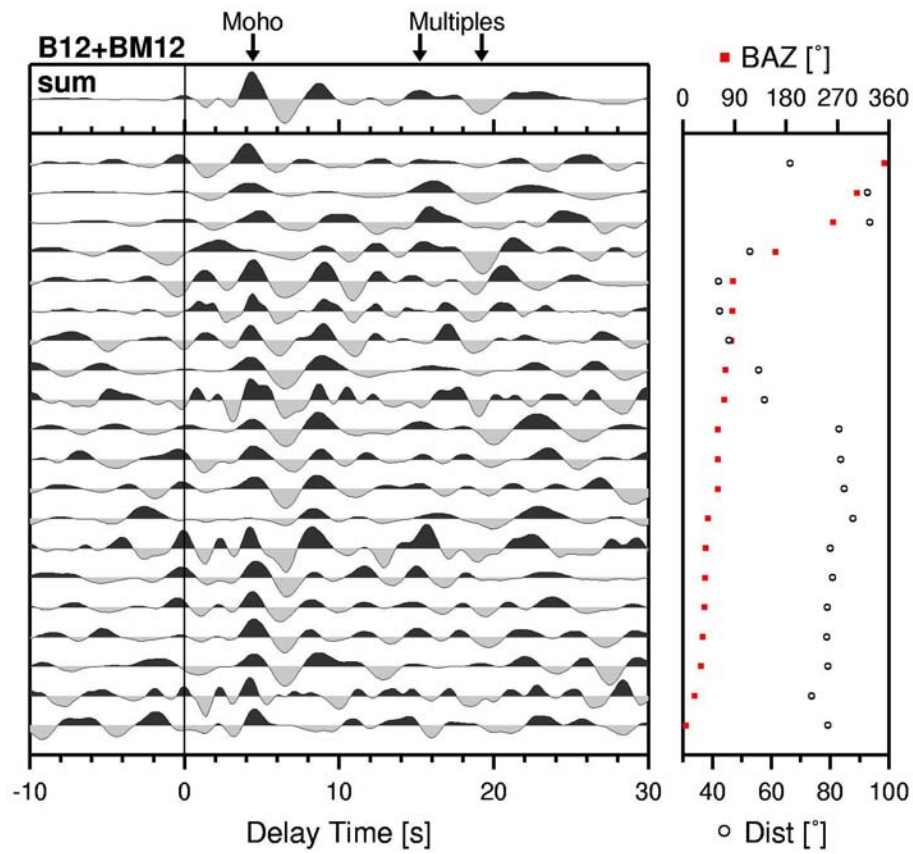
d)



e)



f)



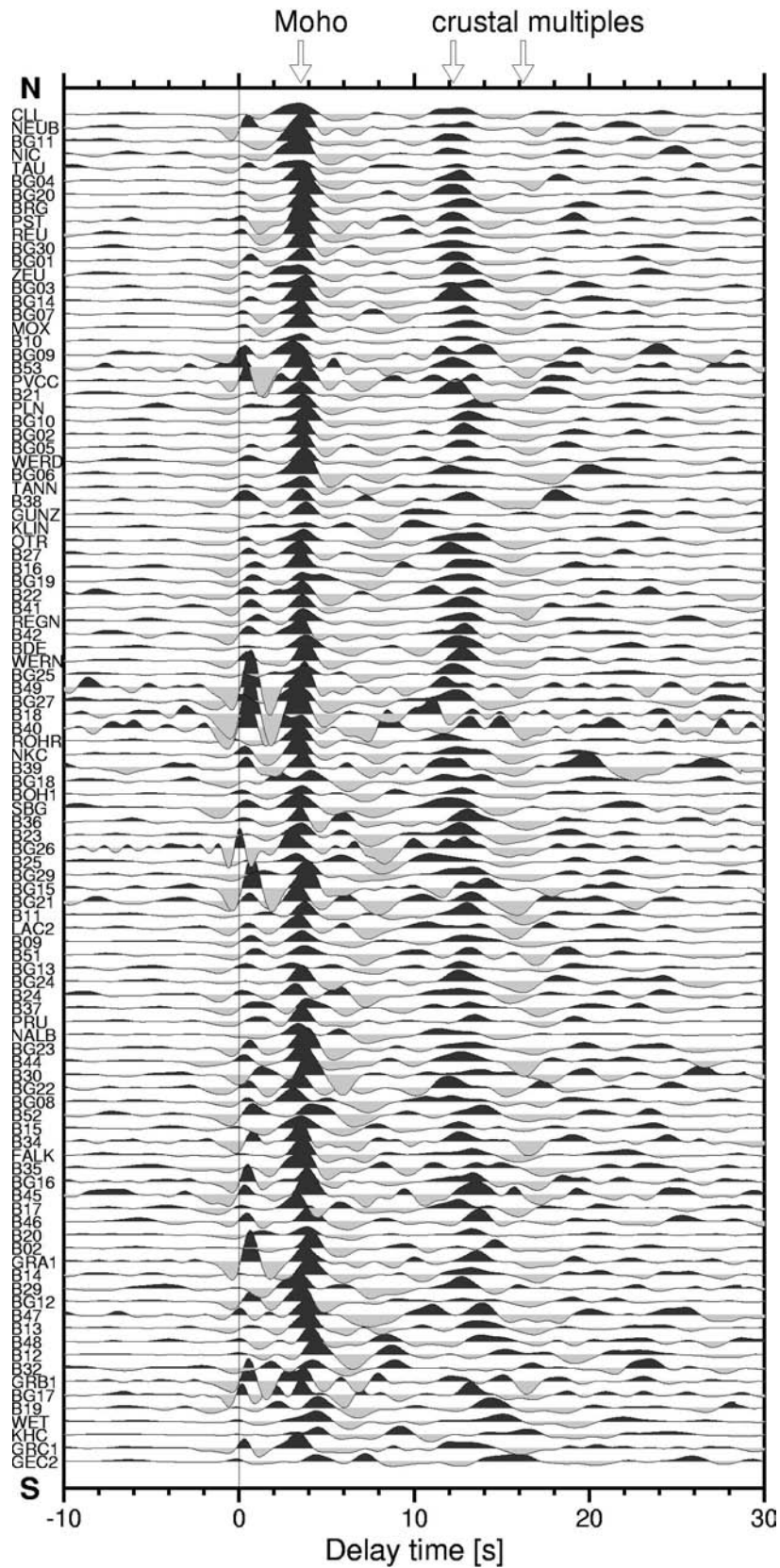


Figure 5.2: Sum traces of receiver functions of all stations of the BOHEMA passive seismic experiment that provided sufficient data for analysis. The time window between -10 and 30 s, which contains the conversion signal from the Moho discontinuity and crustal multiple reverberations is shown.

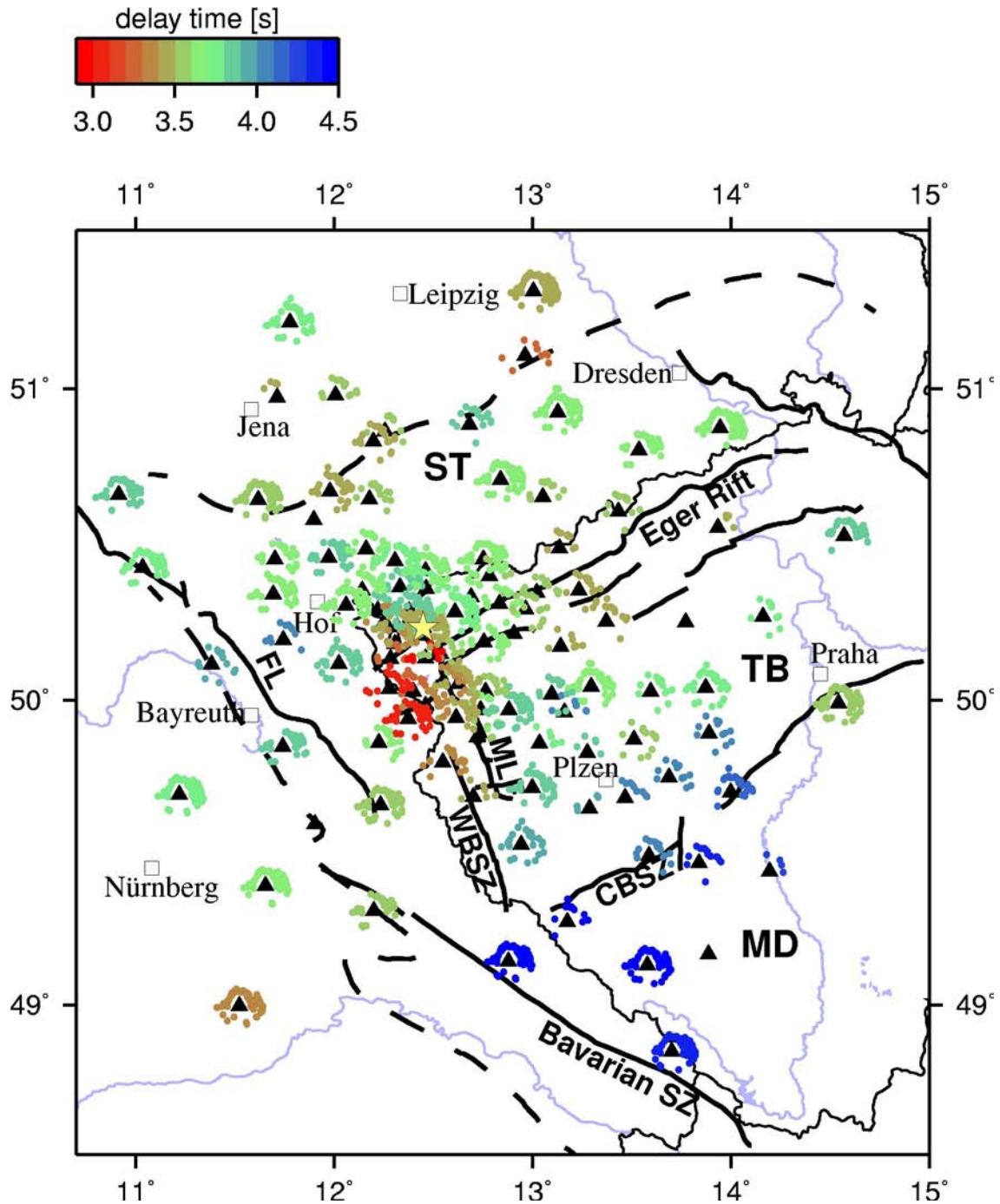


Figure 5.3: Delay times of the P_s conversion from the Moho discontinuity, obtained for stations of the BOHEMA experiment (more than 5000 receiver functions). Delay times vary between 3.0 and 4.5 s and are displayed together with the piercing points of the individual rays at 30 km depth. Stations without results for delay time either had not enough data or bad data quality. The yellow star marks the Nový Kostel main earthquake swarm area. For description of faults and tectonic units see Figure 3.1.

5.3.2 Crustal v_p/v_s ratios

In order to obtain the depth of the Moho discontinuity from the measured delay times of the P_s conversion, the method by *Zhu and Kanamori* (2000) was used to calculate average crustal v_p/v_s ratios for 34 BOHEMA stations with clear Moho P_s conversions and crustal multiples. The sum traces of these 34 stations are shown in Figure 5.4. For the inversion, an average crustal P -wave velocity of 6.3 km/s reported by *Hrubcová et al.* (2005) was used. From the obtained Moho depth and v_p/v_s values for each station, the delay time of the Moho P_s conversion and crustal multiples can be re-calculated to test the accuracy of the results. The re-calculated delay times are also shown in Figure 5.4. They generally agree very well with the measured delay times for all stations.

Examples of inversion results of Moho depth versus v_p/v_s are shown for temporary stations BG10 and BG24 in Figure 5.5. For the other stations, results of the inversion are shown in Appendix C.1. The 34 obtained v_p/v_s ratios are plotted into the map in Figure 5.6. The values vary between 1.66 ± 0.06 (stations PRU, B17) and 1.81 ± 0.08 (station BG25) with an average value of 1.73.

In the Saxothuringian unit, v_p/v_s ratios vary between 1.72 and 1.81 except for station PLN (1.67). In the Teplá-Barrandian unit, there seems to be a division into a northwestern part with values around 1.71 and a southeastern part (near the Central Bohemian Shear Zone) with values around 1.75.

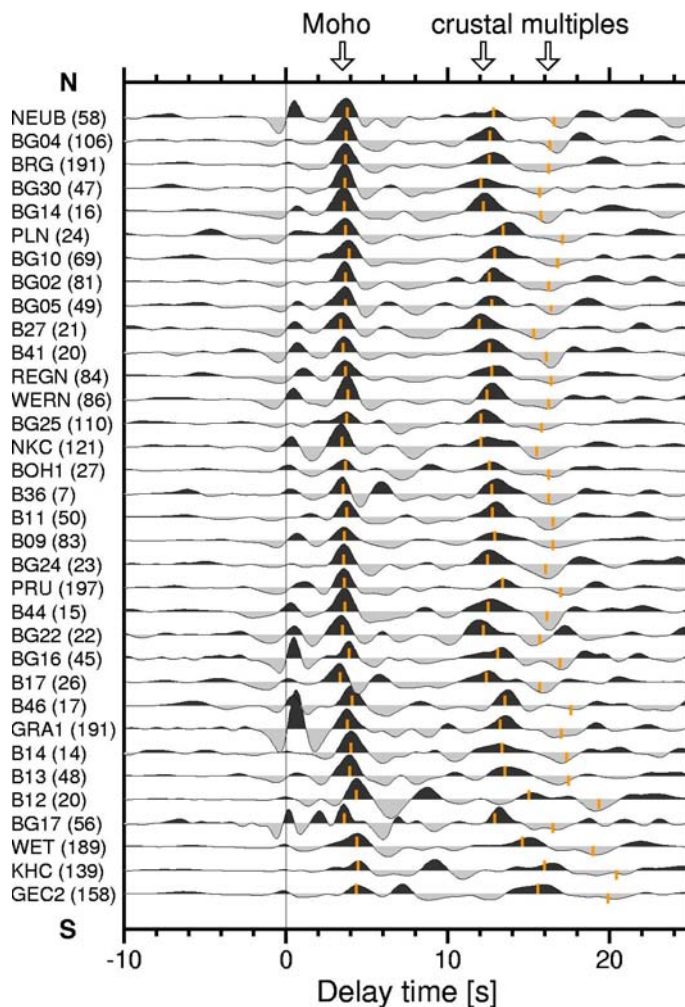


Figure 5.4: Sum traces of 34 BOHEMA stations with clear Moho P_s conversions and crustal multiples that were used for the grid search method by *Zhu and Kanamori* (2000). Stations are sorted from S (bottom) to N (top). Beside each trace, the name of the station and, in brackets, the number of individual traces used for stacking is given. For visual control of the results, the obtained values of Moho depth and v_p/v_s can be used to re-calculate the delay time of the Moho P_s conversion and the crustal multiples at each station. This is shown by the oranges dashes. The reproduced values agree very well with the data.

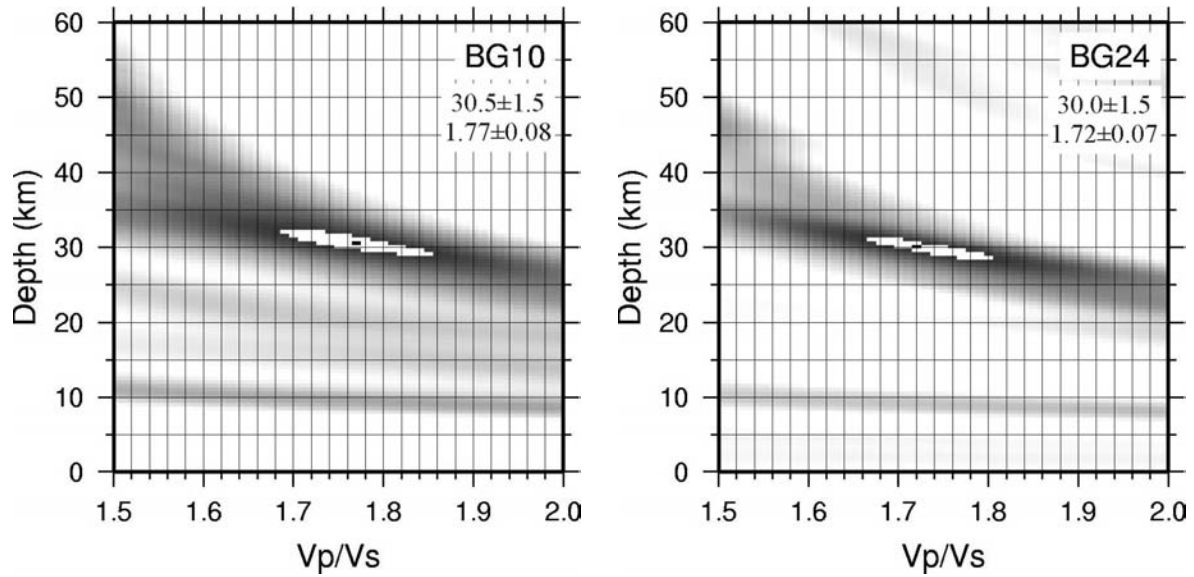


Figure 5.5: Depth of the Moho and v_p/v_s ratio obtained for stations BG10 and BG24 with the method by *Zhu and Kanamori* (2000). The grid search was carried out for an assumed average crustal P -wave velocity of 6.3 km/s in the intervals of 20 to 60 km for the Moho depth and 1.50 to 2.00 for v_p/v_s . The maximum stacked amplitude is marked by a black dot surrounded by a white ellipse. The latter one marks the area of 95% of the maximum stacked amplitude and thus gives an estimate of the uncertainty of the obtained values.

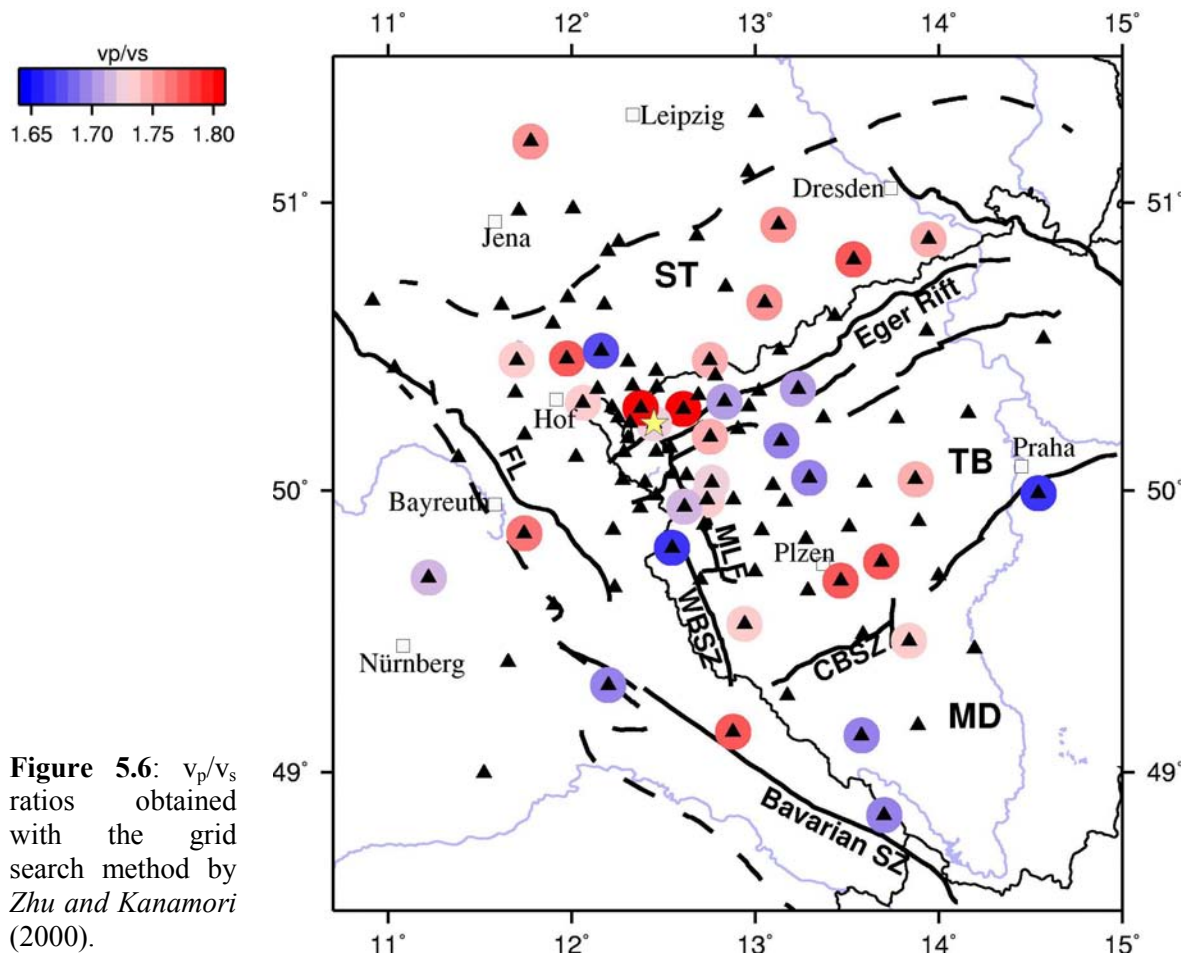


Figure 5.6: v_p/v_s ratios obtained with the grid search method by *Zhu and Kanamori* (2000).

5.4 Discussion

5.4.1 Map of crustal v_p/v_s ratios

In order to calculate Moho depths, v_p/v_s ratios must be provided for all stations. For 34 stations average crustal v_p/v_s ratios were obtained with the method of *Zhu and Kanamori* (2000). For the remaining stations, the investigated area was divided into subareas associated with the tectonometamorphic Variscan units of the Bohemian Massif. This step

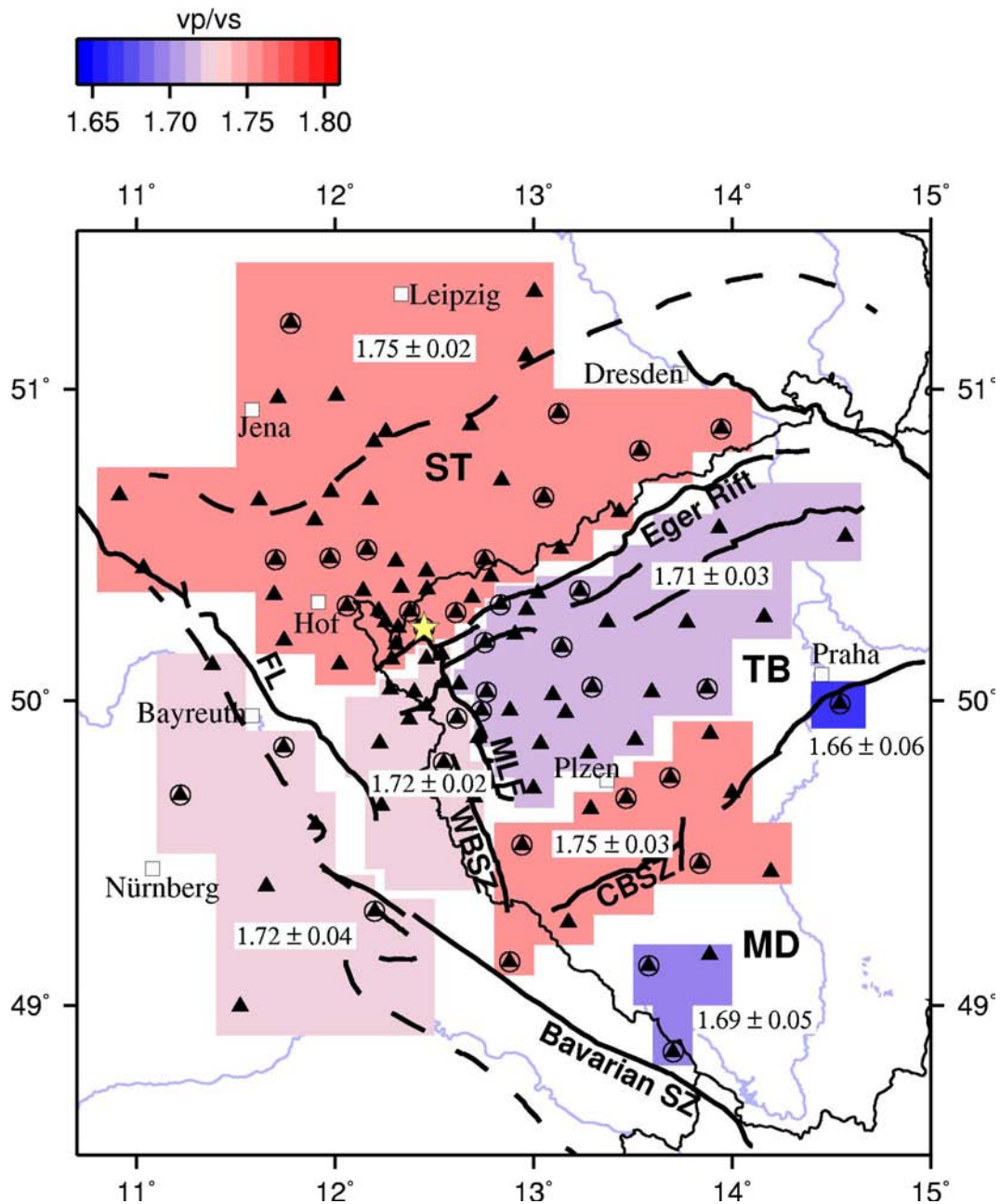


Figure 5.7: Division of the investigation area into subareas associated with the tectonometamorphic units of the Bohemian Massif. Mean v_p/v_s ratios and their standard deviations were calculated from the values obtained with the method by *Zhu and Kanamori* (2000) (Figure 5.6, Table 5.1).

is based on the simplifying assumption that the crust beneath each Variscan structural unit is more or less homogeneous. For the subareas, mean values of v_p/v_s ratios and their standard deviations were calculated of the values obtained with the method by *Zhu and Kanamori* (2000). The results are shown in Figure 5.7. The v_p/v_s ratios of all BOHEMA stations are summarized in Table 5.1.

In the resulting map (Figure 5.7), the Saxothuringian part of the Bohemian Massif displays a relatively high mean v_p/v_s ratio of 1.75 ± 0.02 . To the southeast, the northern part of the Teplá-Barrandian was combined to an area of a mean v_p/v_s ratio of 1.71 ± 0.03 . The transition of the Central Bohemian Shear Zone has a higher value again of 1.75 ± 0.03 . This corresponds to results by *Hrubcová et al.* (2005) who report a v_p/v_s ratio of 1.76 in the upper crust in the vicinity of the Central Bohemian Shear Zone. *Zhu and Kanamori* (2000) also report increased v_p/v_s ratios of more than 1.80 along a major shear zone (Eastern Californian Shear Zone, California). However, the West and North Bohemian Shear Zones do not show such a clear pattern. Station PRU near Prague stands alone with a rather low value of 1.66 ± 0.06 . In the Moldanubian unit southeast of the Central Bohemian Shear Zone, an area of low v_p/v_s ratio of 1.69 ± 0.05 was obtained. Such low v_p/v_s ratios might for example be explained by quartz rich rocks beneath the stations (*Christensen*, 1996). In the Moldanubian region west of the Teplá-Barrandian unit, the mean v_p/v_s ratio is 1.72 ± 0.02 . As there are only two measured values in this rather large subarea, the mean value of each of the neighbouring subareas was included in the calculation. Hence, the standard deviation of this v_p/v_s ratio is also small. Finally, the region southwest of the Bohemian Massif which is covered by Mesozoic sediments, displays a mean v_p/v_s ratio of 1.72 ± 0.04 .

For some locations near the western Eger Rift and north of it, the v_p/v_s ratio changes rapidly over a short distance (e.g. stations BG10/PLN and BG25/B41, Figure 5.6). This could be caused by short-wavelength variation of crustal P and S velocities. It might also be an artefact due to the uncertainty of the v_p/v_s estimation (*Zhu and Kanamori*, 2000). These local differences are levelled out in the map of mean v_p/v_s ratios (Figure 5.7).

A comparison of v_p/v_s ratios obtained in the study by *Geissler et al.* (2005) and in this thesis at stations used in both investigations (Table 5.2) shows that most values agree very well within ± 0.02 , except for station A02/PLN, where the difference is 0.05. Unfortunately, the estimated error of the v_p/v_s ratio is generally high. The crustal v_p/v_s ratio is so far among the least constrained parameters from both laboratory and field measurements.

The reason for the differences is that different teleseismic events and recording time spans were used in the two investigations.

High values of v_p/v_s beneath the western Erzgebirge mountains reported by *Geissler et al.* (2005) can partly be confirmed (stations WERN, BG25), the same is the case for reported low values at the Czech-German border east of KTB (station B17).

Table 5.1: Station parameters of BOHEMA stations (including station code, latitude and longitude), number of stacked receiver function traces (n), delay time of the Moho P_s conversion (t_{Ps}), v_p/v_s ratios and Moho depth H obtained with method by *Zhu and Kanamori (2000)*, v_p/v_s ratios of the subareas (see Figure 5.7) and Moho depth H calculated either with the v_p/v_s ratios from inversion of Moho depth versus v_p/v_s or with v_p/v_s ratios of the related subareas

Station	Lat [°N]	Lon [°E]	n	t_{Ps} [s]	v_p/v_s (Z&K)	H [km] (Z&K)	v_p/v_s subarea	H [km]
B02	49.6992	13.996	51	4.10	-	-	1.75±0.03	33.0±2.0
B09	50.0422	13.2930	83	3.60	1.69±0.07	31.5±1.5	1.69±0.07	31.5±1.5
B10	50.6072	13.4315	16	3.50	-	-	1.75±0.02	28.5±2.0
B11/BM11	50.0382	13.8717	50	3.76	1.74±0.07	30.5±1.5	1.74±0.07	30.5±1.5
B12/BM12	49.4673	13.8379	20	4.40	1.73±0.05	36.0±1.5	1.73±0.05	36.0±1.5
B13/BM13	49.5285	12.9410	48	3.84	1.73±0.07	32.5±1.5	1.73±0.07	32.5±1.5
B14/BM14	49.6811	13.4646	14	3.80	1.77±0.07	31.5±1.5	1.77±0.07	31.5±1.5
B15/BM15	49.8718	13.5108	20	3.48	-	-	1.71±0.03	29.5±2.0
B16	50.3471	13.0187	18	3.52	-	-	1.71±0.03	30.0±2.0
B17	49.7965	12.5460	26	3.32	1.66±0.06	30.5±1.0	1.66±0.06	30.5±1.0
B18	50.252	13.3695	13	3.40	-	-	1.71±0.03	29.0±2.0
B19	49.2743	13.1726	13	4.50	-	-	1.75±0.03	36.5±2.0
B20	49.7126	12.9962	63	3.85	-	-	1.71±0.03	33.0±2.0
B21	50.4903	13.1356	13	3.44	-	-	1.75±0.02	28.0±2.0
B22	50.3326	12.6899	5	3.60	-	-	1.75±0.02	29.0±2.0
B23	50.1497	12.5365	22	3.52	-	-	1.72±0.02	29.5±2.0
B24	50.0264	12.3988	15	3.20	-	-	1.72±0.02	27.0±2.0
B25	50.1325	12.283	22	3.24	-	-	1.75±0.02	26.0±2.0
B27	50.3529	13.2317	21	3.44	1.70±0.10	29.0±1.5	1.70±0.10	29.0±1.5
B29	49.6845	12.7000	8	3.44	-	-	1.72±0.02	29.0±2.0
B30	49.959	13.160	8	4.00	-	-	1.71±0.03	34.0±2.0
B32	49.4393	14.1926	4	4.20	-	-	1.75±0.03	34.0±2.0
B33	49.168	13.886	1	-	-	-	1.69±0.05	-
B34	49.8776	12.7188	4	3.52	-	-	1.72±0.02	29.5±2.0
B35	49.8574	13.0340	8	3.76	-	-	1.71±0.03	32.0±2.0
B36	50.1729	13.1408	7	3.48	1.69±0.05	31.0±1.0	1.69±0.05	31.0±1.0
B37	50.0179	13.0945	17	3.84	-	-	1.71±0.03	32.5±2.0
B38	50.4003	12.7817	9	3.56	-	-	1.75±0.02	29.0±2.0
B39	50.2144	12.9050	3	3.64	-	-	1.71±0.03	31.0±2.0
B40	50.2513	13.7709	5	-	-	-	1.71±0.03	-
B41	50.3097	12.8324	20	3.60	1.70±0.07	30.5±1.5	1.70±0.07	30.5±1.5
B42	50.2917	12.9632	17	3.52	-	-	1.71±0.03	30.0±2.0
B44	49.9660	12.7365	15	3.60	1.73±0.07	30.0±1.5	1.73±0.07	30.0±1.5
B45	49.8266	13.2757	6	3.88	-	-	1.71±0.03	33.0±2.0
B46	49.7481	13.6850	17	4.04	1.77±0.06	32.0±1.0	1.77±0.06	32.0±1.0
B47	49.6457	13.2859	9	3.92	-	-	1.75±0.03	31.5±2.0
B48	49.4909	13.5845	19	4.08	-	-	1.75±0.03	33.0±2.0
B49	50.2696	14.1591	14	3.72	-	-	1.71±0.03	31.5±2.0
B51	50.0258	13.5951	17	3.72	-	-	1.71±0.03	31.5±2.0
B52	49.8909	13.8877	18	4.08	-	-	1.75±0.03	33.0±2.0
B53	50.5557	13.9331	4	3.44	-	-	1.71±0.03	29.5±2.0
BDE	50.2885	12.2198	13	3.80	-	-	1.75±0.02	30.5±2.0
BG01	50.7086	12.8369	141	3.64	-	-	1.75±0.02	29.5±2.0
BG02	50.4538	12.7407	81	3.64	1.74±0.06	30.0±1.0	1.74±0.06	30.0±1.0
BG03	50.6604	10.9144	54	3.80	-	-	1.75±0.02	30.5±2.0
BG04	50.9227	13.1249	106	3.62	1.75±0.06	30.0±1.0	1.75±0.06	30.0±1.0
BG05	50.4534	11.6998	49	3.64	1.73±0.07	30.5±1.5	1.73±0.07	30.5±1.5
BG06	50.4268	11.0356	66	3.72	-	-	1.75±0.02	30.0±2.0
BG07	50.6463	12.1766	31	3.56	-	-	1.75±0.02	29.0±2.0
BG08	49.9380	12.3729	82	3.08	-	-	1.72±0.02	26.0±2.0

continued on next page

MOHO DEPTHS AND CRUSTAL V_P/V_S RATIOS

Station	Lat [°N]	Lon [°E]	n	t_{Ps} [s]	v_p/v_s (Z&K)	H [km] (Z&K)	v_p/v_s subarea	H [km]
BG09	50.5814	11.8954	19	3.04	-	-	1.75±0.02	24.5±2.0
BG10	50.4589	11.9729	69	3.84	1.77±0.08	30.5±1.5	1.77±0.08	30.5±1.5
BG11	51.1030	12.9620	13	3.28	-	-	1.75±0.02	26.5±2.0
BG12	49.6573	12.2322	115	3.56	-	-	1.72±0.02	30.0±2.0
BG13	50.0346	12.2787	36	3.02	-	-	1.72±0.02	25.5±2.0
BG14	50.6534	13.0504	16	3.56	1.75±0.07	29.0±1.5	1.75±0.07	29.0±1.5
BG15	50.1147	11.3821	20	3.92	-	-	1.72±0.04	33.0±2.0
BG16	49.8468	11.7405	45	3.88	1.76±0.05	31.0±1.0	1.76±0.05	31.0±1.0
BG17	49.3096	12.1983	56	3.56	1.69±0.04	31.5±1.0	1.69±0.04	31.5±1.0
BG18	50.1938	11.7432	12	(4.08?)	-	-	1.75±0.02	-
BG19	50.3408	11.6928	62	3.60	-	-	1.75±0.02	29.0±2.0
BG20	50.8852	12.6796	31	3.80	-	-	1.75±0.02	30.5±2.0
BG21	50.0576	12.5476	16	3.36	-	-	1.72±0.02	28.0±2.0
BG22	49.9416	12.6133	22	3.40	1.71±0.06	29.5±1.0	1.71±0.06	29.5±1.0
BG23	49.9668	12.8785	79	3.84	-	-	1.71±0.03	32.5±2.0
BG24	50.0270	12.7614	23	3.58	1.72±0.07	30.0±1.5	1.72±0.07	30.0±1.5
BG25	50.2833	12.6068	110	3.74	1.81±0.08	28.0±1.5	1.81±0.08	28.0±1.5
BG26	50.1336	12.4583	12	2.96	-	-	1.72±0.02	25.0±2.0
BG27	50.2531	12.2525	9	3.36	-	-	1.75±0.02	27.0±2.0
BG28	49.5947	11.9037	20	?	-	-	1.72±0.04	-
BG29	50.1171	12.0219	60	3.88	-	-	1.75±0.02	31.5±2.0
BG30	50.8035	13.5353	47	3.60	1.77±0.06	28.5±1.0	1.77±0.06	28.5±1.0
BOH1	50.1866	12.7538	27	3.60	1.74±0.06	30.0±1.0	1.74±0.06	30.0±1.0
BRG	50.8732	13.9428	191	3.64	1.74±0.07	30.0±1.5	1.74±0.07	30.0±1.5
CLL	51.3077	13.0026	187	3.44	-	-	1.75±0.02	28.0±2.0
FALK	49.8597	12.2236	27	3.60	-	-	1.72±0.02	30.5±2.0
GEC2	48.8451	13.7016	158	4.36	1.69±0.07	38.0±1.75	1.69±0.07	38.0±1.75
GRA1	49.6910	11.2200	191	3.76	1.71±0.06	32.0±1.5	1.71±0.06	32.0±1.5
GRB1	49.3920	11.6540	175	3.68	-	-	1.72±0.04	31.0±2.0
GRC1	48.9960	11.5220	181	3.36	-	-	1.72±0.04	28.0±2.0
GUNZ	50.3635	12.3316	43	3.80	-	-	1.75±0.02	30.5±2.0
KHC	49.1309	13.5782	139	4.48	1.69±0.06	39.0±1.5	1.69±0.06	39.0±1.5
KLIN	50.3584	12.4616	20	(3.76?)	-	-	1.75±0.02	(30.5?)
LAC2	50.0508	12.6250	47	3.40	-	-	1.71±0.03	29.0±2.0
MOX	50.6447	11.6156	176	3.56	-	-	1.75±0.02	29.0±2.0
NALB	49.9812	12.4607	21	3.36	-	-	1.72±0.02	28.0±2.0
NEUB	51.2085	11.7755	58	3.72	1.75±0.07	30.5±1.0	1.75±0.07	30.5±1.0
NIC	50.9782	12.0047	18	3.56	-	-	1.75±0.02	29.0±2.0
NKC	50.2331	12.4479	121	3.40	1.72±0.08	29.0±1.5	1.72±0.08	29.0±1.5
OTR	50.3531	12.1388	30	3.68	-	-	1.75±0.02	29.5±2.0
PLN	50.4860	12.1590	24	3.64	1.67±0.06	33.0±1.5	1.67±0.06	33.0±1.5
PRU	49.9883	14.5417	197	3.56	1.66±0.06	33.0±1.5	1.66±0.06	33.0±1.5
PST	50.8640	12.2550	10	3.56	-	-	1.75±0.02	29.0±2.0
PVCC	50.5282	14.5690	65	3.88	-	-	1.71±0.03	33.0±2.0
REGN	50.3060	12.0606	84	3.64	1.73±0.08	30.5±1.5	1.73±0.08	30.5±1.5
REU	50.8310	12.1960	26	3.44	-	-	1.75±0.02	28.0±2.0
ROHR	50.2346	12.3168	99	3.44	-	-	1.75±0.02	28.0±2.0
SBG	50.1820	12.3050	4	(3.36)	-	-	1.75±0.02	-
TANN	50.4160	12.4600	81	3.60	-	-	1.75±0.02	29.0±2.0
TAU	50.9716	11.7111	6	(3.44)	-	-	1.75±0.02	-
WERD	50.4480	12.3070	55	3.72	-	-	1.75±0.02	30.0±2.0
WERN	50.2874	12.3761	86	3.80	1.80±0.08	29.0±1.0	1.80±0.08	29.0±1.0
WET	49.1440	12.8782	189	4.40	1.77±0.08	34.5±2.0	1.77±0.08	34.5±2.0
ZEU	50.6719	11.9780	43	3.40	-	-	1.75±0.02	27.5±2.0

Table 5.2: Comparison of v_p/v_s ratios obtained in the study by *Geissler et al.* (2005) and in this thesis at stations used in both investigations. In both studies, the values were obtained with the method by *Zhu and Kanamori* (2000). The last column gives the mean v_p/v_s ratio of the subarea in which the station is located (see Figure 5.7). Differences of the values are caused by different recording time spans of teleseismic events in the two investigations.

Station	v_p/v_s (Geissler et al., 2005)	v_p/v_s (this study)	mean v_p/v_s subarea
A02/PLN	1.72±0.08	1.67±0.06	1.75±0.02
A21/REGN	1.74±0.07	1.73±0.08	1.75±0.02
BRG	1.76±0.08	1.74±0.07	1.75±0.02
GRA1	1.73±0.05	1.71±0.06	1.72±0.04
KHC	1.71±0.05	1.69±0.06	1.69±0.05
NKC	1.73±0.07	1.72±0.08	1.75±0.02
WER/WERN	1.79±0.08	1.80±0.08	1.75±0.02
WET	1.79±0.09	1.77±0.08	1.75±0.03

5.4.2 Depth map of the Moho discontinuity

The Moho depth at each station was calculated using the P_s delay time, v_p/v_s ratio and an average crustal P wave velocity of 6.3 km/s (Figure 5.8, Table 5.1) (*Heuer et al.*, 2006). A smoothed map of Moho depths of the central part of the investigated area is given in Figure 5.9. The Moho depth values have an estimated uncertainty of ± 2 km. They were not corrected for topography as topography is relatively small compared to the resolution of the method (see Appendix A.1, altitudes of seismic stations).

Crustal thicknesses display values of 27 to 31 km in the Saxothuringian unit (except for station PLN due to the very low v_p/v_s ratio), 30 to 33 km in the Teplá-Barrandian and 34 to 39 km in the Moldanubian unit east of the Bavarian Shear Zone. Like in the map of delay times of the Moho P_s conversions (Figure 5.5), a prominent feature in the Moho depth map is an area of thin crust of about 26 to 28 km beneath the western Eger Rift. The internal geometry of this updoming seems to be irregular: towards the ENE, the crustal thickness gradually increases to „normal“ values of about 31 km, whereas towards the WSW there seems to be an abrupt depth increase from 26 to 31 km. This apparent Moho updoming was already observed with less resolution by *Geissler et al.* (2005). It corresponds well with the area of CO₂ degassing fields at surface. The main swarm earthquake area of Nový Kostel is situated at the northeastern margin of the Moho updoming area. The Moho depth increases towards the SE and reaches values of almost 40 km between the Central Bohemian and the Bavarian Shear Zone. This result is in good agreement with former seismic studies (e.g. *Hrubcová et al.*, 2005).

At the stations of the German Regional Seismic Network (GRSN) and GRF array in the investigation area, the depth of the Moho has been investigated in previous studies with the receiver function method (*Kind et al.*, 1995; *Wilde- Piórko et al.*, 2005; *Geissler et al.*, 2005). Some of the obtained depth values are compared with values obtained in the present study in Table 5.3. They agree very well with each other. Like in the present study, *Wilde- Piórko et al.* (2005) also find a thick crust of 35-40 km in the southeast, while the crust in the northwestern (Saxothuringian) part is much thinner (28-32 km).

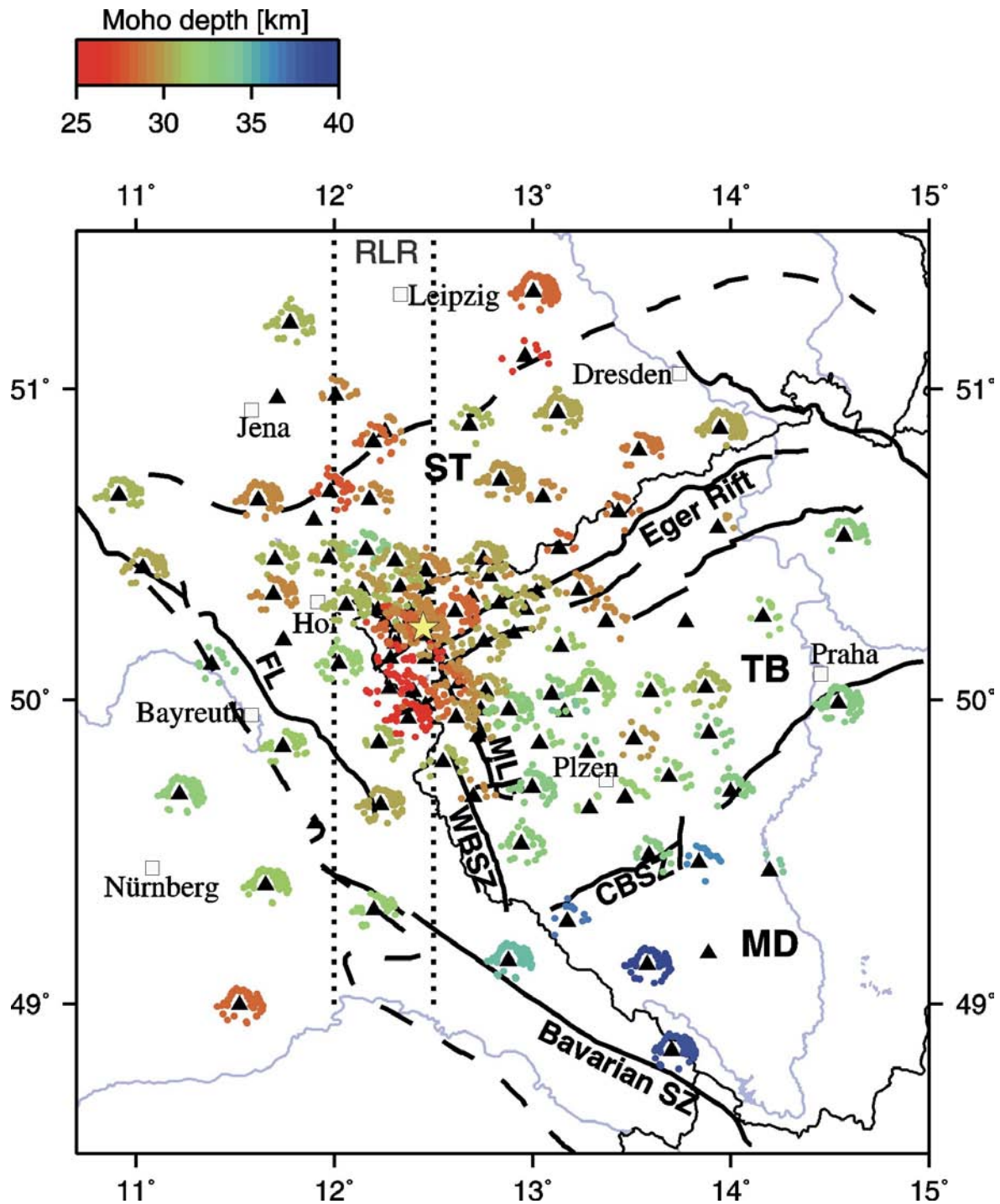


Figure 5.8: Moho depth values of each station were plotted at the piercing points of the individual rays at an interface at 30 km depth.

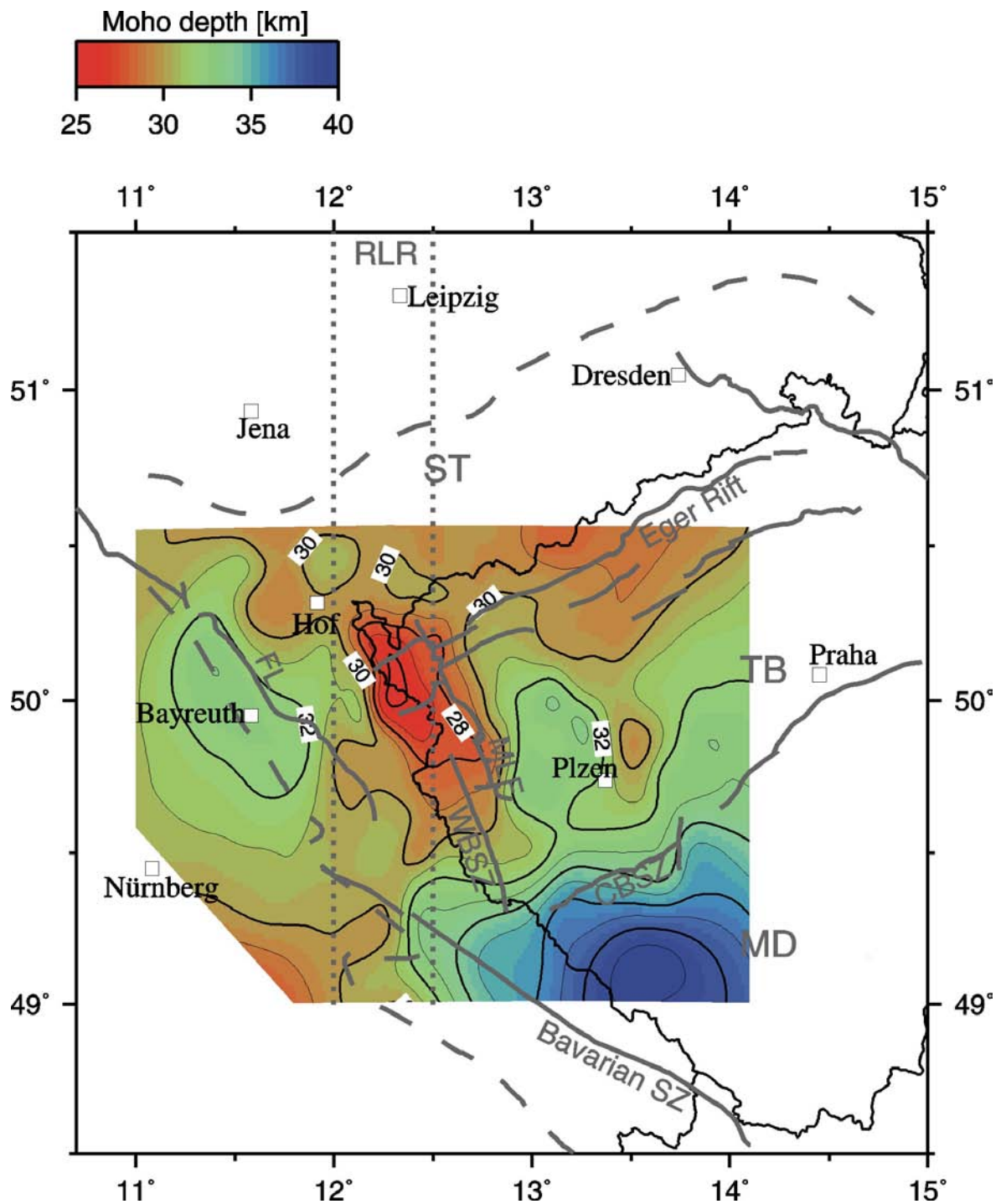


Figure 5.9: Simplified Moho depth map of the central part of the investigation area. The margins of the investigation area were cut off because boundary effects distort the proportions of the isothickness lines. Spacing of the thick lines is 2 km and of thin lines 1 km. The shading of colours is given in steps of 0.5 km.

Table 5.3: Moho depth values obtained in previous receiver function investigations at stations within and around the Bohemian Massif, compared to values of this thesis. RF means receiver function, Z&K means inversion by the grid search method of *Zhu and Kanamori* (2000).

Station	Moho depth [km]					
	<i>Wilde-Piörko et al., 2005</i>				<i>Geissler et al., 2005</i> (Z&K)	<i>this study</i> (Z&K)
	<i>Kind et al., 1995</i> (RF inversion)	RF inversion	RF forward	grid search (Z&K)		
BRG	-	31.5±1.5	32.0±1.0	29.6±2.0	29.3±1.8	30.0±1.5
CLL	-	29.5±1.5	30.0±1.0	28.2±2.0	29.5±2.0	28.0±2.0
MOX	-	29.5±1.5	29.0±1.0	30.6±2.1	30.3±1.8	29.0±2.0
GRA1	32	-	-	-	31.5±0.5	32.0±1.5
GRB1	?	-	-	-	29.8±1.3	31.0±2.0
GRC1	?	-	-	-	30.3±1.8	28.0±2.0
WET	32	34.5±1.5	39.0±2.0	34.4±2.5	34.3±1.8	34.5±2.0
KHC	-	39.5±1.5	39.0±1.0	38.2±2.3	38.3±1.5	39.0±1.5
NKC	-	31.5±1.5	30.0±1.0	28.6±2.1	28.8±1.8	29.0±1.5
PRU	-	33.5±1.5	33.0±2.0	33.2±1.6	33.0±1.0	33.0±1.5

5.4.3 Comparison with seismic refraction profile CEL09

In the Saxothuringian unit, Moho depth generally varies between 27 and 31 km according to the data of this study. This is partly in contradiction to the interpretation of refraction seismic data by *Hrubcová et al.* (2005). They derived a strongly laminated lower crust in the Saxothuringian and partly the Teplá-Barrandian unit with an upper boundary at 25 to 27 km depth and a very gradual Moho as lower boundary at 34 to 35 km depth (see Figure 2.3 in Chapter 2). The Moho updoming observed in this thesis could correspond to the upper boundary of *Hrubcová et al.*'s lower crustal layer (*Heuer et al.*, 2006). Former seismic studies in the Saxothuringian also report a reflective lower crust which appears to be strongly laminated (*DEKORP Research Group*, 1985; *Behr and Heinrichs*, 1987; *DEKORP Research Group*, 1994; *Enderle et al.*, 1998). However, in the receiver function data presented here, an additional layer in the Saxothuringian unit can generally not be observed. Data of stations of the BOHEMA data set located close to the refraction seismic profile CEL09 are shown in Figure 5.10. They do not display indications of a second layer at lower crustal or Moho depth. If there were such a layer, the crustal multiple reflections should split into two phases and thus resolve a two-layered structure. However, one station (BG09) shows indications of an additional layer: the “Moho” P_s converted signal has a very short delay time corresponding to 24.5 km depth, which might as well be interpreted as a strong velocity contrast at the top of a lower crustal layer. And, more importantly, the multiple reverberations show a clear splitting into two peaks (Figure 5.10). Yet the neighbouring stations of BG09 do not show indications for a distinct lower crustal layer.

A comparable case is described by *Mohsen et al.* (2005), who observed a splitting of the multiples into two phases east of the Dead Sea Transform, while the Moho P_s conversion did not show indications for an additional layer. However, while steep angle reflections and receiver functions revealed this additional discontinuity in the lower crust, refraction

seismic data did not display this feature (*Mechie et al.*, 2005) –opposite than in this thesis and the refractions seismic experiment CEL09.

The apparent mismatch may have its origin in (1) different resolution scales of the two methods and (2) the complex nature of the crust mantle boundary in the area under investigation, possibly leading to the existence of two Mohos - a “refraction Moho” and a “RF Moho” (*Heuer et al.*, 2006).

Hrubcová et al. (2005) find that the Moldanubian is characterized by the deepest (39 km) and the most pronounced Moho within the whole Bohemian Massif with a strong velocity contrast, which agrees with the results of this thesis and other seismic studies (e.g. *Geissler et al.*, 2005; *Wilde- Piórko et al.*, 2005).

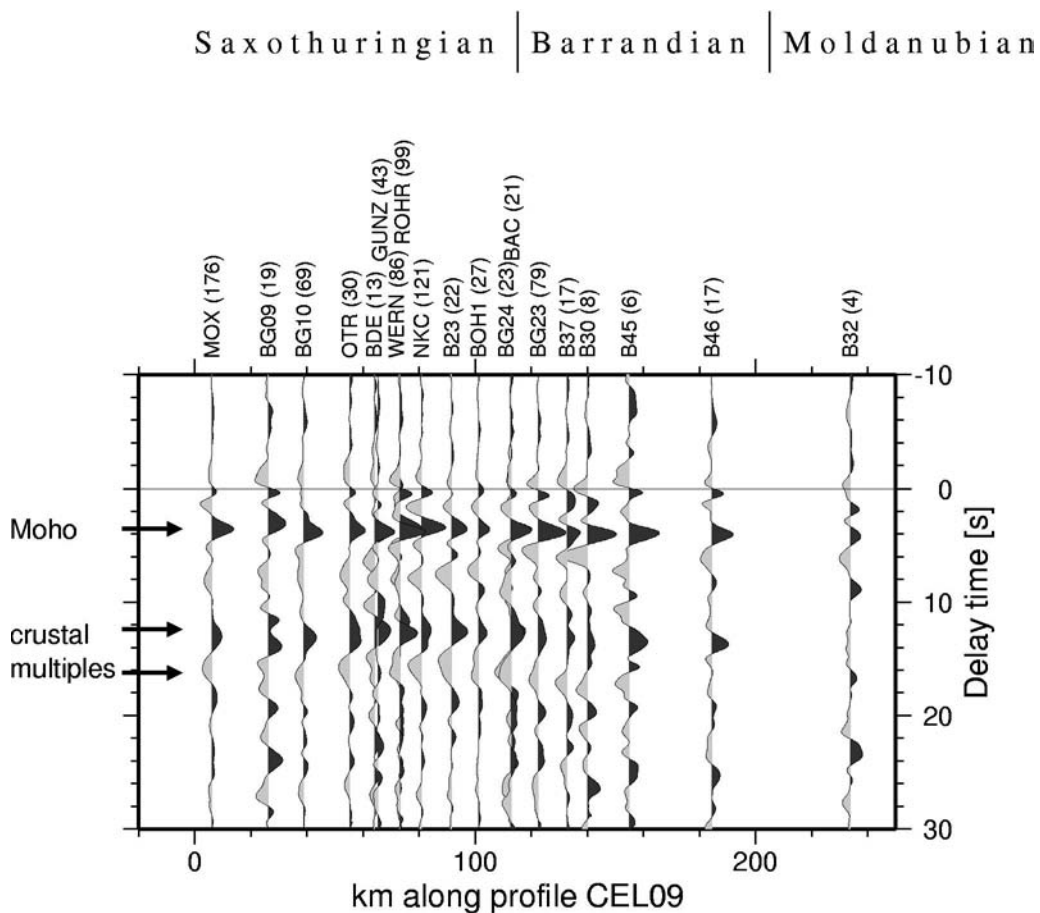


Figure 5.10: Sum traces of receiver functions at BOHEMA stations within 8 km distance from profile CEL09 (*Hrubcová et al.*, 2005). In the Saxothuringian unit, *Hrubcová et al.*, 2005 interpret a strong discontinuity at the top of the lower crust at 25 to 27 km depth and a very gradual Moho as lower boundary at 34 to 35 km depth. Except for station BG09, the receiver functions of the BOHEMA experiment show no indications for an additional discontinuity. In the receiver functions, Moho depth for the displayed stations varies around 29 to 30 km, except for station BG09 (24.5 km) which does not seem to fit to the neighbouring stations and might be an indication for strong discontinuity at the top of a lower crustal layer.

Chapter 6

Structure and thickness of the lithospheric mantle

6.1 Nature of the lithosphere and lithosphere-asthenosphere transition

The terms lithosphere and asthenosphere were originally defined with regards to rheology, with the lithosphere behaving essentially as an elastic solid, and the asthenosphere deforming as a viscous fluid (*Barrell*, 1914). Since then, additional, differing usages of the term lithosphere have been introduced such as thermal, seismic or chemical lithosphere (*Anderson*, 1995). In the context of plate tectonics, the lithosphere is defined as the crust and a part of the upper mantle that translate coherently on the Earth's surface (*Isaacs et al.*, 1968). The lithosphere behaves rigidly on geologic time scales of millions of years. The widely adopted thermal definition considers the lithosphere as a conductive layer above a convecting mantle and associates the lithosphere-asthenosphere boundary with an isotherm of about 1280°C (*McKenzie and Bickle*, 1988). The asthenosphere probably contains a small percentage of molten mantle material (peridotite). The lithosphere is seismologically defined as the high-velocity outer layer of the Earth. It comprises the Earth's crust and the uppermost high-velocity part of the Earth's mantle. At many places it is underlain by a region of diminished velocity or negative velocity gradient in the upper mantle (*Gutenberg*, 1926, 1959), the asthenosphere. While the seismic definition describes the lithosphere-asthenosphere boundary from the point of view of mean isotropic velocities, *Plomerová et al.* (2002) and *Gung et al.* (2003) explain the transition at the bottom of the lithosphere beneath continents as a change in anisotropic structure between frozen-in structure in the lithosphere and anisotropic structure from ongoing dynamic processes in the underlying asthenosphere. The lithosphere-asthenosphere boundary is furthermore associated with a layer of increased electrical conductivity due to partial melting (*Jones*, 1982; *Hjelt*, 1991; *Jones*, 1999, *ERCEUGT-Group*, 1992, *Simpson*, 2002).

As several physical parameters change at the bottom boundary of the lithosphere, it appears to be a significant discontinuity in the seismic stratification of the upper mantle (*Gaherty et al.*, 1999). Although various physical parameters need not necessarily describe the same boundary, several studies demonstrate an agreement between the lithospheric thickness as derived from seismological, thermal and electromagnetic observations (e.g. *Praus et al.*, 1990, *Babuška and Plomerová*, 1993).

So far, most information about the thickness of the lithosphere comes from low-resolution surface-wave observations. High-resolution seismic body-wave observations of

the lithosphere-asthenosphere boundary are very rare. This is in contrast to the Moho, which is globally a much better documented discontinuity. The thickness of the lithosphere is considered to be close to zero at mid-ocean ridges, up to about 200 km beneath stable cratons with 80 to 110 km being the global average. The asthenosphere probably extends in average to 150-250 km depths, where *S* wave velocity rises again to a value corresponding to rigid peridotite. *Lehmann* (1961, 1964) proposed the existence of a general discontinuity in the upper mantle, the Lehmann Discontinuity, at a depth of ca. 220 km. The base of the asthenospheric low velocity zone may correspond to the Lehmann discontinuity, which is shallow in cold, stable cratonic areas and deep in hot, active regions of the world according to *Thybo* (2006). The low velocity zone of the asthenosphere is much better developed under ocean basins than under continental shield areas where it is sometimes barely developed. Hence, oceanic lithosphere is much better defined seismologically than continental lithosphere.

However, velocity-depth profiles through the Earth's upper mantle do not define the top and bottom of the zones of rigid and viscous behaviour precisely because the zones have transitional boundaries. If the lithosphere is simply a thermal boundary layer that is more rigid owing to colder temperatures, mantle flow models (*King and Ritsema*, 2000; *Zaranek et al.*, 2004) indicate that the velocity gradient at its base would occur over tens of kilometres. In contrast, if the asthenosphere is weak owing to volatile enrichment (*Hirth and Kohlstedt*, 1996; *Karato and Jung*, 1998; *Gaherty et al.*, 1999; *Hirth et al.*, 2000) or the presence of partial melt (*Anderson*, 1989), the lithosphere-asthenosphere boundary could occur over a much smaller depth range. Altogether, compared to the main seismic boundaries in the Earth (Moho, 410 km discontinuity, 660 km discontinuity, Core-Mantle-Boundary, boundary between the inner and outer core), the asthenosphere has very weak contrasts in seismic parameters to the surrounding intervals, and its detection requires high-resolution seismic data with a high signal-to-noise ratio (*Thybo*, 2006).

So far, the lithosphere-asthenosphere boundary has not been found globally, perhaps because of significant variations in the depth of the discontinuity (*Rychert et al.*, 2005). However, according to *Thybo* (2006), the upper mantle low velocity zone should be a global continental feature below relatively constant 100 ± 20 km depth with the following characteristics:

- 1-5% lower velocity than in the surrounding intervals,
- strong attenuation of seismic waves, in particular S-waves,
- low electrical resistivity
- it includes seismic scatterers,
- its base is a seismic refractor at variable depth (the Lehmann discontinuity), which is shallow (150-250 km deep) in cold, stable areas and deep (250-400 km depth) in hot, active areas.

Thybo (2006) summarizes effects that may contribute to the creation of seismic low velocity zones, seismic scattering effects, and the origin of the Lehmann discontinuity at the base of the low velocity zone: rocks close to the solidus or in a partially molten state, the presence of fluids, change in anisotropy, change in rheology, metamorphic phase transformations, changes in composition, remnants of subducted slabs, an irregular base of the lithosphere, and magmatic intrusions. *Artemieva* (2003) suggests that in the East European Platform the low velocity zone formed by metasomatic processes as the result of

rifting processes. However, according to *Thybo* (2006) it is unlikely that this mechanism can explain its global occurrence.

Finally it has to be stated that there is still no consistent use of terms regarding discontinuities or gradients within the lithospheric mantle and between the lithosphere and mantle transition zone, which may lead to confusion and misunderstandings (see also *Anderson*, 1995).

In this chapter, observations of additional phases within *P* receiver function data are described first (section 6.2). These additional phases are interpreted to originate at converters in 50 and 65 km depth, respectively, and therefore are proposed to be a distinct feature of the lithospheric mantle beneath the western Bohemian Massif.

The *S* receiver function technique described in Chapter 4 enables observations of the lithosphere-asthenosphere boundary with a resolution so far only known for the Moho. The observations are described in section 6.3. Apart from the prominent signal of the Moho in the *S* receiver functions, a second deeper discontinuity with reversed polarity is observed in this study. Following earlier *S* receiver function studies mentioned above, the latter discontinuity is interpreted as the LAB, although it is not trivial to identify a seismic discontinuity with a mechanical or thermal boundary.

6.2 Additional phases observed in *P* receiver function data

Previous studies indicate the local existence of seismic reflectors and/or converters in the uppermost mantle at 50 to 60 km depth beneath the western Eger Rift as well as the Teplá-Barrandian and Moldanubian units (*Tomek et al.*, 1997; *Geissler et al.*, 2005; *Hrubcová et al.*, 2005). In the receiver functions obtained in this thesis, additional phases were observed in the area of Moho updoming and CO₂ gas emanations (western Eger Rift): a positive phase at about 6 s delay time with respect to the *P* onset, followed by a strong negative phase at about 7 to 8 s (in the following referred to as 7.5 s). Stations NALB and B24 in Figure 5.1 provide examples for the two additional phases; station NKC shows in the sum trace only the negative phase. The positive phase was already observed by *Geissler et al.* (2005) who named it the “6 s phase”. To further investigate these phases, the area was divided into boxes (Figure 6.1). According to their piercing points at an interface of 65 km depth, the single receiver function traces were assigned to the boxes, corrected for moveout and stacked. Only sum traces obtained by at least ten single traces (grey boxes in Figure 6.1) were considered in the following. The boxes with additional phases at 6 s and/or 7.5 s are shaded pink. They form a coherent structure centred on the western Eger Rift. An overview over receiver function data of all boxes is given in Figure 6.2, which shows on top those boxes which contain a negative phase near 7.5 s and partly a positive phase near 6 s. Whereas the positive phase at 6 s occurs mainly in the central and eastern part of the pink shaded area, the negative phase occurs in all pink boxes. The pink area includes the area of CO₂ emanations (white ellipses in Figure 6.1), but also extends further to the north and south partly into the Regensburg-Leipzig-Rostock zone (see Figure 6.1). The area of apparent Moho updoming (see Figures 5.8 and 5.9) corresponds to the southwestern part of the pink shaded area.

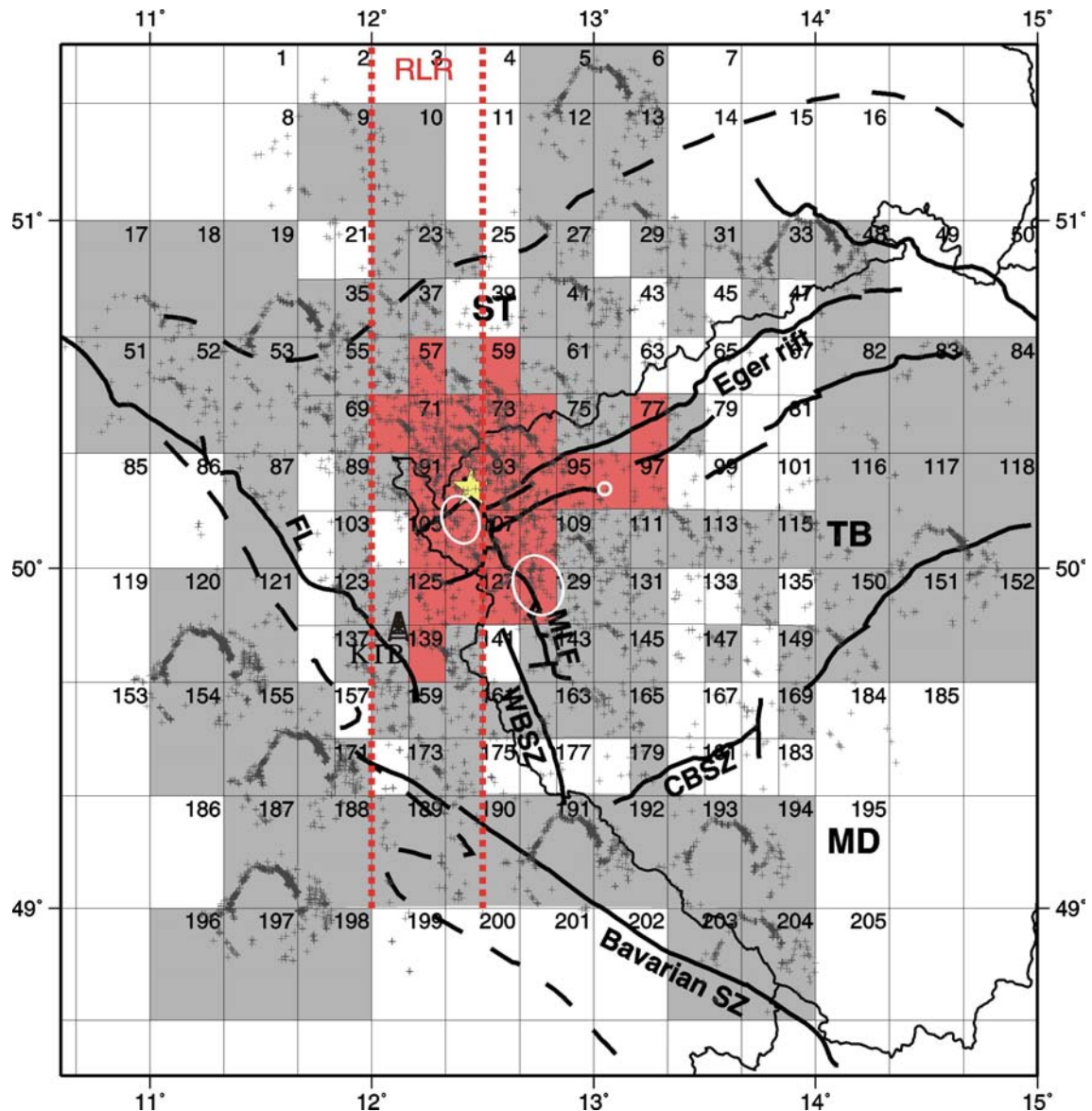


Figure 6.1: Occurrence of a negative phase near 7.5 s delay time. The piercing point of the rays at an interface at 65 km depth are shown by dark grey crosses. The area was divided into 205 boxes and only boxes with at least 10 individual traces were considered. Traces were stacked within each box. Pink boxes show an additional negative phase at 7.5 s, grey boxes do not. The yellow star shows the Nový Kostel main swarm earthquake area, white circles depict the main CO₂ degassing areas, RLR (red dotted lines) gives the approximate location of the Regensburg-Leipzig-Rostock zone (Bankwitz *et al.*, 2003).

6.3 Discussion: Structures within the lithospheric mantle

Figure 6.3 shows data along two profiles in which the additional phases are also shaded pink. The negative 7.5 s phase was not observed by Geissler *et al.* (2005), probably due to too sparse data. The observed additional phases could either be direct signals from structures in the upper mantle, or multiple reverberations from structures within the crust. A first step to test the difference between these two possibilities is an analysis of the distance moveout of the observed phases. For direct *P_s* conversions, the delay time of the

phase decreases with increasing epicentral distance, while for multiple reverberations it is opposite. Therefore, the receiver functions of four coherent boxes showing the additional phases near 6 and 7.5 s (boxes 93, 94, 107, 108, see Figure 6.1) were stacked within epicentral distance intervals of 10° (Figure 6.4). The delay time of the phases (Moho P_s conversion, phases at 6 and 7.5 s, crustal multiple $PpSs/PsPs$) was then measured for each epicentral distance interval. There is a weak trend visible that points to a decrease of delay time of the additional phases at 6 and 7.5 s with increasing epicentral distance, which indicates that they are direct converted phases from a structure in the uppermost mantle (Figure 6.4). However, the effects of moveout are very small in this shallow depth range. The differences are within the resolution limits of the data, therefore the obtained result is an indication rather than evidence. As expected, the crustal multiple $PpSs+PsPs$ shows an increase in delay time with increasing epicentral distance. A test of different moveout corrections (for direct phases P_s and for the crustal multiple $PpPs$) furthermore shows that the amplitudes of both additional phases are slightly higher for the assumption of direct phases than for crustal multiple, which is a further indication for direct conversions rather than multiple reverberations. But again, the differences in amplitudes were very small and thus can not be taken for evidence.

To further test possible origins of these additional phases, synthetic receiver functions were calculated using the plane wave approximation described by *Kind et al.* (1995). *Geissler et al.* (2005) showed that the origin of the positive phase at 6 s could be in the crust or mantle or both (*Geissler et al.*, 2005). In seismic wide-angle data a reflector at 55 to 58 km depth was found by *Hrubcová et al.* (2005) which starts slightly SE of the western Eger Rift and runs SE into the central Moldanubian unit. In seismic reflection studies the reflector was also found (*Tomek et al.*, 1997). In the present study, the positive phase at 6 s is modelled by introducing a velocity increase at 50 km depth (Figure 6.5). However, in the BOHEMA data set this phase exists only in a subset of the pink boxes. The negative phase at 7.5 s could be modelled by assuming a velocity decrease of $3.7 \pm 1.0\%$ at approximately 65 km depth in the uppermost mantle (Figure 6.5). A 5 km thick gradual velocity decrease between 65 and 70 km explains the data equally well. The velocity decrease can be interpreted as a local updoming of the lithosphere-asthenosphere boundary (LAB) beneath the western Eger Rift area. However, this proposed LAB would locally be significantly shallower than the 80 km depth proposed by *Babuška and Plomerová* (2001). In the area of the grey boxes, where the negative phase at 7.5 s is not observed, the LAB might be deeper and therefore its signal might be masked by crustal multiples. The relatively small amplitudes of the crustal multiples in the data traces at 12 s and 16 s compared to the computed traces can be attributed to several causes: (1) the decrease of the amplitudes of the multiples in the data trace due to not optimal stacking of the single traces as the moveout correction was performed for P_s and not for multiples, and (2) the missing effect of lateral crustal heterogeneities in the model (*Heuer et al.*, 2006).

An updoming of the LAB to 65 km depth could account for increased partial melt in the lithospheric mantle which may lead to the mantle-derived degassing of CO_2 . The observed Moho updoming and proposed shallow LAB should induce an increased heat flow. However, it is not clear yet which contribution to the geothermal anomalies measured in the investigation area should be attributed to deeper-seated heat sources, because of the presence of radiogenic heat-producing granite complexes within the upper crust (see *Förster and Förster* (2000); *Emmermann and Lauterjung* (1997)).

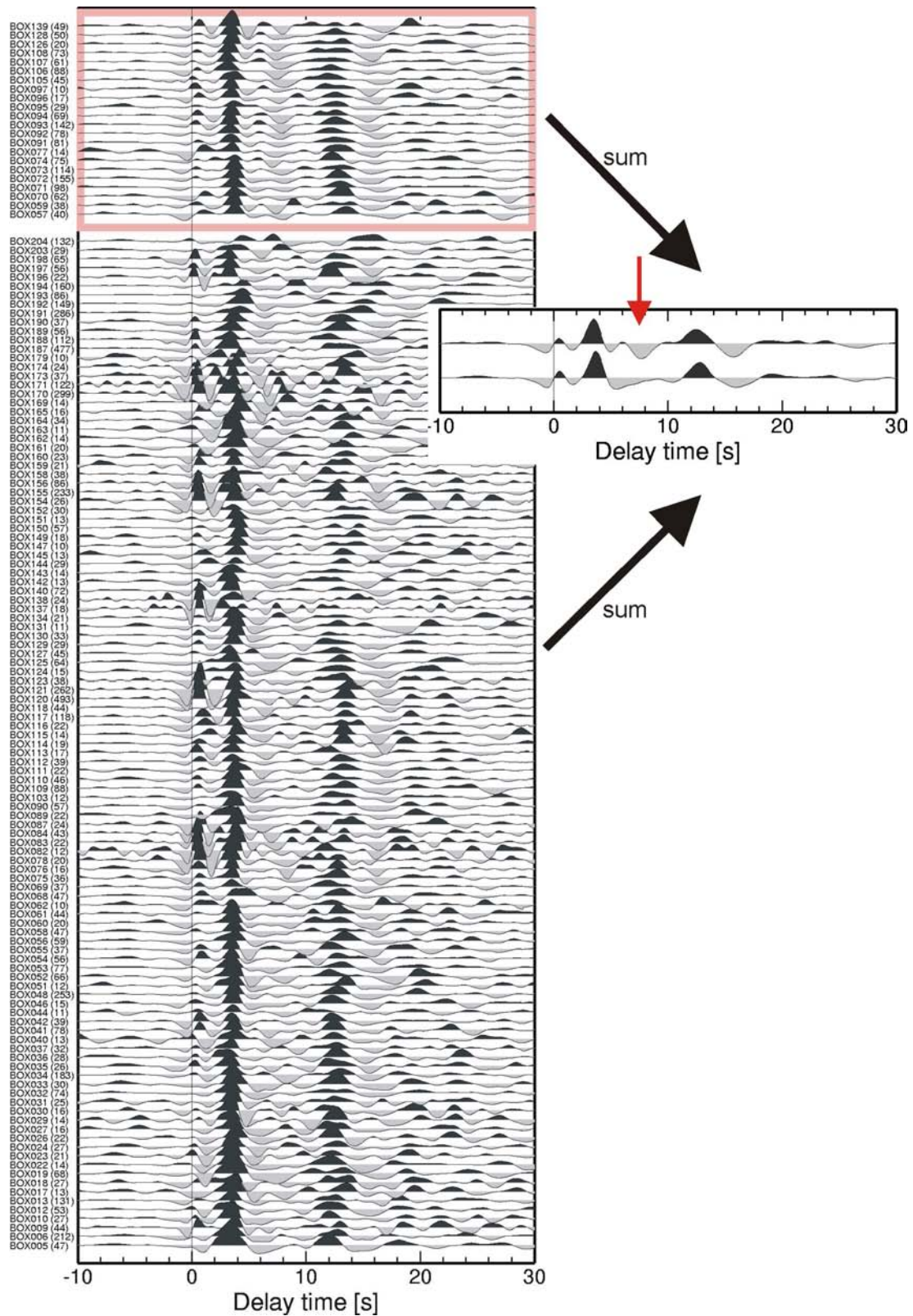


Figure 6.2: Sum traces of all boxes containing at least 10 individual traces (see Figure 6.1). Traces showing a negative phase near 7.5 s are displayed on top of the Figure. Some of them also show the positive phase near 6 s reported by *Geissler et al.* (2005). The traces in the lower part correspond to the grey boxes in Figure 6.1. To the right, the sum trace of all pink boxes (upper trace) and of all grey boxes (lower trace) of Figure 6.1 is shown. They are practically identical except for the time window between 6 and 10 s (red arrow points at observed negative phase).

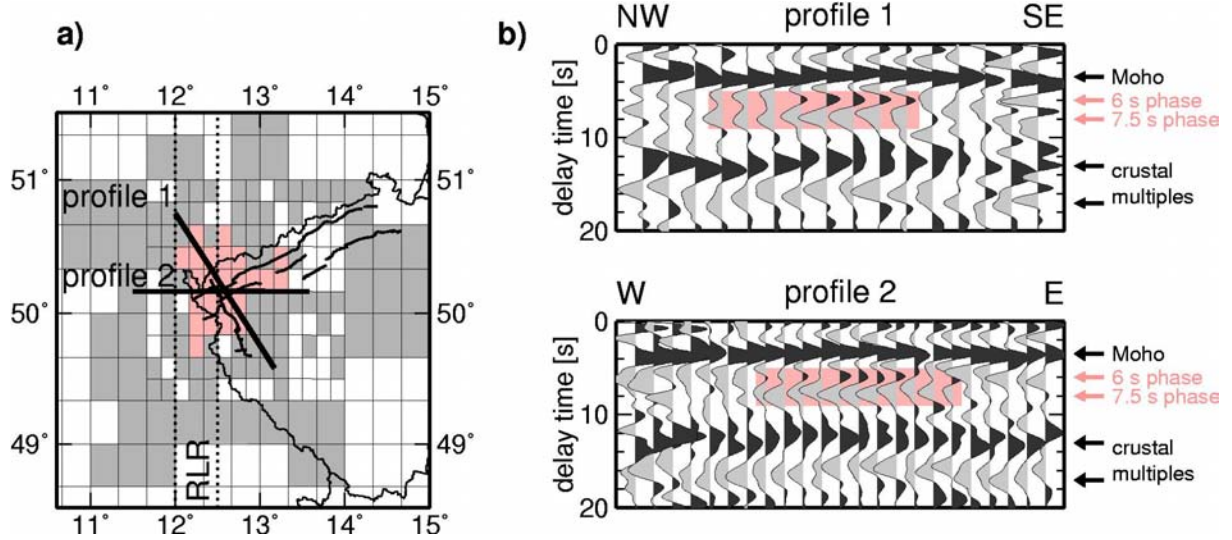


Figure 6.3: Sum traces of the boxes along two profiles in the time domain. **a)** location of the profiles. **b)** The profiles show the Moho Ps conversion at about 3.6 s. Positive/negative phases at about 6 s/7.5 s are shaded pink (Heuer *et al.*, 2006).

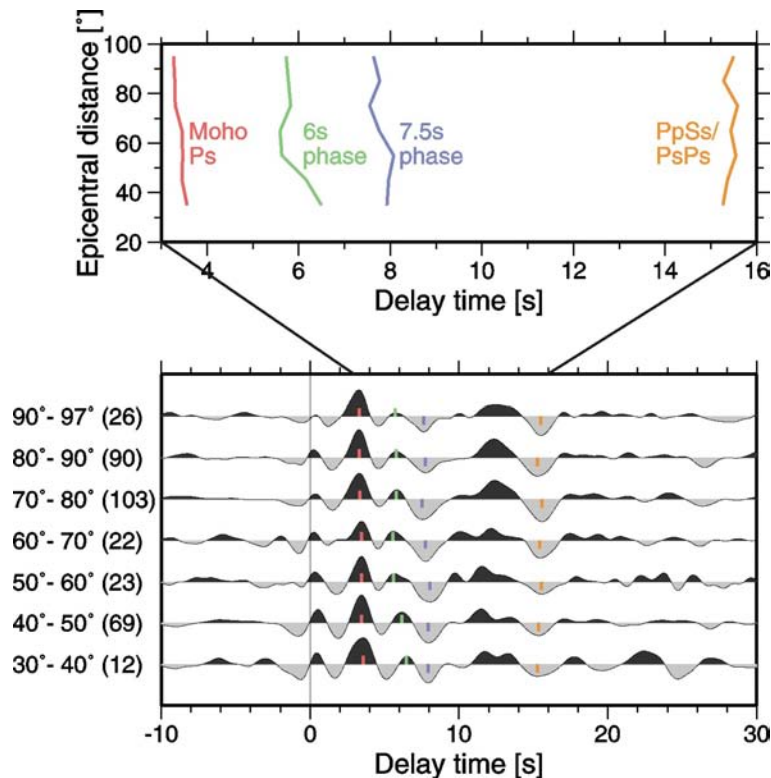


Figure 6.4: Test of the distance moveout of the additional phases near 6 and 7.5 s. Receiver functions of boxes 93, 94, 107, 108 were stacked within epicentral distance intervals of 10°. The stacked traces are shown in the lower part of the Figure. In brackets, the number of stacked individual traces is given. On top, the delay time axis is enlarged and delay times are drawn as lines to make trends better visible. The additional phases at 6 and 7.5 s show a slight decrease of delay time with increasing epicentral distance, which indicates that they might be direct conversions from a structure in the uppermost mantle rather than multiple reverberations from a structure within the crust.

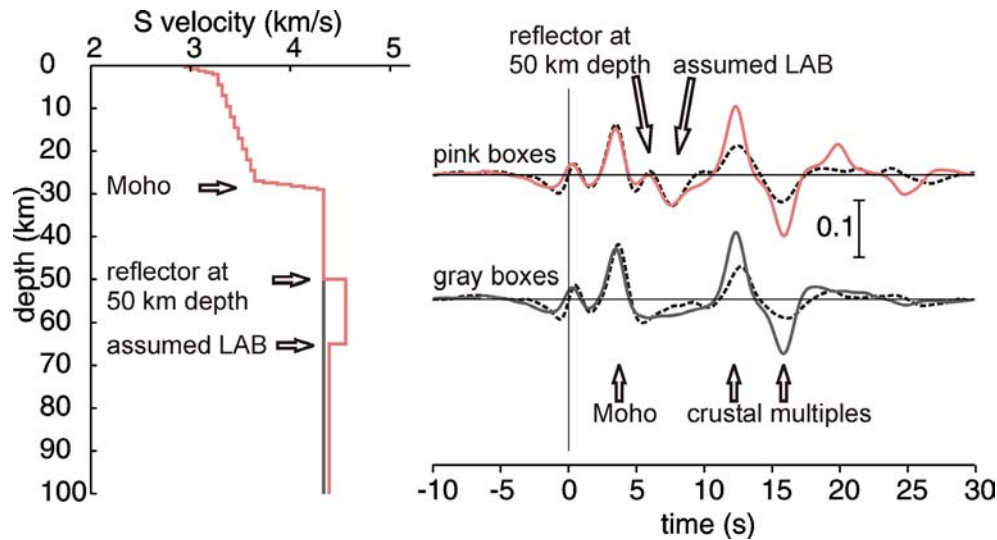


Figure 6.5: **Left:** Two models of S-wave velocity to explain the observed phases in the grey and pink boxes (Heuer *et al.*, 2006). The models are identical down to a depth of 50 km. **Right:** Black dashed line shows the stacked signal of all traces within the pink boxes (top) and grey boxes (bottom). The traces are practically identical except for the phases at 6 s and 7.5 s, interpreted as „reflector at 50 km depth“ and „assumed LAB“, respectively. Amplitudes of the additional phases at 6 s and 7.5 s in the data of the pink boxes are small due to suboptimal stacking of the traces as the delay time of the phases is not exactly the same and the phase at 6 s occurs only in a subset of the pink boxes. The solid line shows the response of the S velocity model on the left. The scale shows the amplitudes in per cent of the incoming P-wave.

An updoming of the LAB should be reproducible by the method of *S* receiver function analysis (see Chapter 4). Thus, *S* receiver function investigation of the data can help to deny or confirm the existence of a possible LAB updoming suggested by the data of *P* receiver functions. This is shown in the next section.

6.4 Observations in *S* receiver function data

6.4.1 *S* receiver functions obtained at the seismic stations

For 80 stations of the BOHEMA experiment and the experiment by Geissler *et al.* (2005) (see Appendices A.1 and A.2), *S* receiver functions were computed as described in Chapter 4. Examples of *S* receiver functions obtained at four stations are shown in Figures 6.6 and 6.7. At 3-4 s delay time after the *S* onset, the strong signal of the Moho *Sp* conversion can be seen. At about 10 to 12 s, a weaker negative phase is observed. Following the current state of research (e.g. Li *et al.*, 2004 ; Kumar *et al.*, 2005a, 2005b, 2006; Sodoudi *et al.*, 2006a,b), this negative phase is attributed to the lithosphere-asthenosphere boundary which has a negative velocity gradient.

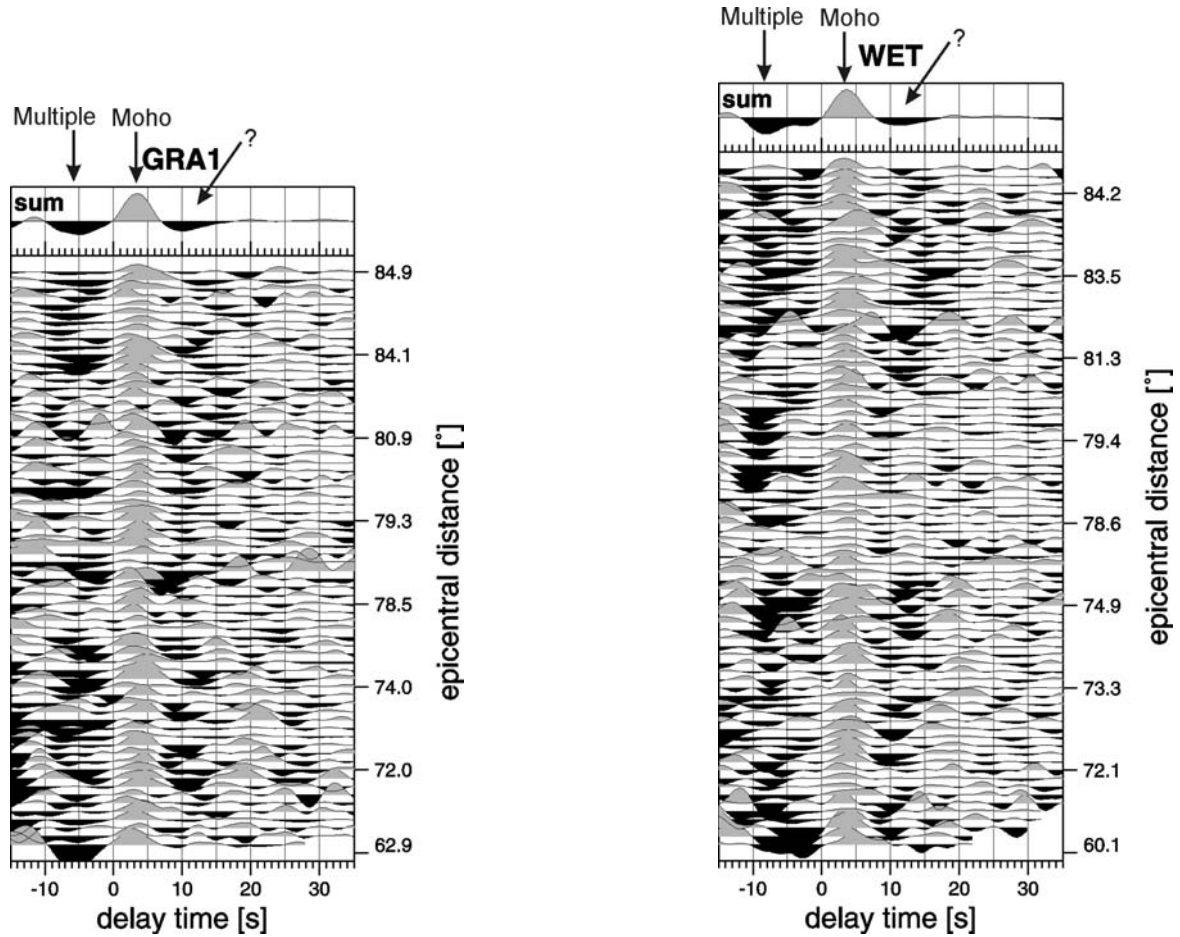


Figure 6.6: *S* receiver functions obtained for permanent stations GRA1 (left) and WET (right) of the German Regional Seismic Network. The delay time of the seismic signals with respect to the time of the *S* onset is shown. Each trace shows the *S* receiver function of a single teleseismic event. A low pass filter of 4 s and moveout correction were applied. The traces are sorted by the epicentral distance of the corresponding event. Note that the scale of epicentral distances is not linear. On top of the Figure, the sum traces of the single traces are shown for each station. At about 3-4 s delay time, the signal of the Moho *Sp* conversion can be seen. At about 10 to 12 s, a negative signal is observed. The signals occurring at negative delay times are attributed to multiple reflections.

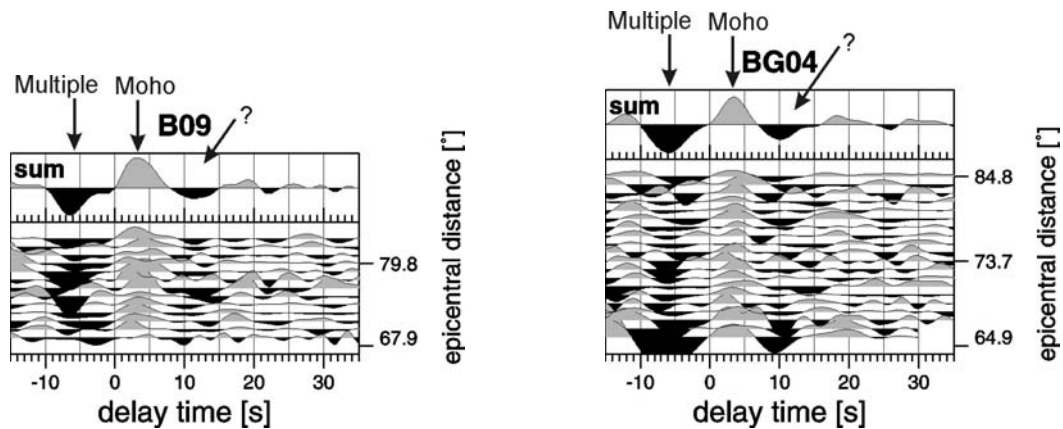


Figure 6.7: *S* receiver functions obtained for temporary stations B09 (left) and BG04 (right) of the BOHEMA network. Description see Figure 6.6.

6.4.2 Dividing the data into local “boxes”

For investigating the lithosphere-asthenosphere transition with S receiver functions it is important to consider the location of origin of the negative phase. Due to the ray geometry, the piercing point of a ray at an interface at 80 km depth is situated approximately 70-155 km away from the station for epicentral distances of $85-60^\circ$, respectively. If the station locations are as close to each other as in this study, the piercing points of different stations strongly overlap. Hence the data must be grouped according to their piercing points at a certain depth rather than stationwise. A map of the piercing points at 80 km depth for the

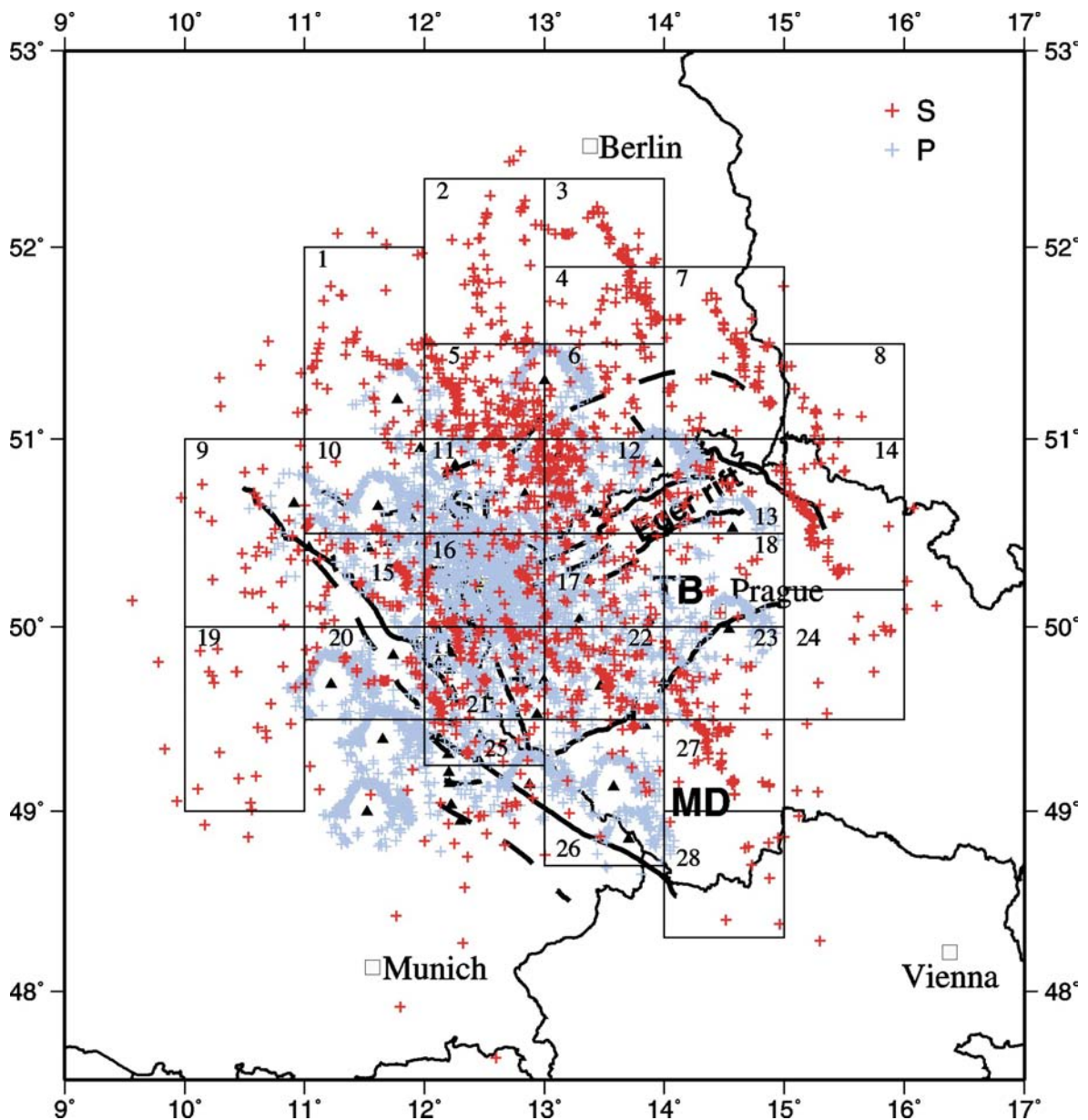


Figure 6.8: Piercing points of P (blue crosses) and S (red crosses) rays at an interface at 80 km depth. Seismic stations are shown by black triangles. For S receiver functions, the piercing points are located approximately 70 to 155 km away from the recording station. As the piercing points of different stations overlap each other, the area was divided into 28 boxes to group the S receiver function data geographically for further investigations.

obtained *S* receiver functions compared to piercing points at 80 km depth for *P* receiver functions is shown in Figure 6.8.

The area was then divided into 28 non-overlapping boxes also shown in Figure 6.8. The width of the boxes is 1° longitude and between 0.4 and 1° latitude, which corresponds to box sizes of approximately 70 km E-W and 45-112 km N-S extension (3200 km^2 to 8000 km^2) at the Earth's surface. Only box 25 is smaller.

The single traces of each box were visually checked for quality. As the delay time of the Moho onset is known from *P* receiver functions to occur around 3 to 4 s, an approximate delay time of 2 to 5 s of the Moho *Sp* conversion signal was one quality criterion. Furthermore, extremely noisy traces were also omitted. Finally, the traces were stacked to improve the signal-to-noise ratio. Examples for *S* receiver functions obtained for individual boxes are shown in Figure 6.9. Like in the examples for individual stations, the Moho *Sp* conversion at 3 to 4 s delay time is very strong and clear. It is followed by a weaker negative signal at 8 to 14 s attributed to the lithosphere-asthenosphere transition. This negative signal does not always seem to be coherent in the individual traces at one station, probably due to scattering of the phase.

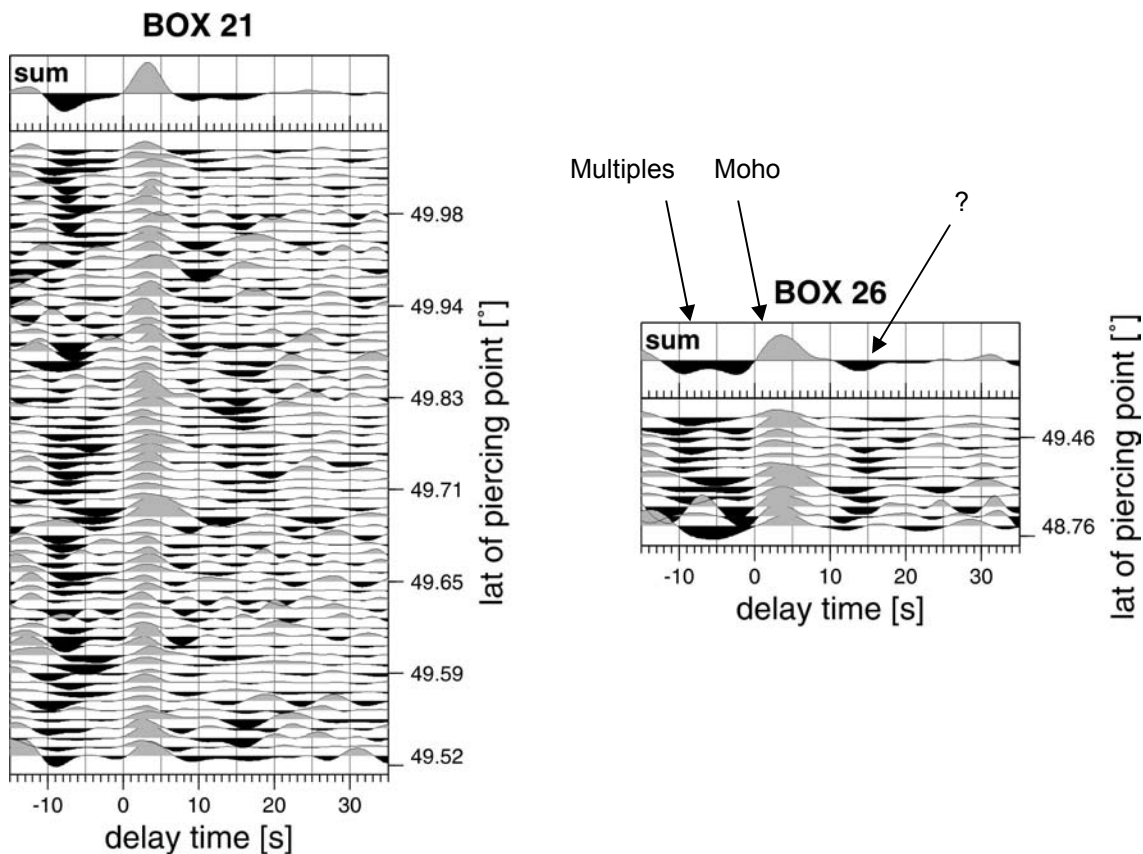


Figure 6.9: Data examples of *S* receiver functions obtained for six boxes. Zero time is the *S* arrival time. The processing of the traces was carried out in the same manner as described in Figure 6.6, only that here the traces are sorted by the latitude of the piercing points at 80 km depth. Note that the scale of latitude of piercing point is not linear. Again, on top of the Figure the sum traces of the single traces are shown for each box (**continued on next page**).

Figure 6.9, continued.

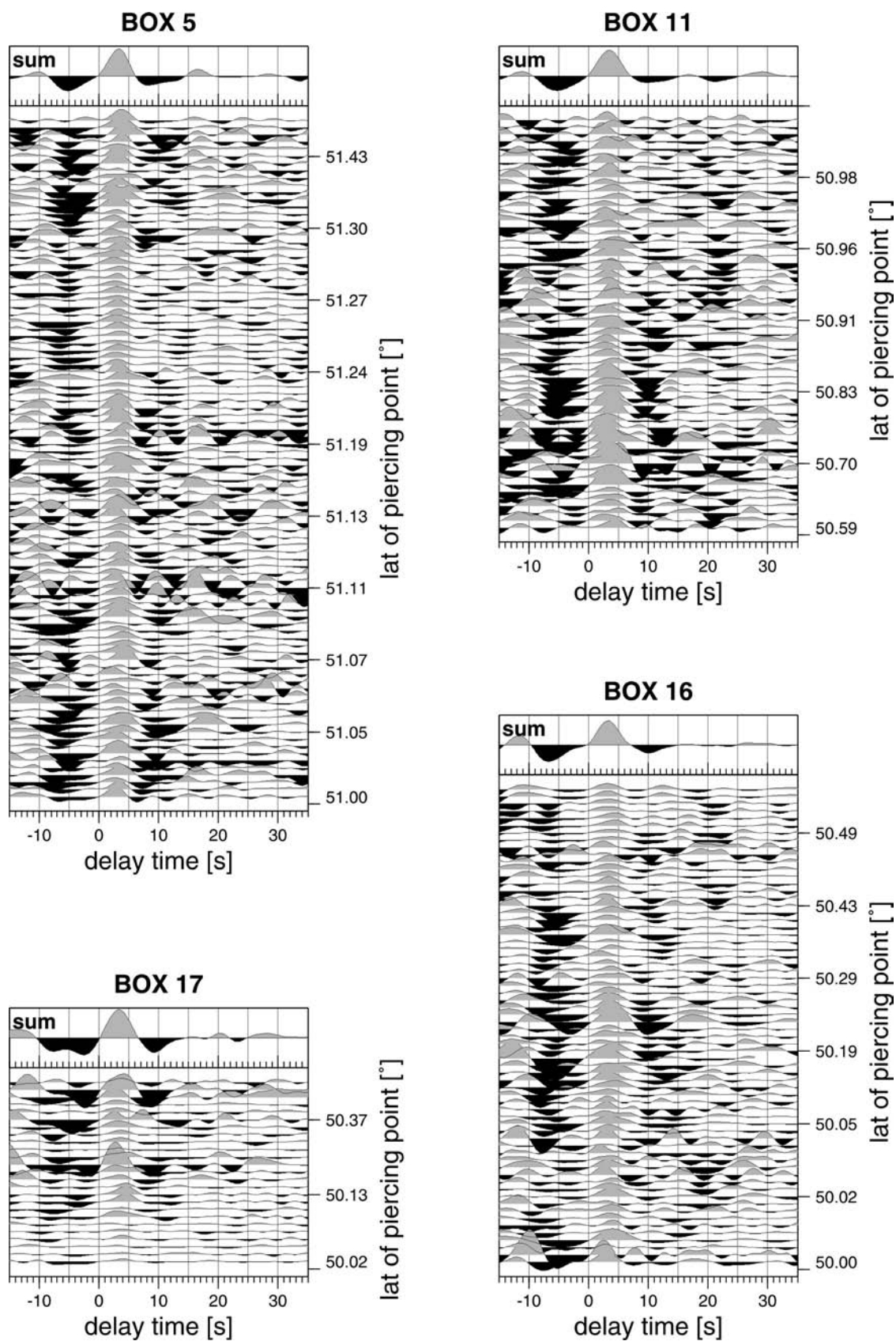


Figure 6.10a shows the summation traces of all 28 boxes sorted by box number. After the Moho signal at 3 to 4 s delay time, the negative phases arrive at 8 to 14 s. They are coherent for most boxes and clearly arrive later in boxes 25 to 28 (at 12 to 14 s versus 8 to 10 s in boxes 1 to 24). As the signal is rather weak and for most boxes arrives directly after the Moho Sp conversion signal, there is also the possibility of it being merely a side lobe of the Moho signal and thus an artefact produced by the deconvolution. This would be the case if the Q component also showed such side lobes in the deconvolved S signal. To investigate this, the Q components were stacked for each box in order to compare the sum traces of the Q components with those of the L components (the S receiver functions). This is shown in Figure 6.10(b). The comparison shows that there are no or only very weak side lobes in the Q summation traces. Therefore it can be excluded that the negative signals observed in the S receiver functions at 8 to 14 s are only artefacts of deconvolution but are most probably the S -to- P conversions generated at the negative velocity gradient of the lithosphere-asthenosphere transition.

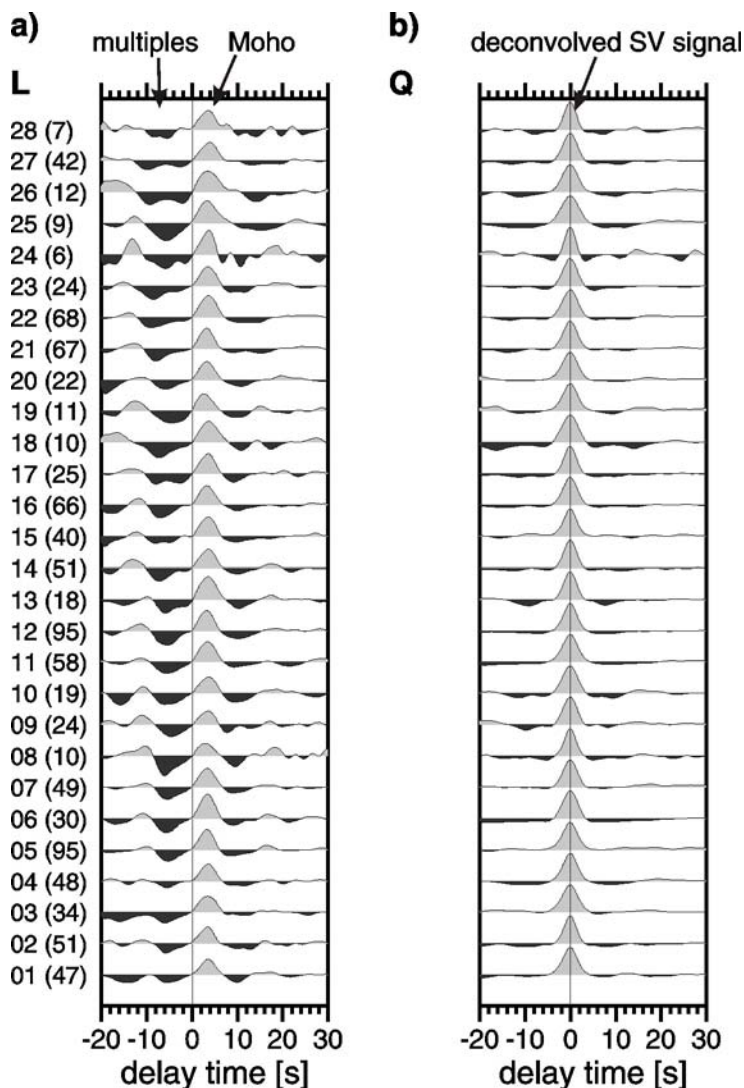


Figure 6.10: Comparison of summation traces of L and Q components for all boxes. On the left, box numbers and, in brackets, the number of stacked traces are shown.

(a) S receiver functions (L components) show a very strong and clear Moho Sp signal at 3 to 4 s delay time. The negative signal attributed to the lithosphere-asthenosphere transition follows at approximately 8 to 14 s and is weaker, but still coherent for most boxes. In boxes 25 to 28, the negative signal clearly arrives later than in the other boxes (at 12 to 14 s).

(b) The Q components show no or only weak side lobes in the deconvolved S signal, so that it can be excluded that the negative phases observed before and after the Moho Sp conversion signal are merely artefacts generated by deconvolution. Instead, the negative phase at around 10 s delay time is most likely the conversion signal from the lithosphere-asthenosphere transition.

6.5 Discussion

6.5.1 Lithospheric thickness beneath the western Bohemian Massif

The boxes that show an unambiguous negative conversion signal after the Moho S_p conversion are shown in Figure 6.11 together with the delay time that was picked for the negative phase. For some boxes (boxes 2-5, 9, 21-23, see Figure 6.10) the negative signal in the sum trace was either doubled or very broad, so that no clear decision for a certain delay time of the signal could be made.

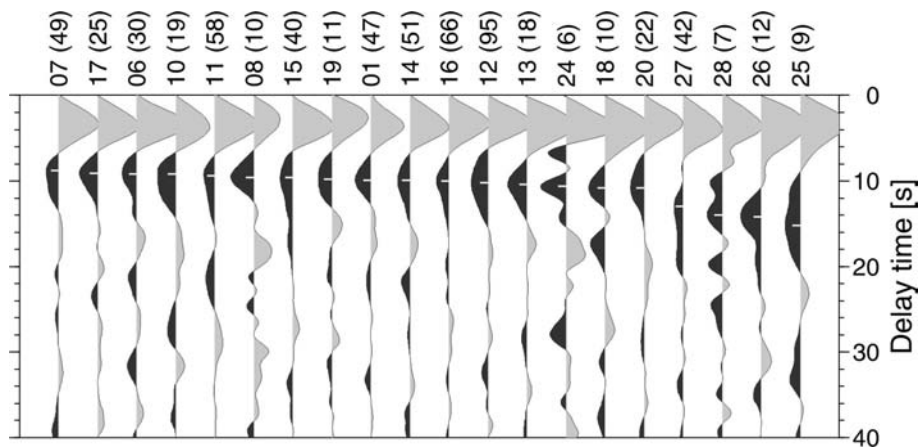


Figure 6.11: Boxes for which an unambiguous delay time of the negative phase could be picked (small black dashes). The boxes are sorted by increasing delay time of the negative phase.

A good approximation of the depth origin of the negative phase can be achieved by multiplying the picked delay time by a factor of 9 based on the IASP91 standard earth model (*Kennett and Engdahl, 1991*). The result of this depth estimation is visualized in the map in Figure 6.12. According to the current state of knowledge, this negative phase is usually interpreted as the conversion from the lithosphere-asthenosphere transition. However, this transition is not very well constrained yet regarding its nature, depth location and width of gradient zone. If it is interpreted as the lithosphere-asthenosphere transition, the map in Figure 6.12 shows lithospheric thickness of 80 to 90 km beneath the Saxothuringian and partly the Teplá-Barrandian unit. Towards the south, the thickness first seems to slightly increase (boxes 20, 18, 24: 95 km) and then strongly increases in the Moldanubian part of the investigation area to 115 to 135 km. Boxes 24, 25 and 28 in the very south show only a scarce data coverage. However, as the obtained depth values of the boxes in the Moldanubian part are quite coherent, the result of a thick lithosphere in this area is considered to be reliable. The obtained values are summarized in table 6.1.

It is interesting to note that the boxes in the transition from the Saxothuringian/Teplá-Barrandian type lithosphere to the thicker Moldanubian lithosphere (boxes 21 to 23) belong to the boxes where it was difficult to determine a clear negative signal in the summation trace. Especially for boxes 21 and 22 a doubling or broadening of the negative signal can be stated which could point to either an abrupt increase of lithospheric thickness

or a very steep slope or possibly even a structure from palaeosubduction within the lithosphere in the mentioned boxes. *Babuška and Plomerová* (2001) observed in the area of box 21 a mixture of anisotropic characteristics of the Saxothuringian and Moldanubian units within the lower lithosphere south of the surface trace of the Saxothuringian/Moldanubian contact. As an explanation the authors suggested underthrusting of a part of the Saxothuringian subcrustal lithosphere beneath the Moldanubian or a hypothetical remnant of the Early Palaeozoic oceanic lithosphere subducted to the south during collision of the Saxothuringian and Moldanubian units.

Table 6.1: Box number, coordinates of the centre of the box, number of traces n stacked within each box, measured delay time of the S_p conversion from the LAB and corresponding calculated LAB depth.

Box №	lon [°E]	lat [°N]	n	delay time LAB [s]	depth LAB [km]
1	11.5	51.5	47	9.9	90
2	12.5	51.925	51	?	?
3	13.5	52.125	34	?	?
4	13.5	51.7	48	?	?
5	12.5	51.25	95	?	?
6	13.5	51.25	30	9.2	85
7	14.5	51.45	49	8.8	80
8	15.5	51.25	10	9.6	85
9	10.5	50.5	24	?	?
10	11.5	50.75	19	9.2	85
11	12.5	50.75	58	9.4	85
12	13.5	50.75	95	10.2	90
13	14.5	50.75	18	10.4	95
14	15.5	50.6	51	9.9	90
15	11.5	50.25	40	9.6	85
16	12.5	50.25	66	10.0	90
17	13.5	50.25	25	9.1	80
18	14.5	50.25	10	10.8	95
19	10.5	49.5	11	9.8	90
20	11.5	49.75	22	10.8	95
21	12.5	49.75	67	?	?
22	13.5	49.75	68	?	?
23	14.5	49.75	24	?	?
24	15.5	49.85	6	10.6	95
25	12.5	49.375	9	15.2	135
26	13.5	49.1	12	14.2	130
27	14.5	49.25	42	13.0	115
28	14.5	48.75	7	14.0	125

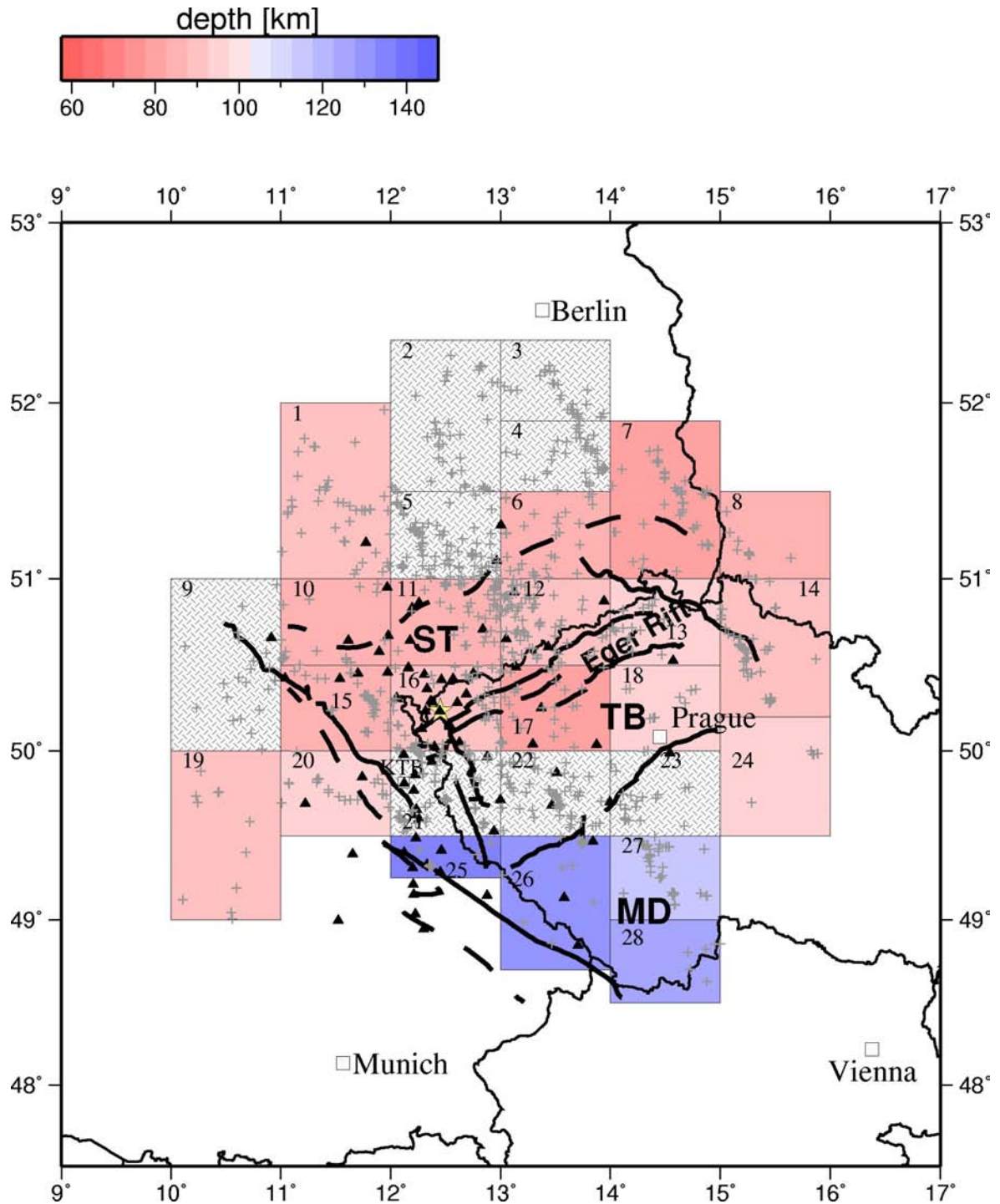


Figure 6.12: Map of the depth origin of the negative phase, which probably represents the lithosphere-asthenosphere transition beneath the western Bohemian Massif. The grey crosses show the data coverage of the boxes – the crosses correspond to piercing points of the rays at 80 km depth. In the Saxothuringian and partly the Teplá-Barrandian unit the depth is 80 to 90 km, in the Moldanubian part of the investigation area it is 115 to 135 km. In the hatched boxes, the negative signal of the lithosphere-asthenosphere transition was either ambiguous or too broad for determining a clear peak.

6.5.2 N-S and E-W Profiles

Figures 6.13-6.18 show three N-S and three E-W profiles of *S* receiver functions (single traces and stacked traces) in the investigation area. They will be discussed in the following.

The N-S profile between 12°-13°E (Figure 6.13) indicates in most parts a lithospheric thickness of approximately 80 to 90 km. North of 51°N, the negative signal is ambiguous both in the single and stacked traces. Nevertheless, north of 51.7°N the amplitudes of a slightly south dipping LAB seem to be quite strong. This is not visible in the map in Figure 6.13, because all traces between 51.5-52.5°N lie within box 2, which in the sum trace gives not such a clear image of a deep LAB but shows a rather broad signal (see Figure 6.10a). South of 50°N the LAB clearly becomes deeper both in the single and stacked traces with delay times around 13 s to more than 15 s, corresponding to LAB depths of 120 to 140 km. The origin of a negative signal at approximately 22 s delay time between 50.5 and 51.2°N is not clear. It could be caused by a downward decrease in seismic velocities in approximately 200 km depth.

The N-S profile between 13°-14°E (Figure 6.14) shows a clear and smooth LAB between 50°-51.5°E at ca. 90 km depth in the single and stacked traces. South of 50.2°N, the LAB again clearly deepens down to 120 to 130 km like in the profile east of it. North of 51.5°N there is generally no clear negative signal visible at the expected LAB delay time both in the single and stacked traces. This is contrary to the profile between 12°-13°E. Only the northernmost trace at about 52.2°N shows a strong negative signal at 12 s delay time.

The third N-S profile between 14°-15°E (Figure 6.15) shows a clear and relatively even LAB signal from about 50.0°N northwards. Between 49.3°-49.8°N there is a small, very shallow negative signal at approximately 7 s delay time, corresponding to a depth of origin of approximately 65 km depth. The origin of this very shallow signal is not clear. In the southern part of the profile (south of 49.3°N), the delay time of the negative signal is not very clear both in the single traces and in the stacked traces. This is probably due to sparse data. However, the adjacent Alpine orogen may also be a cause of the more complicated structure in the south of this profile. The negative signal at about 13 s delay time is interpreted as the LAB signal in the southern part of the profile so that it is coherent with the other N-S profiles. In this profile, the time interval later than 15 s delay time is rather noisy even in the stacked traces. As the data is not very dense, the seemingly coherent structures within later (deeper) parts of the profile should not be overinterpreted.

The southernmost E-W profile, which runs between 49.5°-50.0°N (Figure 6.16), shows in its western part a LAB depth of approximately 100 km. Between about 12.3°-14°E it clearly deepens with a maximum of approximately 135 km depth at 12.7°E. Between 13°-14°E there seems to be a doubling of the negative signal, but as the corresponding N-S profile (Figure 6.14) shows a rather clear phase at 13 to 14 s, the LAB signal in this profile is interpreted accordingly to originate at a depth of 120 to 130 km. The trace with the very shallow negative signal 14.4°E obviously corresponds to the unusually shallow signals observed in the N-S profile between 14-15° (Figure 6.15). The explanation of this signal is not clear yet.

The E-W profile between 50.0°-50.5°N (Figure 6.17) shows in the west up to 12.0°E a 80-90 km deep LAB. At about 12.3°E, the LAB signal is shallower (7 s delay time, corresponding to approximately 65 km depth) and deepens again slightly towards the east

up to about 90 km. A doubling of the negative signal is observed from 13.7°E eastwards which is also observed in the corresponding N-S profile between 14-15°E (Figure 6.15). Although the data is rather sparse in this part of the profile, the doubling is coherent among four (partly overlapping) stacked traces .

The northernmost E-W profile between 50.5°-51.0°N (Figure 6.18) shows a strong and even LAB signal at approximately 90 to 100 km depth.

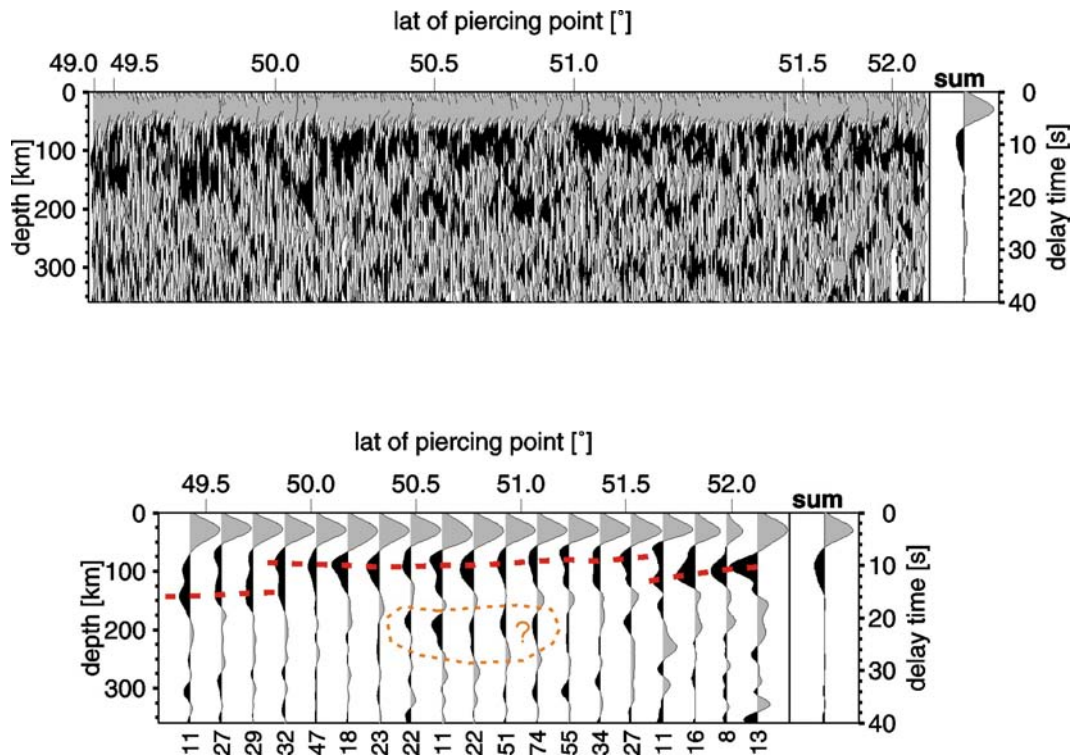


Figure 6.13: N-S profiles of *S* receiver function data between 12°-13°E. In the upper profile, single traces sorted by latitude of their piercing point at 80 km depth are shown with even trace spacing. Thus, the ordinate showing the latitude of the piercing points is not linear. On the right side, the sum trace of all single traces is shown. The right ordinate gives the delay time relative to the *S* onset, the left ordinate shows the approximate corresponding depth. Single traces are filtered with a 6 s low pass filter. In the lower profile, the single traces are stacked within moving geographical windows of 0.25° latitude and 0.1° overlap. Here, the ordinate showing the latitude of piercing points is linear. The stacking process enhances the stable signals while it suppresses some of the noise of the single traces. The stacked traces are filtered with a 4 s low pass filter. Below the stacked traces, the number of individual traces used for stacking is given.

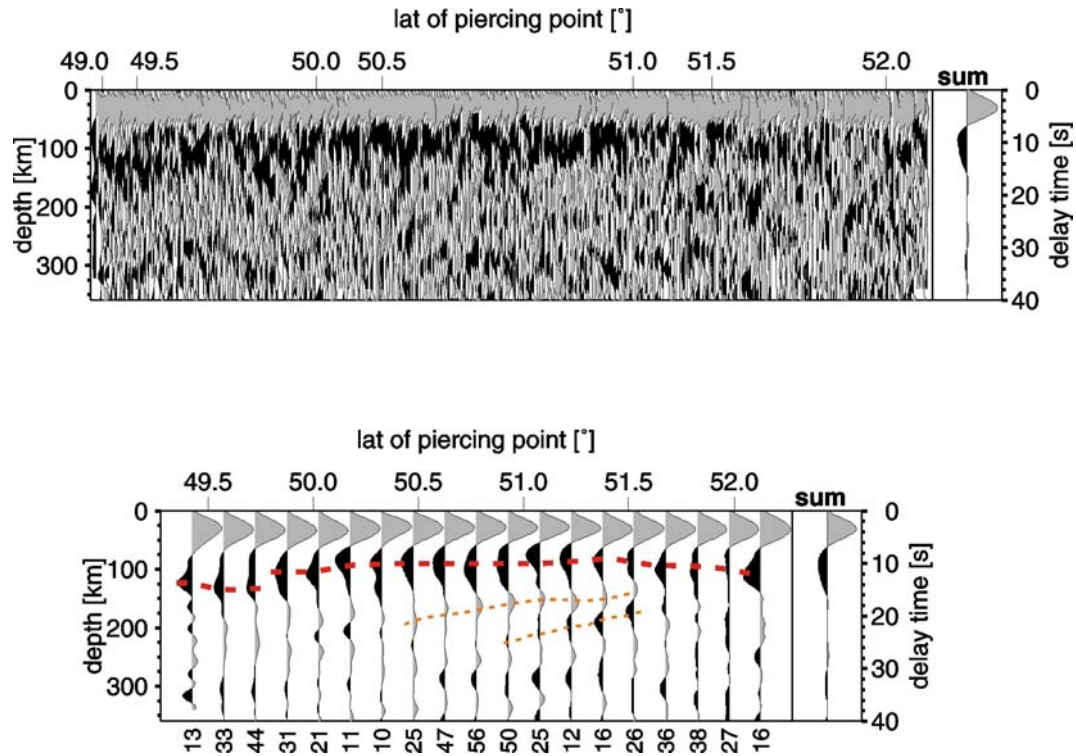


Figure 6.14: N-S profiles of *S* receiver functions between 13°-14°E. Description see Figure 6.13.

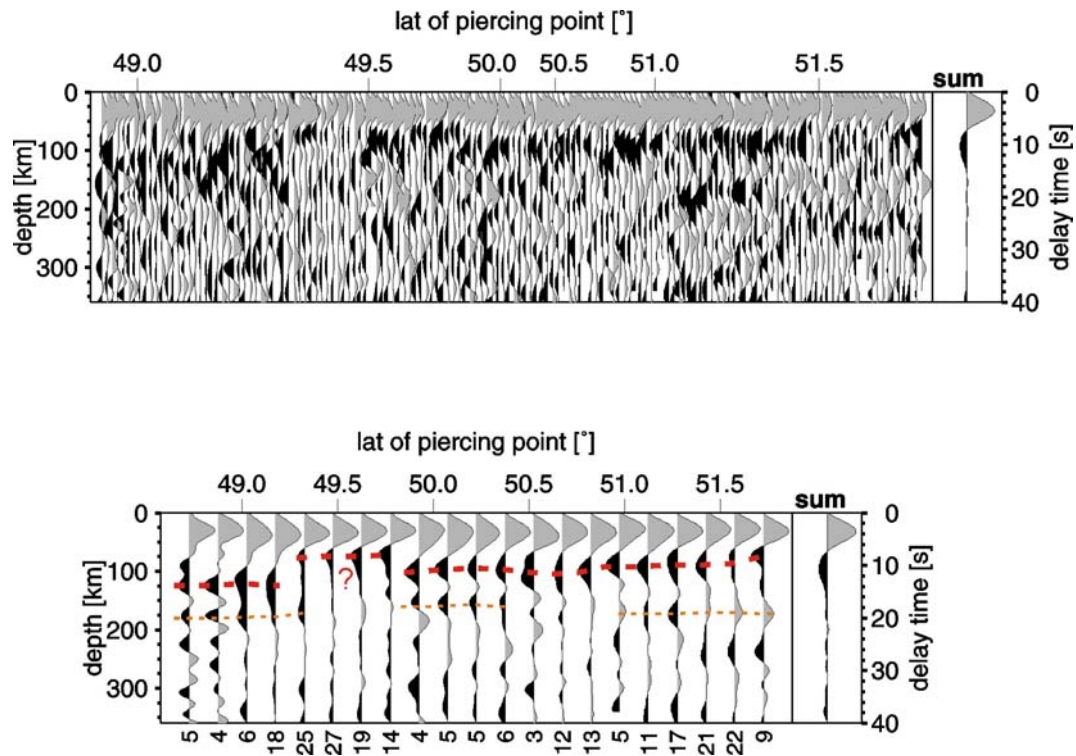


Figure 6.15: N-S profiles of *S* receiver functions between 14°-15°E. Description see Figure 6.13.

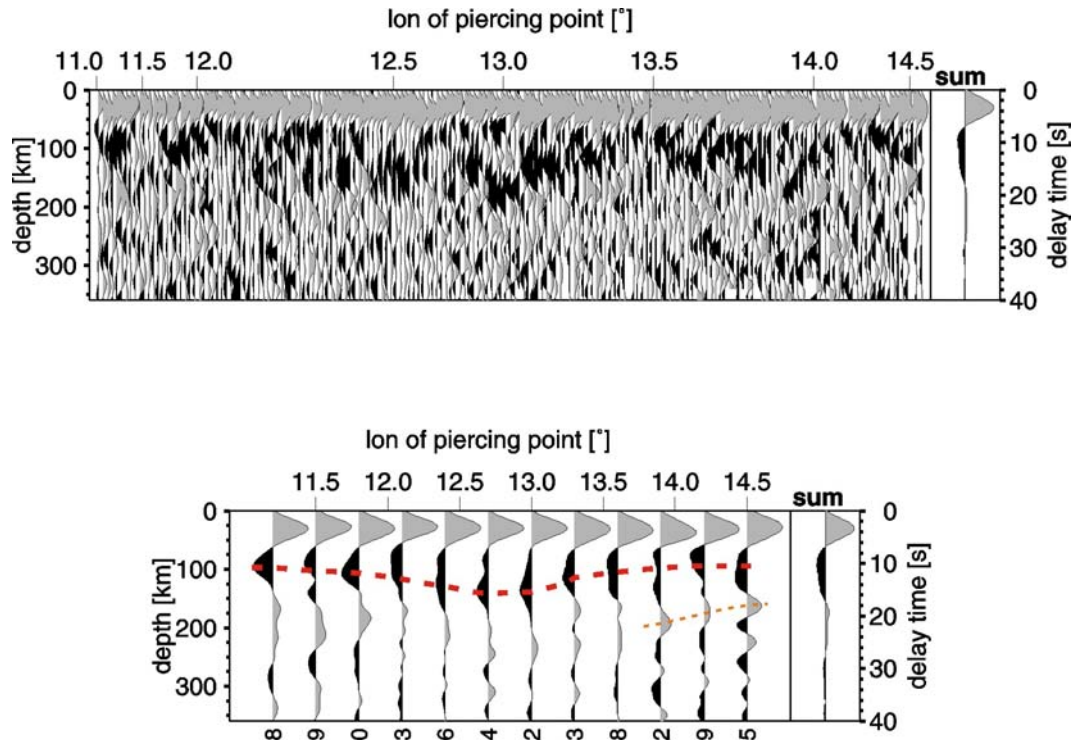


Figure 6.16: E-W profiles of S receiver functions between 49.5° - 50.0° N. Description like Figure 6.13, but for E-W profiles the single traces were stacked within moving geographical windows of 0.3° longitude with an overlap of 0.1° .

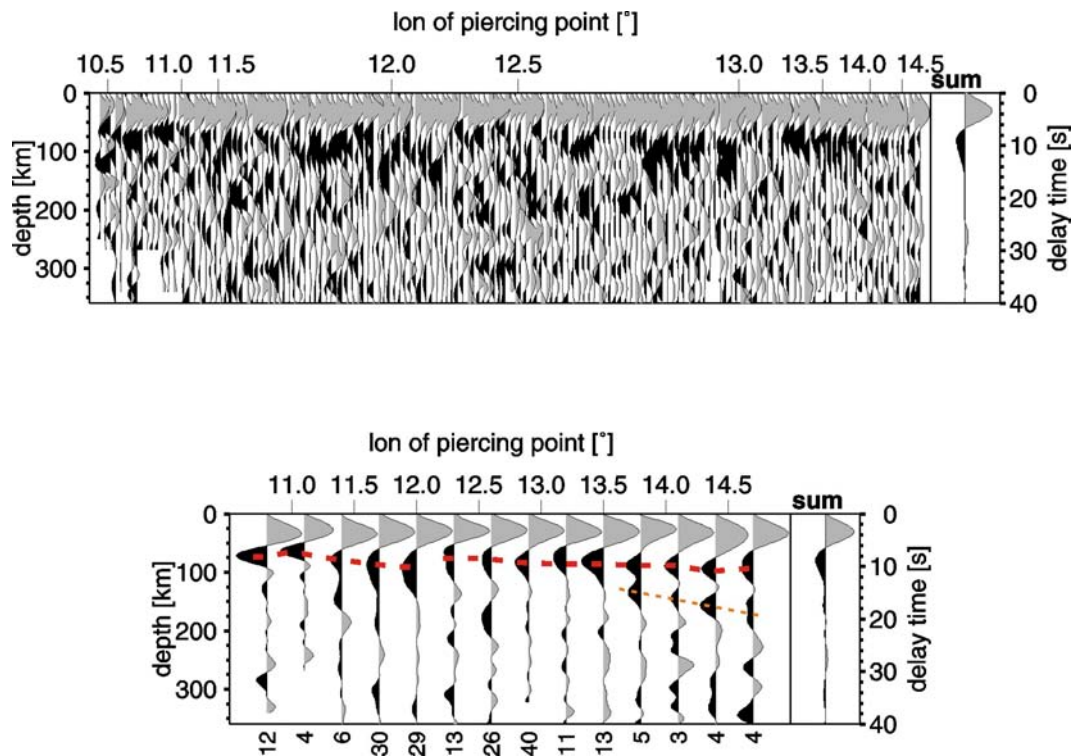


Figure 6.17: E-W profiles of S receiver functions between 50.0° - 50.5° N. Description see Figure 6.16.

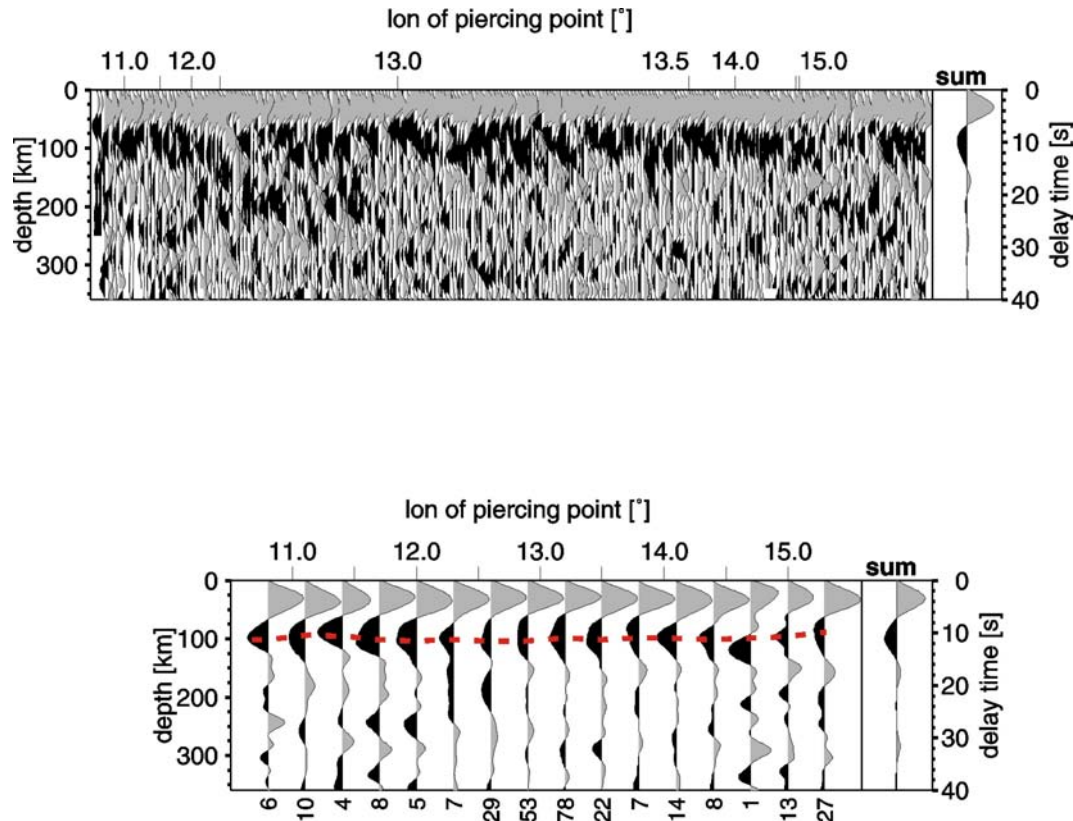


Figure 6.18: E-W profiles of *S* receiver functions 50.5°-51.0°N. Description see Figure 6.16.

Figure 6.19 shows the location of the N-S profile between 12°-13°E again, as it will be further discussed in the following. In Figure 6.20, data of *P* and *S* receiver functions are directly compared. The *S* receiver function profile has already been described above. The *P* receiver functions show a much sharper and better resolved Moho signal at 3.5 s due to their higher frequency content. At approximately 12 and 16 s the strong and coherent crustal multiples appear. In most of the stacked *P* receiver function traces of the profile the negative signal after the Moho *P*_s conversion splits into several peaks and can not be clearly identified. Only in the latitude interval of 49.9° to 50.6° the negative conversion is very clear and unambiguous. No indications for structures in the crust that might cause this negative phase are visible in the data. This area corresponds to the area of pink boxes. However, the positive phase near 6 s delay time does not show in the data, probably because it occurs only in a smaller area than the negative phase near 7.5 s.

By comparing the sum traces of the *P* receiver functions with the sum trace of the *S* receiver functions, it is not clear whether the negative signal observed at about 7.5 to 8 s in the *P* receiver functions corresponds to the negative signal in the *S* receiver functions at about 9 to 10.2 s interpreted as the conversion from the LAB. The superimposed traces of *P* and *S* receiver functions in Figure 6.21 show that in the *S* receiver functions the negative signal occurs about 2 s later than in the *P* receiver functions. The difference of 2 s in the delay times is significant as the stacking of individual traces provides rather stable phases. Furthermore, the value is clearly above the estimated uncertainty of 0.2 s for picking delay times in the receiver function traces.

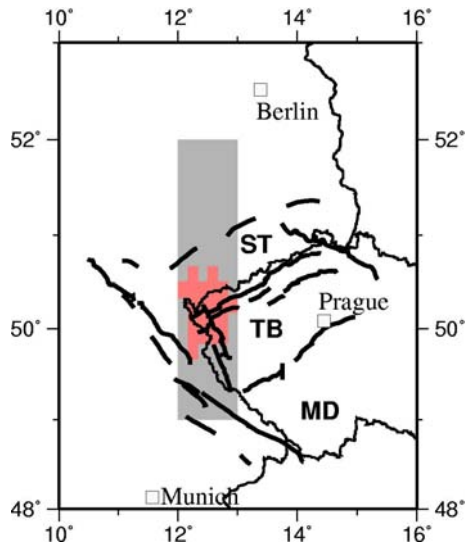


Figure 6.19: The grey shaded band between 12 and 13°E shows the location of the data profiles of Figures 6.20 and 6.21. The red area within the profile corresponds to the area where a negative phase at about 7.5 s delay time and partly a positive phase near 6 s delay time occurs in the *P* receiver functions (see Figure 6.1).

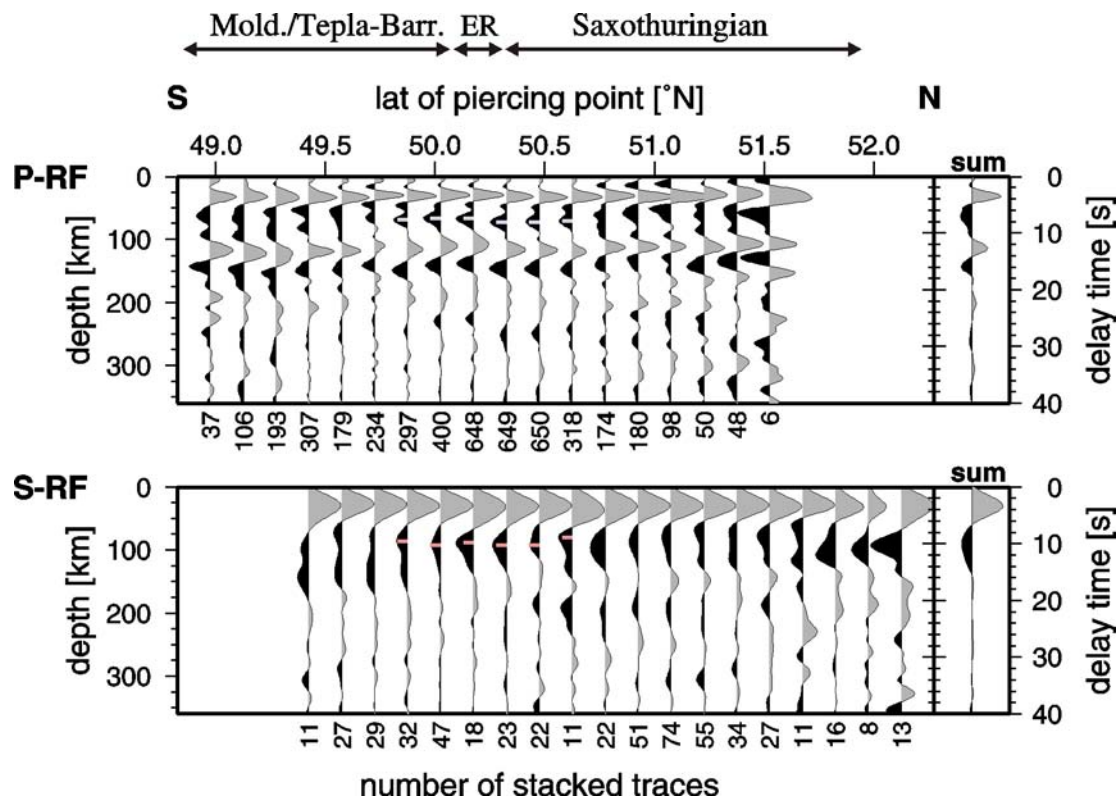


Figure 6.20: Comparison of *P* and *S* receiver functions along the N-S profile between 12°-13°E. Top: *P* receiver functions, stacked in windows of 0.25° latitude with 0.1° overlap and filtered between 2-20 s. Bottom: *S* receiver functions stacked and filtered in the same manner as *P* receiver functions. To the right of each profile, the sum trace of all individual traces is shown. The individual traces were sorted before-hand according to their piercing points in 80 km depth. The maxima of the negative phase after the Moho signal were picked in the area of interest between 49.9°-50.6°N. In the *P* receiver functions, the delay times of the negative phase vary between 7.4 to 8.0 s, in the *S* receiver function between 9.0 to 10.2 s.

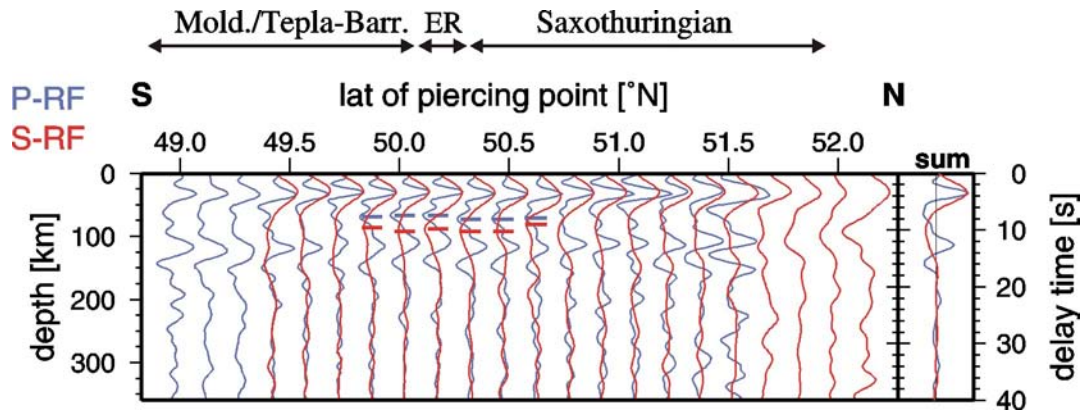


Figure 6.21: The same data profiles as in Figure 6.19, but corresponding traces of P and S receiver functions are super-imposed. The delay time of the Moho conversion signal is nearly identical in most traces. As in Figure 6.19, the maxima of the negative phases that arrive after the Moho P_s conversion are marked in the area of interest. In the S receiver functions, the negative phase arrives approximately 2 s later than in the P receiver functions.

It is not trivial to interpret these structures, because the frequency content of the two methods is different (P receiver functions have dominating wave periods around 1 s, while for S receiver functions wave periods around 5 s prevail) and hence also the resolution. At 80 km depth, a P wave with a period of 1 s and wave speed of 8 km/s has a wave length of $\lambda=8$ km. Assuming a vertical resolution of $\lambda/4$, a layer of at least 2 km thickness can be resolved by P receiver functions. An S wave with a period of 5 s and a wave speed of 4.5 km/s at 80 km depth has a wavelength of 23 km, which means that a layer must be at least 6 km thick to be detectable for S receiver functions. A thin layer of anomalous velocity might thus be detectable by P receiver functions and invisible in S receiver function data. A sharp gradient might be better visible in P receiver function data, while a broad gradient might be better to detect in S receiver function data.

Furthermore, due to the different geometry of the P_s and S_p rays, the incidence angles at the seismic interface and hence the conversion coefficients of the two ray types also differ, which influences the amplitude of converted energy.

Two scenarios are imaginable to explain the occurrence of the negative phase in the P and S receiver functions at slightly but significantly different delay times:

- 1) The negative phases in the P and S receiver functions represent two distinct discontinuities. A thin low velocity layer is detected by the P receiver functions in the lithospheric mantle at approximately 65 km depth. As its thickness is between 2 and 6 km, it can not be detected by the S receiver function method. This low velocity layer could for example be caused by patches of partial melt. As the negative phase in the P receiver functions is observed in the area of CO_2 degassing and occurrence of earthquake swarms, a causal connection between the low velocity area at 65 km depth and these phenomena might be assumed. However, the negative gradient observed in S receiver function data at approximately 9 to 10 s is more or less coherent throughout the whole profile and might thus be interpreted as the lithosphere-asthenosphere transition. However, the thinning of the lithosphere proposed by *Babuška and Plomerová* (2001) would then not be obvious in the S

receiver function data, furthermore the diapiric mantle upwelling suggested by *Granet et al.* (1995) for the Bohemian Massif would show no imprint on the lithosphere-asthenosphere transition.

- 2) The negative phases in the P and S receiver functions represent in principle the same negative velocity gradient, but strongly influenced by the different frequency contents of the P and S waves and by the possible nature of the transition from high to low velocities with increasing depth. For example, if the gradient is steep at about 65 km depth and becomes increasingly less steep at 80 to 90 km depth, then P receiver functions would image also the steep part while S receiver functions would image also the flatter part of the gradient. However, as the negative phase in the P receiver functions is only observed in the broader surroundings of CO_2 degassing at surface and earthquake swarm occurrence, the proposed steep gradient zone would also occur only in this area. Again, this implies a thin region of strongly decreased seismic velocity at about 70 km depth which might be associated with the occurrence of partial melt in this depth range.

Chapter 7

Discontinuities of the mantle transition zone

7.1 Nature of the mantle transition zone

The mantle transition zone marks the transition from the upper to the lower mantle. Its characteristics are important for our understanding of Earth's dynamics. The mantle transition zone is bounded by distinct seismic discontinuities which are named after the average depth in which they occur: the 410-km discontinuity or '410' (*Jeffreys*, 1936), and the 660-km discontinuity or '660' (*Niazi and Anderson*, 1965). Over the past decades, a number of seismic studies have demonstrated the global existence of these discontinuities and have mapped their topography (e.g. *Shearer and Masters*, 1992; *Flanagan and Shearer*, 1998a; *Gossler and Kind*, 1996; *Gu et al.*, 1998). However, the '410' is usually more difficult to detect than the '660' due to its smaller velocity contrast and to a regional strong topography, which makes observations in long period data rather difficult (*Bina and Helffrich*, 1994; *Rost and Weber*, 2002; *Flanagan and Shearer*, 1998b).

Furthermore, a weaker discontinuity at 520 km depth ('520') has been observed locally. However, a global existence of the '520' is still a matter of controversial discussion. Some studies claim that the 520-km discontinuity is a global feature (*Shearer*, 1990, 1996; *Gaherty et al.*, 1999), whereas others find that it can be observed only in certain regions (*Gossler and Kind*, 1996; *Deuss and Woodhouse*, 2001), or that it is not found beneath continental shields (*Gu et al.*, 1998), or that it might not exist at all (e.g. *Cummins et al.*, 1992; *Bock*, 1994).

According to the *IASP91* velocity model (*Kennett*, 1991; *Kennet and Engdahl*, 1991), the velocity increase at the '410' is +3.6% for *P* waves and +4.1% for *S* waves. At the '660' it is +5.8% for *P* waves and +6.3% for *S* waves. For the '520', *Helffrich* (2000) reports a velocity contrast of only 1% or less, and *Bock* (1994) used an impedance contrast of 2% and assumed a second-order seismic discontinuity between 510 and 530 km for calculating synthetic seismograms.

The two main seismic discontinuities in the mantle at 410 and 660 km depth are most probably pressure-induced phase transformations in peridotite rather than a change in chemical composition. Experiments in the mid-1960s (*Ringwood and Major*, 1966) showed that the olivine component of peridotite undergoes successive pressure-dependent transformations: at pressures of 13-14 GPa (corresponding to 410 km depth), olivine transforms into wadsleyite, at pressures of 18 GPa (corresponding to 520 km depth) wadsleyite transforms into ringwoodite, which ultimately breaks down to form perovskite

and magnesiowüstite at pressures of about 23 GPa, corresponding to 660 km depth in the Earth (Bina and Helffrich, 1994; Helffrich, 2000; Helffrich and Wood, 2001). High-pressure mineral-physics studies have shown that transition zone minerals at average mantle temperatures have anomalously high water solubility relative to upper-mantle minerals. Water solubility of the mantle transition zone is about 10-30 times higher than that in the upper and probably lower mantles (Bercovici and Karato, 2003).

The transformations at the '410' and '520' have positive Clapeyron slopes, with dP/dT of approximately $+3 \text{ MPa K}^{-1}$ and $+4 \text{ MPa K}^{-1}$, respectively. In contrast, the breakdown of ringwoodite to perovskite plus magnesiowüstite at the '660' has a negative slope of -2 MPa K^{-1} (Helffrich, 2000). Thus, if the 410- and 660-km discontinuities are entirely due to these phase transformations, regions of abnormally low temperature such as subduction zones should correspond to elevation of the '410' to lower depths and depression of the '660' to greater depths (Figure 7.1). In general, the '660' is depressed under cold regions (slabs) as expected, but the '410' appears to be far more complicated (Gu *et al.*, 2003; Flanagan and Shearer, 1998a,b). The stacked *P*-to-*S* converted phase (receiver function) from the '410' may be rather weak and complicated and sometimes shows negative pulses above the '410' (Gilbert *et al.*, 2003; Song *et al.*, 2004).

However, these discontinuities due to phase transitions are not sharp boundaries but rather gradual transitions. This is due to a coexistence zone of the two mineral phases at each transition (Helffrich, 2000), furthermore to the influence of temperature and water content. From short period data, the thickness of the '410' was estimated to be about 5 km (Yamazaki and Hirahara, 1994; Helffrich, 2000). The '660' is also thought to be less than 10 km thick (Castle and Creager, 2000). The 520-km discontinuity does not reflect shorter period energy (Benz and Vidale, 1993) and is therefore probably a boundary spread over at

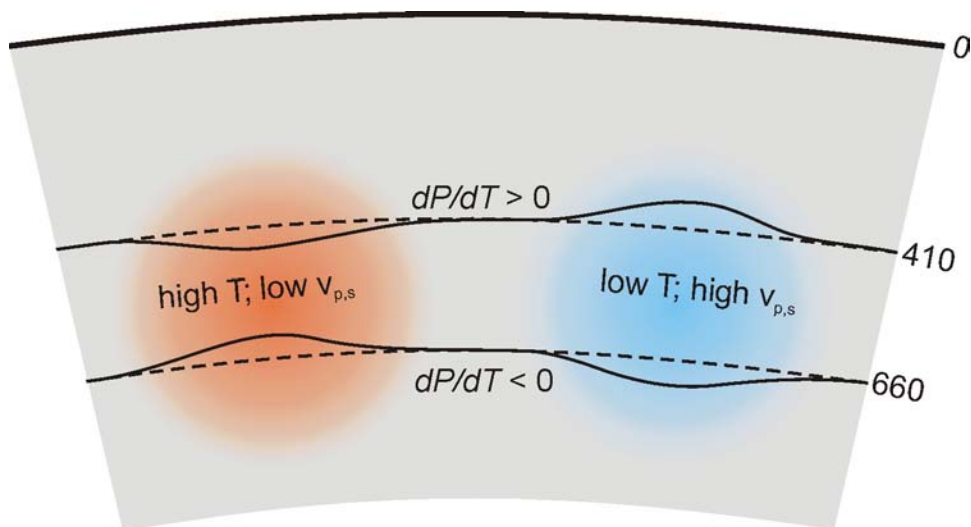


Figure 7.1: Schematic depiction of the mantle transition zone in an olivine-dominant mantle after Lebedev *et al.* (2002). The transition from olivine to wadsleyite and from spinel to perovskite and magnesiowüstite give rise to the 410- and 660-km discontinuities, respectively. The effective Clapeyron slopes dP/dT have opposite signs. Absent lateral variations in composition, relatively low temperatures (*T*) cause thickening of the transition zone and increase in seismic velocities (v_p , v_s), while high temperatures cause thinning of the transition zone and decrease in v_p and v_s .

least 10 km in depth.

The non-olivine component in the mantle is about 30%. Phase changes in the pyroxene and garnet components of mantle peridotite are gradual, and lead to changes in slope of the curves of seismic velocity versus depth rather than discrete discontinuities (*Helffrich and Wood, 2001*) and/or to multiple discontinuities especially in the lower part of the mantle transition zone (e.g. *Akaogi et al., 2002; Simmons and Gurrola, 2000; Deuss and Woodhouse, 2001*).

7.2 Observation of the upper mantle discontinuities in the study area

In order to investigate the ‘410’ and ‘660’ with the receiver function data, it is necessary to take into account that due to the ray geometry, the obtained information stem from a region 80-170 km (‘410’) and 150-310 km (‘660’) away from the receiver. Therefore, the piercing points of the rays at depth interfaces of 410 km and 660 km were plotted (Figure 7.2). The data comprise more than 5500 receiver functions that can be used for investigating the upper mantle discontinuities. As most events were recorded from northeastern directions, the area northeast of the western Bohemian Massif, between Berlin and Prague, is sampled best. Nevertheless, there is still a fairly good data coverage beneath the western Bohemian Massif and west of it. To the south, there is a data gap especially in the piercing points at 660 km depth.

The amplitudes of *Ps* conversions from the upper mantle discontinuities are about four times weaker than the Moho *Ps* conversion signal. Hence it is necessary to stack individual traces in order to enhance the signals from the ‘410’ and ‘660’. Therefore the area was divided into 43 non-overlapping boxes of $1^\circ \times 1^\circ$, which corresponds to approximately 70 km (E-W) \times 112 km (N-S) at the surface (Figure 7.2). The data were corrected for distance moveout and stacked according to the distribution of piercing points within the boxes at 410 km and 660 km depth, respectively. Data examples for two boxes are given in Figures 7.3 and 7.4 for the ‘410’ and ‘660’. Different filters were tested beforehand in order to enhance the signals of the ‘410’ and ‘660’. This led to the choice of a bandpass filter between 2-20 s.

Figure 7.5 shows the receiver function data sorted by piercing points at 410 km depth and stacked for each box that contains at least 25 traces. Table 7.1 gives the values of measured delay time and difference to the delay time predicted by the reference model *IASP91*. The measured delay times vary between 44.0 and 45.6 s between individual boxes (see Table 7.1). Especially the southernmost boxes (numbers 37 to 41) show significantly increased delay times of 44.8 to 45.6 s. However, the data coverage in the southern boxes is not as dense as in most of the other boxes, which makes the observation less stable. The sum trace of all individual traces shows the *Ps* conversion signal from the ‘410’ at 44.8 s, which is 0.7 s later than predicted by the *IASP91* reference model.

A similar image is given in Figure 7.6 for the traces with piercing points at 660 km depth, which means that the same data were sorted in a different manner than for the discontinuity at 410 km depth. Here the delay times of individual boxes vary between 67.6 and 71.0 s (see Table 7.1). Like for the ‘410’, the southernmost boxes (numbers 36 to 42) show the largest delay times of 69.6 to 71.0 s while the data coverage is clearly less than in most of the other boxes.

Furthermore, a signal at 54.4 s delay time, which may be attributed to the discontinuity at 520 km depth is visible in the sum trace of Figures 7.5 and 7.6 (sum traces are identical as the same set of individual traces is stacked). The signal can be followed through most of the individual boxes and appears to be rather coherent.

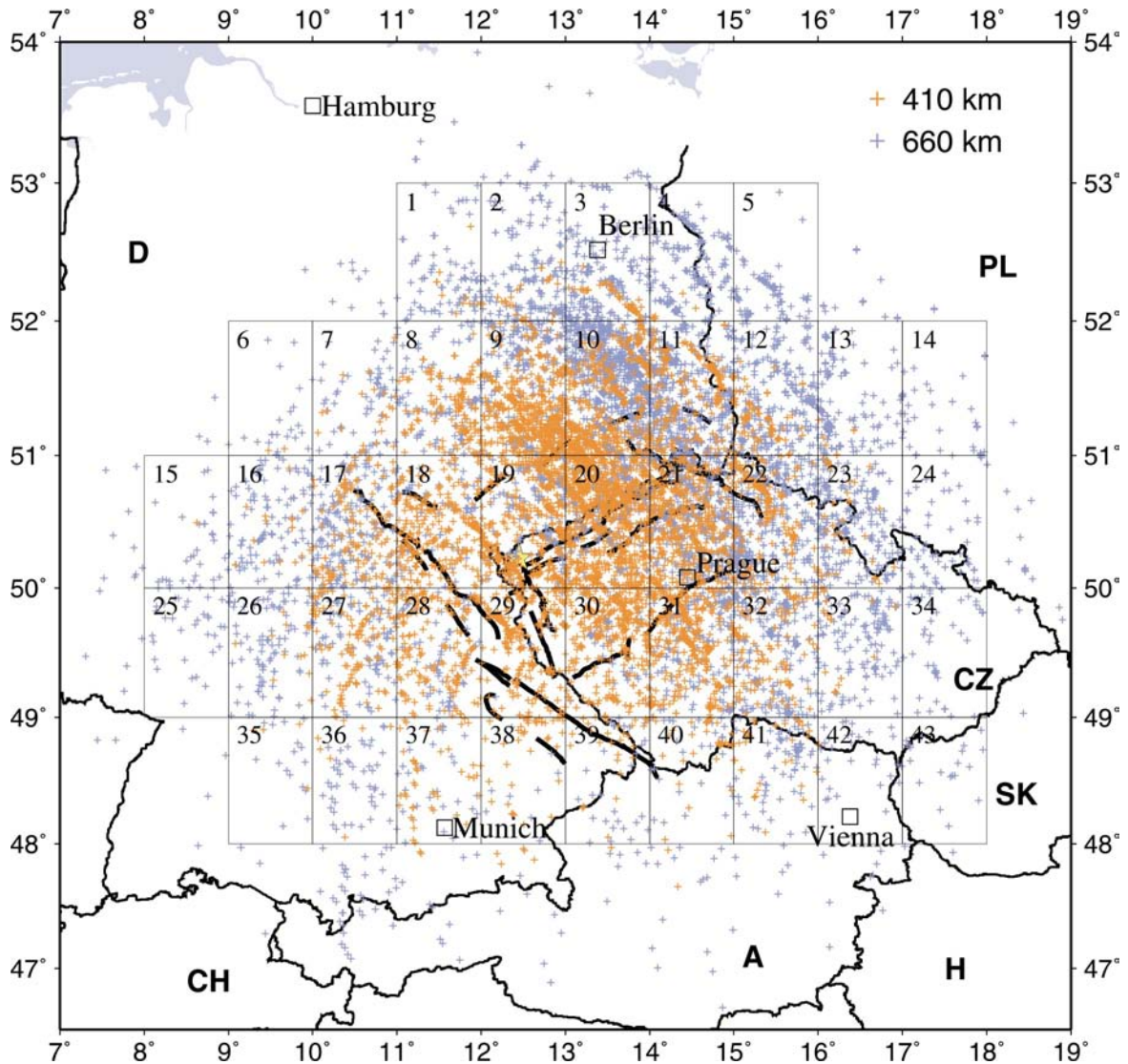
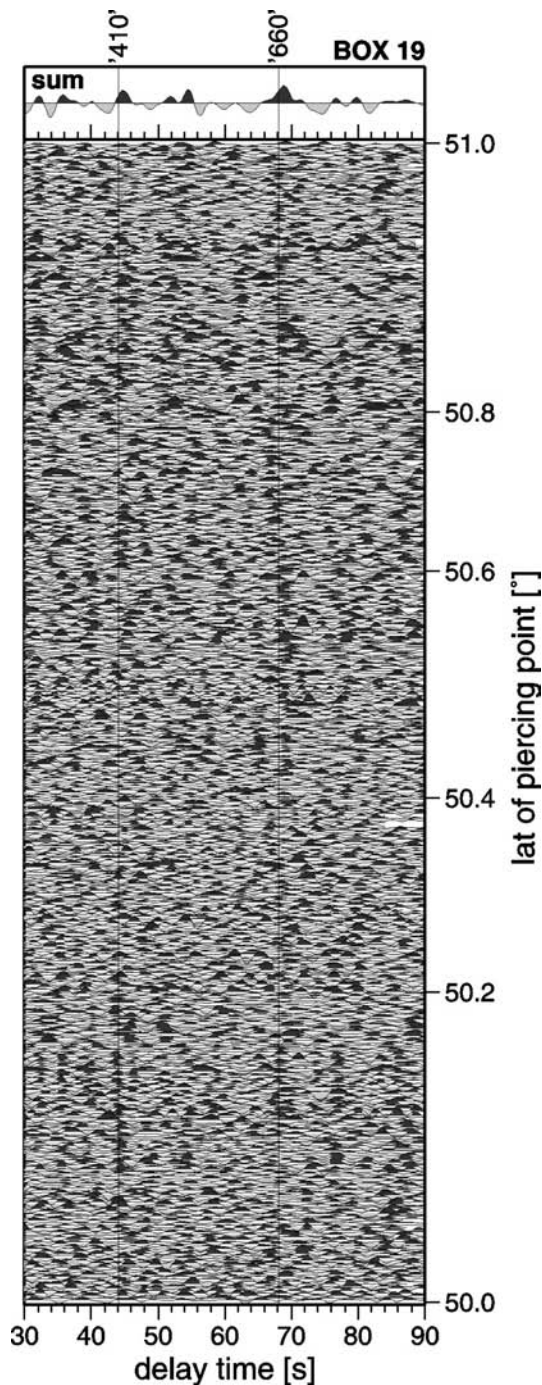


Figure 7.2: Piercing points of the *P*-to-*S* converted phases at interfaces at 410 km (orange) and 660 km depth (blue). The piercing points are located 80-170 km and 150-310 km away from the recording station for the 410- and 660-km discontinuity, respectively. For both depth values the same division of the area into boxes of $1^\circ \times 1^\circ$ was chosen. Hence, the boxes are sampled by different numbers and locations of piercing points at 410 and 660 km deep interfaces.

piercing points at 410 km depth



piercing points at 660 km depth

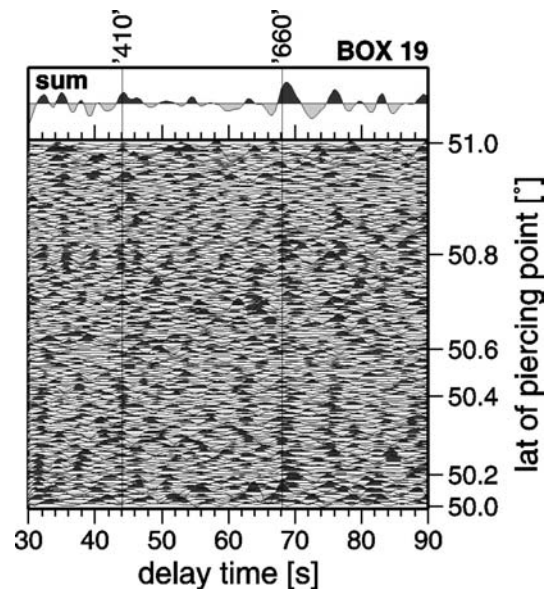
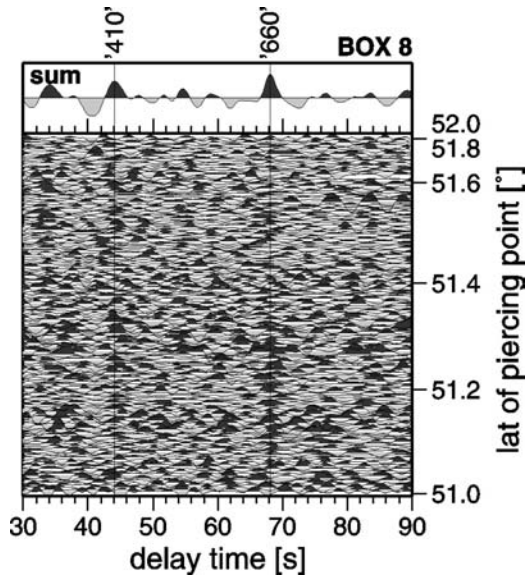


Figure 7.3: Data example (Box 19) in the time window between 30 to 90 s after the *P* onset. For different depth layers, the data gathered within the same box is different. **Left:** traces were sorted according to piercing points at 410 km depth. **Right:** traces were sorted according to piercing points at 660 km depth.

Single traces were filtered between 2-20 s, moveout-corrected and stacked. On top of the single traces, the sum trace is displayed. The *P_s* conversion signals from the 410- and 660-km discontinuities are rather weak in the single traces but clear in the sum trace.

piercing points at 410 km depth



piercing points at 660 km depth

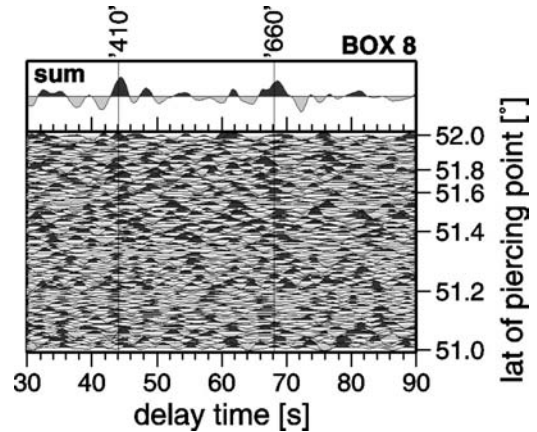


Figure 7.4: Data example (Box 08) in the time window between 30 to 90 s after the *P* onset. For different depth layers, the data gathered within the same box is different. **Left:** traces were sorted according to piercing points at 410 km depth. **Right:** traces were sorted according to piercing points at 660 km depth. The single traces were processed as described in Figure 7.3.

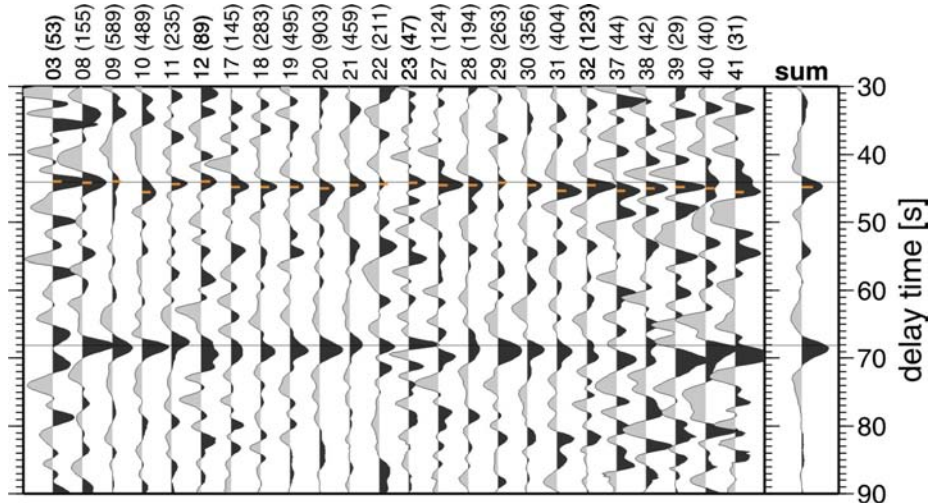


Figure 7.5: Stacked receiver functions of boxes containing at least 25 traces with piercing points at 410 km depth. The stacked traces are sorted by box number, the vertical ordinate shows the delay time with respect to the *P* onset. On top of each trace, the box number and, in brackets, the number of stacked traces are given. The single traces were moveout-corrected and filtered between 2-20 s before stacking. On the right of the Figure, the sum trace of all boxes is given. Lines at 44.1 s and 68.1 s mark the delay times of the 410- and 660-km discontinuities according to the *IASP91* reference model. Coherent positive arrivals near the delay times predicted by *IASP91* are clearly visible for both the '410' and '660'. The orange dash shows the delay time of the '410' that was picked for each box and for the sum trace. Most boxes display slightly longer delay times than predicted by *IASP91*. In the sum trace, the delay of the signal from the '410' is 44.8 s, i.e. 0.7 s later than predicted by *IASP91*. Furthermore, at 54.4 s delay time, a signal attributed to the 520-km discontinuity (not included in *IASP91* model) is visible in the sum trace and can be followed through most of the boxes.

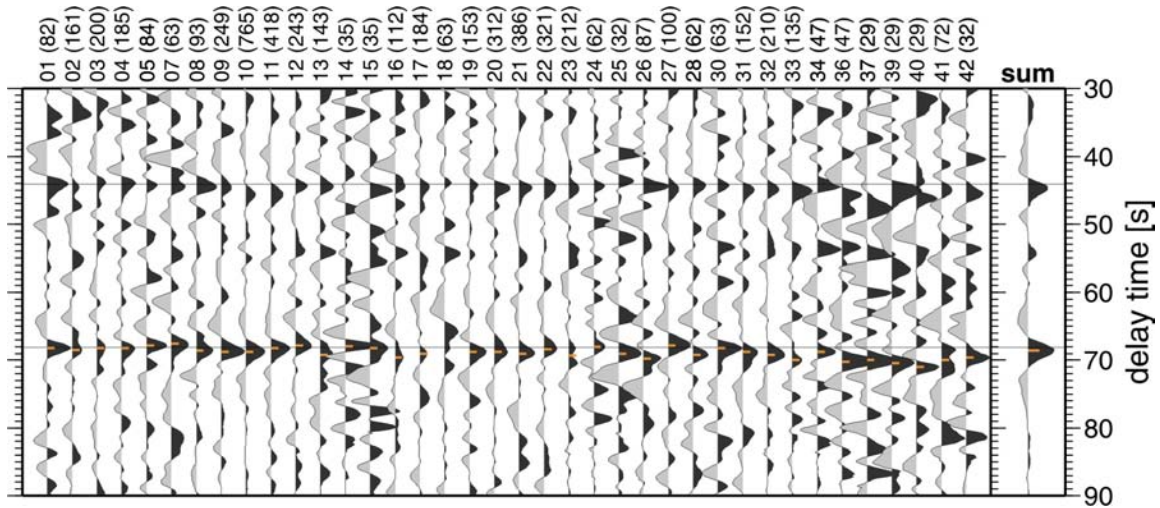


Figure 7.6: Same as Figure 7.4, but single traces were sorted by their piercing points at 660 km depth. The orange dash shows the delay time of the ‘660’ that was picked for each box and for the sum trace. As for the 410-km discontinuity, most boxes display slightly longer delay times than predicted by *IASP91*. In the sum trace, the delay of the signal from the ‘660’ is 68.6 s, i.e. 0.5 s later than predicted by *IASP91*. As in Figure 7.4, a signal from the discontinuity at 520 km depth is visible in the sum trace at 54.4 s delay time and in many boxes.

Table 7.1: Box number, number n of stacked traces for each box for the ‘410’ and ‘660’, delay times of the P_S conversions $t_{Ps,410}$ and $t_{Ps,660}$ and delay time difference for the conversions from the two discontinuities within each box.

Box №	n (‘410’)	n (‘660’)	$t_{Ps,410}$ [s]	$t_{Ps,660}$ [s]	$(t_{Ps,660}-t_{Ps,410})$ [s]
1	11	82	-	68.2	-
2	24	161	-	68.5	-
3	53	200	44.0	68.2	24.2
4	6	185	-	68.2	-
5	0	84	-	67.8	-
6	2	22	-	-	-
7	22	63	-	67.6	-
8	155	93	44.2	68.6	24.4
9	589	249	44.0	68.8	24.8
10	489	765	45.6	68.8	23.2
11	235	418	44.4	68.2	23.8
12	89	243	44.0	67.8	23.8
13	8	143	-	69.2	-
14	0	35	-	67.9	-
15	1	35	-	68.2	-
16	17	112	-	69.6	-
17	145	184	44.8	69.0	24.2
18	283	63	44.8	?	-
19	495	153	44.8	68.8	24.0
20	903	312	45.0	68.8	23.8
21	459	386	44.6	69.0	24.4
22	211	321	44.4	68.4	24.0
23	47	212	44.2	69.3	25.1

continued on next page

Box №	n ('410')	n ('660')	$t_{Ps,410}$ [s]	$t_{Ps,660}$ [s]	$(t_{Ps,660}-t_{Ps,410})$ [s]
24	0	62	-	68.0	-
25	0	32	-	69.0	-
26	17	87	-	69.8	-
27	124	100	44.6	67.8	23.2
28	194	62	44.6	69.2	24.6
29	263	7	44.2	-	-
30	356	63	44.6	68.2	23.6
31	404	152	45.4	68.8	23.4
32	123	210	44.6	69.2	24.6
33	17	135	-	70.0	-
34	0	47	-	68.8	-
35	4	16	-	-	-
36	7	47	-	70.2	-
37	44	29	45.4	70.0	24.6
38	42	9	45.0	-	-
39	29	29	44.8	70.4	25.6
40	40	29	45.0	71.0	26.0
41	31	72	45.6	70.0	24.4
42	1	32	-	69.6	-
43	0	20	-	-	-

7.3 Discussion

The obtained delay times for the signals from the '410' and '660' were compared with the delay times predicted by the reference model *IASP91*, which are approximately 44.1 s and 68.1 s, respectively. The differences between measured delay time and predicted delay time are plotted in Figures 7.7 and 7.8 for the '410' and '660', respectively.

The distribution of delay time differences for the **410-km discontinuity** generally displays a slight increase in delay times from north to south. The largest values are obtained below the northern Austrian Alps and Alpine foreland (+0.7 to +1.5 s within boxes 37-41). However, the data coverage of these southernmost boxes (boxes 37-41) is not very dense, making the results less reliable. In the north and northeast of the covered area (boxes 3-12 and 23), there is no difference in delay time to the *IASP91* reference model. However, box 10 (+1.5 s) is an exception with a striking contrast to box 9 (-0.1 s). As in both boxes data is densely spaced, the measured values are considered to be reliable. One possibility to explain such strong differences could be the distribution of piercing points within the box. However, the piercing points of the 410-km discontinuity in box 9 cluster in the southeast of the box and those of box 10 in the southwest (Figure 7.7), making it implausible that the piercing points should sample two completely separate regions. As the signals of *Ps* conversions from the upper mantle discontinuities are very weak themselves, the most probable explanation is that some particularly noisy traces or a scatterer strongly influence the sum trace although so many traces were stacked.

The uncertainty introduced by picking of the delay time of the signal is ± 0.1 s, the uncertainty introduced by bandpass filtering is ± 0.1 s (derived by filtering tests). Obviously the uncertainty introduced by noise depends on the number of stacked traces but can still not easily be estimated as the above discussion about boxes 9 and 10 shows. If an

uncertainty of ± 0.2 s for boxes with at least 25 traces is assumed, the overall uncertainty amounts to ± 0.4 s for a delay time value of mantle discontinuities within an individual box.

The sum trace in Figure 7.5 shows a delay of $+0.7$ s compared to the *IASP91* reference model. As the sum trace is stacked of more than 5500 individual traces, the uncertainty introduced by random noise should be negligible, so that delay time values of the mantle discontinuities in the sum trace is ± 0.2 s.

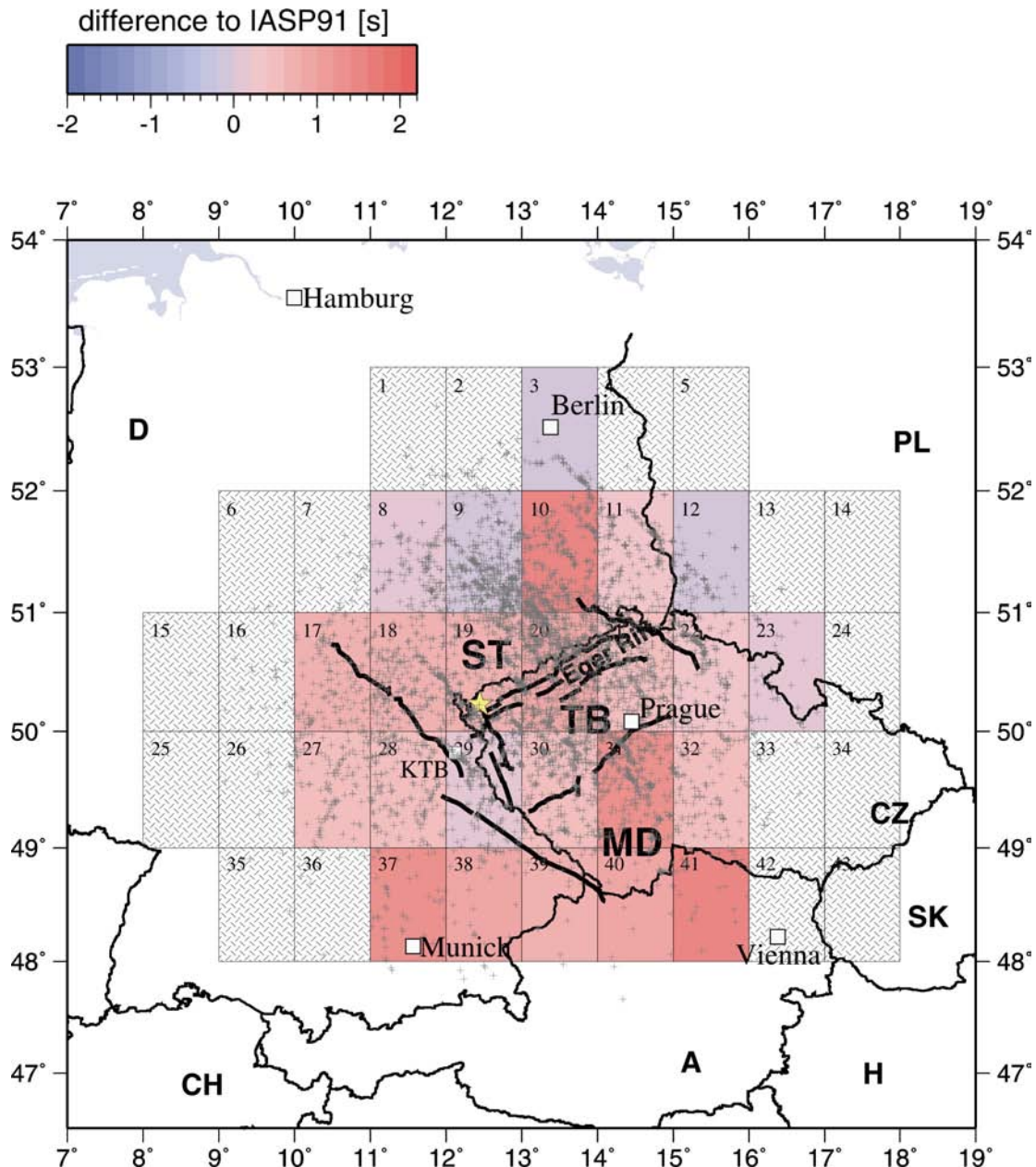


Figure 7.7: Difference between measured and theoretical delay time for the 410-km discontinuity. Red colours show longer and blue colours shorter delay times than predicted by the *IASP91* reference model, which could correspond to hot and cool temperatures near the discontinuity, respectively. Values vary between -0.1 s (boxes 3, 9, 12) and $+1.5$ s (boxes 10, 41), the average is $+0.7$ s.

The **discontinuity at 660 km depth** does also show a deepening trend towards south (Figure 7.8). This effect is strongly reinforced by the values measured in the southernmost boxes 36-42 (+1.5 s to +2.9 s in relation to *IASP91*), which represent the area beneath the northern Alps and Alpine foreland. These boxes are not very well covered by data. However, as they show a coherent behaviour, the trend is assumed to be real. The delay time increase in these boxes is even stronger than the increase obtained for the same boxes for the 410-km discontinuity (see above).

In the majority of the boxes in the northern and central part of the area, the delay time of the *Ps* conversion from the ‘660’ corresponds well with the value predicted by the *IASP91* model or is only slightly higher.

Again, there are some striking contrasts between neighbouring boxes. Mostly they occur at the margins, where the data coverage is less dense. Therefore it is suggested that these strong contrasts are caused by noise in the individual traces that could not be eliminated by stacking. The estimated uncertainty of the measured delay time values of the *Ps* conversion from the ‘660’ is again ± 0.4 s for the sum traces of individual boxes.

The sum trace in Figure 7.6 shows a delay of $+0.5 \pm 0.2$ s of the *Ps* conversion from the ‘660’ compared to the *IASP91* reference model.

Geissler et al. (2005) found delays of the *Ps* conversion signals from the ‘410’ and ‘660’ in the investigation area of up to 2 s compared to *IASP91*. This is somewhat higher than the values found for most boxes in this thesis. Only in the southernmost boxes for the ‘660’, larger values are found in the present study. However, *Geissler et al.* (2005) used less data and stacked the data stationwise and not according to boxes as in the present study. As most of the data used by *Geissler et al.* (2005) are included in the investigation of the mantle transition zone in this thesis, the values obtained here should be more reliable.

A receiver function investigation by *Grunewald et al.* (2001) showed no deviations of the depth of the ‘410’ and ‘660’ in the area investigated in this thesis and therefore supports the results found here. However, in the northern Austrian Alps and south Germany, where in this thesis longer delay times of the *Ps* conversions from the ‘410’ and ‘660’ are observed, *Grunewald et al.* (2001) also did not find any anomalies. Their study focused deeper on the Eifel volcanic region in the Rhenish massif of western Germany. This region is geologically comparable to the western Bohemian Massif as both are of Variscan origin and it is also overprinted by the European Cenozoic Rift system with its Tertiary and Quaternary volcanism and recent CO₂ emanations. The proposed plume beneath the Eifel volcanic region (*Ritter*, 2001) is further supported by *Grunewald et al.*’s findings of a 150 km wide and 20 km deep depression of the 410-km discontinuity in the upper mantle beneath the Eifel region. This is indicative of a zone of increased (by about 200 K) temperature and/or reduced seismic velocities in the mantle above 400 km depth. As such a feature cannot be found in this thesis, there is no hint to a comparable temperature or velocity anomaly beneath the western Bohemian Massif.

No indication for an anomaly of the ‘660’ was found under the Eifel, which argues against a thermal anomaly at the bottom of the mantle transition zone (*Grunewald et al.*, 2001). The same is the case for the ‘660’ beneath the western Bohemian Massif investigated in this thesis.

It is necessary to point out that structures significantly smaller than 150 km laterally can not be resolved by the receiver function method. The 1 s isochrones at 410 km depth have a diameter of comparable size (200 km).

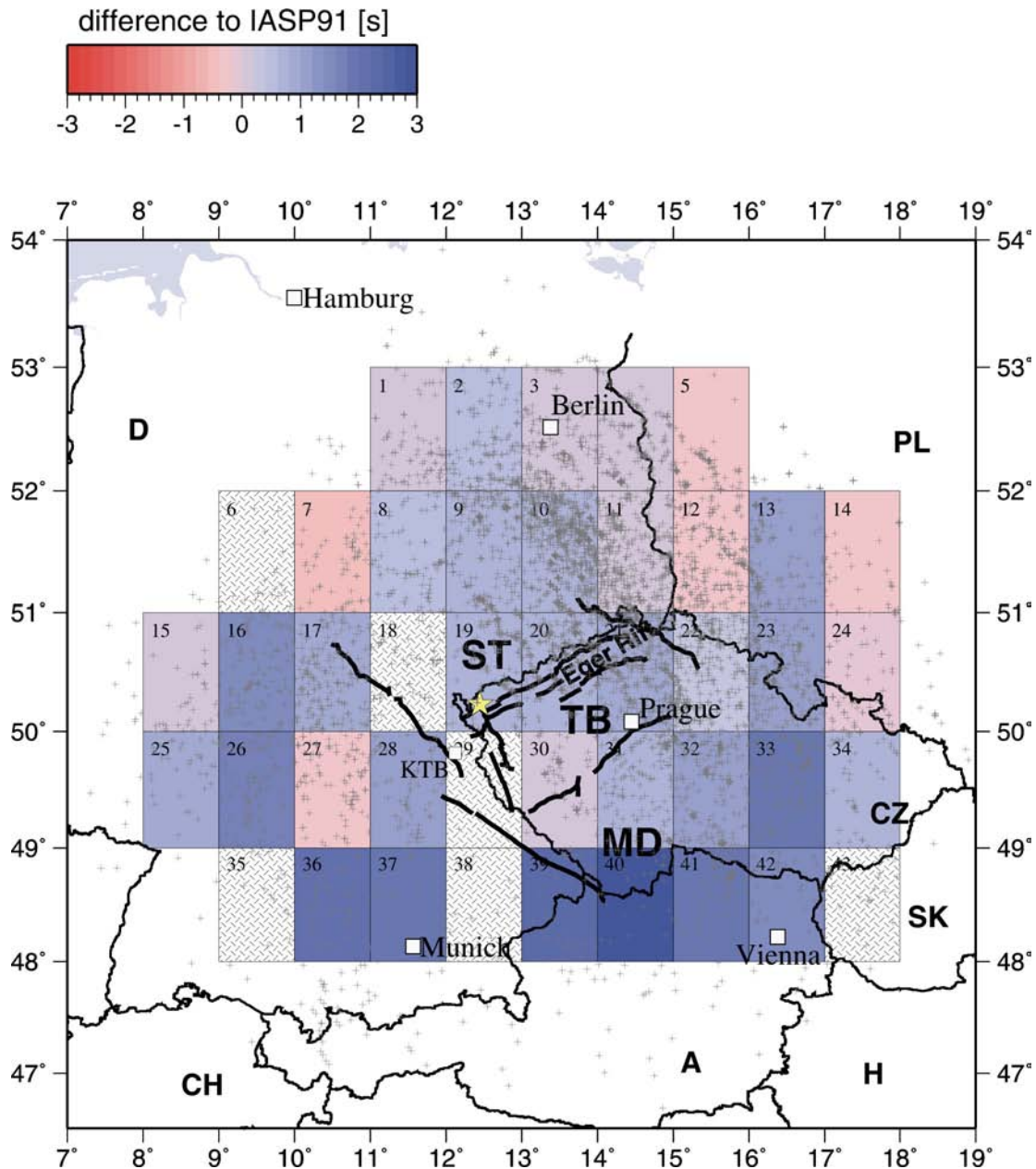


Figure 7.8: Difference between measured and theoretical delay time for the 660-km discontinuity. The colour scale is opposite to the scale in Figure 7.7 as the 660-km discontinuity has a negative *Clapeyron* slope dP/dT . Blue colours show longer and red colours shorter delay times than predicted by the *IASP91* reference model, which could correspond to cool or hot temperatures near the discontinuity, respectively. Values vary between -0.5 s (box 7) and +2.9 s (box 40), the average is +0.5 s.

An important value for discussion of temperature variations within and above the mantle transition zone is the delay time difference between the two discontinuities (*Li et al.*, 2003b), which is a good estimate of the **thickness of the mantle transition zone**. As the ‘410’ and ‘660’ have opposing *Clapeyron* slopes, a temperature increase across the mantle transition zone would reduce the distance between the two discontinuities, while a temperature decrease would increase the distance between them. If a temperature anomaly occurs in the uppermost mantle above the mantle transition zone, the delay times of both

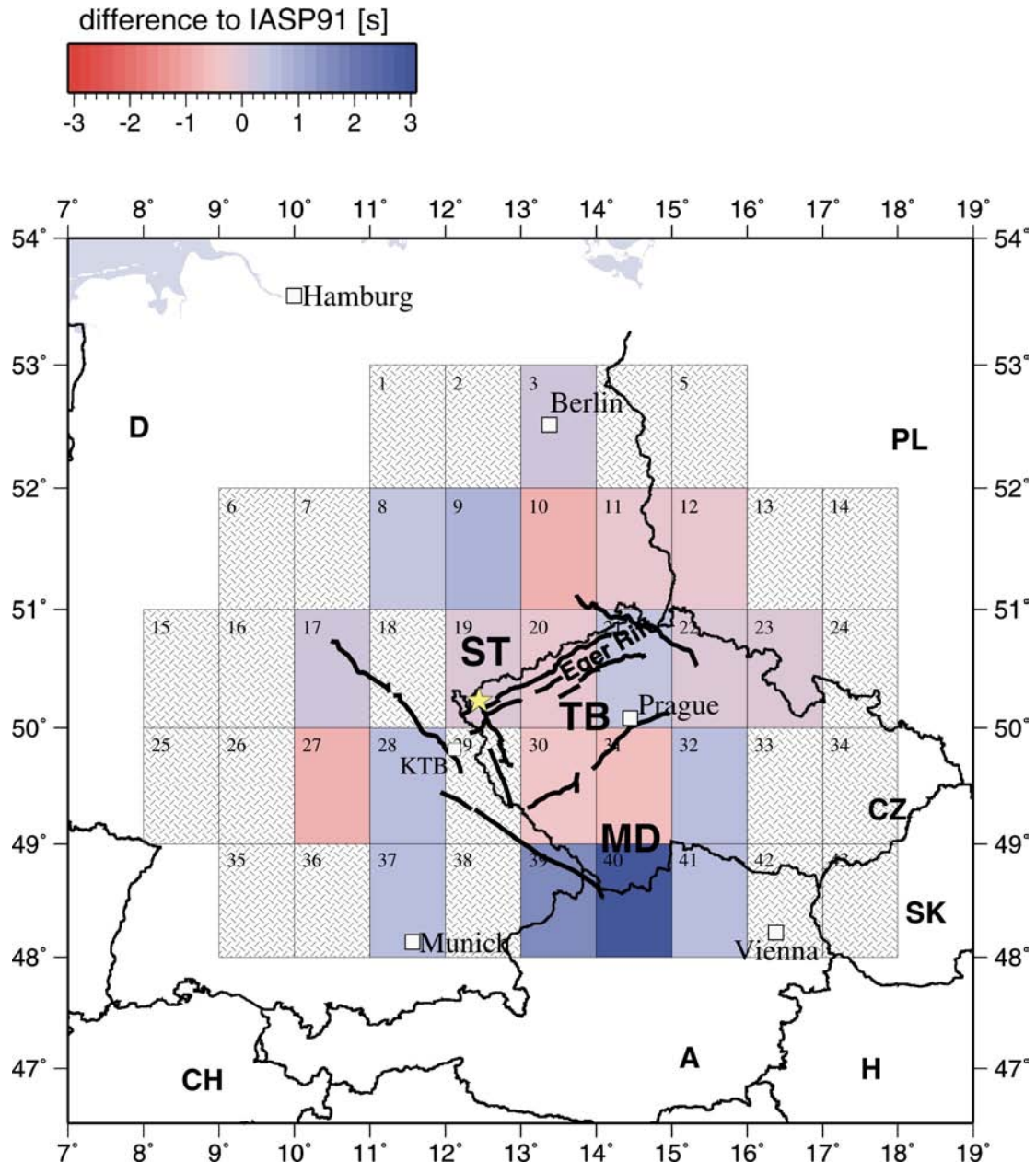


Figure 7.9: The difference of the delay times between the P_s conversions from the ‘660’ and the ‘410’ is predicted to be 24.0 s by the *IASP91* reference model. This value was subtracted from the measured delay time difference of the two discontinuities and plotted into this map. Blue colours indicate a thicker, red colours a thinner mantle transition zone than predicted by *IASP91*. The values within the boxes vary between -0.8 s (boxes 10, 27) to +2.0 s (box 40). Coverage with piercing points is not shown because it is different for the two discontinuities within one box.

discontinuities would be affected in the same direction while the time difference between them remains constant.

The difference between the measured delay time difference and the theoretical one predicted by *IASP91* (24.0 s) is shown in Figure 7.9. The values vary between -0.8 s (boxes 10, 27) to +2.0 s (box 40). These extreme values appear in boxes that already showed extreme behaviour for either the '410' or the '660' as described above. The other boxes show mostly smaller values and no trend or coherent structure can be postulated.

Therefore it is concluded that the generally very small positive and negative differences to the *IASP91* reference model measured in the investigated area are mainly due to noise. Hence the overall thickness of the mantle transition zone in the investigation area corresponds to the thickness given by the *IASP91* reference model (250 km). Only in the southernmost area beneath the northern Alps and Alpine foreland, there is a trend of thickening of the mantle transition zone. It is caused by an increase of delay times of both *Ps* conversions from the 410- and 660-km discontinuities with a relatively stronger increase for the '660'.

For the northern and central part of the area covered by data, the good agreement between measured and predicted delay times differences of the 410- and 660-km discontinuities points to normal temperatures of the mantle transition zone in this area. As both phases are slightly delayed compared to the *IASP91* reference model (+0.7±0.2 s and +0.5±0.2 s for the '410' and the '660', respectively), this points to decreased *S* wave velocities in the upper mantle above the mantle transition zone. The *IASP91* reference model contains no low velocity zone representing the asthenosphere. The existence of an asthenosphere with an increased v_p/v_s ratio beneath the investigated area could explain at least some part of the increased delay times of the '410' and '660' with respect to the reference model.

If the manifold processes that point to magmatic activity beneath the western Bohemian Massif should have their origin in a diapiric mantle upwelling as predicted by *Granet et al.* (1995), the absence of a distinct topography of the upper mantle discontinuities leads to the conclusion that this predicted mantle finger does not show an imprint on the upper mantle discontinuities. If it exists, it either needs to have its origin well above the mantle transition zone, or its diameter is significantly smaller than 150 km at the depth of the mantle transition zone and thus too narrow to be resolved by teleseismic receiver functions.

At 54.4 s delay time after the *P* onset, a weak positive phase is visible in the sum trace as well as in the individual boxes of the *P* receiver functions (Figures 7.5, 7.6), that can be attributed to the **520-km discontinuity**. As calculations of synthetic receiver functions by *Geissler* (2004) from earth models without a velocity discontinuity at 520 km depth do not show any artefacts that could be mistaken for a discontinuity, it seems very probable that the observation of a '520' in the investigated area is reliable. However, the phase was not analysed in more detail. Therefore, scattered phases or effects of deconvolution that might have led to an artificial occurrence of this phase can not be completely ruled out.

Several studies show a low velocity zone on top of the 410-km discontinuity (e.g. *Song et al.*, 2004; *Gilbert et al.*, 2003; *Vinnik et al.*, 2003; *Revenaugh and Sipkin*, 1994; *Nolet and Zielhuis*, 1994). *Bercovici and Karato* (2003) present a model of the Earth's mantle which predicts the presence of a layer of melt or partial melt above the 410-km discontinuity of the order of less than 10 km. However, the data used in the present study

does not show a coherent phase atop the 410-km discontinuity. Only very few non-coherent boxes (e.g. boxes 08, 17, 37-39) show a strong negative phase in front of the *P*-to-*S* conversion from the '410'. This indicates that the low velocity layer predicted by *Bercovici and Karato* (2003) is probably not a global feature. This is in agreement with *Huang et al.* (2005), who infer that the water content in the mantle transition zone varies regionally and that therefore the low velocity zone on top of the '410' should be a regional feature, too.

Chapter 8

Summary and Conclusions

During the passive seismic experiment BOHEMA (2002/2003) in the western Bohemian Massif, a large data set was obtained, which was analysed with the P and S receiver function methods. The aim was to obtain images of the discontinuities in the Earth's lithosphere (Moho, lithosphere-asthenosphere boundary) and upper mantle ('410' and '660') beneath the western Bohemian Massif. The investigated region is characterized by the occurrence of earthquake swarms, emanation of upper-mantle derived CO_2 in mineral springs and mofettes, Tertiary and Quaternary volcanism, and neotectonic crustal movements. To explain these phenomena, the existence of active magmatic reservoirs near the crust-mantle boundary has been suggested in the past. In the geologically comparable regions of the Eifel and French Massif Central, tomography studies imaged plume-like structures which were suggested to also exist beneath the Bohemian Massif.

Figure 8.1 gives an overview about the P -to- S converted phases observed at stations of the BOHEMA experiment. Phases that can be clearly identified are conversions from the Moho, multiple reverberations within the crust, and the converted phases from the discontinuities of the mantle transition zone at 410 and 660 km depth. Furthermore there are indications for a conversion from the still-debated discontinuity at 520 km depth.

For investigation of the lithosphere-asthenosphere transition, S -to- P converted phases were also analysed. The data set was complemented by data from an earlier seismic experiment by *Geissler et al.* (2005).

The results obtained for the various discontinuities are summarized in this chapter 'from top to bottom'. Finally, a model is shown that incorporates the results and may help during the ongoing discussion about the existence of a "baby plume" and/or asthenospheric updoming beneath the investigation area.

8.1 Moho depths and crustal v_p/v_s ratios beneath the western Bohemian Massif

By analysis of more than 5000 P receiver functions recorded at 110 broad band and short period seismic stations of the BOHEMA experiment, crustal thickness beneath each station could be calculated. This results in the highest resolution Moho map of this large area until now. The map of Moho depths is displayed in Figures 5.8 and 5.9. It shows crustal thicknesses of 27 to 31 km in the Saxothuringian unit, 30 to 33 km in the Teplá-Barrandian and 34 to 39 km in the Moldanubian unit east of the Bavarian Shear Zone. A dominant

feature in the Moho depth map is an area of thin crust of about 26 to 28 km beneath the western Eger Rift. The internal geometry of this updoming seems to be irregular: crustal thickness gradually increases towards the ENE to „normal“ values of about 31 km, whereas towards the WSW there seems to be an abrupt depth increase from 26 to 31 km. This apparent Moho updoming was already observed with less resolution by *Geissler et al.* (2005). It corresponds well with the area of CO₂ degassing fields at surface. The main swarm earthquake area of Nový Kostel is situated at the northeastern margin of the Moho updoming area. The Moho depth increases towards the SE and reaches values of almost 40 km between the Central Bohemian and the Bavarian Shear Zones. This result is in good agreement with former seismic studies and compilations (e.g. *Hrubcová et al.*, 2005; *Wilde-Piórko et al.*, 2005; *Dèzes and Ziegler*, 2001). The Moho depth values have an estimated uncertainty of ± 2 km.

Furthermore, a map of average crustal v_p/v_s ratios is presented for the investigation area (Figure 5.7). Before, v_p/v_s ratios were only provided for selected locations (e.g. *Geissler et al.*, 2005). The v_p/v_s ratios were obtained with the grid search method by *Zhu and Kanamori* (2000) for 34 stations of the BOHEMA experiment with clear Moho P_s conversions and crustal multiples (Table 5.1, Figures 5.4 and 5.6). The values vary between 1.66 and 1.81, with an average value of 1.73. For the remaining stations, the investigation area was divided into subareas associated with the Variscan tectonometamorphic units of the Bohemian Massif. For these subareas, mean values of v_p/v_s ratios and their standard deviations were calculated of the single values obtained with the method by *Zhu and Kanamori* (2000). The resulting map (Figure 5.7) displays a relatively high mean v_p/v_s ratio of 1.75 ± 0.02 for the Saxothuringian part of the Bohemian Massif. To the southeast, the northern part of the Teplá-Barrandian forms an area of mean v_p/v_s ratio of 1.71 ± 0.03 . The transition of the Central Bohemian Shear Zone has a higher value again of 1.75 ± 0.03 . This corresponds to results by *Hrubcová et al.* (2005) who report a v_p/v_s ratio of 1.76 in the upper crust in the vicinity of the Central Bohemian Shear Zone. Station PRU near Prague stands alone with a rather low value of 1.66 ± 0.06 . In the Moldanubian unit southeast of the Central Bohemian Shear Zone, an area of low v_p/v_s ratio of 1.69 ± 0.05 was obtained. In the Moldanubian region west of the Teplá-Barrandian unit, the mean v_p/v_s ratio is 1.72 ± 0.02 . Finally, the region southwest of the Bohemian Massif which is covered by Mesozoic sediments, displays a mean v_p/v_s ratio of 1.72 ± 0.04 .

High values of v_p/v_s beneath the western Erzgebirge mountains reported by *Geissler et al.* (2005) could partly be confirmed (stations WERN, BG25), as well as low values at the Czech-German border east of KTB (station B17).

One possibility to explain low v_p/v_s ratios at station PRU near Prague (1.66 ± 0.06) and in the Moldanubian region between Central Bohemian and Bavarian Shear Zone (1.69 ± 0.05) might be the existence of quartz rich rocks beneath the stations (*Christensen*, 1996).

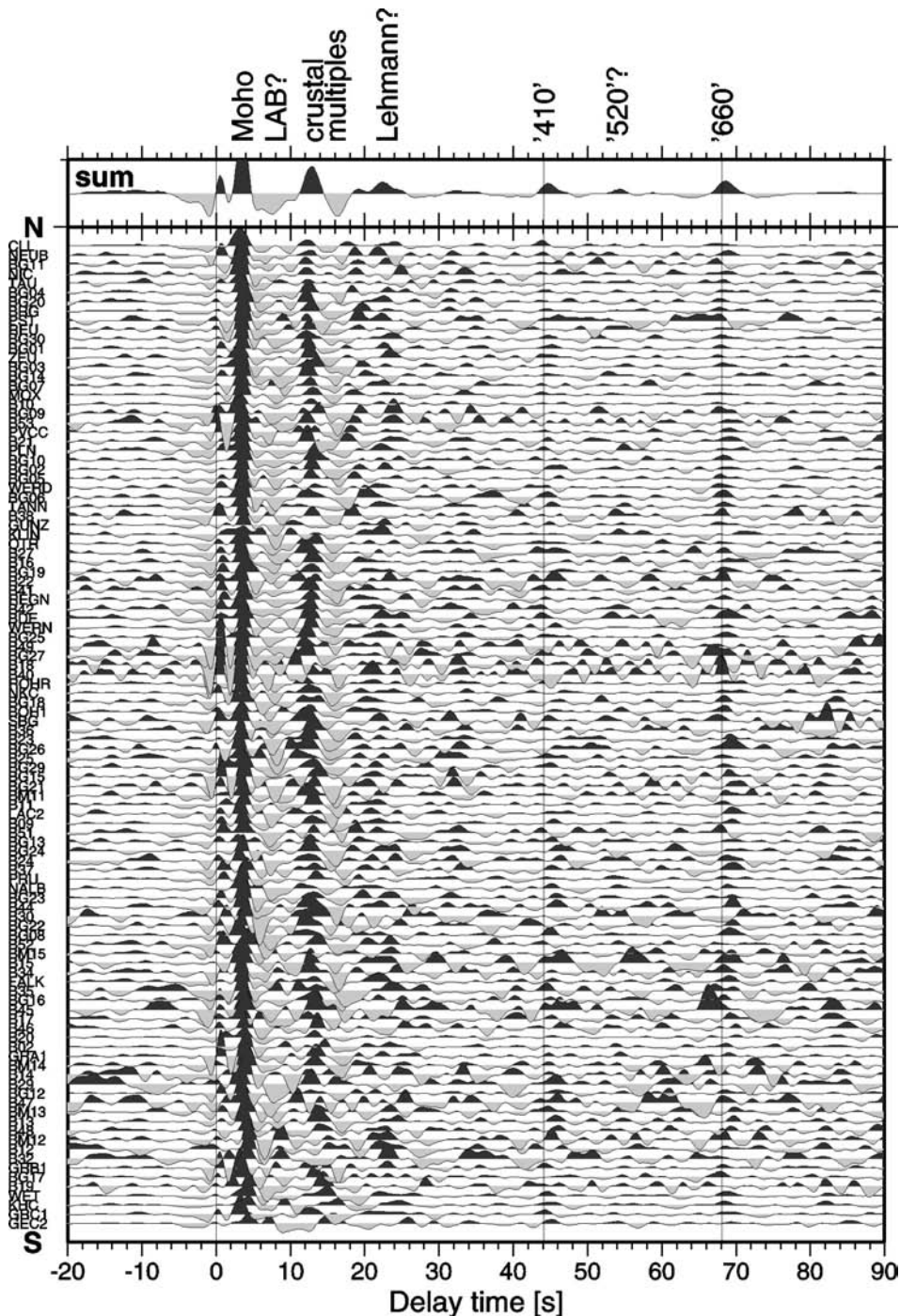


Figure 8.1: Sum traces of all stations of the BOHEMA experiment that were used for P receiver function analysis. The horizontal axis gives the differential time between the P -to- S converted phases and the P onset (zero time). Before stacking, the individual traces were filtered between 2 and 20 s and corrected for distance moveout. Stations are sorted from south (bottom) to north (top). On top of the figure, the sum trace of all individual traces is shown together with an interpretation of the observed converted phases. The phases that can be clearly identified are conversions from the Moho, multiple reverberations within the crust, and the converted phases from the '410' and '660'. Furthermore there are indications for a conversion from the still-debated discontinuity at 520 km depth. The negative signal at approximately 8 s delay time in the sum trace and the positive signal at approximately 23 s might perhaps be associated with the lithosphere-asthenosphere boundary and the Lehmann discontinuity, respectively. However, further tests are necessary to allow these interpretations.

8.2 Structure and thickness of the lithospheric mantle

In the area of Moho updoming and mantle-derived CO₂ emanations another interesting feature was observed in the *P* receiver functions: a positive phase at about 6 s delay time with respect to the *P* onset, followed by a strong negative phase at about 7 to 8 s. A mapping of the occurrence of these additional phases showed that they form a coherent structure centred on the western Eger Rift (Figure 6.1). While the positive phase near 6 s was already observed by *Geissler et al.* (2005), the negative phase at 7.5 s was not - probably due to too sparse data. However, in this thesis the negative phase turns out to be larger in amplitude than the positive phase near 6 s and to cover a larger area of 5300 km², which includes the occurrence of the positive “6 s phase” (*Geissler et al.*, 2005) as a subarea in the central and eastern part of the pink shaded area in Figure 6.1. A test of the distance moveout behaviour of the two additional phases indicates that they are direct conversions rather than multiple reverberations, meaning that they image a structure in the uppermost mantle rather than within the crust. However, as moveout effects at such shallow depths are not very strong, the indications are only weak and thus not very reliable.

The phases at 6 s and 7.5 s can be modelled by a velocity increase at 50 km suggested by results of seismic reflection and refraction investigations (*Hrubcová et al.*, 2005; *Tomek et al.*, 1997) and by a velocity decrease at 65 km depth. The velocity decrease might be explained by local asthenospheric updoming and/or a confined body of partial melt, which might be the cause for high CO₂ mantle fluid flow and earthquake swarm activity in this presently nonvolcanic, intracontinental rift area.

An updoming of the lithosphere-asthenosphere boundary had already been proposed earlier by *Babuška and Plomerová* (2001). However, their suggested lithospheric thickness of 80 to 90 km beneath the contact of Saxothuringian and Moldanubian unit would be considerably deeper than the 65 km suggested by the *P* receiver function data shown here. Asthenospheric upwelling beneath the western Eger Rift is also indicated by e.g. *Faber et al.* (1986), *Plomerová and Babuška* (1988), *Passier and Snieder* (1996), and *Plomerová et al.* (1998).

To test the idea of lithospheric thinning and to map the lithosphere-asthenosphere boundary in the west Bohemia region, an analysis of *S*-to-*P* converted phases (*S* receiver function method) was carried out in this thesis. The data show a very clear Moho signal approximately 3 to 4 s delay time after the *S* onset, corresponding very well to the delay time obtained by *P* receiver function analysis. After the Moho *Sp* conversion, a coherent negative phase arrives at 8 to 10 s and for the southern Moldanubian part at 12 to 14 s. The possibility of the negative signal being merely a side lobe of the Moho signal and thus an artefact produced by the deconvolution is ruled out by a test that compares the side lobes of the deconvolved *P* and *SV* signals. Therefore it is concluded that the negative signals observed in the *S* receiver functions at 8 to 14 s are most probably the *S*-to-*P* converted phases generated at a negative velocity gradient, which might be interpreted as the lithosphere-asthenosphere transition (LAB). However, from previous research this transition is not very well constrained yet regarding its nature, depth location and width of gradient zone (see Chapter 6).

An approximation of the depth origin of the negative phase was achieved by multiplying the picked delay time by a factor of 9 based on the *IASP91* standard earth model (Kennett, 1991; Kennett and Engdahl, 1991). The results are displayed in Figure 6.12. If the negative gradient is interpreted as the lithosphere-asthenosphere transition, the map in Figure 6.12 shows lithospheric thickness of 80 to 90 km beneath the Saxothuringian and partly the Teplá-Barrandian unit. Towards the south, the thickness strongly increases in the Moldanubian part of the investigation area to 115 to 135 km. For the Saxothuringian unit in the north, Babuška and Plomerová (2001) obtained a slightly thicker lithosphere of 90 to 120 km, while their thickness of 120 to 140 km in the Moldanubian unit (Figure 2.5) agrees very well with the values obtained in this thesis. The transition from the Saxothuringian/Teplá-Barrandian LAB in the north to the Moldanubian LAB in the south does not show a single clear negative peak but seems to represent a transition from the thinner to the thicker lithosphere with partly doubling of the negative signals. Babuška and Plomerová (2001) interpret the patterns of *P* wave residuals and shear wave splitting parameters in the transition from the Saxothuringian to the Moldanubian as possible underthrusting of a part of the Saxothuringian subcrustal lithosphere beneath the Moldanubian or a hypothetical remnant of the Early Palaeozoic oceanic lithosphere subducted to the south during collision of the Saxothuringian and Moldanubian units.

However, a clear asthenospheric updoming beneath the contact of the Saxothuringian and Moldanubian units centred beneath the western Eger Rift as suggested in *P* receiver function data, cannot be stated from *S* receiver functions.

Two scenarios can be imagined to explain the occurrence of the negative phase in the *P* and *S* receiver functions at different depths (Figure 8.2):

- 1) The negative phases in the *P* and *S* receiver functions represent two distinct discontinuities. A thin low velocity layer is detected by the *P* receiver functions in the lithospheric mantle at approximately 65 km depth. As its thickness is between 2 and 6 km, it can not be detected by the *S* receiver function method. This low velocity layer could for example be caused by patches of partial melt. As the negative phase in the *P* receiver functions is observed in the area of CO₂ degassing and occurrence of earthquake swarms, a causal connection between the low velocity area at 65 km depth and these phenomena might be assumed. The negative gradient observed in *S* receiver function data at approximately 9 to 10 s is more or less coherent throughout the whole profile and might thus be interpreted as the lithosphere-asthenosphere transition. However, the thinning of the lithosphere proposed by Babuška and Plomerová (2001) would then not be obvious in the *S* receiver function data, furthermore the diapiric mantle upwelling suggested by Granet *et al.* (1995) for the Bohemian Massif would show no imprint on the lithosphere-asthenosphere transition.
- 2) The negative phases in the *P* and *S* receiver functions represent in principle the same negative velocity gradient, but strongly influenced by the different frequency contents of the *P* and *S* waves and by the possible nature of the transition from high to low velocities with increasing depth. For example, if the gradient is steep at about 70 km depth and becomes increasingly less steep at 80 to 90 km depth, then *P* receiver functions would image the steep part while *S* receiver functions would

image also the flatter part of the gradient. However, as the negative phase in the P receiver functions is only observed in the broader surroundings of CO_2 degassing at surface and earthquake swarm occurrence, the proposed steep gradient zone would also occur only in this area. Again, this implies a thin region of strongly decreased seismic velocity at about 65 km depth which might be associated with the occurrence of partial melts at this depth range.

8.3 Upper mantle discontinuities at 410 and 660 km depth

The sum trace of all individual P receiver functions used in this study shows a slightly increased delay time for the Ps conversions from both the ‘410’ and ‘660’ compared to the *IASP91* global reference model (Kennett, 1991; Kennett and Engdahl, 1991) (see Figures 7.5 and 7.6). The ‘410’ shows a delay time increased by $+0.7 \pm 0.2$ s, while the delay time of the ‘660’ is increased by $+0.5 \pm 0.2$ s.

Looking in more detail at the two discontinuities, both show a slightly deepening trend towards the south (Figures 7.7 and 7.8). In the north and northeast of the investigated area, the values do not significantly differ from the values predicted by the *IASP91* reference model. The largest delay times are measured in the southernmost part of the sampled area, i.e. beneath the Austrian Alps with values increased by $+0.7$ to $+1.5$ s for the ‘410’ and $+1.5$ s to $+2.9$ s for the ‘660’ in relation to *IASP91*. However, data coverage is not very dense in this area so that the values are not reliable.

A low velocity layer atop the 410-km discontinuity as suggested by some previous studies was not observed in this thesis. Only very few non-coherent patches of the investigated area show such a velocity reduction.

The difference between the delay times of the ‘410’ and ‘660’ do not significantly differ from the value predicted by the *IASP91* global reference model. That means that the thickness of the mantle transition zone is neither increased nor decreased and thus points to normal temperatures in this depth area. This is supported by observations of Grunewald *et al.* (2001) who also found no deviations of the depths of the ‘410’ and ‘660’ in the area investigated in this thesis. The diapiric mantle upwelling beneath the western Bohemian Massif predicted by Granet *et al.* (1995) would thus have no impact on the topography of the 410- and 660-km discontinuity. If such a mantle finger exists, it is either too narrow to be detected by teleseismic receiver functions (diameter significantly smaller than 150 km at the depth of the mantle transition zone), or it should have its origin above the mantle transition zone.

Most probably, the slightly increased delay times of the signals from the ‘410’ and ‘660’ are caused by an increased v_p/v_s ratio in the upper mantle above the mantle transition zone. This means that the ‘410’ and ‘660’ really are located at 410 and 660 km depth, but their conversion signals experience some relative delay when they pass the layers above. As the *IASP91* global reference model does not contain an asthenosphere, an increased v_p/v_s ratio within an existing asthenosphere beneath the investigation area might explain at least some part of the observed time delay of the discontinuities of the mantle transition zone.

Furthermore, a coherent Ps conversion is observed in the boxes of P receiver function data and in the sum trace at 54.4 s (Figures 7.5 and 7.6). It might be attributed to the so-called 520-km discontinuity. However, the phase was not analysed in more detail.

8.4 Model of the lithosphere and upper mantle beneath the western Bohemian Massif

Finally, two models are shown that summarize the results about location and topography of seismic discontinuities within the lithosphere and upper mantle (Figure 8.2). The models differ in their interpretation of the negative phases in the P and S receiver functions in the mantle lithosphere.

As the models combine all discontinuities observed with P and S receiver functions in this study, it becomes clearer that the area of Moho updoming beneath the western Eger Rift, the possible occurrence of additional high and low velocity zones and the transition from thinner lithosphere of the Saxothuringian/Teplá-Barrandian units to the thicker lithosphere of the Moldanubian unit coincide vertically. The occurrence of a low velocity layer at about 65 km depth ends to the south just where the steep increase in lithospheric thickness occurs. The models furthermore shows no topography of the discontinuities at 410 and 660 km depth. A slight deepening of both discontinuities in the south is indicated, but more data are necessary to confirm or deny this trend. Furthermore, a phase that might be interpreted as a discontinuity at 520 km depth within the mantle transition zone has been observed.

A comparison with the crustal and uppermost mantle model along the seismic refraction profile CEL09 suggested by *Hrubcová et al.* (2005) (see Figure 2.3) shows that the thickness of the crust of the Moldanubian unit agrees very well with the almost 40 km found in this thesis. However, crustal thickness for the Saxothuringian unit differs in the two models as *Hrubcová et al.* (2005) suggest a strong velocity contrast on top of a lower crustal layer at about 26 to 28 km depth and a gradual Moho transition at about 35 km depth. In this thesis, a crustal thickness of 27 to 31 km was obtained for the Saxothuringian unit, while there were generally no indications for the existence of a further strong discontinuity within the crust (Figure 5.10).

The model of the lithosphere beneath the western Eger Rift obtained by *Geissler et al.* (2006) (see Figure 2.8) shows an updoming of the Moho beneath the western Eger Rift that could be confirmed and mapped in more detail by the present study. It turned out that this Moho updoming seems to have an irregular internal geometry. While in *Geissler's* model a positive converter at about 55 km depth is the most pronounced structure in the subcrustal mantle beneath the western Eger Rift, in this thesis an additional negative phase was observed that extends over a larger area and probably corresponds to a negative gradient (LAB?) at about 65 km depth. A local asthenospheric updoming with steep flanks as indicated in *Geissler's* model does not seem likely from viewpoint of this thesis. However, the top of *Geissler's* asthenospheric updoming corresponds to the relatively shallow depth of about 65 km at which indications for a steep negative velocity gradient was found within P receiver functions in this thesis.

A comparison with the model of the lithosphere beneath the western Bohemian Massif presented by *Babuška and Plomerová* (2001) (see Figure 2.5) shows that the model correlates well with the lithospheric thickness found in this thesis. However, the increase in thickness from the Saxothuringian to Moldanubian lithosphere obtained here is much steeper than in the model by *Babuška and Plomerová* (2001). However, the nature of this “step” is not clear. Some of the data obtained in this study show a doubling or broadening

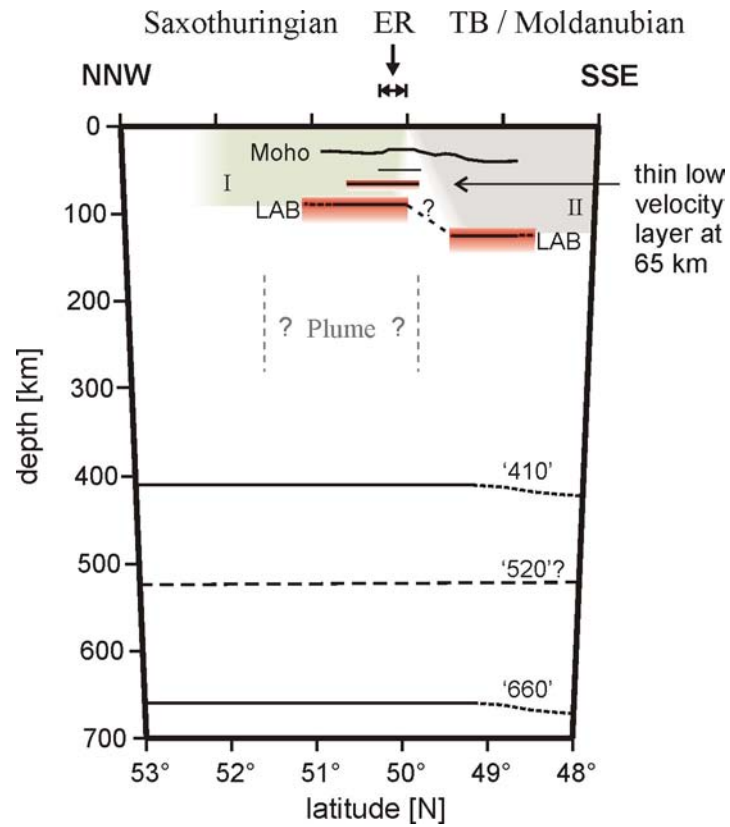
of the negative signal (Figure 6.13; boxes 21 and 22 in Figure 6.10a), which could point to either an abrupt increase of lithospheric thickness, or a very steep slope, or possibly even a structure from palaeosubduction within the lithosphere of this part of the investigated area. *Babuška and Plomerová* (2001) observed a mixture of anisotropic characteristics of the Saxothuringian and the Moldanubian unit within the lower lithosphere at the transition from the Saxothuringian to the Moldanubian unit. They suggested underthrusting of a part of the Saxothuringian subcrustal lithosphere beneath the Moldanubian or a hypothetical remnant of the Early Palaeozoic oceanic lithosphere subducted to the south during collision of the Saxothuringian and Moldanubian units.

Present strong CO₂ emanations of upper mantle origin, Moho updoming beneath the western Eger Rift and Tertiary/Quaternary volcanic activity comparable to the Eifel region and French Massif Central demand an explanation for these phenomena, like for example the assumption of a diapiric mantle upwelling (“baby plume”) as suggested by *Granet et al.* (1995) (see Figure 2.6) and/or the existence of magmatic reservoirs near the crust-mantle boundary as suggested by e.g. *Weinlich et al.*, 1999, *Bräuer et al.*, 2005 or *Geissler et al.*, 2005. However, the seismic discontinuities of the lithosphere and upper mantle beneath the western Bohemian Massif as observed in this study do not give rise to the assumption of a “baby plume” beneath the western Bohemian Massif. On the other hand, the possible existence of such a structure in the upper mantle above the mantle transition zone could not be completely ruled out. Teleseismic tomography carried out with the BOHEMA data set also does not show clear indications for a plume-like structure (*Plomerová et al.*, 2006, submitted). Nevertheless the observation of a negative velocity gradient at 65 km depth in this study suggests the presence of relatively hot mantle material with decreased *S* wave velocity, or even partial melts within the lithosphere, which might be the cause of at least some of the described phenomena beneath the western Bohemian Massif.

Figure 8.2 (next page): Cartoon of the seismic discontinuities beneath the western Bohemian Massif as observed in this study. The section represents a NNW-SSE profile across the western Eger Rift (ER) with true proportions. TB is the Teplá-Barrandian unit. With increasing depth, the aperture of the rays allows to observe a larger area, however with less resolution. At approximately 30 km depth the Moho is observed, with an updoming beneath the western Eger Rift to approximately 27 km and deepening towards the Moldanubian. The thin black line beneath the western Eger Rift represents a velocity increase at about 50 km depth, which was modelled from the local occurrence of a positive phase near 6 s delay time in *P* receiver functions. In the *P* and *S* receiver functions, negative phases are observed at about 7.5 s and 9 to 10 s, respectively. They can for example be interpreted as two distinct structures with negative velocity gradients (**a**), or as one single discontinuity with changing steepness of gradient, so that the different wave types image the part of the gradient that they are most sensitive to (**b**). The negative gradient observed in the *S* receiver functions was interpreted as lithosphere-asthenosphere boundary in this study. At the transition to the Moldanubian unit, lithospheric thickness strongly increases. However, a clear image of the nature of this increase could not be obtained. Furthermore, the angle of the contact between Saxothuringian (I) and Moldanubian lithosphere (II) is not known.

The upper mantle discontinuities at 410 and 660 km depth do not show any significant topography apart from a slight deepening in the southernmost part of the area. A phase at 54.4 s delay time observed in *P* receiver function data might perhaps be interpreted as the 520-km discontinuity. The possible existence of a plume-like velocity anomaly in the upper mantle above the mantle transition zone cannot be completely ruled out by this study.

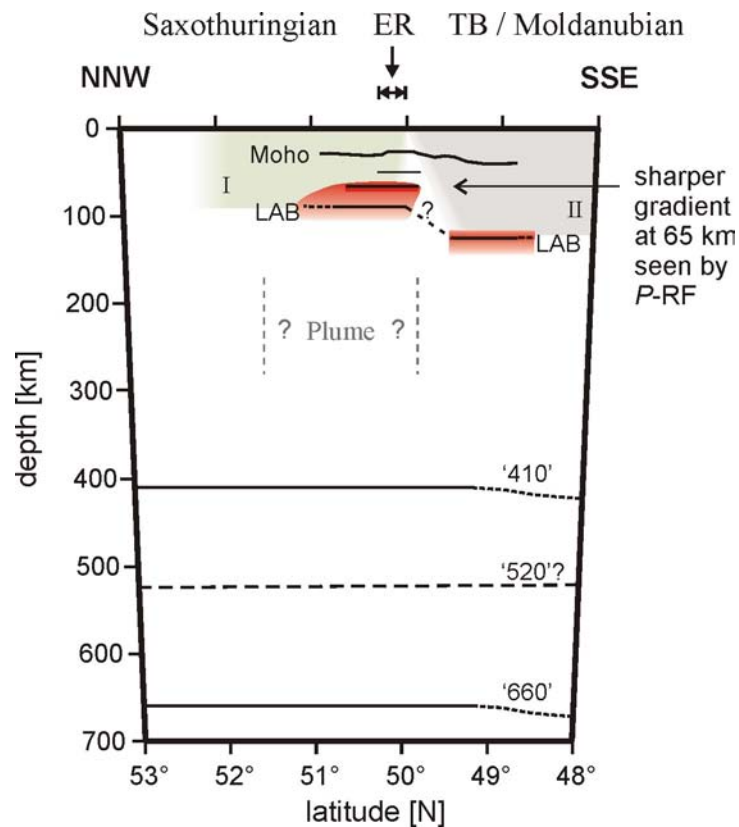
(a)



I: Saxothuringian lithosphere

II: Moldanubian lithosphere

(b)



8.5 Open questions/ Outlook

As usual, during the effort to answer one question, many other questions arise. Furthermore, many aspects that need to be investigated could not be touched within the frame of this work.

Synthetic tests and modelling of the observed phases within the lithospheric mantle at 6 s and 7.5 s delay time and of the lithosphere-asthenosphere transition are necessary in order to decide which of the suggested scenarios for the velocity reduction in the lithospheric mantle is more probable.

The receiver function investigation presented in this thesis has been carried out under the assumption of isotropic, horizontal layers beneath the western Bohemian Massif. This is, of course, a simplification of the real situation. From anisotropy studies it is known that the lithospheric mantle beneath the western Bohemian Massif shows anisotropy (e.g. *Babuška and Plomerová*, 1993, 2001; *Plomerová et al.*, 1998, 2002, 2006). A future task could thus be the investigation of anisotropy or dipping layers within the receiver function data by investigating azimuthal behaviour and by using also *T* components of rotated and deconvolved seismograms.

The Moho depth map obtained within this thesis revealed a rather steep increase in Moho depth across the Central Bohemian Shear Zone (Figure 5.10). This and the continuation of Moho depth from the Moldanubian to the southwest across the Bavarian shear zone should be investigated in more detail with the receiver function technique with more seismic stations. The station distribution of the BOHEMA experiment did not provide enough data to answer this question. Ongoing projects of Czech and Austrian colleagues will hopefully make it possible soon.

Recent results regarding the composition and flux rates of CO₂ emanations with signature of subcontinental lithospheric mantle indicate that there are very recent changes and dynamics observable (*Bräuer et al.*, 2005; *H. Kämpf, personal communication*), which points to presently active magmatic processes in the uppermost mantle beneath the intersection area of Eger Rift and Regensburg-Leipzig-Rostock zone. In order to even better resolve possible magmatic underplating or the occurrence of partial melts that might lead to the described processes, an extremely dense network or profiles of seismometers within this region (station spacing 2 to 3 kilometres) might help to map the fine structure of the Moho as well as seismic discontinuities within the lithospheric mantle.

Magnetotelluric sounding, which has been used to estimate the depth of the lithosphere-asthenosphere transition, should also be able to detect partial melting above or below the crust-mantle boundary. Therefore magnetotelluric measurements within the investigation area might be helpful to test the existence and depth location of areas of partial melt within the lithosphere.

In order to better constrain the location of the lithosphere-asthenosphere transition and of the discontinuities at 410 and 660 km depth, more data from stations in eastern and southern Bavaria have to be included. As most of the teleseismic events have northern to eastern backazimuths, the investigation area would then show better data coverage than in the present thesis. As current research aims at a better knowledge of lithospheric thickness beneath Europe, it will be possible to compare and connect the results of this thesis with the future results of research.

Receiver functions obtained with the BOHEMA data set also show indications of *P*-to-*S* converted phases from the base of the asthenosphere (Lehmann discontinuity) and from the discontinuity at 520 km depth. However, the signal from a possible Lehmann discontinuity probably interferes with multiples from the Moho and lithosphere-asthenosphere boundary. If it exists, it might be better constrained with the *S* receiver function method. However, the *S* receiver functions analysed in this thesis for the lithosphere-asthenosphere transition do so far not give hints to a *S*-to-*P* converted signal from the Lehmann discontinuity. The data has to be analysed in more detail. To further constrain the existence and depth of the '520', synthetic tests are necessary.

Finally, future research in this area would certainly benefit from further comparison or parallel research activities in the Eifel volcanic fields and French Massif Central.

Acknowledgements

I would like to sincerely thank my supervisor Prof. Dr. Rainer Kind for providing me the subject of this research work, for guidance and far-reaching freedom, discussions, motivation and a literally always open door.

I am deeply grateful to Dr. Wolfram Geissler for his part in initiating the project, introducing the receiver function method to me and for a lot of voluntary help during deploying and running temporary seismic stations in the Czech Republic and Germany for almost two years. He freely shared his vast knowledge about the investigation area and was a very pleasant and reliable partner for cooperation.

Close cooperation with Dr. Horst Kämpf included many interesting discussions about geological, geochemical and geophysical processes in western Bohemia. Horst always encouraged and motivated me a lot with his enthusiasm, cheerfulness and creative ideas.

I would very much like to thank Prof. Dr. Serge Shapiro for serving as co-referee.

One of the main initiators of the German part of the BOHEMA seismic experiment was Prof. Dr. Michael Korn, to whom I would like to express my gratitude.

German temporary BOHEMA stations were provided by the Geophysical Instrument Pool Potsdam, whose staff also helped when technical problems occurred. Data of other permanent and temporary stations were provided by members of the BOHEMA working group. I am especially thankful for good cooperation with the colleagues from the Geophysical Institute of the Czech Academy of Sciences, Prague. Station deployment and maintenance would not have been possible without the help of Manfred Brunner and Dr. Klaus Klinge and people who provided station locations, sometimes even in their private homes. During archiving of the huge amount of data into the GEOFON data archive, Dr. Winfried Hanka helped me when problems occurred. To complement the BOHEMA data set, I had the possibility to use data of a previous seismic experiment in the western Bohemian Massif, for which I would like to thank the authors of *Geissler et al.* (2005).

Many of the programs I used were written by Dr. Xiaohui Yuan. Data processing was carried out with Dr. Klaus Stammler's software package *SeismicHandler*. My "Hiwi" Dr. Kai Hahne helped me much with routine processing of the data. Most of the figures were created with the free software GMT (*Wessel and Smith*, 1998).

During the start of the BOHEMA experiment, I was still at SZGRF Erlangen/BGR. I am grateful to the colleagues from Erlangen for good cooperation and a lot of support. At GFZ Potsdam I shared the office for three years with Dr. Forough Sodoudi. She was not only a very amiable and helpful colleague, but also became a close friend.

I had a nice time working in section 2.4 of GFZ Potsdam with very pleasant colleagues and (former) PhD students who supported me and provided a very good working atmosphere. Therefore I would like to thank all of them, particularly Benjamin Heit, Ingo Wölbern, Jörn Kummerow, Xiaohui Yuan, Xueqing Li, Susanne Hemmleb, Ivan Koulakov, Amerika Manzanares, Mirjam Bohm, Karl-Heinz Jäckel, Manfred Stiller, Joachim Saul, and Heiko Sperlich. Furthermore I would like to thank Wolfram Geissler, Horst Kämpf, and Kai Hahne for carefully reading the manuscript.

Last but not least, I would like to thank the German Research Foundation (DFG) for funding of the BOHEMA project, as well as GFZ Potsdam for further financial support and providing an excellent infrastructure. I would also like to thank the people who initiated and run the Betriebskindertagesstätte "Geolino" on the Telegrafenberg, which made it much easier to start working again after staying at home with the baby.

References

- Achauer, U., J. Plomerová, V. Babuška, L. Vecsey, M. Granet, and BOHEMA working group (2005), Upper mantle structure in the western Bohemian Massif – results of isotropic tomography and seismic anisotropy (BOHEMA project), *Geophys. Res. Abstracts*, 7, 04262.
- Akaogi, M., A. Tanaka, and E. Ito (2002), Garnet-ilmenite-perovskite transitions in the system $\text{Mg}_4\text{Si}_4\text{O}_{12}\text{-Mg}_3\text{Al}_2\text{Si}_3\text{O}_{12}$ at high pressures and high temperatures: phase equilibria, calorimetry and implications for mantle structure, *Phys. Earth Planet. Inter.*, 132, 303-324.
- Anderson, D.L. (1989), *Theory of the Earth*, Blackwell Scientific, Boston, Massachusetts.
- Anderson, D.L. (1995), Lithosphere, asthenosphere, and perisphere, *Rev. Geophys.*, 33 (1), 125-149, 94RG-02785.
- Artemieva, I.M. (2003), Lithospheric structure, composition, and thermal regime of the East European Craton: implications for the subsidence of the Russian platform. *Earth Planet. Sci. Lett.*, 213, 431-446.
- Babuška, V., and J. Plomerová (1992), The lithosphere in central Europe – seismological and petrological aspects, *Tectonophysics*, 207, 141-163.
- Babuška, V., and J. Plomerová (1993), Lithosphere thickness and velocity anisotropy – seismological and geothermal aspects, *Tectonophysics*, 225, 79-89.
- Babuška, V., and J. Plomerová (2001), Subcrustal lithosphere around the Saxothuringian-Moldanubian Suture Zone – a model derived from anisotropy of seismic wave velocities, *Tectonophysics*, 332, 185-199.
- Babuška, V. J. Plomerová, and the BOHEMA working group (2003), Seismic Experiment Searches for Active Magmatic Source in Deep Lithosphere, Central Europe, *EOS, Trans. AGU*, 84 (40), 409-418.
- Bankwitz, P., G. Schneider, H. Kämpf, and E. Bankwitz (2003), Structural characteristics of epicentral areas in Central Europe: study case Cheb Basin (Czech Republic), *J. Geodyn.*, 35, 5-32.
- Barrell, J. (1914), The strength of the Earth's crust, *Journal of Geology*, 22, 28-48.
- Båth, M., and R. Stefánsson (1966), S-P conversions at the base of the crust, *Ann. Geofis.*, 19, 119-130.
- Behr, H.-J., and T. Heinrichs (1987), Geological interpretation of DEKORP 2-S: a deep seismic reflection profile across the Saxothuringian and possible implications for the late Variscan structural evolution of central Europe, *Tectonophysics*, 142, 173-202.
- Behr, H.-J., H.-J. Dürbaum, and P. Bankwitz (1994), Crustal structure of the Saxothuringian zone: results of the deep seismic profile MVE-90(East), *Z. Geol. Wiss.*, 22(6), 647-769.
- Behrmann, J.H., and D.C. Tanner (1997), Carboniferous tectonics of the Variscan basement collage in eastern Bavaria and western Bohemia, *Geol. Rundschau*, 86, 15-27.
- Benz, H.M., and J.E. Vidale (1993), Sharpness of upper-mantle discontinuities determined from high-frequency reflections, *Nature*, 365, 147-150.
- Bercovici, D., and S.-I. Karato (2003), Whole-mantle convection and the transition-zone water filter, *Nature*, 425, 39-44.
- Bina, C.R., and G.R. Helffrich (1994), Phase transition Clapeyron slopes and transition zone seismic discontinuity topography, *J. Geophys. Res.*, 99, 15 853-15 860.

REFERENCES

- Bleibinhaus, F., D. Stich, M. Simon, and H. Gebrande (2003), New results from amplitude preserving prestack depth migration of the Münchberg/Vogtland segment of the MVE deep seismic survey, *J. Geodyn.*, **35**, 33-43.
- Bock, G. and R. Kind (1991), A global study of S-to-P and P-to-S conversions from the upper mantle transition zone, *Geophys. J. Int.*, **107**, 117-129.
- Bock, G. (1994), Synthetic seismogram images of upper mantle structure: No evidence for a 520-km discontinuity, *J. Geophys. Res.*, **99**, 15 843-15 851.
- Bräuer, K., H. Kämpf, G. Strauch, and S.M. Weise (2003), Isotopic evidence ($^3\text{He}/^4\text{He}$, $^{13}\text{C}_{\text{CO}_2}$) of fluid-triggered intraplate seismicity, *J. Geophys. Res.*, **108**(B2), 2070, doi:10.1029/2002JB002077.
- Bräuer, K., H. Kämpf, S. Niedermann, G. Strauch and S.M. Weise (2004), Evidence for a nitrogen flux directly derived from the European subcontinental mantle in the western Eger Rift, Central Europe, *Geochim. Cosmochim. Acta*, **68**, 4935-4947.
- Bräuer, K., H. Kämpf, S. Niedermann, and G. Strauch (2005): Evidence for ascending upper mantle-derived melt beneath the Cheb basin, central Europe, *Geophys. Res. Lett.*, **32**, L08303, doi:10.1029/2004GL022205, 2005.
- Bues, C., W. Dörr, J. Fiala, Z. Vejnar, and G. Zulauf (2002), Emplacement depth and radiometric ages of Paleozoic plutons of the Neukirchen-Kdyne massif: Differential uplift and exhumation of Cadomian basement due to Carboniferous orogenic collapse (Bohemian Massif), *Tectonophysics*, **352**, 225-243.
- Burdick, L.J., and C.A. Langston (1977), Modeling crustal structure through the use of converted phases in teleseismic body-wave forms, *Bull. Seism. Soc. Am.*, **67**, 677-691.
- Castle, J.C., and K.C. Creager (2000), Local sharpness and shear wave speed jump across the 660-km discontinuity, *J. Geophys. Res.*, **105**, 6191-6200.
- Christensen, N.I. (1996), Poisson's ratio and crustal seismology, *J. Geophys. Res.*, **101**(B2), 3139-3156.
- Credner, H. (1900), Die vogtländischen Erdbebenschwärme während des Juli und August 1900, *Ber. Ü. Verh. Kgl. Sächs. Ges. Wiss. Leipzig, Math-phys. Kl.* **52**, 153-177.
- Čermák, V. (1994), Results of Heat Flow Studies in Czechoslovakia, in *Crustal Structure of the Bohemian Massif and the West Carpathians* Bucha, edited by V. and M. Blížkovský, Springer Verlag Berlin Heidelberg New York.
- Cummins, P., B.L.N. Kennett, J.R. Bowman, and M. Bostock (1992), The 520 km discontinuity?, *Bull. Seismol. Soc. Am.*, **82**, 323-336.
- Dallmeyer, R.D, W. Franke, K. Weber (Eds.) (1995), *Pre-Permian Geology of Central and Eastern Europe*, Springer-Verlag Berlin Heidelberg New York.
- Dahm, T., J. Horálek, and J. Šílený (2000), Comparison of absolute and relative moment tensor solutions for the January 1997 West Bohemia earthquake swarm, *Studia geophys. et geod.*, **44**(2), 233-250.
- DEKORP Research Group (1985), First results and preliminary interpretation of deep-reflection seismic recordings along profile DEKORP 2-South, *J. Geophys.*, **57**, 137-163.
- DEKORP Research Group (1988), Results of the DEKORP 4/KTB Oberpfalz deep seismic reflection investigations, *J. Geophys.*, **62**, 69-101.
- DEKORP Research Group (1994), The deep reflection seismic profiles DEKORP 3/MVE 90, *Z. Geol. Wiss.*, **22**(6), 623-824.
- Deuss, A., and J.H. Woodhouse (2001), Seismic Observation of Splitting of the Mid-Transition Zone Discontinuity in Earth's Mantle, *Science*, **294**, 354-357.
- Dèzes, P., and P.A. Ziegler (2001), European map of the Mohorovičić discontinuity. 2nd EUCOR-URGENT Workshop (Upper Rhinegraben Evolution and Neotectonics), Mt. St. Odile, France. <http://compl.geol.unibas.ch>.

- Dèzes, P., S.M. Schmidt, and P.A. Ziegler (2004), Evolution of the European Cenozoic Rift System: Interaction of the Alpine and Pyrenean orogens with their foreland lithosphere, *Tectonophysics*, 389, 1-33.
- Dörr, W., G. Zulauf, J. Fiala, W. Franke, and Z. Vejnar (2002), Neoproterozoic to Early Cambrian history of an active plate margin in the Teplá-Barrandian unit – a correlation of U-Pb isotopic-dilution-TIMS ages (Bohemia, Czech Republic), *Tectonophysics*, 352, 65-85.
- Emmertmann, R., and J. Lauterjung (1997), The German continental deep drilling program KTB: Overview and major results, *J. Geophys. Res.*, 102(B8), 18 179-18 201.
- Enderle, U., K. Schuster, C. Prodehl, A. Schulze, and J. Briebach (1998), The refraction seismic experiment GRANU'95 in the Saxothuringian belt, southeastern Germany, *Geophys. J. Int.*, 133, 245-259.
- ERCEUGT-Group, 1992, An electrical resistivity crustal section from the Alps to the Baltic Sea (central segment of the EGT), *Tectonophysics*, 207, 123-139.
- Faber, S., and G. Müller (1980), Sp phases from the transition zone between the upper and lower mantle, *Bull. Seism. Soc. Am.*, 70, 487-508.
- Faber, S., J. Plomerová, and V. Babuška (1986), Deep-seated lateral variations beneath the GRF array inferred from mislocation patterns and P residuals, *J. Geophys.*, 60, 139-148.
- Farra, V., and L. Vinnik (2000), Upper mantle stratification by P and S receiver functions, *Geophys. J. Int.*, 141, 699-712.
- Fischer, T. (2003), The August-December 2000 earthquake swarm in NW Bohemia: the first results based on automatic processing of seismograms, *J. Geodyn.*, 35, 59-81.
- Fischer, T., and J. Horálek (2003), Space-time distribution of earthquake swarms in the principal focal zone of the NW Bohemia/Vogtland seismoactive region: period 1985-2001, *J. Geodyn.*, 35, 125-144.
- Fischer, T., and J. Horálek (2005), Slip-generated patterns of swarm microearthquakes from West Bohemia/Vogtland (central Europe): Evidence of their triggering mechanism?, *J. Geophys. Res.*, 110, B05S21, doi:10.1029/2004JB003363.
- Flanagan, M.P., and P.M. Shearer (1998a), Global mapping of topography on transition zone velocity discontinuities by stacking SS precursors, *J. Geophys. Res.*, 103, 2673-2692.
- Flanagan, M.P., and P.M. Shearer (1998b), Topography on the 410 km seismic velocity discontinuity near subduction zones from stacking of sS, sP and pP precursors, *J. Geophys. Res.*, 103, 21 165-21 182.
- Förster, A., and H.-J. Förster (2000), Crustal composition and mantle heat flow: Implications from surface heat flow and radiogenic heat production in the Variscan Erzgebirge (Germany), *J. Geophys. Res.*, 105(B12), 27 917-27 938.
- Franke, W. (1989), The geological framework of the KTB drill site, Oberpfalz, in *The German Continental Deep Drilling Program (KTB)*, edited by R. Emmertmann, R. and J. Wohlenberg, pp. 37-55, Springer, Heidelberg.
- Franke, W. (1992), Phanerozoic structures and events in Central Europe, in *A continent revealed: the European Geotraverse*, edited by D. Blundell et al., pp. 164-179, Cambridge Univ. Press, Cambridge.
- Franke, W., R.D. Dallmeyer, and K. Weber (1995), Geodynamic evolution, in *Pre-Permian Geology of Central and Western Europe*, edited by D. Dallmeyer, pp. 579-593, Springer-Verlag Berlin Heidelberg New York.
- Franke, W. (2000), The mid-European segment of the Variscides: tectonostratigraphic units, terrane boundaries and plate tectonic evolution, in *Orogenic processes:*

REFERENCES

- Quantification and Modelling in the Variscan Belt*, edited by W. Franke et al., pp. 35-61, No. 179, The Geological Society, London.
- Freudenberger, W. (1996), Tektonik. Deckgebirge nördlich der Donau. in *Bayerisches Geologisches Landesamt. Geologische Karte von Bayern, 1:500000*, München.
- Gaherty, J.B., M. Kato, and T.H. Jordan (1999), Seismological structure of the upper mantle: a regional comparison of seismic layering, *Phys. Earth Planet. Inter.*, **110**, 21-41.
- Geissler, W.H. (2004), Seismic and Petrological Investigations of the Lithosphere in the Swarm-Earthquake and CO₂ Degassing Region Vogtland/NW-Bohemia, *Doctoral Thesis*, Free University of Berlin.
- Geissler, W.H., H. Kämpf, R. Kind, K. Bräuer, K. Klinge, T. Plenefisch, J. Horálek, J. Zednik, and V. Nehybka (2005), Seismic structure and location of a CO₂ source in the upper mantle of the western Eger (Ohře) Rift, central Europe, *Tectonics*, **24**, TC5001, doi:10.1029/2004TC001672.
- Geissler, W.H., H. Kämpf, W. Seifert, and P. Dulski (2006), Petrological and seismic studies of the lithosphere in the earthquake swarm region Vogtland/NW-Bohemia, Central Europe, *Journal of Volcanology and Geothermal Research*, in press.
- Giese, P. (1995), Main Features of Geophysical Structures in Central Europe, in *Pre-Permian Geology of Central and Western Europe*, edited by D. Dallmeyer, pp. 7-26, Springer-Verlag Berlin Heidelberg New York.
- Gilbert, H.J., A.F. Sheehan, K.G. Dueker, and P. Molnar (2003), Receiver functions in the western United States, with implications for upper mantle structure and dynamics, *J. Geophys. Res.*, **109**, doi:10.1029/2001JB001194.
- Gossler, J., and R. Kind (1996), Seismic evidence for very deep roots of continents, *Earth Planet. Sci. Lett.*, **138**, 1-13.
- Granet, M., M. Wilson, and U. Achauer (1995), Imaging a mantle plume beneath the Massif Central (France), *Earth Planet. Sci. Lett.*, **136**, 281-296.
- Griesshaber, E., R.K. O’Nions, and E.R. Oxburgh (1992), Helium and carbon isotope systematics in crustal fluids from the Eifel, the Rhine Graben and Black Forest, F.R.G., *Chem. Geol.*, **99**, 213-235.
- Grosse, S., W. Conrad, H.J. Behr, and T. Heinrichs (1990), Major gravity axis and anomalies in central Europe, in *Proc. 5th EGT Study Centre*, edited by R. Freeman et al., pp. 35-146, European Science Foundation, Strasbourg.
- Grünthal, G. (1989), About the history of earthquake activity in the focal region Vogtland/Western Bohemia, in *Monitoring and Analysis of the Earthquake Swarm 1985/1986 in the Region Vogtland/Western Bohemia*, edited by P. Bormann, pp. 30-34, Akad. der Wissensch. der DDR, Potsdam.
- Grunewald, S., M. Weber, and R. Kind (2001), The upper mantle under Central Europe: indications for the Eifel plume, *Geophys. J. Int.*, **147**, 590-601.
- Gu, Y., A.M. Dziewonski, and C.B. Agee (1998), Global de-correlation of the topography of transition zone discontinuities, *Earth Planet. Sci. Lett.*, **157**, 57-67.
- Gu, Y., A.M. Dziewonski, and G. Ekström (2003), Simultaneous inversion for mantle shear velocity and topography of transition zone discontinuities, *Geophys. J. Int.*, **154**, 559-583.
- Gung, Y., M. Panning, and B. Romanowicz (2003), Global anisotropy and the thickness of continents, *Nature*, **422**, 707-711.
- Gutenberg, B. (1926), Untersuchungen zur Frage bis zu welcher Tiefe die Erde kristallin ist, *Z. Geophys.*, **2**, 24-29.
- Gutenberg, B. (1959), *Physics of the Earth’s Interior*, 240pp, Academic Press, New York.
- Hainzl, S. (2003), Self-organization of earthquake swarms, *J. Geodyn.*, **35**, 157-172.

- Heinicke, J., and U. Koch (2000), Slug flow – a possible explanation for hydrogeochemical earthquake precursors at Bad Brambach, Germany, *Pure Appl. Geophys.*, *157*(10), 1621-1641.
- Helffrich, G.R. (2000), The Earth's mantle, *Rev. Geophys.*, *38*, 141-158.
- Helffrich, G.R., and B.J. Wood (2001), The Earth's mantle, *Nature*, *412*, 501-507.
- Hemmann, A., T. Meier, G. Jentzsch, and A. Ziegert (2003), Similarity of waveforms and relative relocalisation of the earthquake swarm 1997/1998 near Werdau, *J. Geodyn.*, *35*, 191-208.
- Heuer, B., W.H. Geissler, R. Kind, and H. Kämpf (2006), Seismic evidence for asthenospheric updoming beneath the western Bohemian Massif, central Europe, *Geophys. Res. Lett.*, *33*, L05311, doi:10.1029/2005GL025158.
- Hill, D.P. (1977), A model for earthquake swarms, *J. Geophys. Res.*, *82*, 1347-1352.
- Hill, D.P. and S. Prejean (2005), Magmatic unrest beneath Mammoth Mountain, California, *Journal of Volcanology and Geothermal Research*, *146*, 257-283.
- Hirth, G., Evans, R.L., and A.D. Chave (2000), Comparison of continental and oceanic mantle electrical conductivity: Is the Archean lithosphere dry? *Geochem. Geophys. Geosyst.*, *1*, 2000GC00048.
- Hirth, G. and D.L. Kohlstedt (1996), Water in the oceanic upper mantle: implications for rheology, melt extraction and the evolution of the lithosphere, *Earth Planet. Sci. Lett.*, *144*, 93-108.
- Hjelt, S.-E. (1991), Geoelectric studies and conductivity structures of the eastern and northern parts of the Baltic Shield, *Tectonophysics*, *189*, 249-260.
- Hofmann, Y., T. Jahr, and G. Jentzsch (2003), Three-dimensional gravimetric modelling to detect the deep structure of the region Vogtland/NW-Bohemia, *J. Geodyn.*, *35*, 209-220.
- Hofstetter, R., and G. Bock (2004), Shear-wave velocity structure of the Sinai sub-plate from receiver function analysis, *Geophys. J. Int.*, *158*, 67-84.
- Horálek, J., T. Fischer, A. Boušková, P. Jedlička (2000a), Western Bohemia/Vogtland region in the light of the WEBNET network, *Studia geophys. et geod.*, *44*, 107-125.
- Horálek, J., J. Šílený, T. Fischer, A. Slancová, and A. Boušková (2000b), The scenario of the January 1997 West Bohemia Earthquake Swarm, *Studia geophys. et geod.*, *44*(4), 491-521.
- Hrubcová, P., P. Šroda, A. Špičák, A. Guterch, M. Grad, R. Keller, E. Brückl and H. Thybo (2005), Crustal and uppermost mantle structure of the Bohemian Massif based on CELEBRATION 2000 data, *J. Geophys. Res.*, *110*, B11305, doi:10.1029/2004JB003080.
- Huang, X., Y. Xu, and S.-I. Karato (2005), Water content in the transition zone from electrical conductivity of wadsleyite and ringwoodite, *Nature*, *434*, 746-749.
- Isaacs, B., J. Oliver, and L.R. Sykes (1968), Seismology and the new global tectonics, *J. Geophys. Res.*, *73*, 5855-5899.
- Ibs-von Seht, M., K. Klinge, and T. Plenefisch (2006), Seismicity of intracontinental swarm earthquake areas – a comparison of selected cases in America, Africa and Europe, *IASPEI Publ. Series for the IDNDR*, Beijing, in press.
- Jeffreys, H. (1936), The structure of the earth down to the 20° discontinuity, *Monthly Notices of the Royal Astronomical Society, Geophysical Supplement*, *3*(9), 401-422.
- Jones, A.G. (1982), Observations of the electrical asthenosphere beneath Scandinavia, *Tectonophysics*, *90*, 37-55.
- Jones, A.G. (1999), Imaging the continental upper mantle using electromagnetic methods, *Lithos*, *48*, 57-80.

REFERENCES

- Kämpf, H., K. Bräuer, G. Strauch, and S.M. Weise (1999), Indications for an Active Magma Chamber in the Upper Mantle Below the Western Eger Graben, Czech Republic, *EOS, Spring Meeting*, V52A-03 (abstract).
- Karato, S.-I., and H. Jung (1998), Water, partial melting and the origin of the seismic low velocity and high attenuation zone in the upper mantle, *Earth Planet. Sci. Lett.*, **157**, 193-207.
- Kárník, V., Z. Schenková, and V. Schenk (1986), Time pattern of the swarm of December 1985-March 1986 in West Bohemia, in *Earthquake swarm 1985/86 in Western Bohemia*, edited by D. Procházková, pp. 328-342, Geophys. Inst. Czechosl. Acad. Sci., Praha.
- Kennett, B.L.N. (1991), *IASPEI 1991 Seismological Tables*, 167 pp., Research School of Earth Sciences, Australian National University, Canberra.
- Kennett, B.L.N., and E.R. Engdahl (1991), Travel times for global earthquake location and phase identification, *Geophys. J. Int.*, **105**, 429-465.
- Kind, R., and L.P. Vinnik (1988), The upper-mantle discontinuities underneath the GRF array from P-to-S converted phases, *J. Geophys.*, **62**, 138-147.
- Kind, R., G.L. Kosarev, and N.V. Petersen (1995), Receiver functions at the stations of the German Regional Seismic Network (GRSN), *Geophys. Journ. Int.*, **121**, 191-202.
- Kind, R., X. Yuan, J. Saul, D. Nelson, S.V. Sobolev, J. Mechie, W. Zhao, G. Kosarev, J. Ni, U. Achauer, and M. Jiang (2002), Seismic images of crust and upper mantle beneath Tibet: Evidence for Eurasian plate subduction, *Science*, **298**, 1219-1221.
- King, S.D. and J. Ritsema (2000), African hot spot volcanism: small scale convection in the upper mantle beneath cratons, *Science*, **290**, 1137-1140.
- Knett, J. (1899), Das Erzgebirgische Schwarmbeben zu Hartenberg vom 1. Jänner bis Feber 1824, *Sitzungsber. Deutsch. Naturwiss.-med. Ver. Böhmen, Lotos Prag N.F.*, **19**, 167-191.
- Koch, U., J. Heinicke, and M. Voßberg (2003), Hydrogeological effects of the latest Vogtland-NW Bohemian swarmquake period (August to December 2000), *J. Geodyn.*, **35**, 107-123.
- Kopecký, L. (1978), Neoidic taphrogenic evolution and young alkaline volcanism of the Bohemian Massif, *Sbor. geol. Ved. R. Geol.*, **26**, 91-107.
- Kosarev, G.L., N.V. Petersen, L.P. Vinnik, and S.W. Roecker (1993), Receiver function for the Tien Shan analog broadband network: contrast in the evolution of structure across the Talasso-Fargana fault, *J. Geophys. Res.*, **98**, 4437-4448.
- Kosarev, G., R. Kind, S.V. Sobolev, X. Yuan, W. Hanka, and S. Oreshin (1999), Seismic evidence for a detached Indian lithospheric mantle beneath Tibet, *Science*, **283**, 1306-1309.
- Kumar, P., X. Yuan, R. Kind, and G. Kosarev (2005a), The lithosphere-asthenosphere boundary in the Tien Shan-Karakoram region from S receiver functions: Evidence for continental subduction, *Geophys. Res. Lett.*, **32**, L07305, doi:10.1029/2004GL022291.
- Kumar, P., R. Kind, W. Hanka, K. Wylegalla, Ch. Reigber, X. Yuan, I. Wölbern, P. Schwintzer, K. Fleming, T. Dahl-Jensen, T.B. Larsen, J. Schweitzer, K. Priestley, O. Gudmundsson, and D. Wolf (2005b), The lithosphere-asthenosphere boundary in the North-West Atlantic region, *Earth Planet. Sci. Lett.*, **236**, 249-257, doi:10.1016/j.epsl.2005.05.029.
- Kumar, P., X. Yuan, R. Kind, and J. Ni (2006), Imaging the colliding Indian and Asian lithospheric plates beneath Tibet, *J. Geophys. Res.*, **111**, B06308, doi:10.1029/2005JB003930.
- Langston, C.A. (1979), Structure under Mount Rainier, Washington, inferred from teleseismic body waves, *J. Geophys. Res.*, **84**, 4749-4762.

- Lay, T., and T.C. Wallace (1995), *Modern Global Seismology*, Academic Press, New York.
- Lebedev, S., S. Chevrot, and R.D. van der Hilst (2002), Seismic Evidence for Olivine Phase Changes at the 410- and 660-Kilometer Discontinuities, *Science*, *296*, 1300-1302.
- Lehmann, I. (1961), S and the structure of the upper mantle, *Geophysical Journal, London*, *4*, 124-138.
- Lehmann, I. (1964), On the velocity of P in the upper mantle, *Bull. Seismol. Soc. Am.*, *54*, 1097-1103.
- Li, S., R. Kind, K. Priestley, S.V. Sobolev, F. Tilmann, X. Yuan, and M. Weber (2000), Mapping the Hawaiian plume conduit with converted seismic waves, *Nature*, *405*, 938-941.
- Li, X., R. Kind, and X. Yuan (2003a), Seismic study of upper mantle and transition zone beneath hotspots, *Phys. Earth Planet. Inter.*, *136*, 79-92.
- Li, X., R. Kind, X. Yuan, S.V. Sobolev, W. Hanka, D.S. Ramesh, Y. Gu, and A.M. Dziewonski (2003b), Seismic observation of narrow plumes in the oceanic upper mantle, *Geophys. Res. Lett.*, *30*, doi:10.1029/2002GL015411.
- Li, X., R. Kind, X. Yuan, I. Wölbern, and W. Hanka (2004), Rejuvenation of the lithosphere by the Hawaiian plume, *Nature*, *427*, 827-829.
- Matte, P. (1986), Tectonics and plate tectonics model for the Variscan belt of Europe, *Tectonophysics*, *126*, 329-374.
- Matte, P., H. Maluski, P. Rajlich, and W. Franke (1990), Terrane boundaries in the Bohemian Massif: results of large-scale Variscan shearing, *Tectonophysics*, *177*, 151-170.
- Matte, P. (1991), Accretionary history and crustal evolution of the Variscan belt in Western Europe, *Tectonophysics*, *196*, 309-337.
- Matte, P. (2001), The Variscan collage and orogeny (480-290 Ma) and the tectonic definition of the Armorica microplate: a review, *Terra Nova*, *13*, 122-128.
- Matthews, A., C. Fouillac, R. Hill, R.K. O'Nions, and E.R. Oxburgh (1987), Mantle-derived volatiles in continental crust: The Massif Central of France, *Earth Planet. Sci. Lett.*, *85*, 117-128.
- May, F. (2002), *Quantifizierung des CO₂-Flusses zur Abbildung magmatischer Prozesse im Untergrund der Westeifel*, 170pp, Shaker Verlag, Aachen.
- McKenzie, D., and M.J. Bickle (1988), The volume and composition of melt generated by extension of the lithosphere, *J. Petrol.*, *29*, 625-679.
- Mechie, J., K. Abu-Ayyash, Z. Ben-Avraham, R. El-Kelani, A. Mohsen, G. Rümper, J. Saul, and M. Weber (2005), Crustal Shear velocity structure across the Dead Sea Transform from two-dimensional modelling of DESERT project explosion seismic data, *Geophys. J. Int.*, *160*, 910-924, doi:10.1111/j.1365-246X.2005.02526.x.
- Mogi, K. (1963), Some discussions on aftershocks, foreshocks and earthquake swarms – the fracture of a semi finite body caused by an inner stress origin and its relation to the earthquake phenomena, *Bull. Earthquake Res. Inst.*, *41*, 615-658.
- Mohorovičić, A. (1910), Earthquake of 8 October 1909, *Yearly report of the Zagreb meteorological observatory for the year 1909*, 63pp, English translation: *Geofizika*, *9*, 3-55, 1992.
- Mohsen, A., R. Hofstetter, G. Bock, R. Kind, M. Weber, K. Wylegalla, G. Rümper, and the DESERT Group (2005), A receiver function study across the Dead Sea Transform, *Geophys. J. Int.*, *160*, 948-960, doi:10.1111/j.1365-246X.2005.02534.x.
- Neunhöfer, H., and T. Meier (2004), Seismicity in the Vogtland/Western Bohemia earthquake region between 1962 and 1998, *Studia geophys. et geod.*, *48*, 539-562.

REFERENCES

- Neunhöfer, H., and A. Hemmann (2005), Earthquake swarms in the Vogtland/Western Bohemia region: Spatial distribution and magnitude-frequency distribution as an indication of the genesis of swarms?, *J. Geodyn.*, 39(4), 361-385, doi:10.1016/j.jog.2005.01.004.
- Niazi, M. and D.L. Anderson (1965), Upper mantle structure of western North America from apparent velocities of P waves, *J. Geophys. Res.*, 70, 4633-4640.
- Nolet, G., and A. Zielhuis (1994), Low S velocities under the Tornquist-Teisseyre zone: evidence for water injection into the transition zone by subduction, *J. Geophys. Res.*, 99, 15813-15820.
- O’Nions, R.K., E. Griesshaber, and E.R. Oxburgh (1989), Rocks that are too hot to handle, *Nature*, 341, 391.
- Owens, T.J., G. Zandt, and S.R. Taylor (1984), Seismic evidence for an ancient rift beneath the Cumberland Plateau, Tennessee: A detailed analysis of broadband teleseismic P waveforms, *J. Geophys. Res.*, 89, 7783-7795.
- Parotidis, M., E. Rothert, and S.A. Shapiro (2003), Pore-pressure diffusion: A possible triggering mechanism for the earthquake swarms 2000 in Vogtland/NW-Bohemia, central Europe, *Geophys. Res. Lett.*, 30(20), 2075, doi:10.1029/2003GL018987.
- Parotidis, M., S.A. Shapiro, and E. Rothert (2005), Evidence for triggering of the Vogtland swarms 2000 by pore pressure diffusion, *J. Geophys. Res.*, 110, B05S10, doi:10.1029/2004JB003267.
- Passier, M.L. and R.K. Snieder (1996), Correlation between shear wave upper mantle structure and tectonic surface expressions: Application to central and southern Germany, *J. Geophys. Res.*, 101, 25293-25304.
- Plenefisch, T., and K. Klinge (2003), Temporal variations of focal mechanisms in the Novy Kostel focal zone (Vogtland/NW-Bohemia) – comparison of the swarms of 1994, 1997 and 2000, *J. Geodyn.*, 35, 145-156.
- Plomerová, J. and V. Babuška (1988), Lithosphere thickness in the contact zone of the Moldanubicum and Saxothuringicum in central Europe, *Phys. Earth Planet. Inter.*, 51, 159-165.
- Plomerová, J., V. Babuška, J. Šílený, and J. Horálek (1998), Seismic Anisotropy and Velocity Variations in the Mantle beneath the Saxothuringicum-Moldanubicum Contact in Central Europe, *Pure appl. geophys.*, 151, 365-394.
- Plomerová, J., D. Kouba, and V. Babuška (2002), Mapping the lithosphere-asthenosphere boundary through changes in surface-wave anisotropy, *Tectonophysics*, 358, 175-185.
- Plomerová, J., U. Achauer, V. Babuška, M. Granet, and BOHEMA working group (2003), BOHEMA 2001-2003: Passive Seismic Experiment to Study Lithosphere-Asthenosphere System in the Western Part of the Bohemian Massif, *Studia geophys. et geod.*, 47, 691-701.
- Plomerová, J., U. Achauer, V. Babuška, L. Vecsey and BOHEMA working group (2006), Upper mantle beneath the Eger Rift (Central Europe): plume or asthenosphere upwelling? *Geophys. J. Int.*, submitted.
- Praus, O., J. Pěčová, V. Petr, V. Babuška, and J. Plomerová (1990), Magnetotelluric and seismological determination of the lithosphere-asthenosphere transition in Central Europe, *Phys. Earth Planet. Inter.*, 60, 212-228.
- Prodehl, C., S. Müller, and V. Haak (1995), The European Cenozoic rift system, in *Continental rifts: evolution, structure, tectonics*, edited by K.H. Olsen, pp. 133-212, Developments in Geotectonics, 25, Elsevier.
- Ramesh, D.S., R. Kind, and X. Yuan (2002), Receiver function analysis of the North American crust and upper mantle, *Geophys. J. Int.*, 150, 91-108.

- Revenaugh, J., and S.A. Sipkin (1994), Seismic evidence for silicate melt atop the 410-km discontinuity, *Nature*, **369**, 474-476.
- Ringwood, A.E., and A. Major (1966), High-pressure transformations in pyroxenes, *Earth Planet. Sci. Lett.*, **1**, 241-245.
- Ritter, J.R.R., M. Jordan, U.R. Christensen, and U. Achauer (2001), A mantle plume below the Eifel volcanic fields, Germany, *Earth Planet. Sci. Lett.*, **186**, 7-14.
- Rost, S., and M. Weber (2002), The upper mantle transition zone discontinuities in the Pacific as determined by short-period array data, *Earth Planet. Sci. Lett.*, **204**, 347-361.
- Rothert, E., S.A. Shapiro, S. Buske, and M. Bohnhoff (2003), Mutual relationship between microseismicity and seismic reflectivity: Case study at the German Continental Deep Drilling Site (KTB), *Geophys. Res. Lett.*, **30**(17), 1893, doi:10.1029/2003GL017848.
- Rychert, C.A., K.M. Fischer, and S. Rondenay (2005), A sharp lithosphere-asthenosphere boundary imaged beneath eastern North America, *Nature*, **436**, 542-545, doi:10.1038/nature03904.
- Sacks, I.S., and J.A. Snoke (1977), The use of converted phases to infer the depth of the lithosphere-asthenosphere boundary beneath South America, *J. Geophys. Res.*, **82**, 2011-2017.
- Sandvol, E., D. Seber, A. Calvert, and M. Barazangi (1998), Grid search modelling of receiver functions: implications for crustal structure in the Middle East and North Africa, *J. Geophys. Res.*, **103**, 26899-26917.
- Savage, M.K. (1998), Lower crustal anisotropy or dipping boundaries? Effects on receiver functions and a case study in New Zealand, *J. Geophys. Res.*, **103**, 15069-15087.
- Scheuvens, D., and G. Zulauf (2000), Exhumation, strain localization, and emplacement of granitoids along the western part of the Central Bohemian shear zone (central European Variscides, Czech Republic), *Int. J. Earth Sci.*, **89**, 617-630.
- Schönenberg, R., and J. Neugebauer (1997), *Einführung in die Geologie Europas*, Rombach Verlag, Freiburg im Breisgau.
- Schott, B., and H. Schmeling (1998), Delamination and detachment of a lithospheric root, *Tectonophysics*, **296**, 225-247.
- Shapiro, S.A., J. Kummerow, C. Dinske, G. Asch, E. Rothert, J. Erzinger, H.-J. Kümpel, and R. Kind (2006), Fluid induced seismicity guided by a continental fault: Injection experiment of 2004/2005 at the German Deep Drilling Site (KTB), *Geophys. Res. Lett.*, **33**, L01309, doi:10.1029/2005GL024659.
- Shearer, P.M. (1990), Seismic imaging of upper-mantle structure with new evidence for a 520-km discontinuity, *Nature*, **344**, 121-126.
- Shearer, P.M., and T.G. Masters (1992), Global mapping of topography on the 660-km discontinuity, *Nature*, **355**, 791-796.
- Shearer, P.M. (1996), Transition zone velocity gradients and the 520-km discontinuity, *J. Geophys. Res.*, **101**(B2), 3053-3066.
- Shomali, Z.H., R.G. Roberts, L.B. Pedersen, and the TOR Working Group (2006), Lithospheric structure of the Tornquist Zone resolved by nonlinear P and S teleseismic tomography along the TOR array, *Tectonophysics*, **416**, 133-149, doi:10.1016/j.tecto.2005.11.019.
- Simmons, N.A., and H. Gurrola (2000), Multiple seismic discontinuities near the base of the transition zone in the Earth's mantle, *Nature*, **405**, 559-562.
- Simpson, F. (2002), A comparison of electromagnetic distortion and resolution of upper mantle conductivities beneath continental Europe and the Mediterranean using islands as windows, *Phys. Earth Planet. Inter.*, **129**, 117-130.

REFERENCES

- Soudoudi, F., R. Kind, D. Hatzfeld, K. Priestley and Greece working group (2006a), Lithospheric structure of the Aegean obtained from P and S receiver functions, *J. Geophys. Res.*, *in revision*.
- Soudoudi, F., X. Yuan, Q. Liu, R. Kind, and J. Chen (2006b), Lithospheric thickness beneath the Dabie Shan, central eastern China from S receiver functions, *Geophys. J. Int.*, *in press*.
- Song, T.A., D.V. Helmberger, and S.P. Grand (2004), Low-velocity zone atop the 410-km seismic discontinuity in the northwestern United States, *Nature*, *427*, 530-533.
- Špičák, A., J. Horálek, A. Boušková, Č. Tomek, and J. Vaněk (1999), Magma intrusions and earthquake swarm occurrence in the western part of the Bohemian Massif, *Studia geophys. et geod.*, *43*, 87-106.
- Špičák, A. (2000), Earthquake swarms and accompanying phenomena in intraplate regions: A review, *Studia geophys. et geod.*, *44*(2), 89-106.
- Špičák, A., and J. Horálek (2001), Possible role of fluids in the process of earthquake swarm generation in the West Bohemia/Vogtland seismoactive region, *Tectonophysics*, *336*, 151-161.
- Špičáková, L., D. Uličný, and G. Koudelková (2000), Tectonosedimentary Evolution of the Cheb Basin (NW Bohemia, Czech Republic) between Late Oligocene and Pliocene: A Preliminary Note; *Studia geophys. et geod.*, *44*(4), 556-580.
- Thybo, H. (2006), The heterogeneous upper mantle low velocity zone, *Tectonophysics*, *416*, 53-79, doi:10.1016/j.tecto.2005.11.021.
- Tollmann, A. (1982), Großräumiger variszischer Deckenbau im Moldanubikum und neue Gedanken zum Varisikum Europas, *Geotekton. Forschungen*, *64*.
- Tomek, Č., V. Dvořáková, and S. Vrána (1997), Geological interpretation of the 9HR and 503M seismic profiles in Western Bohemia, in *Geological model of Western Bohemia related to the KTB borehole in Germany*, edited by S. Vrána and V. Štědrá, *J. Geol. Sci., Geology*, *47*, 43-50.
- Ulrych, J., and E. Pivec (1997), Age related Contrasting Alkaline Volcanic Series in North Bohemia, *Chem. Erde*, *57*, 311-336.
- Ulrych, J., F.E. Lloyd, and K. Balogh (2003), Age Relations and Geochemical Constraints of Cenozoic Alkaline Volcanic Series in W Bohemia: A Review, *Geolines*, *15*, 168-180.
- Vavryčuk, V. (2001), Inversion for parameters of tensile earthquakes, *J. Geophys. Res.*, *106*, 16339-16355.
- Vavryčuk, V. (2002), Non-double-couple earthquakes of January 1997 in West Bohemia, Czech Republic: Evidence of tensile faulting, *Geophys. J. Int.*, *149*, 364-373.
- Vinnik, L.P. (1977), Detection of waves converted from P to SV in the mantle, *Phys. Earth Planet Inter.*, *15*, 39-45.
- Vinnik, L., and V. Farra (2002), Subcratonic low-velocity layer and flood basalts, *Geophys. Res. Lett.*, *29*, 1049, doi:10.1029/2001GL014064.
- Vinnik, L., M.R. Kumar, R. Kind, and V. Farra (2003), Super-deep low-velocity layer beneath the Arabian plate, *Geophys. Res. Lett.*, *30*, 1415, doi:10.1029/2002GL016590.
- Vinnik, L., V. Farra, and R. Kind (2004), Deep structure of the Afro-Arabian hotspot by S receiver functions, *Geophys. Res. Lett.*, *31*, L11608, doi:10.1029/2004GL019574.
- Wagner, G.A., D.A. Coyle, J. Duyster, F. Henjes-Kunst, A. Peterek, B. Schröder, B. Stöckhert, K. Wemmer, G. Zulauf, H. Arendt, R. Bischoff, E. Hejl, J. Jacobs, D. Menzel, Nand Lal, P. Van den haute, C. Vercoutere, and B. Welzel (1997), Post-Variscan thermal and tectonic evolution of the KTB site and its surroundings, *J. Geophys. Res.*, *102*(B8), 18221-18232.

- Wagner, G.A., K. Gögen, R. Jonckheere, I. Wagner, and C. Woda (2002), Dating of Quaternary volcanoes Komorní Hůrka (Kammerbühl) and Železná Hůrka (Eisenbühl), Czech Republic, by TL, ESR, alpha-recoil and fission track chronometry, *Z. geol. Wiss.*, 30(3), 191-200.
- Walter, R. (1995), *Geologie von Mitteleuropa*, 5th edition, E. Schweizerbart'sche Verlagsbuchhandlung, Stuttgart.
- Warner, M. (1990), Basalts, water or shear zones in the lower continental crust?, *Tectonophysics*, 173, 163-174.
- Weinlich, F.H., K. Bräuer, H. Kämpf, G. Strauch, J. Tesař, and S.M. Weise (1999), An active subcontinental mantle volatile system in the western Eger rift, Central Europe: Gas flux, isotopic (He, C, and N) and compositional fingerprints, *Geochim. Cosmochim. Acta*, 63, 3653-3671.
- Weinlich, F.H., K. Bräuer, H. Kämpf, G. Strauch, J. Tesař, and S.M. Weise (2003), Gas Flux and Tectonic Structure in the Western Eger Rift, Karlovy Vary – Oberpfalz and Oberfranken, Bavaria, *Geolines*, 15, 181-187.
- Wessel, P., and W.H.F. Smith (1998), New, improved version of Generic Mapping Tools released, *EOS Trans. Am. Geophys. Union*, 79(47), 579.
- Wilde- Piórko, M., J. Saul, and M. Grad (2005), Differences in the crustal and uppermost mantle structure of the Bohemian Massif from teleseismic receiver functions, *Studia geophys. et geod.*, 49, 85-107.
- Willner, A.P., E. Sebazungu, T.V. Gerya, W.V. Maresch, and A. Krohe (2002), Numerical modelling of PT-paths related to rapid exhumation of high-pressure rocks from the crustal root in the Variscan Erzgebirge Dome (Saxony/Germany), *J. Geodyn.*, 33, 281-314.
- Wilson, M. and H. Downes (1991), Tertiary-Quaternary Extension-Related Alkaline Magmatism in Western and Central Europe, *J. Petrology*, 32, 811-849.
- Wilson, M. and H. Downes (1992), Mafic alkaline magmatism associated with the European Cenozoic rift system, *Tectonophysics*, 208, 173-182.
- Wirth, W., T. Plenefisch, K. Klinge, and K. Stammler (2000), Focal mechanisms and stress field in the region Vogtland/NW-Bohemia, *Studia geophys. et geod.*, 44(2), 126-141.
- Wittlinger, G., V. Farra, and J. Vergne (2004), Lithospheric and upper mantle stratifications beneath Tibet: New insights from Sp conversions, *Geophys. Res. Lett.*, 31, L19615, doi:10.1029/2004GL020955.
- Yamashita, T. (1999), Pore creation due to fault slip in a fluid permeated fault zone and its effect on seismicity: generation mechanism of earthquake swarm, *Pure and Applied Geophysics*, 155, 625-647.
- Yamazaki, A., and K. Hirahara (1994), The thickness of upper mantle discontinuities as inferred from short-period J-Array data, *Geophys. Res. Lett.*, 21, 1811-1814.
- Yuan, X., J. Ni, R. Kind, J. Mechie, and E. Sandvol (1997), Lithospheric and upper mantle structure of southern Tibet from a seismological passive source experiment, *J. Geophys. Res.*, 102, 27491-27500.
- Yuan, X., S.V. Sobolev, R. Kind, O. Oncken, G. Bock, G. Asch, B. Schurr, F. Graeber, A. Rudloff, W. Hanka, K. Wylegalla, R. Tibi, Ch. Haberland, A. Rietbrock, P. Giese, P. Wigger, P. Röwer, G. Zandt, S. Beck, T. Wallace, M. Pardo, and D. Comte (2000), Subduction and collision processes in the Central Andes constrained by converted seismic phases, *Nature*, 408, 958-961.
- Yuan, X., S.V. Sobolev, and R. Kind (2002), Moho topography in the central Andes and its geodynamic implications, *Earth Planet. Sci. Lett.*, 199, 389-402.

REFERENCES

- Yuan, X., R. Kind, X. Li, and R. Wang (2006), The S receiver functions: synthetics and data example, *Geophys. J. Int.*, 165(2), 555-564, doi:10.1111/j.1365-246X.2006.02885.x.
- Zandt, G., S.C. Myers, and T.C. Wallace (1995), Crust and mantle structure across the Basin and Range-Colorado Plateau boundary at 37°N latitude and implications for Cenozoic extensional mechanism, *J. Geophys. Res.*, 100, 10 529-10 548.
- Zarnek, S.E., E.M. Parmentier, and K.M. Fischer (2004), Effects of basal drag and ablation on the evolution of cratonic lithosphere, *Eos*, 85 (17), T41C-03.
- Zhu, H. and H. Kanamori (2000), Moho depth variations in southern California from teleseismic receiver functions, *J. Geophys. Res.*, 105, 2969-2980.
- Ziegler, P.A. (1992), European Cenozoic rift system, *Tectonophysics*, 208, 91-111.
- Zoback, M., and H.-P. Harjes (1997), Injection induced earthquakes and the crustal stress at 9 km depth at the KTB deep drilling site, Germany, *J. Geophys. Res.*, 102, 18477-18492.
- Zulauf, G. (1994), Ductile normal faulting along the West Bohemian shear zone (Moldanubian/Teplá-Barrandian boundary): evidence for late Variscan extensional collapse in the Variscan internides. *Geol. Rundsch.*, 83, 276-292.
- Zulauf, G. (1997), Rheological collapse of a Bohemian Tibetan plateau: The Teplá-Barrandian unit (Central European Variscides), *J. Czech Geol. Soc.*, 42(3), 79-84.
- Zulauf, G., C. Bues, W. Dörr, Z. Vejnar (2002a), 10 km Minimum throw along the West Bohemian shear zone: Evidence for dramatic crustal thickening and high topography in the Bohemian Massif (European Variscides), *Int. J. Earth Sci. (Geol. Rundsch.)*, 91, 850-864, doi:10.1007/s00531-001-0250-y.
- Zulauf, G., W. Dörr, J. Fiala, J. Kotková, H. Maluski, and P. Valverde-Vaquero (2002b), Evidence for high-temperature diffusional creep preserved by rapid cooling of lower crust (North Bohemian shear zone, Czech Republic), *Terra Nova*, 14, 343-354.
- Zulauf, G. (2005), Cadomian, Variscan and Alpine imprints in the Bohemian Massif, *Schriftenreihe der Deutschen Gesellschaft für Geowissenschaften*, 39, 425-426.

Appendices

A.1 Station parameters of the BOHEMA experiment

Parameters of BOHEMA stations used for receiver function analysis (station abbreviation, latitude, longitude and altitude) and specification of instruments (Eigenperiod T_0 , Seismometer type, operating institution, data period used for receiver function analysis). IG Prague - Geophysical Institute, CAS, Prague; EOST – Institute de Physique du Globe, Université Strasbourg; LITHOSCOPE – Université J. Fourier, Grenoble; IRSM – Institute of Rock Structure and Mechanics, CAS, Prague; GIPP – Geophysical Instrument Pool Potsdam, GFZ Potsdam; Leipzig – Institut für Geophysik und Geologie, Universität Leipzig; Jena – Institut für Geowissenschaften, Universität Jena; SZGRF – Seismological Central Observatory, Erlangen; GRSN – German Regional Seismic Network.

Station	Lat [°N]	Lon [°E]	Alt [m]	T_0 [s]	Seismometer	Institution	Data period
PRU	49.9883	14.5417	302	120	STS-2	IG_Prague	01/2001-09/2004
KHC	49.1309	13.5782	700	120	STS-2	IG_Prague	01/2001-09/2004
LAC2	50.0508	12.6250	838	120	STS-2	IG_Prague	05/2002-06/2003
NKC	50.2331	12.4479	564	120	STS-2	IG_Prague	01/2001-09/2004
PVCC	50.5282	14.5690	311	120	STS-2	IG_Prague	09/2003-09/2004
B02	49.6992	13.996	466	100	CMG-3T	IG_Prague	07/2001-02/2003
B09	50.0422	13.2930	534	30	CMG-3ESP	IG_Prague	09/2001-08/2003
B10	50.6072	13.4315	660	100	CMG-3T	IG_Prague	04/2002-02/2003
BM11	50.0382	13.8717	310	120	STS-2	IG_Prague	10/2001-05/2002
B11	50.0382	13.8717	310	120	STS-2	EOST	06/2002-12/2002
BM12	49.4673	13.8379	530	120	STS-2	IG_Prague	10/2001-05/2002
B12	49.4673	13.8379	530	60	CMG-40T	LITHOSCOPE	08/2002-01/2003
BM13	49.5285	12.9410	380	120	STS-2	IG_Prague	10/2001-05/2002
B13	49.5285	12.9410	380	120	STS-2	EOST	06/2002-12/2002
BM14	49.6811	13.4646	566	120	STS-2	IG_Prague	10/2001-05/2002
B14	49.6811	13.4646	566	60	CMG-40T	LITHOSCOPE	08/2002-01/2003
BM15	49.8718	13.5108	370	120	STS-2	IG_Prague	10/2001-05/2002
B15	49.8718	13.5108	370	60	CMG-40T	LITHOSCOPE	08/2002-12/2002
B16	50.3471	13.0187	440	20	LE3D-20	EOST	10/2001-09/2002
B17	49.7965	12.5460	713	20	LE3D-20	EOST	11/2001-09/2002
B18	50.2523	13.3695	364	30	CMG-3ES	IG_Prague	02/2002-02/2003
B19	49.2743	13.1726	570	5	S5S	IG_Prague	05/2002-04/2003
B20	49.7126	12.9962	468	30	CMG-3ES	IG_Prague	03/2002-08/2003
B21	50.4903	13.1356	718	30	CMG-40T	IRSM	08/2002-12/2002
B22	50.3326	12.6899	765	30	CMG-40T	IRSM	08/2002-12/2002
B23	50.1497	12.5365	534	30	CMG-40T	IRSM	08/2002-06/2003
B24	50.0264	12.3988	521	60	CMG-40T	LITHOSCOPE	08/2002-12/2002
B25	50.1325	12.283	502	60	CMG-40T	LITHOSCOPE	08/2002-01/2003
B26	50.1052	12.7027	726	5	LE3D-5s	LITHOSCOPE	08/2002-01/2003
B27	50.3529	13.2317	400	5	LE3D-5s	LITHOSCOPE	08/2002-01/2003
B29	49.6845	12.7000	590	1	LE3D-1s	EOST	03/2002-12/2002
B30	49.959	13.160	570	1	LE3D-1s	EOST	03/2002-12/2002
B31	49.478	13.285	380	1	LE3D-1s	EOST	03/2002-12/2002
B32	49.4393	14.1926	330	1	LE3D-1s	EOST	03/2002-12/2002
B33	49.168	13.886	510	1	LE3D-1s	EOST	03/2002-12/2002
B34	49.8776	12.7188	590	1	LE3D-1s	EOST	03/2002-12/2002
B35	49.8574	13.0340	533	1	LE3D-1s	EOST	03/2002-12/2002
B36	50.1729	13.1408	735	1	LE3D-1s	EOST	03/2002-12/2002
B37	50.0179	13.0945	666	5	LE3D-5s	LITHOSCOPE	08/2002-12/2002

continued on next page

APPENDICES

Station	Lat [°N]	Lon [°E]	Alt [m]	T ₀ [s]	Seismometer	Institution	Data period
B38	50.4003	12.7817	1049	60	CMG-40T	LITHOSCOPE	08/2002-12/2002
B39	50.2144	12.9050	661	1	LE3D-1s	EOST	03/2002-12/2002
B40	50.2513	13.7709	454	1	LE3D-1s	EOST	03/2002-12/2002
B41	50.3097	12.8324	508	5	LE3D-5s	LITHOSCOPE	08/2002-01/2003
B42	50.2917	12.9632	513	5	LE3D-5s	LITHOSCOPE	08/2002-01/2003
B43	50.1990	12.6190	438	5	LE3D-5s	LITHOSCOPE	08/2002-01/2003
B44	49.9660	12.7365	720	5	LE3D-5s	LITHOSCOPE	08/2002-01/2003
B45	49.8266	13.2757	404	5	LE3D-5s	LITHOSCOPE	08/2002-01/2003
B46	49.7481	13.6850	497	5	LE3D-5s	LITHOSCOPE	08/2002-01/2003
B47	49.6457	13.2859	363	5	LE3D-5s	LITHOSCOPE	08/2002-01/2003
B48	49.4909	13.5845	526	5	LE3D-5s	LITHOSCOPE	08/2002-01/2003
B49	50.2696	14.1591	209	5	LE3D-5s	LITHOSCOPE	08/2002-01/2003
B50	49.4788	12.7377	652	60	CMG-40T	LITHOSCOPE	08/2002-01/2003
B51	50.0258	13.5951	482	5	LE3D-5s	LITHOSCOPE	08/2002-01/2003
B52	49.8909	13.8877	473	5	LE3D-5s	LITHOSCOPE	08/2002-01/2003
B53	50.5557	13.9331	835	60	CMG-40T	LITHOSCOPE	08/2002-01/2003
WERN	50.2874	12.3761	672	5	LE3D-5s	Leipzig	03/2002-01/2004
GUNZ	50.3635	12.3316	669	5	LE3D-5s	Leipzig	02/2002-01/2004
TANN	50.416	12.460	825	120	STS-2	Leipzig	02/2002-01/2004
WERD	50.448	12.307	589	5	LE3D-5s	Leipzig	06/2002-01/2004
ROHR	50.2346	12.3168	626	30	CMG-3ESP	Leipzig	04/2002-01/2004
OTR	50.3543	12.1406	510	1	Mark L4-3D	GIPP	04/2002-12/2003
NEUB	51.1942	11.7719	.	120	CMG-3ESPD	GIPP	04/2002-01/2004
BG01	50.7086	12.8369	493	120	CMG-3ESPD	GIPP	02/2002-02/2004
BG02	50.4541	12.7523	894	120	CMG-3ESPD	GIPP	02/2002-02/2004
BG03	50.6604	10.9144	533	120/100	CMG-3ESPD/-3T	GIPP	02/2002-01/2004
BG04	50.9227	13.1248	.	120	CMG-3ESPD	GIPP	03/2002-02/2004
BG05	50.4533	11.6997	447	1	Mark L4-3D	GIPP	04/2002-10/2003
BG06	50.4268	11.0356	550	1	Mark L4-3D	GIPP	04/2002-12/2003
BG07	50.6464	12.1765	378	1	Mark L4-3D	GIPP	04/2002-02/2004
BG08	49.9380	12.3730	642	1	Mark L4-3D	GIPP	05/2002-12/2003
BG09	50.5814	11.8955	461	1	Mark L4-3D	GIPP	06/2002-12/2003
BG10	50.4589	11.9730	609	1	Mark L4-3D	GIPP	06/2002-12/2003
BG11	51.103	12.962	320	30	CMG-3ESP	Leipzig	02/2002-09/2002
BG12	49.6573	12.2322	610	120	CMG-3ESPD	GIPP	04/2002-02/2004
BG13	50.0346	12.2788	615	120	CMG-3ESPD	GIPP	03/2002-05/2003
BG14	50.6534	13.0504	590	1	Mark L4-3D	GIPP	04/2002-11/2003
BG15	50.1141	11.3824	.	1	Mark L4-3D	GIPP	05/2002-07/2003
BG16	49.8469	11.7406	550	1	Mark L4-3D	GIPP	05/2002-12/2003
BG17	49.3096	12.1982	480	1	Mark L4-3D	GIPP	05/2002-12/2003
BG18	50.1938	11.7432	620	1	Mark L4-3D	GIPP	06/2002-09/2003
BG19	50.3409	11.6927	590	1	Mark L4-3D	GIPP	06/2002-12/2003
BG20	50.8852	12.6796	.	5	Mark L4-3D	GIPP	07/2002-01/2004
BG21	50.0576	12.5474	465	1	Mark L4-3D	GIPP	04/2002-12/2003
BG22	49.9416	12.6133	700	1	Mark L4-3D	GIPP	04/2002-12/2003
BG23	49.9666	12.8779	700	120	CMG-3ESPD	GIPP	04/2002-12/2003
BG24	50.0271	12.7615	750	1	Mark L4-3D	GIPP	04/2002-12/2003
BG25	50.2830	12.6070	670	120	CMG-3ESPD	GIPP	04/2002-12/2003
BG26	50.1337	12.4583	430	1	Mark L4-3D	GIPP	04/2002-12/2003
BG28	49.5947	11.9037	510	5	LE3D-5s	Leipzig	11/2002-08/2003
BG29	50.1177	12.0189	540	120	CMG-3ESPD	GIPP	09/2002-02/2004
BG30	50.8035	13.5353	650	1/120	Mark L4-3D/ CMG-3ESPD	GIPP	07/2003-02/2004
PLN	50.4860	12.1590	414	30	CMG-3ESP	Jena	09/2002-05/2003
PST	50.8640	12.2550	270	30	CMG-40T	Jena	07/2002-05/2003
ZEU	50.6719	11.9780	331	30	CMG-3ESP	Jena	07/2002-05/2003
REU	50.8310	12.1960	454	10	CMG-40T	Jena	07/2002-05/2003
BDE	50.2885	12.2198	420	1	Mark L4-3D	Jena	08/2002-05/2003

continued on next page

Station	Lat [°N]	Lon [°E]	Alt [m]	T ₀ [s]	Seismometer	Institution	Data period
KLIN	50.3584	12.4616	640	1	Mark L4-3D	SZGRF	01/2000-05/2002
BOH1	50.1866	12.7538	500	1	Mark L4-3D	SZGRF	08/2000-10/2002
SBG	50.182	12.305	580	10	TSJ	SZGRF	05/2000-09/2002
FALK	49.8597	12.2236	460	1	Mark L4-3D	SZGRF	02/2002-10/2002
NALB	49.9812	12.4606	660	10	CMG-3ESPD	GIPP	05/2003-02/2004
REGN	50.3060	12.0606	520	30	CMG-3ESP	GIPP	01/2002-10/2003
GRA1	49.691	11.220	.	20	STS-1	SZGRF	01/1999-06/2004
GRB1	49.392	11.654	.	20	STS-1	SZGRF	01/1999-06/2004
GRC1	48.996	11.522	.	20	STS-1	SZGRF	01/1999-06/2004
WET	49.1440	12.8782	.	120	STS-2	GRSN	01/1999-06/2004
MOX	50.6447	11.6156	.	120	STS-2	GRSN	01/1999-06/2004
CLL	51.3077	13.0026	.	120	STS-2	GRSN	01/1999-06/2004
BRG	50.8732	13.9428	.	120	STS-2	GRSN	01/1999-06/2004
GEC2	48.8451	13.7016	.	120	STS-2	GRSN	01/1999-06/2004

A.2 Station parameters of the experiment by Geissler et al. (2005)

Parameters of stations by *Geissler et al. (2005)* used for receiver function analysis and specification of instruments (for explanation see appendix A.1).

Station	Lat [°N]	Lon [°E]	Alt [m]	Seismometer	Institution	Data period
CLL	51.308	13.003	230	STS-2	GRSN	1993 - 1997
BRG	50.873	13.943	296	STS-2	GRSN	1993 - 1997
MOX	50.645	11.616	455	STS-2	GRSN	1992 - 1997
WET	49.144	12.878	613	STS-2	GRSN	1991 - 1997
GRA1	49.692	11.222	500	STS-1	SZGRF	1980 - 1997
GRB1	49.391	11.652	494	STS-1	SZGRF	1980 - 1997
GRC1	48.996	11.521	512	STS-1	SZGRF	1980 - 1997
NKC	50.233	12.448	564	STS-2	IG CAS	2000 - 2003
PRU	49.988	14.542	302	CMG-3T	IG CAS	2000 - 2003
KHC	49.131	13.578	700	STS-2	IG CAS	2000 - 2003
BOH1*	50.187	12.754	420	40T/MARK/TSJ	GFZ/SZGRF	1997- 2001
BOH2*	49.967	12.874	660	GURALP-40T	GFZ/SZGRF	1997 - 1998
BOH3	49.920	12.760	610	MARK-L-4-3D	GFZ/SZGRF	1997 - 1998
BOH4	49.872	12.651	540	MARK-L-4-3D	GFZ/SZGRF	1997 - 1998
BOH5*	49.520	12.910	380?	GURALP-40T	GFZ/SZGRF	1997 - 1998
NOTT	49.811	12.122	490	STS-2	KTB/Munich	1995
FALK	49.861	12.225	465	STS-2	KTB/Munich	1995
ROTZ	49.768	12.208	430	STS-2	KTB/Munich	1995
A01	50.863	12.255	270	GURALP-3T	GFZ/SZGRF	1995 - 1996
A02	50.487	12.159	414	GURALP-3T	GFZ/SZGRF	1995 - 1996
A03	50.294	12.364	610	GURALP-3T	GFZ/SZGRF	1995 - 1996
A04	50.424	12.568	900	STS-2	GFZ/SZGRF	1995 - 1996
A05	50.187	12.104	670	3T/MARK	GFZ/SZGRF	1995 - 1996
A06	49.970	12.119	635	GURALP-3T	GFZ/SZGRF	1995 - 1996
A07	50.952	11.967	260	GURALP-3T	GFZ/SZGRF	1995 - 1996
A08	49.465	12.229	470	GURALP-3T	GFZ/SZGRF	1995 - 1996
A09	49.692	11.222	500	STS-2	GFZ/SZGRF	1995 - 1996
A10	49.599	12.258	570	GURALP-3T	GFZ/SZGRF	1995 - 1996
A11	49.656	12.233	630	STS-2	GFZ/SZGRF	1995 - 1996
A12	50.422	11.538	680	STS-2	GFZ/SZGRF	1995 - 1996
A13	49.311	12.200	460	STS-2	GFZ/SZGRF	1995 - 1996
A14	49.150	12.211	520	STS-2	GFZ/SZGRF	1995 - 1996
A15	49.213	12.205	370	STS-2	GFZ/SZGRF	1995 - 1996
A16	49.033	12.224	400	STS-2	GFZ/SZGRF	1995 - 1996
A17	48.944	12.303	330	STS-2	GFZ/SZGRF	1995 - 1996
A18	49.402	12.122	380	STS-2	GFZ/SZGRF	1995 - 1996
A19*	49.414	12.459	580	GURALP-40T	GFZ/SZGRF	1995 - 1996
A20	49.330	12.328	500	STS-2	GFZ/SZGRF	1995 - 1996
A21	50.312	12.056	530	GURALP-3T	GFZ/SZGRF	1995 - 1996
A24	49.286	12.449	530	GURALP-3T	GFZ/SZGRF	1995 - 1996
A25*	49.447	12.389	555	GURALP-40T	GFZ/SZGRF	1995 - 1996
WER	50.287	12.376	670	MARK-L-4-3D	GFZ/SZGRF	1999 - 2000
GUN	50.364	12.332	660	MARK/TSJ-10	GFZ/SZGRF	1999 - 2000
KLIN	50.358	12.462	640	MARK-L-4-3D	GFZ/SZGRF	1999 - 2001
SELB	50.154	12.179	580	MARK/TSJ-10	GFZ/SZGRF	1999 - 2001
NALB	49.981	12.461	640	MARK/STS2/ TSJ	GFZ/SZGRF	2000 - 2001
BAC	50.086	12.840	530	TSJ-10	GFZ/SZGRF	2000 - 2001
SBG	50.182	12.305	595	TSJ-10	GFZ/SZGRF	1998 - 2001
BRAU	50.082	12.087	600	MARK-L-4-3D	GFZ/SZGRF	1998 - 1999

* GURALP-40T seismometers were provided by the Dublin Institute for Advanced Studies (DIAS).

A.3 Members of the BOHEMA working group

- *Institute of Geophysics, CAS, Prague*: V. Babuška, J. Plomerová, L. Vecsey, J. Zedník, P. Jedlička, V. Vavryčuk, J. Horálek, A. Boušková, T. Fischer and B. Růžek;
- *Inst. of Rock Structure and Mechanics, CAS, Prague*: M. Brož, J. Málek;
- *Inst. of Phys. Earth, Masaryk University, Brno*: V. Nehybka;
- *Dept. of Geophysics, Charles University, Prague*: O. Novotný;
- *Institut de Physique du Globe, Univ. Strasbourg*: M. Granet, U. Achauer, T. Piquet;
- *GeoForschungsZentrum Potsdam*: R. Kind, H. Kämpf, W. Geissler, B. Heuer
- *Institut für Geophysik, Univ. Leipzig*: M. Korn, S. Wendt, S. Funke;
- *SZGRF, Erlangen*: K. Klinge, T. Plenefisch, K. Stammer, M. Lindemann;
- *Umweltforschungszentrum Leipzig-Halle*: K. Bräuer;
- *Institut für Geowissenschaften, Univ. Jena*: G. Jentzsch, P. Malischewski, M. Brunner;

B.1 Teleseismic events used for P receiver function analysis, recorded at BOHEMA stations

The following events were used for P receiver function analysis. The events written in red correspond to the operative period of the BOHEMA experiment and correspond to the red dots in Figure 3.3. The other events were recorded by permanent stations before and after the BOHEMA experiment.

Day	Month	Year	UTM Time	Lat [°]	Lon [°]	Depth [km]	Magnitude
12	JAN	1999	02:32:25.059	26.74	140.17	440	6
24	JAN	1999	00:37:04.063	30.62	131.09	33	6.4
25	JAN	1999	18:19:16.087	4.46	-75.72	17	6.4
28	JAN	1999	08:10:05.042	52.89	-169.12	67	6.6
25	FEB	1999	18:58:29.04	51.6	104.86	10	6
4	MAR	1999	05:38:26.052	28.34	57.19	33	6.6
8	MAR	1999	12:25:48.099	52.06	159.52	56	7
18	MAR	1999	17:55:43.024	41.1	142.97	41	6
20	MAR	1999	10:47:45.093	51.59	-177.67	33	7
21	MAR	1999	16:16:02.02	55.9	110.21	10	6
28	MAR	1999	19:05:11.003	30.51	79.4	15	6.6
31	MAR	1999	05:54:42.013	5.83	-82.62	10	7
8	APR	1999	13:10:34.008	43.61	130.35	565	7.1
5	MAY	1999	22:41:30.017	14.36	-94.67	33	6.3
6	MAY	1999	23:00:53.012	29.5	51.88	33	6.3
7	MAY	1999	14:13:52.036	56.42	-152.94	20	6.2
8	MAY	1999	19:44:35.095	45.45	151.63	62	6.2
12	MAY	1999	17:59:22.04	43.03	143.84	102	6.5
15	JUN	1999	20:42:05.093	18.39	-97.44	70	7
21	JUN	1999	17:43:04.052	18.32	-101.54	68	6.3
2	JUL	1999	11:45:31.029	49.37	-129.2	10	6.4
3	JUL	1999	05:30:10.009	26.32	140.48	430	6.1
7	JUL	1999	18:52:57.002	49.23	155.56	33	6.1
11	JUL	1999	14:14:16.053	15.78	-88.33	10	7
14	AUG	1999	00:16:52.029	-5.89	104.71	101	6.4
20	AUG	1999	10:02:21.01	9.04	-84.16	20	6.9
28	AUG	1999	12:40:06.019	-1.29	-77.55	196	6.3
29	AUG	1999	00:46:13.046	3.1	65.86	10	6
20	SEP	1999	17:47:18.049	23.77	120.98	33	7.7
20	SEP	1999	21:46:42.087	23.39	120.96	33	6.5
22	SEP	1999	00:14:39.015	23.73	121.17	26	6.4
25	SEP	1999	23:52:48.066	23.74	121.16	17	6.5
28	SEP	1999	05:00:42.096	54.59	168.26	33	6.2
30	SEP	1999	16:31:15.069	16.06	-96.93	60	7.5
13	OCT	1999	01:33:40.013	54.66	-161.19	30	6.4
16	OCT	1999	09:46:44.013	34.59	-116.27	0	7.4
24	OCT	1999	04:21:41.011	44.61	149.44	33	6.4
1	NOV	1999	17:53:00.012	23.38	121.52	33	6.3
8	NOV	1999	16:45:43.002	36.52	71.24	228	6.5
11	NOV	1999	02:41:05.007	49.31	155.63	33	6.4
11	NOV	1999	18:05:43.053	1.28	100.32	211	6.2
15	NOV	1999	05:42:43.022	-1.34	88.98	10	7.7
26	NOV	1999	00:29:00.027	55.13	165.36	33	6
6	DEC	1999	23:12:33.092	57.41	-154.49	66	7
11	DEC	1999	18:03:36.045	15.77	119.74	33	7.3
29	DEC	1999	05:19:46.091	18.24	-101.43	69	6.1

continued on next page

Day	Month	Year	UTM Time	Lat [°]	Lon [°]	Depth [km]	Magnitude
19	JAN	2000	07:09:33.058	36.37	70.38	206	6
20	JAN	2000	06:13:02.066	56.62	-161.87	220	6
28	JAN	2000	14:21:07.034	43.05	146.84	61	6.8
28	JAN	2000	16:39:24.028	26.08	124.5	193	6.1
12	MAR	2000	22:21:30.047	14.98	-92.44	62	6.3
28	MAR	2000	11:00:22.051	22.34	143.73	126	7.6
12	MAY	2000	23:10:29.098	35.97	70.66	107	6.3
2	JUN	2000	11:13:49.038	44.51	-130.08	10	6.5
3	JUN	2000	08:54:49.02	35.55	140.46	62	6.2
4	JUN	2000	16:28:26.017	-4.72	102.09	33	8.3
6	JUN	2000	09:58:06.077	-5.09	102.7	33	6.3
6	JUN	2000	14:57:02.022	29.42	131.42	33	6.4
7	JUN	2000	21:46:55.09	26.86	97.24	33	6.5
7	JUN	2000	23:45:26.068	-4.61	101.9	33	6.7
9	JUN	2000	08:00:24.015	-5.55	102.68	33	6
9	JUN	2000	23:31:45.029	30.49	137.73	485	6.3
10	JUN	2000	18:23:29.032	23.84	121.22	33	6.4
15	JUN	2000	11:10:46.021	29.37	132.08	10	6.1
25	JUN	2000	06:34:42.088	31.18	131.21	10	6
1	JUL	2000	07:01:55.058	34.22	139.13	10	6.8
7	JUL	2000	15:46:44.056	51.41	179.98	31	6.4
8	JUL	2000	04:52:55.041	-5.41	102.7	33	6.1
8	JUL	2000	18:57:44.047	34.05	139.13	10	6.6
10	JUL	2000	09:58:18.099	46.83	145.42	359	6.1
11	JUL	2000	01:32:28.052	57.37	-154.21	43	6.8
15	JUL	2000	01:30:30.05	34.32	139.26	10	6.1
16	JUL	2000	03:21:45.053	20.25	122.04	33	6.8
17	JUL	2000	22:53:47.03	36.28	70.92	141	6.6
20	JUL	2000	18:39:18.082	36.51	140.98	47	6.2
21	JUL	2000	01:53:35.081	9.42	-85.33	33	6.4
30	JUL	2000	12:25:45.057	33.9	139.38	10	7.1
4	AUG	2000	21:13:02.071	48.79	142.25	10	7.1
6	AUG	2000	07:27:12.09	28.86	139.56	394	7.4
9	AUG	2000	11:41:47.09	18.2	-102.48	45	6.5
19	AUG	2000	17:26:27.094	43.82	147.17	62	6
1	SEP	2000	11:56:51.083	1.44	96.59	33	6
12	SEP	2000	00:27:58.062	35.39	99.34	10	6.3
12	SEP	2000	16:27:24.058	-5.43	101.82	33	6.1
22	SEP	2000	18:22:03.015	-4.96	102.1	33	6.7
2	OCT	2000	02:25:31.031	-7.98	30.71	34	6.7
3	OCT	2000	04:13:30.049	40.28	143.12	33	6.3
5	OCT	2000	13:39:11.067	31.73	-40.96	10	6.3
6	OCT	2000	04:30:19.015	35.46	133.13	10	7.4
27	OCT	2000	04:21:51.06	26.27	140.46	388	6.3
8	NOV	2000	06:59:58.086	7.04	-77.83	17	6.5
13	NOV	2000	15:57:21.061	42.49	144.76	33	6
4	DEC	2000	04:43:09.059	14.88	-93.94	33	6.1
6	DEC	2000	17:11:06.04	39.57	54.8	30	7.5
22	DEC	2000	10:13:01.011	44.79	147.2	140	6.3
10	JAN	2001	16:02:44.023	57.08	-153.21	33	7
16	JAN	2001	13:25:09.083	-4.02	101.78	28	6.9
26	JAN	2001	03:16:40.05	23.42	70.23	16	8
1	FEB	2001	18:19:30.039	51.44	-177.8	33	6
13	FEB	2001	19:28:30.026	-4.68	102.56	36	7.4
25	FEB	2001	02:21:59.059	36.42	70.88	202	6.2
26	FEB	2001	05:58:22.043	46.81	144.52	392	6.1
28	FEB	2001	18:54:32.083	47.15	-122.73	51	6.8
23	MAR	2001	11:30:10.052	44.07	148.05	33	6

continued on next page

APPENDICES

Day	Month	Year	UTM Time	Lat [°]	Lon [°]	Depth [km]	Magnitude
24	MAR	2001	06:27:53.058	34.08	132.53	50	6.8
14	APR	2001	23:27:26.066	30.09	141.77	10	6
26	APR	2001	17:48:57.047	43.1	145.92	86	6
20	MAY	2001	04:21:43.082	18.82	-104.45	33	6.3
25	MAY	2001	00:40:50.06	44.27	148.39	33	6.7
14	JUN	2001	19:48:47.085	51.16	-179.83	18	6.5
24	JUN	2001	13:18:51.071	44.19	148.51	33	6
3	JUL	2001	13:10:42.06	21.64	142.98	290	6.5
28	JUL	2001	07:32:43.001	59.03	-155.12	131	6.8
2	AUG	2001	23:41:06.017	56.26	163.79	14	6.3
13	AUG	2001	20:11:23.04	41.05	142.31	38	6.4
25	AUG	2001	02:02:02.05	7.63	-82.77	24	6.1
2	SEP	2001	02:25:54.009	0.89	82.5	10	6.1
7	SEP	2001	02:45:59.00	-13.17	97.3	10	6.2
12	SEP	2001	22:23:44.009	27.69	141.91	33	6
14	SEP	2001	04:45:08.00	48.69	-128.71	10	6
22	SEP	2001	03:23:38.022	3.87	-75.97	178	6
8	OCT	2001	18:14:26.044	52.59	160.32	48	6.5
8	OCT	2001	18:20:38.025	52.63	160.21	33	6.4
9	OCT	2001	23:53:37.003	47.76	155.1	33	6.5
12	OCT	2001	05:02:34.00	52.63	-132.2	20	6.1
9	NOV	2001	00:47:55.002	9.64	-82.3	10	6.1
14	NOV	2001	09:26:10.001	35.95	90.54	10	8
15	NOV	2001	01:03:06.006	-1.59	-15.58	10	6.3
23	NOV	2001	20:43:03.055	36.39	71.51	106	6.1
28	NOV	2001	14:32:32.072	15.57	-93.11	84	6.4
2	DEC	2001	13:01:53.067	39.4	141.09	123	6.5
8	DEC	2001	20:29:34.023	28.25	129.57	33	6.2
18	DEC	2001	04:02:58.028	23.95	122.73	14	7.3
3	JAN	2002	07:05:27.067	36.09	70.69	129	6.2
16	JAN	2002	23:09:52.008	15.5	-93.13	80	6.4
1	FEB	2002	21:55:20.099	45.46	136.72	355	6.2
3	MAR	2002	12:08:19.074	36.5	70.48	225	7.4
25	MAR	2002	14:56:33.082	36.06	69.32	8	6.2
26	MAR	2002	03:45:48.07	23.35	124.09	33	6.6
31	MAR	2002	06:52:50.049	24.28	122.18	32	7.4
12	APR	2002	04:00:23.074	35.96	69.42	10	5.9
14	APR	2002	02:04:21.014	38.53	73.4	117	5.5
26	APR	2002	07:15:11.05	53.51	160.63	62	5.9
3	MAY	2002	11:20:51.054	86	31.59	10	5.4
8	MAY	2002	19:45:18.086	53.81	160.77	39	5.9
12	MAY	2002	01:29:35.044	39.22	140.99	95	5.3
21	MAY	2002	20:04:16.016	44.43	146.62	149	5.5
25	MAY	2002	05:36:31.097	53.81	-161.12	33	6.5
28	MAY	2002	16:45:17.01	24.07	122.26	33	6.1
31	MAY	2002	06:09:20.09	52.81	171.79	33	5.5
12	JUN	2002	19:52:47.036	-0.68	-20.72	10	5.5
16	JUN	2002	02:46:14.003	8.78	-83.99	35	6.4
22	JUN	2002	02:58:21.03	35.63	49.05	10	6.5
28	JUN	2002	17:19:30.027	43.75	130.67	566	7.3
11	JUL	2002	07:36:26.006	24.08	122.29	43	5.8
13	JUL	2002	20:06:27.054	30.8	69.98	33	5.8
17	JUL	2002	02:20:33.083	48.52	153.26	147	5.6
23	JUL	2002	20:05:31.088	37.25	142.22	33	5.7
25	JUL	2002	12:31:01.044	43.66	147.55	33	5.7
31	JUL	2002	00:16:44.061	7.93	-82.79	10	6.5
2	AUG	2002	23:11:39.013	29.28	138.97	426	6.3
7	AUG	2002	23:59:14.054	7.85	-82.89	10	6

continued on next page

Day	Month	Year	UTM Time	Lat [°]	Lon [°]	Depth [km]	Magnitude
20	AUG	2002	10:59:32.002	30.99	141.97	9	6.3
24	AUG	2002	18:40:53.044	43.11	146.12	42	6.2
28	AUG	2002	17:05:33.085	22.11	121.58	33	5.7
30	AUG	2002	05:58:21.005	44.48	149.08	31	5.7
31	AUG	2002	05:27:18.024	2.71	-84.38	23	5.7
1	SEP	2002	17:14:59.089	14.28	51.94	10	6
5	SEP	2002	11:03:05.085	39.77	72.01	31	5.3
11	SEP	2002	04:50:32.086	83.14	-6.08	10	5.6
13	SEP	2002	22:28:29.046	13.04	93.07	21	6.7
14	SEP	2002	19:58:36.095	13.06	93.16	33	5.8
15	SEP	2002	08:39:32.07	44.83	129.92	586	6.4
26	SEP	2002	12:55:29.078	-19.65	-12.01	10	5.7
12	OCT	2002	20:09:11.046	-8.3	-71.74	534	6.9
14	OCT	2002	14:12:43.075	41.17	142.25	61	6.1
16	OCT	2002	10:12:21.043	51.95	157.32	102	6.2
19	OCT	2002	12:09:05.038	44.3	149.96	33	6.4
23	OCT	2002	11:27:19.043	63.51	-147.91	4	6.7
24	OCT	2002	06:08:37.098	-1.88	29	11	6.3
24	OCT	2002	21:53:43.019	6.03	94.42	64	6.2
2	NOV	2002	01:26:10.07	2.82	96.08	30	7.6
2	NOV	2002	09:46:46.07	2.95	96.39	27	6.4
3	NOV	2002	03:37:42.007	38.89	141.98	39	6.4
3	NOV	2002	22:12:41.00	63.52	-147.44	4	8.5
16	NOV	2002	12:06:25.017	50.38	156.56	96	5.6
17	NOV	2002	04:53:53.054	47.82	146.21	459	7.3
20	NOV	2002	21:32:30.081	35.41	74.51	33	6.5
26	NOV	2002	00:48:15.004	51.47	-173.54	20	6.1
28	DEC	2002	09:36:08.048	51.43	-168.53	10	5.8
22	JAN	2003	02:06:34.061	18.77	-104.1	24	7.6
6	FEB	2003	18:48:40.006	43.29	148.09	49	5.3
19	FEB	2003	03:32:36.036	53.65	-164.64	19	6.6
24	FEB	2003	02:03:41.045	39.61	77.23	11	6.4
2	MAR	2003	22:46:46.084	37.68	141.72	42	5.8
15	MAR	2003	19:41:28.07	52.25	160.39	30	6.1
17	MAR	2003	16:36:17.031	51.27	177.98	33	7.1
26	MAR	2003	04:22:30.007	12.52	92.56	33	5.9
2	APR	2003	03:43:11.058	35.28	-35.73	10	6.3
17	APR	2003	00:48:38.058	37.53	96.48	14	6.4
24	APR	2003	10:56:21.098	48.76	154.99	43	6.1
29	APR	2003	13:53:17.03	43.71	147.8	62	6
12	MAY	2003	03:03:05.041	1.17	98.95	78	5.7
14	MAY	2003	06:03:35.086	18.27	-58.63	41	6.7
22	MAY	2003	18:11:53.037	42.86	72.81	10	5.3
26	MAY	2003	09:24:33.04	38.85	141.57	68	7
28	MAY	2003	16:15:18.094	-17.65	66.12	10	6.2
10	JUN	2003	08:40:30.083	23.52	121.63	44	6
15	JUN	2003	19:24:33.015	51.55	176.92	20	6.5
16	JUN	2003	22:08:02.014	55.49	160	174	6.9
20	JUN	2003	06:19:38.091	-7.61	-71.72	558	7.1
23	JUN	2003	12:12:34.047	51.44	176.78	20	7
25	JUL	2003	22:13:29.097	38.42	141	6	6.1
27	JUL	2003	06:25:31.095	47.15	139.25	470	6.8
11	AUG	2003	21:22:30.042	12.12	93.53	100	6
25	AUG	2003	06:28:35.018	14.03	-91.07	100	6
31	AUG	2003	23:08:00.026	43.39	132.27	481	6.2
1	SEP	2003	23:16:35.005	38.6	75.32	10	6
21	SEP	2003	18:16:13.041	19.92	95.67	10	6.9
22	SEP	2003	04:45:36.024	19.78	-70.67	10	6.6

continued on next page

APPENDICES

Day	Month	Year	UTM Time	Lat [°]	Lon [°]	Depth [km]	Magnitude
25	SEP	2003	19:50:06.036	41.81	143.91	27	8.3
26	SEP	2003	20:38:22.01	41.99	144.58	33	6
27	SEP	2003	11:33:25.008	50.04	87.81	16	7.5
27	SEP	2003	18:52:46.098	50.09	87.76	10	6.6
29	SEP	2003	02:36:53.014	42.45	144.38	25	6.5
1	OCT	2003	01:03:25.024	50.21	87.72	10	7.1
8	OCT	2003	09:06:55.034	42.65	144.57	32	6.7
28	OCT	2003	21:48:21.001	43.84	147.75	65	6.1
31	OCT	2003	01:06:28.028	37.81	142.62	10	7
5	NOV	2003	00:58:51.011	4.97	-77.77	33	6
9	NOV	2003	19:52:36.082	-0.67	-19.69	10	6.6
12	NOV	2003	08:26:43.074	33.17	137.07	384	6.4
17	NOV	2003	06:43:06.08	51.15	178.65	33	7.8
18	NOV	2003	17:14:22.062	12.02	125.42	35	6.5
1	DEC	2003	01:38:31.096	42.9	80.51	10	6
5	DEC	2003	21:26:09.048	55.54	165.78	10	6.7
9	DEC	2003	12:44:01.068	51.33	-179.27	33	6.2
10	DEC	2003	04:38:11.059	23.04	121.36	10	6.8
22	DEC	2003	19:15:56.00	35.71	-121.1	7	6.5
26	DEC	2003	01:56:52.044	29	58.31	10	6.8
22	FEB	2004	06:46:27.004	-1.56	100.49	42	6.3
8	MAR	2004	23:39:11.034	10.48	-43.92	10	6.1
27	MAR	2004	18:47:29.02	33.95	89.18	8	6
3	APR	2004	23:02:00.087	36.43	141.01	31	6
5	APR	2004	21:24:04.00	36.51	71.03	187	6.6
11	APR	2004	18:06:12.048	42.92	144.84	41	6.1
14	APR	2004	01:54:09.022	55.23	162.66	51	6.2
29	APR	2004	00:57:21.008	10.81	-86	10	6.2
11	MAY	2004	08:28:48.028	0.41	97.82	21	6.2
19	MAY	2004	07:04:11.071	22.66	121.5	20	6.2
28	MAY	2004	12:38:44.027	36.25	51.62	17	6.4
29	MAY	2004	20:56:09.06	34.25	141.41	16	6.6
10	JUN	2004	15:19:57.075	55.68	160	188	6.9
28	JUN	2004	09:49:47.00	54.8	-134.25	20	6.8

B.2 Teleseismic events used for P receiver function analysis, recorded at stations by Geissler et al. (2005)

The following events recorded during the experiment by *Geissler et al. (2005)* were used for *P* receiver function analysis of the mantle transition zone. Events between 1980-1991 were recorded only by stations GRA1, GRB1 and GRC1. Temporary stations operated between 1995-1996.

Day	Month	Year	UTM Time	Lat [°]	Lon [°]	Depth [km]	Magnitude
19	JAN	1980	07:02:35.00	51.317	-178.488	50	5.8
15	FEB	1980	14:25:48.90	44.533	149.739	35	5.8
22	FEB	1980	03:02:47.20	30.506	88.583	33	5.8
23	FEB	1980	05:51:03.20	43.53	146.753	44	6.3
23	FEB	1980	22:38:53.50	43.243	146.9	45	5.9
26	MAR	1980	20:43:37.90	23.867	-45.558	10	5.9
31	MAR	1980	07:32:31.80	35.448	135.473	359	5.8
31	MAR	1980	12:41:47.70	16.129	121.962	43	5.9
3	MAY	1980	09:30:08.50	51.233	173.679	33	5.8
8	MAY	1980	08:03:37.60	34.419	140.25	62	5.8
25	MAY	1980	16:33:44.70	37.6	-118.84	5	6.1
29	JUN	1980	07:20:05.50	34.808	139.181	15	5.8
29	JUL	1980	14:58:40.80	29.598	81.092	18	6.1
30	JUL	1980	06:56:16.70	5.276	-82.665	10	5.8
24	SEP	1980	17:54:24.10	35.45	139.964	73	6
24	OCT	1980	14:53:35.10	18.211	-98.24	72	6.4
26	OCT	1980	05:14:19.10	11.751	125.502	48	6
4	NOV	1980	20:26:00.70	53.817	160.741	33	5.9
8	NOV	1980	10:27:34.00	41.117	-124.253	19	6.2
31	DEC	1980	10:32:11.00	46.06	151.453	33	6.1
18	JAN	1981	18:11:28.40	38.58	142.82	33	5.9
18	JAN	1981	18:17:24.40	38.64	142.75	33	6.1
22	JAN	1981	19:34:40.10	38.215	142.672	20	6.1
23	JAN	1981	04:58:31.50	42.524	142.122	116	6.3
23	JAN	1981	10:22:34.90	38.149	142.775	33	5.8
30	JAN	1981	08:52:44.10	51.744	176.274	33	6.3
19	FEB	1981	19:36:11.60	44.639	149.342	33	5.9
8	APR	1981	23:42:47.90	45.667	152.32	33	5.9
2	MAY	1981	16:04:55.60	36.355	71.085	229	6.3
6	MAY	1981	21:36:06.80	-1.886	-80.885	33	6
8	MAY	1981	23:34:44.90	42.66	139.129	200	6
3	JUN	1981	05:47:44.44	-35.56	-17.04	10	5.8
11	JUN	1981	07:24:25.23	29.913	57.715	33	6.1
23	AUG	1981	12:00:26.55	48.718	157.39	40	6
3	SEP	1981	05:35:44.80	43.621	147.031	45	6.6
4	SEP	1981	11:15:13.61	9.964	124.035	644	6
12	SEP	1981	07:15:54.17	35.693	73.594	33	6.2
13	SEP	1981	09:19:30.90	24.866	-46.301	10	5.8
14	SEP	1981	12:44:29.80	18.32	-68.891	170	5.9
1	OCT	1981	17:04:44.92	50.733	160.429	33	5.9
15	OCT	1981	01:47:52.97	40.229	142.287	47	6
25	OCT	1981	03:22:15.57	18.048	-102.084	33	6.2
22	NOV	1981	15:05:20.56	18.752	120.839	24	6.2
27	NOV	1981	17:21:45.80	42.913	131.076	543	5.8
12	DEC	1981	04:52:37.16	23.932	125.856	10	6.1
11	JAN	1982	06:10:06.49	13.752	124.358	45	6
23	JAN	1982	17:37:30.26	31.696	82.246	33	6

continued on next page

APPENDICES

Day	Month	Year	UTM Time	Lat [°]	Lon [°]	Depth [km]	Magnitude
20	FEB	1982	19:18:20.24	33.579	140.999	18	6.2
6	APR	1982	19:56:53.45	14.315	-92.082	64	6
17	APR	1982	09:20:57.86	19.871	120.526	10	6.2
24	MAY	1982	07:25:32.34	48.826	154.969	29	5.9
29	MAY	1982	12:21:08.39	42.812	143.164	75	5.8
31	MAY	1982	10:21:15.01	55.138	165.401	33	6
4	JUN	1982	03:01:04.12	51.597	-177.333	58	5.8
7	JUN	1982	06:52:37.37	16.607	-98.149	40	6
7	JUN	1982	10:59:40.16	16.558	-98.358	33	6.3
19	JUN	1982	06:21:58.00	13.313	-89.339	81	6.2
30	JUN	1982	01:57:34.15	44.679	151.143	33	6.6
1	JUL	1982	07:41:53.26	51.426	-179.943	47	6.3
4	JUL	1982	01:17:14.47	49.995	78.856	0	6.1
4	JUL	1982	01:20:06.80	27.929	136.967	536	6.3
23	JUL	1982	14:23:53.57	36.194	141.702	36	6.2
31	JUL	1982	06:29:15.52	51.755	176.137	37	6.2
19	AUG	1982	15:59:01.53	6.718	-82.68	10	6.2
3	SEP	1982	01:32:00.28	43.913	148.478	33	6
6	SEP	1982	01:47:02.73	29.325	140.36	175	6.5
16	DEC	1982	00:40:48.72	36.148	69.011	36	6.2
24	JAN	1983	08:17:39.61	16.146	-95.232	56	6.3
24	JAN	1983	23:09:21.43	12.942	93.582	78	6.1
14	FEB	1983	03:20:04.47	54.931	-159.189	47	5.9
14	FEB	1983	08:10:03.61	54.969	-159.236	33	6
26	FEB	1983	07:10:59.16	49.243	155.601	56	6
27	FEB	1983	12:14:20.77	35.869	139.916	78	5.9
10	MAR	1983	00:27:48.36	43.813	147.397	33	6.2
3	APR	1983	02:50:01.18	8.717	-83.123	37	6.5
4	APR	1983	02:51:34.36	5.723	94.722	78	6.6
4	APR	1983	19:04:20.64	52.931	159.858	38	6
4	APR	1983	23:12:47.19	49.408	155.602	51	6.1
8	APR	1983	02:28:25.58	11.429	57.52	10	5.9
11	APR	1983	08:18:10.12	10.419	-62.764	40	6
12	APR	1983	12:07:54.52	-4.843	-78.103	104	6.5
18	APR	1983	10:58:51.26	27.793	62.054	64	6.5
30	APR	1983	14:03:49.23	41.473	143.764	30	6.5
1	MAY	1983	18:10:40.39	46.353	153.453	24	6.1
2	MAY	1983	23:42:37.76	36.219	-120.317	10	6.2
29	MAY	1983	04:45:41.02	49.246	155.366	46	5.8
8	AUG	1983	03:47:57.16	35.498	139.069	24	5.9
17	AUG	1983	10:55:54.13	55.867	161.287	62	6.6
25	AUG	1983	20:23:33.32	33.509	131.484	126	6.1
7	SEP	1983	19:22:05.15	60.976	-147.5	45	6.2
12	SEP	1983	15:42:08.55	36.502	71.082	208	6.1
21	SEP	1983	19:20:42.46	24.095	122.148	28	6
28	OCT	1983	14:06:06.61	44.058	-113.857	10	6.2
20	NOV	1983	00:44:43.56	43.706	148.444	29	5.9
22	NOV	1983	14:21:03.08	0.482	-79.877	54	6.3
30	NOV	1983	02:56:47.28	41.79	142.772	56	5.8
30	NOV	1983	17:46:00.67	-6.852	72.11	10	6.6
2	DEC	1983	03:09:05.66	14.066	-91.924	67	5.9
3	DEC	1983	17:43:14.84	-6.463	71.417	10	6.3
22	DEC	1983	04:11:29.23	11.866	-13.529	11	6.4
30	DEC	1983	23:52:39.93	36.372	70.738	214	6.6
1	FEB	1984	07:28:28.70	49.063	146.59	573	5.9
1	FEB	1984	14:22:07.90	34.616	70.484	33	5.9
16	FEB	1984	17:18:41.61	36.431	70.826	207	6.1
6	MAR	1984	02:17:21.26	29.384	138.935	457	6.2

continued on next page

Day	Month	Year	UTM Time	Lat [°]	Lon [°]	Depth [km]	Magnitude
19	MAR	1984	20:28:38.24	40.32	63.35	14	6.5
21	MAR	1984	02:44:24.35	49.176	155.385	40	6
24	MAR	1984	09:44:02.60	44.117	148.192	44	6.1
20	APR	1984	06:31:10.63	50.12	148.745	582	6
22	APR	1984	06:14:21.58	-0.541	-19.857	10	5.8
23	APR	1984	21:40:35.51	47.45	146.692	414	6
24	APR	1984	04:11:29.09	30.909	138.431	403	6.1
26	APR	1984	10:11:10.28	-6.825	71.495	10	6
24	JUN	1984	11:17:11.92	17.984	-69.338	23	6
1	JUL	1984	10:12:20.95	36.471	70.906	203	5.8
2	JUL	1984	04:50:44.13	16.804	-98.441	46	5.9
14	JUL	1984	01:09:10.57	49.891	78.963	0	6.2
19	JUL	1984	23:25:12.88	28.106	129.524	47	6.1
28	AUG	1984	19:04:30.56	27.431	128.524	57	5.9
10	SEP	1984	03:14:10.10	40.503	-126.831	10	6.1
13	SEP	1984	23:48:49.97	35.789	137.488	10	6
18	SEP	1984	17:02:44.31	34.006	141.5	47	6.6
13	OCT	1984	17:18:13.83	15.024	-94.304	31	6.1
26	OCT	1984	20:22:21.83	39.155	71.328	33	6
1	NOV	1984	04:48:50.27	8.185	-38.794	10	6.5
1	NOV	1984	18:43:44.12	55.209	163.692	49	5.8
6	NOV	1984	07:58:51.32	-18.876	67.352	10	6.2
17	NOV	1984	06:49:30.02	0.197	98.027	33	6.3
3	DEC	1984	04:08:35.10	44.212	148.138	64	6.4
16	DEC	1984	03:55:02.75	49.957	78.862	0	6.1
28	DEC	1984	10:37:53.76	56.194	163.46	33	6.2
28	FEB	1985	20:53:47.86	27.462	128.449	60	5.9
6	MAR	1985	22:31:53.27	55.241	162.043	47	5.8
16	MAR	1985	14:54:00.72	17.013	-62.448	13	6.3
27	MAR	1985	12:48:12.35	44.335	146.666	154	5.9
28	MAR	1985	16:07:06.84	40.31	140.362	166	6.1
10	APR	1985	16:26:20.57	29.962	138.927	420	5.8
23	APR	1985	16:15:12.02	15.344	120.61	188	6.3
1	MAY	1985	13:27:56.14	-9.196	-71.23	599	6
2	MAY	1985	08:55:16.31	48.871	156.329	43	5.9
14	MAY	1985	13:24:57.83	-10.61	41.423	10	6
14	MAY	1985	18:11:08.95	-10.562	41.424	10	6.4
19	MAY	1985	08:07:48.21	53.611	160.526	62	6.1
24	MAY	1985	22:04:43.41	51.422	-178.43	34	5.8
25	MAY	1985	23:29:21.72	54.055	160.992	45	5.9
6	JUN	1985	02:40:12.95	0.932	-28.432	10	6.3
15	JUN	1985	00:57:00.79	49.889	78.881	0	6
17	JUN	1985	19:12:38.86	30.276	132.681	26	5.8
30	JUN	1985	02:39:02.79	49.861	78.696	0	6
29	JUL	1985	07:54:44.07	36.19	70.896	98	6.6
2	AUG	1985	07:46:53.30	36.174	70.78	120	6.1
9	AUG	1985	19:59:44.07	16.9	120.186	21	5.8
11	AUG	1985	09:59:44.16	54.139	168.731	50	5.9
12	AUG	1985	03:49:18.09	37.771	141.773	51	6
23	AUG	1985	12:41:56.16	39.431	75.224	6	6.4
11	SEP	1985	20:45:49.54	39.356	75.407	15	5.8
19	SEP	1985	13:17:47.35	18.19	-102.533	27	6.8
21	SEP	1985	01:37:13.47	17.802	-101.647	30	6.3
5	OCT	1985	15:24:02.27	62.237	-124.266	10	6.5
9	OCT	1985	09:33:32.48	54.765	-159.613	30	6.2
18	OCT	1985	04:19:06.40	46.323	146.272	271	5.9
29	OCT	1985	13:13:44.62	36.681	54.75	52	6
31	OCT	1985	19:33:06.56	53.249	-166.936	30	5.8

continued on next page

APPENDICES

Day	Month	Year	UTM Time	Lat [°]	Lon [°]	Depth [km]	Magnitude
23	DEC	1985	05:16:03.33	62.222	-124.239	6	6.4
3	FEB	1986	20:47:35.34	27.791	139.552	508	5.8
12	FEB	1986	02:59:30.42	36.384	141.128	30	6.1
7	APR	1986	22:43:29.60	15.54	-94.423	48	5.8
16	APR	1986	12:52:16.07	43.89	147.57	23	6.3
30	APR	1986	07:07:18.12	18.404	-102.973	26	6.2
2	MAY	1986	10:30:02.85	55.172	163.843	14	6
7	MAY	1986	20:43:31.26	51.384	-174.809	22	6.1
7	MAY	1986	22:47:10.87	51.52	-174.776	33	6.4
8	MAY	1986	04:03:50.08	51.14	-176.442	33	5.8
8	MAY	1986	05:37:20.26	51.336	-175.363	18	6
9	MAY	1986	19:04:28.42	51.46	-174.243	33	5.8
11	MAY	1986	01:24:25.79	26.743	125.205	193	5.9
16	MAY	1986	16:51:12.31	47.204	154.109	24	5.8
17	MAY	1986	16:20:22.23	52.327	-174.504	26	5.8
20	MAY	1986	05:25:46.96	24.125	121.619	19	6.1
21	MAY	1986	05:47:10.87	43.684	148.416	39	6.1
8	JUN	1986	11:02:25.87	43.269	146.491	56	6
11	JUN	1986	13:48:01.39	10.597	-62.928	18	6
17	JUN	1986	00:42:35.40	53.88	160.388	33	5.9
19	JUN	1986	09:09:09.21	56.331	-152.914	16	6
19	JUN	1986	18:12:27.84	7.799	94.517	164	5.9
20	JUN	1986	17:12:46.94	31.24	86.847	33	5.9
24	JUN	1986	02:53:11.25	34.794	140.595	62	6.1
6	JUL	1986	19:24:22.99	34.424	80.161	9	5.8
7	JUL	1986	16:26:56.61	10.389	56.832	7	6.4
8	JUL	1986	09:20:44.50	34	-116.61	12	5.8
13	JUL	1986	09:12:10.71	16.061	-93.901	80	5.9
18	JUL	1986	17:22:38.24	10.77	-69.428	7	5.9
19	JUL	1986	05:59:36.21	47.264	151.127	141	5.9
21	JUL	1986	14:42:26.60	37.537	-118.447	9	6
26	AUG	1986	09:43:00.39	37.724	101.496	8	6.2
15	SEP	1986	21:42:29.29	36.714	71.092	88	5.8
17	SEP	1986	21:25:15.06	10.497	56.983	10	5.8
14	NOV	1986	21:20:10.55	23.901	121.574	33	6.3
5	JAN	1987	12:11:55.77	52.448	-169.381	33	6.1
9	JAN	1987	06:14:44.87	39.895	141.677	67	6.4
14	JAN	1987	11:03:48.75	42.565	142.85	102	6.5
24	JAN	1987	08:09:21.30	41.529	79.318	28	5.9
18	FEB	1987	00:00:52.54	51.298	-179.279	33	6.2
27	FEB	1987	08:31:54.40	53.47	-167.291	10	6.2
3	MAR	1987	01:32:12.31	46.347	152.013	96	5.8
6	MAR	1987	01:54:50.49	0.048	-77.653	14	6.1
6	MAR	1987	04:10:41.96	0.151	-77.821	10	6.5
18	MAR	1987	03:36:30.33	32.034	131.837	54	6.4
21	MAR	1987	10:41:35.97	52.056	-177.547	93	6
22	MAR	1987	02:49:15.90	51.594	-173.574	19	5.9
7	APR	1987	00:40:43.40	37.363	141.796	29	6.4
22	APR	1987	20:13:23.15	37.155	141.573	30	6.1
25	APR	1987	12:16:52.44	16.066	120.301	107	6.3
25	APR	1987	19:22:07.20	2.244	98.866	11	5.9
29	APR	1987	01:45:22.63	27.437	56.109	8	5.9
5	MAY	1987	15:40:47.52	36.48	70.673	202	5.8
6	MAY	1987	04:06:14.15	51.272	-179.898	20	6.3
7	MAY	1987	03:05:49.17	46.736	139.232	430	6
18	MAY	1987	03:07:34.13	49.282	147.693	542	6.1
5	JUN	1987	04:59:58.39	41.584	88.737	0	6.2
7	JUN	1987	05:49:43.63	20.429	121.366	14	5.8

continued on next page

Day	Month	Year	UTM Time	Lat [°]	Lon [°]	Depth [km]	Magnitude
20	JUN	1987	00:53:04.83	49.913	78.735	0	6.1
21	JUN	1987	05:46:10.01	54.211	-162.601	33	6.2
3	JUL	1987	10:10:43.78	31.196	130.322	168	5.8
6	JUL	1987	00:23:25.65	51.508	-174.721	33	5.8
10	JUL	1987	18:49:53.91	55.137	165.525	33	6.1
15	JUL	1987	07:16:13.55	17.522	-97.153	67	5.9
4	SEP	1987	04:27:08.88	49.293	156.41	33	5.9
23	SEP	1987	07:15:43.25	45.96	149.519	130	5.9
3	OCT	1987	11:00:05.29	36.454	71.437	95	5.9
4	OCT	1987	18:34:22.61	55.585	161.623	53	6
6	OCT	1987	20:11:35.14	52.956	159.972	33	6.1
18	NOV	1987	16:27:05.27	12.845	124.77	22	5.9
24	NOV	1987	13:15:56.40	33.01	-115.84	2	6
30	NOV	1987	19:23:19.59	58.679	-142.786	10	6.7
12	DEC	1987	04:51:50.51	29.692	140.025	164	6.3
17	DEC	1987	02:08:19.92	35.362	140.214	62	6
18	DEC	1987	16:24:03.05	28.191	56.677	19	5.8
7	FEB	1988	18:15:05.63	50.785	173.465	33	6.2
16	FEB	1988	04:22:36.16	51.564	175.041	33	5.9
24	FEB	1988	03:52:03.29	13.477	124.616	24	6
26	FEB	1988	06:17:31.53	-37.319	47.989	10	6.1
29	FEB	1988	05:31:41.47	55.149	167.43	33	6.1
6	MAR	1988	22:35:38.14	56.953	-143.032	10	6.8
10	MAR	1988	06:17:23.31	10.402	-60.587	56	6.2
21	MAR	1988	23:31:21.68	77.601	125.451	10	6
25	MAR	1988	19:36:46.47	62.154	-124.182	10	6.1
3	APR	1988	01:33:05.85	49.917	78.945	0	6.1
3	APR	1988	14:27:09.04	4.687	94.419	30	5.9
7	MAY	1988	01:59:26.24	42.601	143.751	72	6.1
20	MAY	1988	14:58:43.53	8.116	-38.413	10	5.8
18	JUN	1988	22:49:42.37	26.856	-110.996	10	5.9
21	JUN	1988	06:26:16.64	24.878	-45.867	25	5.9
24	JUN	1988	08:57:53.33	10.209	-60.559	38	6
6	JUL	1988	15:54:19.14	41.744	144.199	30	5.9
20	JUL	1988	23:15:36.65	23.902	121.598	50	5.8
30	JUL	1988	21:07:21.16	44.771	149.89	61	6.3
31	JUL	1988	15:22:48.79	-31.891	57.448	10	5.8
6	AUG	1988	00:36:24.65	25.149	95.127	90	6.8
6	AUG	1988	09:03:21.95	36.461	71.043	195	6.1
20	AUG	1988	23:09:09.56	26.755	86.616	57	6.4
7	SEP	1988	11:53:24.13	30.245	137.431	485	6.1
21	SEP	1988	09:58:53.57	46.187	152.205	51	5.9
6	NOV	1988	13:03:19.34	22.789	99.611	17	6.1
15	NOV	1988	08:41:42.35	52.109	-171.103	22	5.9
22	JAN	1989	22:20:17.97	41.806	144.282	25	6
10	MAR	1989	21:49:45.86	-13.702	34.42	30	6.2
11	APR	1989	03:56:36.91	49.488	159.185	16	6.3
15	APR	1989	20:34:08.93	29.987	99.195	13	6.2
20	APR	1989	22:59:54.07	57.166	121.976	26	6.1
25	APR	1989	02:13:20.83	30.048	99.419	7	6.2
25	APR	1989	14:29:00.51	16.773	-99.328	19	6.2
30	APR	1989	08:22:54.01	10.96	-68.325	20	5.9
3	MAY	1989	05:53:01.17	30.091	99.475	14	6.1
3	MAY	1989	15:41:30.88	30.053	99.499	7	5.8
5	MAY	1989	18:28:39.45	-8.281	-71.381	593	6.4
19	MAY	1989	02:21:56.38	54.305	-165.574	104	6.1
24	MAY	1989	13:31:14.48	56.177	164.264	18	5.9
11	JUN	1989	13:24:32.07	35.107	-35.008	9	5.8

continued on next page

APPENDICES

Day	Month	Year	UTM Time	Lat [°]	Lon [°]	Depth [km]	Magnitude
12	JUN	1989	00:04:09.76	21.861	89.763	5	6.1
16	JUN	1989	10:51:21.56	57.755	-153.992	58	5.8
16	JUN	1989	23:42:35.12	31.807	137.982	359	5.9
25	JUN	1989	20:37:32.46	1.134	-79.616	15	5.9
24	JUL	1989	03:27:48.77	36.085	71.069	95	5.8
3	AUG	1989	11:31:20.43	23.043	121.965	10	5.9
20	AUG	1989	11:16:56.51	11.766	41.942	11	5.8
20	AUG	1989	19:25:56.51	11.904	41.824	11	6.2
21	AUG	1989	01:09:06.63	11.874	41.87	15	6.3
21	AUG	1989	05:03:05.60	11.942	41.769	9	5.8
30	AUG	1989	11:38:12.76	55.609	161.358	73	5.8
4	SEP	1989	13:14:58.25	55.543	-156.835	11	6.5
9	SEP	1989	01:40:35.77	2.435	-79.761	6	6
16	SEP	1989	23:20:53.22	16.497	-93.671	108	6
22	SEP	1989	02:25:50.88	31.583	102.433	14	6.1
7	OCT	1989	15:48:29.06	51.314	-179.028	19	6.1
18	OCT	1989	00:04:15.24	37.036	-121.883	18	6.5
26	OCT	1989	17:06:41.62	39.812	143.539	8	5.8
27	OCT	1989	01:45:55.08	39.823	143.692	9	5.8
29	OCT	1989	05:25:38.27	39.571	143.333	9	6
17	APR	1990	01:59:33.40	39.436	74.9	33	6
26	APR	1990	09:37:15.04	35.986	100.245	8	6.5
28	APR	1990	01:23:11.51	8.887	-83.5	22	5.9
1	MAY	1990	16:12:21.44	58.84	-156.858	211	6.1
8	MAY	1990	00:01:40.02	6.905	-82.622	9	6.2
12	MAY	1990	04:50:08.71	49.037	141.847	605	6.5
15	MAY	1990	14:25:20.69	36.043	70.428	113	5.9
17	MAY	1990	23:28:00.12	26.619	127.846	32	6
20	MAY	1990	02:22:01.62	5.121	32.145	14	6.7
24	MAY	1990	19:34:44.24	5.277	31.829	16	5.9
29	MAY	1990	18:31:12.29	56.956	-153.569	24	5.9
30	MAY	1990	02:34:05.88	-6.016	-77.229	24	6.1
14	JUN	1990	07:40:56.21	11.76	121.899	18	6
14	JUN	1990	12:47:28.82	47.869	85.076	57	6.1
17	JUN	1990	04:51:45.51	27.398	65.719	14	5.9
20	JUN	1990	21:00:09.98	36.957	49.409	18	6.4
21	JUN	1990	09:02:14.62	36.636	49.799	15	5.8
9	JUL	1990	15:11:20.38	5.395	31.654	12	5.9
14	JUL	1990	05:54:25.49	0.003	-17.376	11	6.2
16	JUL	1990	07:26:34.61	15.679	121.172	25	6.5
17	JUL	1990	21:14:43.86	16.495	120.981	23	6.1
26	JUL	1990	06:53:56.38	27.247	65.508	18	5.8
3	AUG	1990	09:15:06.15	47.963	84.961	33	6
5	AUG	1990	01:34:55.83	29.551	137.63	496	6
5	AUG	1990	03:36:22.29	36.31	141.072	26	5.8
16	AUG	1990	04:59:57.69	41.564	88.77	0	6.2
20	AUG	1990	00:03:52.78	46.189	142.289	309	5.9
26	AUG	1990	07:53:41.69	19.592	-77.874	10	5.9
2	SEP	1990	04:26:48.07	-0.143	-80.283	14	5.8
30	SEP	1990	19:05:02.46	24.248	125.215	35	5.9
16	OCT	1990	06:13:13.74	49.043	155.076	82	6
17	OCT	1990	14:30:13.16	-10.97	-70.776	598	6.7
25	OCT	1990	04:53:59.98	35.121	70.486	113	6
6	NOV	1990	18:45:52.23	28.251	55.462	10	6.2
6	NOV	1990	20:14:29.74	53.452	169.871	24	6.3
12	NOV	1990	12:28:51.52	42.959	78.071	19	5.9
13	NOV	1990	02:35:07.87	46.104	138.637	14	6.2
15	NOV	1990	02:34:32.40	3.908	97.457	48	6

continued on next page

Day	Month	Year	UTM Time	Lat [°]	Lon [°]	Depth [km]	Magnitude
21	NOV	1990	01:48:26.40	51.65	-171.331	33	5.8
13	DEC	1990	03:01:48.05	23.916	121.636	12	5.9
13	DEC	1990	19:50:17.88	23.722	121.627	10	5.9
31	JAN	1991	23:03:33.67	35.993	70.423	142	6.4
16	FEB	1991	01:23:40.44	48.268	154.328	38	6.3
21	FEB	1991	02:35:34.05	58.427	-175.45	20	6.2
1	MAR	1991	17:30:26.05	10.939	-84.637	196	6.1
8	MAR	1991	11:36:28.43	60.904	167.023	13	6.4
26	MAR	1991	03:58:23.26	21.704	121.789	17	5.8
4	APR	1991	03:22:57.91	7.017	-78.153	32	6.1
14	APR	1991	08:08:55.70	27.155	127.419	83	6.2
22	APR	1991	21:56:51.82	9.685	-83.073	10	6.3
3	MAY	1991	02:14:14.43	28.08	139.585	433	6
7	MAY	1991	13:09:28.75	39.43	144.714	10	6.4
13	MAY	1991	16:28:15.44	-3.463	82.824	21	5.9
30	MAY	1991	13:17:41.97	54.567	-161.606	28	6.3
10	JUN	1991	17:35:49.48	23.771	-45.368	9	6.1
2	JUL	1991	05:14:30.19	-1.068	99.843	53	5.8
6	JUL	1991	12:19:49.56	-13.108	-72.187	104	6.2
13	JUL	1991	02:50:14.69	42.182	-125.641	11	6.2
14	JUL	1991	09:09:11.91	36.334	71.119	212	6.4
20	JUL	1991	11:48:47.18	54.565	-161.654	32	5.8
23	JUL	1991	13:25:47.32	3.775	95.932	46	5.8
6	AUG	1991	02:17:31.60	3.827	95.374	18	6
6	AUG	1991	14:49:30.57	35.725	141.044	28	5.9
17	AUG	1991	19:29:40.00	40.235	-124.348	12	6
17	AUG	1991	22:17:14.68	41.821	-125.397	13	6.2
26	AUG	1991	14:59:44.91	42.1	144.635	28	5.8
26	AUG	1991	20:54:23.02	6.882	94.609	21	5.8
3	SEP	1991	08:44:48.60	33.649	138.778	27	5.9
19	OCT	1991	21:23:14.30	30.78	78.774	10	6.5
19	NOV	1991	22:28:51.09	4.554	-77.442	21	6.4
26	NOV	1991	19:40:48.57	42.051	142.523	56	6.1
27	NOV	1991	05:03:31.35	48.237	154.807	27	5.9
13	DEC	1991	02:33:51.85	45.578	151.56	30	6.1
13	DEC	1991	18:59:06.56	45.521	151.707	18	6.1
17	DEC	1991	06:38:17.32	47.393	151.499	157	5.8
19	DEC	1991	01:33:40.43	45.253	151.176	27	6
22	DEC	1991	08:43:13.41	45.533	151.021	24	6.3
27	DEC	1991	09:09:37.50	51.019	98.15	13	5.8
17	FEB	1992	00:01:56.61	79.191	124.482	10	5.9
2	MAR	1992	12:29:39.59	52.915	159.886	38	6.5
5	MAR	1992	14:39:10.25	52.9	159.619	45	6.3
7	MAR	1992	01:53:37.76	10.21	-84.323	78	6.2
6	APR	1992	13:54:40.22	50.724	-130.091	19	6
19	APR	1992	18:32:19.00	23.861	121.594	15	5.8
23	APR	1992	14:18:35.15	22.437	98.904	12	5.8
25	APR	1992	18:06:04.21	40.368	-124.316	15	6.3
26	APR	1992	07:41:39.73	40.415	-124.603	20	5.9
26	APR	1992	11:18:25.79	40.378	-124.575	22	6.5
7	MAY	1992	06:23:36.15	41.175	144.7	12	5.8
18	MAY	1992	23:19:20.87	7.446	-82.311	17	5.9
20	MAY	1992	12:20:32.85	33.377	71.317	16	6
21	MAY	1992	04:59:57.57	41.604	88.813	0	6.5
25	MAY	1992	16:55:04.17	19.613	-77.872	23	6.3
28	MAY	1992	21:24:46.34	47.625	155.562	14	6
30	MAY	1992	12:42:03.52	30.694	141.59	20	5.9
3	JUN	1992	06:10:54.32	51.13	178.743	21	5.9

continued on next page

APPENDICES

Day	Month	Year	UTM Time	Lat [°]	Lon [°]	Depth [km]	Magnitude
15	JUN	1992	02:48:56.25	24.027	95.932	17	5.8
26	JUN	1992	11:32:27.18	6.129	-82.349	10	5.8
28	JUN	1992	11:57:34.12	34.201	-116.436	1	6.2
10	JUL	1992	09:31:27.59	44.695	149.482	19	6.2
12	JUL	1992	11:08:55.36	41.457	142.031	63	6
13	JUL	1992	18:11:33.71	-3.919	-76.602	96	6.1
17	JUL	1992	04:19:28.65	44.809	150.286	18	5.9
18	JUL	1992	08:36:58.70	39.419	143.33	28	6.2
18	JUL	1992	13:56:54.48	39.48	142.956	27	5.8
25	JUL	1992	02:53:28.33	38.731	143.012	17	5.9
29	JUL	1992	04:30:47.72	39.495	143.501	15	5.9
30	JUL	1992	08:24:46.65	29.584	90.163	14	5.9
7	AUG	1992	18:19:20.44	57.589	-142.846	13	6.3
11	AUG	1992	15:14:55.13	32.536	141.641	15	5.8
19	AUG	1992	00:57:40.27	50.502	-174.922	9	6.2
19	AUG	1992	02:04:37.41	42.142	73.575	27	6.6
24	AUG	1992	06:59:39.91	41.977	140.66	120	6.2
28	AUG	1992	18:18:46.44	-0.965	-13.562	15	6.3
29	AUG	1992	19:19:05.59	33.19	137.975	289	6
11	SEP	1992	03:57:26.50	-6.087	26.651	10	6.7
27	SEP	1992	17:48:13.03	53.933	-157.299	33	5.8
28	SEP	1992	14:06:02.64	24.121	122.648	29	5.8
30	SEP	1992	03:27:59.14	51.41	-178.63	26	5.9
30	SEP	1992	05:34:00.30	51.281	-178.037	33	6.1
1	OCT	1992	05:02:34.19	51.123	-177.997	14	5.9
17	OCT	1992	08:32:40.51	6.845	-76.806	14	6.2
18	OCT	1992	15:11:59.11	7.075	-76.862	10	6.6
30	OCT	1992	02:49:48.17	29.941	138.975	393	6
30	NOV	1992	09:32:37.57	35.692	-34.584	19	6.1
15	JAN	1993	11:06:05.95	43.3	143.691	102	6.9
7	FEB	1993	13:27:42.01	37.634	137.245	10	6.3
25	MAR	1993	07:08:18.93	41.8	143.467	33	5.8
6	MAY	1993	13:03:18.11	-8.472	-71.485	572	5.8
13	MAY	1993	11:59:49.25	55.177	-160.458	32	6.4
15	MAY	1993	03:12:32.72	16.698	-98.395	20	6.1
15	MAY	1993	21:52:25.34	51.374	-178.669	32	6.2
17	MAY	1993	23:20:49.22	37.171	-117.775	6	6
18	MAY	1993	10:19:33.78	19.914	122.45	168	6.4
25	MAY	1993	23:16:43.44	55.021	-160.513	36	6.2
29	MAY	1993	06:50:13.42	19.072	-26.476	12	5.9
8	JUN	1993	13:03:36.48	51.218	157.829	70	6.4
12	JUN	1993	20:33:25.70	51.259	157.692	44	5.9
12	JUL	1993	13:17:11.96	42.851	139.197	16	6.6
22	JUL	1993	04:57:07.05	6.47	-71.21	20	6.1
4	AUG	1993	11:31:18.03	-1.629	99.615	31	5.9
7	AUG	1993	00:00:37.07	26.585	125.612	155	6
7	AUG	1993	19:42:41.91	41.985	139.839	13	6.2
9	AUG	1993	11:38:30.53	36.436	70.711	204	5.8
9	AUG	1993	12:42:48.19	36.379	70.868	214	6.2
28	AUG	1993	20:14:45.87	6.571	94.668	132	5.8
1	SEP	1993	11:48:38.44	-4.331	102.567	71	5.8
1	SEP	1993	14:03:19.16	2.986	96.122	34	5.9
3	SEP	1993	12:35:00.27	14.523	-92.713	26	5.8
4	SEP	1993	11:38:38.93	36.429	70.812	194	5.9
10	SEP	1993	19:12:54.62	14.717	-92.645	34	6.2
16	SEP	1993	00:59:26.40	44.533	149.036	33	5.8
18	SEP	1993	05:02:27.01	36.421	71.592	112	6.1
20	SEP	1993	10:17:42.06	0.75	-29.354	10	5.8

continued on next page

Day	Month	Year	UTM Time	Lat [°]	Lon [°]	Depth [km]	Magnitude
29	SEP	1993	22:25:48.62	18.066	76.451	6	6.3
30	SEP	1993	18:27:50.81	15.417	-94.698	19	5.8
2	OCT	1993	08:42:32.71	38.19	88.663	14	6.2
11	OCT	1993	15:54:21.24	32.02	137.832	350	6.4
24	OCT	1993	07:52:15.63	16.755	-98.717	20	6.3
26	OCT	1993	11:38:21.96	38.477	98.655	8	5.9
11	NOV	1993	00:28:33.54	50.2	-177.446	18	6.3
13	NOV	1993	01:18:04.18	51.934	158.647	34	6.5
17	JAN	1994	12:30:55.39	34.213	-118.537	18	6.4
23	FEB	1994	08:02:04.72	30.853	60.596	6	6.1
24	FEB	1994	00:11:12.32	30.775	60.495	9	6.1
1	MAR	1994	03:49:00.83	29.096	52.617	12	5.8
14	MAR	1994	04:30:15.75	-1.278	-23.569	10	6.2
14	MAR	1994	20:51:24.96	15.994	-92.428	164	5.8
8	APR	1994	01:10:40.84	40.608	143.683	13	6
10	APR	1994	23:45:55.76	23.71	126.852	10	5.9
1	MAY	1994	12:00:35.76	36.901	67.163	18	6
2	MAY	1994	17:14:00.88	-1.116	97.487	15	6.2
3	MAY	1994	16:36:43.65	10.241	-60.758	36	5.8
7	MAY	1994	08:31:37.68	52.958	159.99	49	5.9
11	MAY	1994	08:18:15.67	-2.007	99.77	20	6
18	MAY	1994	03:54:00.55	44.727	149.401	26	6
23	MAY	1994	01:41:42.29	18.165	-100.527	55	6
23	MAY	1994	15:16:57.16	24.065	122.56	25	6
24	MAY	1994	04:00:42.18	23.959	122.448	16	6.2
24	MAY	1994	21:13:19.33	56.17	161.169	95	5.9
29	MAY	1994	14:11:50.96	20.556	94.16	35	6.2
31	MAY	1994	17:41:55.58	7.414	-72.033	11	6.3
5	JUN	1994	01:09:30.15	24.511	121.905	11	6.1
6	JUN	1994	20:47:40.53	2.917	-76.057	12	6.4
9	JUN	1994	00:33:16.23	-13.841	-67.553	631	7
20	JUN	1994	09:09:02.91	28.968	52.614	8	5.9
29	JUN	1994	18:22:33.58	32.567	93.673	9	5.9
30	JUN	1994	09:23:21.35	36.326	71.13	226	6.1
1	JUL	1994	10:12:41.21	40.232	53.383	40	6
4	JUL	1994	21:36:41.96	14.888	-97.322	14	6.1
21	JUL	1994	18:36:31.74	42.34	132.865	471	6.5
29	JUL	1994	00:17:45.41	52.398	-168.333	11	6
2	AUG	1994	14:17:52.19	52.428	158.044	144	6
8	AUG	1994	21:08:31.66	24.721	95.2	121	6
14	AUG	1994	00:46:20.44	44.709	150.103	16	6
16	AUG	1994	10:09:32.84	37.842	142.462	19	5.9
18	AUG	1994	00:45:47.20	-7.433	31.751	25	6
18	AUG	1994	04:42:57.38	44.767	150.158	14	6.2
20	AUG	1994	02:21:11.09	44.606	149.325	22	6
20	AUG	1994	04:38:50.57	44.656	149.176	24	6.2
21	AUG	1994	15:55:59.21	56.761	117.9	12	5.8
28	AUG	1994	18:37:20.67	44.783	150.061	18	6.1
30	AUG	1994	06:13:35.83	44.737	150.117	50	6.2
31	AUG	1994	09:07:25.93	43.719	146.013	76	6
1	SEP	1994	15:15:53.08	40.402	-125.68	10	6.6
13	SEP	1994	04:28:01.02	29.287	129.91	34	5.8
13	SEP	1994	10:01:32.09	7.054	-76.678	13	5.8
16	SEP	1994	06:20:18.74	22.528	118.711	13	6.5
4	OCT	1994	13:22:55.84	43.773	147.321	14	7.3
5	OCT	1994	20:37:29.31	43.592	147.449	13	5.8
9	OCT	1994	07:55:39.58	43.905	147.916	33	6.5
16	OCT	1994	05:10:00.93	45.749	149.167	116	6.4

continued on next page

APPENDICES

Day	Month	Year	UTM Time	Lat [°]	Lon [°]	Depth [km]	Magnitude
18	OCT	1994	17:12:50.92	43.576	147.097	60	6.2
25	OCT	1994	00:54:34.30	36.359	70.957	238	5.9
9	NOV	1994	18:21:02.68	43.556	147.144	53	6.2
14	NOV	1994	19:15:30.66	13.525	121.067	31	6.1
15	NOV	1994	20:39:37.25	47.451	154.927	12	5.8
10	DEC	1994	16:17:38.51	18.136	-101.384	48	6.6
28	DEC	1994	12:19:23.03	40.525	143.419	26	6.4
1	JAN	1995	06:59:55.95	40.701	143.549	15	5.8
6	JAN	1995	22:37:34.32	40.246	142.175	26	6.7
7	JAN	1995	02:36:06.77	40.258	142.364	32	6.3
16	JAN	1995	20:46:52.12	34.583	135.018	21	6.3
19	JAN	1995	15:05:03.41	5.05	-72.916	17	6.3
21	JAN	1995	08:47:29.64	43.377	146.72	58	6.5
8	FEB	1995	18:40:25.38	4.104	-76.622	73	6.3
14	FEB	1995	20:47:40.47	44.022	148.031	32	5.9
19	FEB	1995	04:03:16.19	40.556	-125.539	10	6
21	FEB	1995	02:09:50.94	46.012	151.527	31	5.8
8	MAR	1995	03:45:58.69	16.562	-59.559	8	6.3
11	MAR	1995	15:21:10.89	44.07	148.079	33	5.9
31	MAR	1995	14:01:40.08	38.212	135.012	354	6
8	APR	1995	17:45:12.92	21.833	142.691	267	6.4
17	APR	1995	07:14:35.22	33.763	-38.576	10	5.8
17	APR	1995	23:28:06.89	45.928	151.283	23	6.1
19	APR	1995	03:50:04.61	44.046	148.144	26	5.9
21	APR	1995	00:09:54.36	12.011	125.656	20	6.2
23	APR	1995	02:55:55.11	51.334	179.714	16	6.2
23	APR	1995	05:08:01.97	12.39	125.396	24	6.1
28	APR	1995	16:30:00.70	44.072	148.004	28	6.5
2	MAY	1995	06:06:05.69	-3.792	-76.917	97	6.5
5	MAY	1995	03:53:45.05	12.626	125.297	16	6.2
6	MAY	1995	01:59:07.13	24.987	95.294	117	6.4
18	MAY	1995	00:06:27.46	-0.893	-21.996	12	6.2
27	MAY	1995	13:03:52.65	52.629	142.827	11	6.7
25	JUN	1995	06:59:06.24	24.6	121.7	52	5.8
27	JUN	1995	10:09:58.06	18.835	-81.719	10	5.8
29	JUN	1995	07:45:09.94	48.793	154.446	64	5.9
30	JUN	1995	11:58:56.88	24.688	-110.228	10	5.9
7	JUL	1995	21:15:19.70	33.972	137.127	333	5.8
8	JUL	1995	05:42:53.09	39.678	143.352	11	5.9
8	JUL	1995	17:15:25.76	53.578	-163.74	21	6
11	JUL	1995	21:46:39.78	21.966	99.196	12	6.1
12	JUL	1995	18:38:49.83	12.324	125.058	34	5.9
27	JUL	1995	05:51:18.94	-12.59	79.228	16	6.2
19	AUG	1995	21:43:31.92	5.139	-75.577	119	6.2
6	SEP	1995	22:48:49.60	14.943	-94.253	12	5.8
14	SEP	1995	14:04:31.43	16.779	-98.597	23	6.4
3	OCT	1995	01:51:23.90	-2.75	-77.881	24	6.5
3	OCT	1995	12:44:58.09	-2.778	-77.851	16	6
6	OCT	1995	18:09:45.90	-2.045	101.436	33	5.8
8	OCT	1995	08:55:45.82	41.048	72.153	14	5.9
9	OCT	1995	15:35:53.91	19.055	-104.205	33	6.6
18	OCT	1995	10:37:26.38	27.929	130.175	28	6.4
19	OCT	1995	02:41:36.19	28.094	130.147	19	6.3
21	OCT	1995	02:38:57.12	16.84	-93.469	159	6.3
5	NOV	1995	16:29:58.35	-4.92	103.22	36	6.4
8	NOV	1995	07:14:18.61	1.833	95.05	33	6.2
24	NOV	1995	17:24:11.87	44.537	149.103	27	6.1
27	NOV	1995	15:52:56.91	44.568	149.143	20	6

continued on next page

Day	Month	Year	UTM Time	Lat [°]	Lon [°]	Depth [km]	Magnitude
30	NOV	1995	23:37:36.39	44.473	149.342	23	5.9
2	DEC	1995	17:13:18.63	44.505	149.237	18	6
3	DEC	1995	18:01:08.99	44.663	149.3	33	6.6
7	DEC	1995	19:30:24.23	44.907	149.527	27	6
30	DEC	1995	12:11:05.66	40.752	143.339	22	5.8
31	JAN	1996	20:30:42.37	44.468	149.37	20	5.9
1	FEB	1996	07:18:04.23	44.853	146.273	170	5.8
3	FEB	1996	11:14:20.12	27.291	100.276	11	6.4
7	FEB	1996	21:36:46.30	45.324	149.892	42	6.3
14	FEB	1996	20:31:07.06	45.46	150.374	36	5.8
16	FEB	1996	09:44:58.41	-1.496	-15.279	10	6.2
16	FEB	1996	15:22:58.83	37.353	142.38	40	6.3
18	FEB	1996	23:49:28.16	-1.266	-14.273	10	6.3
22	FEB	1996	14:59:08.98	45.263	148.542	124	6.3
25	FEB	1996	03:08:15.87	15.978	-98.07	21	6.1
5	MAR	1996	14:52:28.68	24.092	122.215	29	6.1
16	MAR	1996	22:04:06.24	28.983	138.944	477	5.9
28	MAR	1996	07:28:28.12	11.919	57.805	10	5.8
28	MAR	1996	23:03:49.81	-1.036	-78.737	33	5.8
30	MAR	1996	13:05:17.43	52.214	-168.734	33	5.9
7	MAY	1996	23:20:00.68	43.708	147.607	53	6.2
2	JUN	1996	02:52:09.55	10.797	-42.254	10	6.1
2	JUN	1996	09:37:46.48	27.424	128.483	41	5.8
8	JUN	1996	23:19:15.17	51.491	-178.128	33	5.9
10	JUN	1996	04:03:35.48	51.564	-177.632	33	6.6
10	JUN	1996	15:24:56.00	51.478	-176.847	26	5.9
11	JUN	1996	18:22:55.73	12.614	125.154	33	6
21	JUN	1996	13:57:10.02	51.568	159.119	20	6
6	JUL	1996	21:36:28.72	21.968	142.83	241	5.8
16	JUL	1996	03:48:28.34	56.084	164.998	33	5.8
30	JUL	1996	17:38:30.71	14.509	119.954	33	6.1
10	AUG	1996	18:12:17.35	38.909	140.53	10	6
5	SEP	1996	23:42:06.15	21.898	121.498	20	6.4
11	SEP	1996	02:37:14.99	35.537	140.943	55	6.1
24	SEP	1996	11:42:18.87	15.191	-61.443	146	6
1	OCT	1996	15:50:23.66	12.434	58.066	10	5.8
2	OCT	1996	09:48:01.56	11.761	125.484	33	6
2	OCT	1996	11:24:48.42	45.133	151.168	33	6.1
6	OCT	1996	20:13:09.18	49.047	-127.88	10	5.8
18	OCT	1996	10:50:20.86	30.568	131.093	10	6
19	OCT	1996	14:44:40.79	31.885	131.468	22	6.3
24	OCT	1996	19:31:53.93	66.986	-173.229	19	6
4	NOV	1996	17:24:57.43	7.306	-77.393	14	6
6	NOV	1996	20:00:58.85	27.999	143.538	9	6.4
19	NOV	1996	10:44:46.06	35.345	78.133	33	6.1
2	DEC	1996	22:17:59.24	31.789	131.314	49	6
9	DEC	1996	11:28:48.61	29.85	-42.855	10	5.9
10	DEC	1996	08:36:18.70	0.87	-30.039	10	6
22	DEC	1996	14:53:27.62	43.207	138.92	226	6
11	JAN	1997	20:28:26.02	18.219	-102.756	33	6.5
17	JAN	1997	15:53:13.43	28.814	129.953	33	5.9
4	FEB	1997	10:37:47.14	37.661	57.291	10	5.9
27	FEB	1997	21:08:02.36	29.976	68.208	33	6.3
28	FEB	1997	11:32:18.98	43.921	147.876	33	6.1
17	MAR	1997	08:05:48.41	-6.614	105.514	33	5.8
26	MAR	1997	02:08:57.27	51.277	179.533	33	6
8	APR	1997	18:07:09.57	18.315	120.953	70	6
11	APR	1997	05:34:42.78	39.527	76.941	15	5.8

continued on next page

APPENDICES

Day	Month	Year	UTM Time	Lat [°]	Lon [°]	Depth [km]	Magnitude
22	APR	1997	09:31:23.25	11.112	-60.892	5	6
1	MAY	1997	11:37:36.15	18.993	-107.35	33	6.1
8	MAY	1997	13:29:24.60	51.717	-170.799	33	5.8
10	MAY	1997	07:57:29.72	33.825	59.809	10	6.4
13	MAY	1997	14:13:45.74	36.411	70.945	196	6.1
21	MAY	1997	22:51:28.73	23.083	80.041	36	6
22	MAY	1997	07:50:53.52	18.684	-101.604	70	5.9
17	JUN	1997	21:03:40.26	51.347	-179.332	33	6.4
8	JUL	1997	02:24:07.32	23.799	142.696	33	5.8
9	JUL	1997	19:24:13.17	10.598	-63.486	19	6.2
14	JUL	1997	16:09:35.52	43.249	146.381	33	5.9
13	AUG	1997	04:45:04.86	25.03	125.77	55	6
20	AUG	1997	07:15:15.97	4.358	96.494	33	5.9
2	SEP	1997	12:13:22.92	3.849	-75.749	198	6.5
28	OCT	1997	06:15:19.20	-4.34	-76.71	130	6.5
8	NOV	1997	10:02:52.61	35.069	87.325	33	6.2
9	NOV	1997	22:56:44.80	13.85	-88.85	196	5.5
10	NOV	1997	23:06:44.30	31.187	140.486	86	5.8
15	NOV	1997	07:05:16.64	43.813	145.019	161	5.8
23	NOV	1997	03:51:01.70	39.96	138.82	33	5.8
28	NOV	1997	22:53:42.30	-13.55	-68.76	587	6.3
5	DEC	1997	11:26:55.00	54.89	162.11	33	6.3
5	DEC	1997	18:48:22.79	53.752	161.746	33	6.2
11	DEC	1997	07:56:28.85	3.929	-75.787	177	6
17	DEC	1997	04:38:53.30	51.19	178.89	33	5.8
10	JAN	1998	08:20:05.20	14.22	-91.59	33	6.3
3	FEB	1998	03:02:00.80	16.02	-96.24	33	5.9
14	MAR	1998	19:40:27.10	30.15	57.57	9	5.9
21	MAR	1998	16:33:11.70	80.02	1.79	10	5.9
21	MAR	1998	18:22:28.10	36.45	70.13	225	5.8
22	MAR	1998	01:08:57.50	-11.39	66.26	10	5.4
29	MAR	1998	07:14:58.50	-0.33	-17.88	10	5.5
1	APR	1998	17:56:20.70	-0.5	99.28	33	6.2
10	APR	1998	16:40:37.70	-1.5	-15.59	10	5.4
3	MAY	1998	23:30:22.00	22.3	125.3	33	6.4
10	MAY	1998	06:05:58.70	13.63	-90.85	33	5.4
14	MAY	1998	18:56:23.30	40.25	143.25	33	5.6
27	MAY	1998	20:41:34.50	52.16	159.55	33	5.4
28	MAY	1998	21:11:43.80	37.29	78.9	33	5.3
9	JUL	1998	05:19:07.50	38.73	-28.6	10	5.7
27	OCT	2000	04:21:51.06	26.266	140.46	388	6.3
8	NOV	2000	06:59:58.086	7.042	-77.829	17	6.5
8	NOV	2000	18:36:21.07	23.251	124.15	14	5.7
13	NOV	2000	15:57:21.061	42.489	144.765	33	6
4	DEC	2000	04:43:09.059	14.876	-93.944	33	6.1
6	DEC	2000	17:11:06.04	39.566	54.799	30	7.5
22	DEC	2000	10:13:01.011	44.79	147.196	140	6.3
10	JAN	2001	16:02:44.023	57.078	-153.211	33	7
13	JAN	2001	17:33:32.038	13.049	-88.66	60	7.7
16	JAN	2001	13:25:01.008	-3.957	101.746	33	0
26	JAN	2001	03:16:40.05	23.419	70.232	16	7.7
28	JAN	2001	01:02:10.07	23.507	70.517	10	5.8
1	FEB	2001	18:19:30.039	51.437	-177.797	33	6
13	FEB	2001	19:28:30.026	-4.68	102.562	36	7.4
25	FEB	2001	02:21:59.059	36.424	70.881	202	6.2
28	FEB	2001	18:54:32.083	47.149	-122.727	51	6.8
15	MAR	2001	01:22:43.037	8.656	94.013	33	6
23	MAR	2001	11:30:10.052	44.071	148.054	33	6

continued on next page

Day	Month	Year	UTM Time	Lat [°]	Lon [°]	Depth [km]	Magnitude
24	MAR	2001	06:27:53.058	34.083	132.526	50	6.8
14	APR	2001	23:27:26.066	30.092	141.768	10	6
17	APR	2001	21:54:02.06	51.239	-179.78	33	5.9
9	MAY	2001	15:47:36.075	53.641	-164.319	42	5.5
20	MAY	2001	04:21:43.082	18.816	-104.446	33	6.3
25	MAY	2001	00:40:50.06	44.268	148.393	33	6.7
10	JUN	2001	01:52:08.001	39.873	53.89	34	5.4
13	JUN	2001	13:17:55.015	24.463	122.397	77	5.6
14	JUN	2001	02:35:25.081	24.513	122.033	32	5.9
14	JUN	2001	19:48:47.085	51.16	-179.828	18	6.5
15	JUN	2001	16:19:07.061	13.903	51.679	10	6
20	JUN	2001	00:04:30.082	45.522	152.036	33	5.7
24	JUN	2001	13:18:51.071	44.189	148.51	33	6
26	JUN	2001	14:05:37.00	61.34	-140.07	10	5.7
3	JUL	2001	13:10:42.06	21.641	142.984	290	6.5
4	JUL	2001	12:09:03.084	-17.003	-65.711	33	6.2
12	JUL	2001	06:12:16.079	-7.429	-13.378	10	5.7
19	JUL	2001	18:00:40.038	57.203	-151.036	33	5.9
28	JUL	2001	07:32:43.001	59.025	-155.116	131	6.8
2	AUG	2001	23:41:06.017	56.26	163.79	14	6.3
13	AUG	2001	20:11:23.04	41.046	142.308	38	6.4
17	AUG	2001	22:25:49.001	25.748	126.19	33	5.9
20	AUG	2001	04:12:37.047	25.653	126.208	33	5.4
25	AUG	2001	02:02:02.05	7.633	-82.766	24	6.1
1	SEP	2001	13:08:11.061	47.325	142.551	10	5.2
2	SEP	2001	02:25:54.009	0.889	82.501	10	6.1
7	SEP	2001	02:45:59.00	-13.166	97.297	10	5.9
12	SEP	2001	22:23:44.009	27.692	141.907	33	5.7
14	SEP	2001	04:45:08.00	48.69	-128.71	10	6
8	OCT	2001	18:14:26.044	52.591	160.324	48	6.5
8	OCT	2001	18:20:38.025	52.631	160.214	33	6.4
12	OCT	2001	05:02:34.00	52.63	-132.2	20	6.1
31	OCT	2001	22:04:32.035	5.361	94.359	33	5.7
9	NOV	2001	00:47:55.002	9.643	-82.3	10	6.1
14	NOV	2001	09:26:10.001	35.946	90.541	10	7.8
18	NOV	2001	21:59:52.053	35.726	93.691	10	5.6
19	NOV	2001	17:45:23.045	35.763	93.672	10	5.4
23	NOV	2001	20:43:03.055	36.392	71.506	106	6.1
28	NOV	2001	14:32:32.072	15.571	-93.106	84	6.4
2	DEC	2001	13:01:53.067	39.402	141.089	123	6.5
8	DEC	2001	20:29:34.023	28.251	129.574	33	6.2
18	DEC	2001	04:02:58.028	23.954	122.734	14	6.8
23	DEC	2001	10:21:28.025	27.871	141.75	35	5.9
3	JAN	2002	07:05:27.067	36.088	70.687	129	6.2
16	JAN	2002	23:09:52.008	15.502	-93.133	80	6.4
1	FEB	2002	21:55:20.099	45.464	136.719	355	5.9
3	MAR	2002	12:08:19.074	36.502	70.482	225	7.4
14	MAR	2002	16:08:31.04	51.531	-173.083	33	5.9
17	MAR	2002	03:57:47.03	51.464	-173.275	33	5.5
31	MAR	2002	06:52:50.049	24.279	122.179	32	7.1
12	APR	2002	04:00:23.074	35.959	69.417	10	5.9
26	APR	2002	07:15:11.05	53.508	160.632	62	5.8
8	MAY	2002	19:45:18.086	53.813	160.774	39	5.9
21	MAY	2002	20:04:16.016	44.43	146.619	149	5.5
25	MAY	2002	05:36:31.097	53.815	-161.116	33	6.5
28	MAY	2002	16:45:17.01	24.069	122.264	33	6
12	JUN	2002	19:52:47.036	-0.676	-20.722	10	5.5
22	JUN	2002	02:58:21.03	35.626	49.047	10	6.5

continued on next page

APPENDICES

Day	Month	Year	UTM Time	Lat [°]	Lon [°]	Depth [km]	Magnitude
28	JUN	2002	17:19:30.027	43.752	130.666	566	7.3
11	JUL	2002	07:36:26.006	24.075	122.288	43	5.8
23	JUL	2002	20:05:31.088	37.251	142.216	33	5.6
25	JUL	2002	12:31:01.044	43.661	147.548	33	5.7
31	JUL	2002	00:16:44.061	7.929	-82.793	10	6.5
2	AUG	2002	23:11:39.013	29.28	138.97	426	6.3
13	AUG	2002	08:37:22.077	14.749	55.85	10	5.8
28	AUG	2002	17:05:33.085	22.115	121.577	33	5.6
30	AUG	2002	05:58:21.005	44.479	149.081	31	5.5
13	SEP	2002	22:28:29.046	13.036	93.068	21	6.5
14	SEP	2002	19:58:36.095	13.055	93.157	33	5.8
15	SEP	2002	08:39:32.07	44.833	129.923	586	6.4
25	SEP	2002	22:28:11.092	31.995	49.329	10	5.6
12	OCT	2002	20:09:11.046	-8.295	-71.738	534	6.9
14	OCT	2002	14:12:43.075	41.174	142.249	61	6.1
16	OCT	2002	10:12:21.043	51.952	157.323	102	6.2
23	OCT	2002	11:27:19.043	63.514	-147.912	4	6.7
24	OCT	2002	06:08:37.098	-1.884	29.004	11	6.2
24	OCT	2002	21:53:43.019	6.03	94.419	64	5.7
2	NOV	2002	01:26:10.07	2.824	96.085	30	7.4
2	NOV	2002	09:46:46.07	2.954	96.394	27	6.4
3	NOV	2002	03:37:42.007	38.886	141.977	39	6.4
3	NOV	2002	22:12:41.00	63.517	-147.444	4	7.9
7	NOV	2002	15:14:06.076	51.197	179.334	33	6.6
17	NOV	2002	04:53:48.046	47.946	146.419	470	7.3
20	NOV	2002	21:32:30.081	35.414	74.515	33	6.4
26	NOV	2002	00:48:15.004	51.465	-173.537	20	6.1
28	DEC	2002	09:36:08.048	51.429	-168.526	10	5.8
22	JAN	2003	02:06:34.061	18.77	-104.104	24	7.6
19	FEB	2003	03:32:36.036	53.645	-164.643	19	6.6
24	FEB	2003	02:03:41.045	39.61	77.23	11	6.4
2	MAR	2003	16:42:56.033	-36.958	-20.879	10	6.2
15	MAR	2003	19:41:28.07	52.249	160.387	30	6
17	MAR	2003	16:36:17.031	51.272	177.978	33	7
19	MAR	2003	14:43:36.029	52.207	160.716	33	6.2

B.3 Teleseismic events used for *S* receiver function analysis

The following events were used for *S* receiver function analysis. The events written in red correspond to the operative period of the BOHEMA experiment and correspond to the red dots in Figure 3.4. The other events were recorded by permanent stations or stations by *Geissler et al.* (2005) before and after the BOHEMA experiment.

Day	Month	Year	UTM time	Lat [°]	Lon [°]	Depth	Magnitude
21	JAN	1995	08:47:29.70	43.28	146.71	65	6.6
8	MAR	1995	03:45:59.00	16.59	-59.54	10	6.2
31	MAR	1995	14:01:41.20	38.11	135.12	368	6
23	APR	1995	02:55:54.70	51.36	179.66	16	6.2
6	MAY	1995	01:59:07.10	25.01	95.35	119	6.3
27	MAY	1995	13:03:55.50	52.53	142.85	33	6.6
7	JUL	1995	21:15:18.60	33.96	137.13	325	5.8
8	JUL	1995	17:15:29.00	53.75	-163.37	33	5.7
9	JUL	1995	20:31:32.00	21.96	99.21	12	5.7
21	JUL	1995	22:44:07.40	36.32	103.16	33	5.7
19	AUG	1995	21:43:31.092	5.139	-75.577	119	6.7
18	OCT	1995	10:37:26.038	27.929	130.175	28	7.1
18	OCT	1995	23:25:58.077	28.203	130.211	27	6.1
19	OCT	1995	00:32:06.044	28.164	130.156	33	6.3
19	OCT	1995	02:41:36.019	28.094	130.148	19	6.8
23	OCT	1995	22:46:50.081	26.003	102.227	10	6.5
8	NOV	1995	07:14:18.061	1.833	95.05	33	7.1
24	NOV	1995	17:24:12.00	44.39	149.13	33	6.1
27	NOV	1995	15:52:56.091	44.568	149.143	20	6.3
30	NOV	1995	15:09:22.049	44.277	145.619	136	6
30	NOV	1995	23:37:36.039	44.473	149.342	23	6.3
2	DEC	1995	17:13:18.70	44.49	149.34	19	6
3	DEC	1995	18:01:08.099	44.663	149.3	33	7.9
7	DEC	1995	05:12:22.40	44.5	149.39	33	5.8
7	DEC	1995	19:30:24.023	44.907	149.527	27	6
10	DEC	1995	22:23:12.035	44.351	149.742	16	6.4
31	JAN	1996	20:30:42.037	44.468	149.37	20	6
1	FEB	1996	07:18:04.023	44.853	146.273	170	6.2
3	FEB	1996	11:14:20.012	27.291	100.276	11	6.6
7	FEB	1996	21:36:46.03	45.324	149.892	42	7.2
16	FEB	1996	15:22:58.083	37.353	142.38	40	6.7
22	FEB	1996	14:59:08.098	45.263	148.542	124	6.3
5	MAR	1996	14:52:28.068	24.092	122.215	29	6.3
22	MAR	1996	03:24:20.001	51.221	178.695	20	6.8
30	MAR	1996	13:05:17.043	52.214	-168.734	33	6.3
16	JAN	1999	10:44:39.049	56.23	-147.43	21	6
24	JAN	1999	00:37:04.063	30.62	131.09	33	6.4
25	JAN	1999	18:19:16.087	4.46	-75.72	17	6.4
28	JAN	1999	08:10:05.042	52.89	-169.12	67	6.6
8	MAR	1999	12:25:48.099	52.06	159.52	56	7
18	MAR	1999	17:55:43.024	41.1	142.97	41	6
20	MAR	1999	10:47:45.093	51.59	-177.67	33	7
8	APR	1999	13:10:34.008	43.61	130.35	565	7.1
7	MAY	1999	14:13:52.036	56.42	-152.94	20	6.2
8	MAY	1999	19:44:35.095	45.45	151.63	62	6.2
12	MAY	1999	17:59:22.04	43.03	143.84	102	6.5
2	JUL	1999	11:45:31.029	49.37	-129.2	10	6.4
7	JUL	1999	18:52:57.002	49.23	155.56	33	6.1

continued on next page

APPENDICES

Day	Month	Year	UTM time	Lat [°]	Lon [°]	Depth	Magnitude
11	JUL	1999	14:14:16.053	15.78	-88.33	10	7
29	AUG	1999	00:46:13.046	3.1	65.86	10	6
18	SEP	1999	21:28:33.017	51.21	157.56	60	6
20	SEP	1999	17:47:18.049	23.77	120.98	33	7.7
20	SEP	1999	18:03:44.029	23.57	121.3	33	6.6
20	SEP	1999	21:46:42.087	23.39	120.96	33	6.5
22	SEP	1999	00:14:39.015	23.73	121.17	26	6.4
25	SEP	1999	23:52:48.066	23.74	121.16	17	6.5
28	SEP	1999	05:00:42.096	54.59	168.26	33	6.2
13	OCT	1999	01:33:40.013	54.66	-161.19	30	6.4
16	OCT	1999	09:46:44.013	34.59	-116.27	0	7.4
24	OCT	1999	04:21:41.011	44.61	149.44	33	6.4
1	NOV	1999	17:53:00.012	23.38	121.52	33	6.3
11	NOV	1999	02:41:05.007	49.31	155.63	33	6.4
15	NOV	1999	05:42:43.022	-1.34	88.98	10	7.7
26	NOV	1999	00:29:00.027	55.13	165.36	33	6
29	NOV	1999	03:46:30.018	-1.27	89.04	10	6.9
1	DEC	1999	19:23:06.001	17.65	-82.36	10	6.3
6	DEC	1999	23:12:33.092	57.41	-154.49	66	7
7	DEC	1999	00:19:49.061	57.36	-154.51	40	6.5
6	JAN	2000	10:42:25.00	58.04	-136.87	1	6.2
28	JAN	2000	14:21:07.034	43.05	146.84	61	6.8
3	FEB	2000	10:24:59.003	65.01	-154.24	7	6.1
26	FEB	2000	18:24:39.022	9.41	-78.53	65	6.1
7	APR	2000	19:08:27.083	-18.05	65.52	10	6.3
21	APR	2000	04:35:17.069	51.42	-178.14	33	6.2
2	JUN	2000	11:13:49.038	44.51	-130.08	10	6.5
3	JUN	2000	08:54:49.02	35.55	140.46	62	6.2
6	JUN	2000	14:57:02.022	29.42	131.42	33	6.4
7	JUN	2000	21:46:55.09	26.86	97.24	33	6.5
10	JUN	2000	18:23:29.032	23.84	121.22	33	6.4
15	JUN	2000	11:10:46.021	29.37	132.08	10	6.1
25	JUN	2000	06:34:42.088	31.18	131.21	10	6
1	JUL	2000	07:01:55.058	34.22	139.13	10	6.8
7	JUL	2000	15:46:44.056	51.41	179.98	31	6.4
8	JUL	2000	18:57:44.047	34.05	139.13	10	6.6
10	JUL	2000	09:58:18.099	46.83	145.42	359	6.1
11	JUL	2000	01:32:28.052	57.37	-154.21	43	6.8
15	JUL	2000	01:30:30.05	34.32	139.26	10	6.1
20	JUL	2000	18:39:18.082	36.51	140.98	47	6.2
30	JUL	2000	12:25:45.057	33.9	139.38	10	7.1
4	AUG	2000	21:13:02.071	48.79	142.25	10	7.1
19	AUG	2000	17:26:27.094	43.82	147.17	62	6
1	SEP	2000	11:56:51.083	1.44	96.59	33	6
12	SEP	2000	00:27:58.062	35.39	99.34	10	6.3
2	OCT	2000	02:25:31.031	-7.98	30.71	34	6.7
3	OCT	2000	04:13:30.049	40.28	143.12	33	6.3
4	OCT	2000	14:37:44.015	11.12	-62.56	110	6.2
6	OCT	2000	04:30:19.015	35.46	133.13	10	7.4
8	NOV	2000	06:59:58.086	7.04	-77.83	17	6.5
13	NOV	2000	15:57:21.061	42.49	144.76	33	6
29	NOV	2000	10:35:48.011	63.88	-150.15	22	6
22	DEC	2000	10:13:01.011	44.79	147.2	140	6.3
10	JAN	2001	16:02:44.023	57.08	-153.21	33	7
11	JAN	2001	00:04:03.00	48.89	-129.31	10	6
1	FEB	2001	18:19:30.039	51.44	-177.8	33	6
17	FEB	2001	20:11:30.00	53.92	-133.61	20	6.2
24	FEB	2001	21:53:54.019	37.22	142.15	33	5.9

continued on next page

Day	Month	Year	UTM time	Lat [°]	Lon [°]	Depth	Magnitude
26	FEB	2001	05:58:22.043	46.81	144.52	392	6.1
28	FEB	2001	18:54:32.083	47.15	-122.73	51	6.8
7	MAR	2001	18:10:58.065	-6.81	-12.91	10	6
15	MAR	2001	01:22:43.037	8.66	94.01	33	6
23	MAR	2001	11:30:10.052	44.07	148.05	33	6
24	MAR	2001	06:27:53.058	34.08	132.53	50	6.8
25	APR	2001	14:40:06.004	32.82	132.02	33	5.7
26	APR	2001	17:48:57.047	43.1	145.92	86	6
25	MAY	2001	00:40:50.06	44.27	148.39	33	6.7
14	JUN	2001	02:35:25.081	24.51	122.03	32	5.9
14	JUN	2001	19:48:47.085	51.16	-179.83	18	6.5
20	JUN	2001	00:04:30.082	45.52	152.04	33	5.7
24	JUN	2001	13:18:51.071	44.19	148.51	33	6
26	JUN	2001	14:05:37.00	61.34	-140.07	10	5.8
5	JUL	2001	01:41:18.009	32.16	139.58	33	5.7
19	JUL	2001	18:00:40.038	57.2	-151.04	33	5.9
28	JUL	2001	07:32:43.001	59.03	-155.12	131	6.8
2	AUG	2001	23:41:06.017	56.26	163.79	14	6.3
5	AUG	2001	05:16:16.089	12.22	93.35	96	5.9
13	AUG	2001	20:11:23.04	41.05	142.31	38	6.4
2	SEP	2001	02:25:54.009	0.89	82.5	10	6.1
14	SEP	2001	04:45:08.00	48.69	-128.71	10	6
16	SEP	2001	23:20:09.00	48.54	-128.6	10	5.8
8	OCT	2001	18:14:26.044	52.59	160.32	48	6.5
9	OCT	2001	23:53:37.003	47.76	155.1	33	6.5
12	OCT	2001	05:02:34.00	52.63	-132.2	20	6.1
17	OCT	2001	11:29:09.092	19.35	-64.93	33	6
31	OCT	2001	22:04:32.035	5.36	94.36	33	5.7
2	DEC	2001	13:01:53.067	39.4	141.09	123	6.5
8	DEC	2001	20:29:34.023	28.25	129.57	33	6.2
18	DEC	2001	04:02:58.028	23.95	122.73	14	7.3
26	MAR	2002	03:45:48.07	23.35	124.09	33	6.6
31	MAR	2002	06:52:50.049	24.28	122.18	32	7.4
26	APR	2002	07:15:11.05	53.51	160.63	62	5.9
8	MAY	2002	19:45:18.086	53.81	160.77	39	5.9
15	MAY	2002	03:46:05.076	24.64	121.92	10	6.2
21	MAY	2002	06:02:59.094	17.78	-81.91	10	5.7
25	MAY	2002	05:36:31.097	53.81	-161.12	33	6.4
28	MAY	2002	16:45:17.01	24.07	122.26	33	6.1
28	JUN	2002	17:19:30.027	43.75	130.67	566	7.3
9	JUL	2002	18:40:35.063	43.52	-127.17	10	5.9
11	JUL	2002	07:36:26.006	24.08	122.29	43	5.8
23	JUL	2002	20:05:31.088	37.25	142.22	33	5.7
24	AUG	2002	18:40:53.044	43.11	146.12	42	6.1
28	AUG	2002	17:05:33.085	22.11	121.58	33	5.7
13	SEP	2002	22:28:29.046	13.04	93.07	21	6.7
14	SEP	2002	19:58:36.095	13.06	93.16	33	5.8
15	SEP	2002	08:39:32.07	44.83	129.92	586	6.4
26	SEP	2002	12:55:29.078	-19.65	-12.01	10	5.7
14	OCT	2002	14:12:43.075	41.17	142.25	61	6.1
16	OCT	2002	10:12:21.043	51.95	157.32	102	6.2
19	OCT	2002	12:09:05.038	44.3	149.96	33	6.3
23	OCT	2002	11:27:19.043	63.51	-147.91	4	6.7
2	NOV	2002	01:26:10.07	2.82	96.08	30	7.6
2	NOV	2002	09:46:46.07	2.95	96.39	27	6.4
3	NOV	2002	03:37:42.007	38.89	141.98	39	6.4
3	NOV	2002	22:12:41.00	63.52	-147.44	4	8.5
7	NOV	2002	15:14:06.076	51.2	179.33	33	6.6

continued on next page

APPENDICES

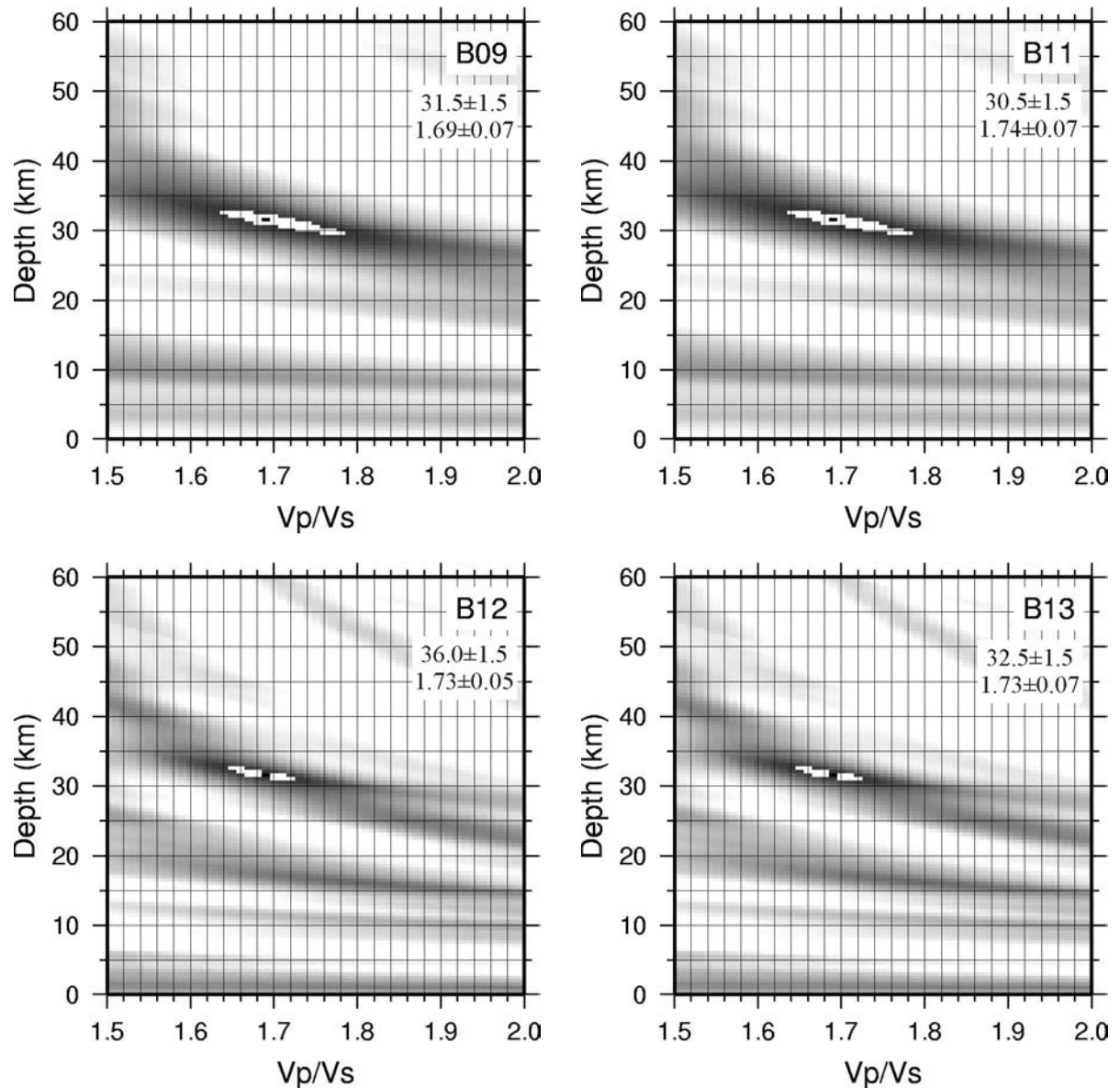
Day	Month	Year	UTM time	Lat [°]	Lon [°]	Depth	Magnitude
17	NOV	2002	04:53:53.054	47.82	146.21	459	7.3
26	NOV	2002	00:48:15.004	51.47	-173.54	20	6.1
10	DEC	2002	21:02:19.09	34.3	141.6	10	5.7
23	DEC	2002	13:46:11.036	16.96	-85.58	33	6
19	FEB	2003	03:32:36.036	53.65	-164.64	19	6.6
19	FEB	2003	05:01:40.027	44.15	141.8	214	5.9
15	MAR	2003	19:41:28.07	52.25	160.39	30	6.1
17	MAR	2003	16:36:17.031	51.27	177.98	33	7.1
17	MAR	2003	18:55:47.088	51.29	177.97	33	6.2
26	MAR	2003	04:22:30.007	12.52	92.56	33	5.9
7	APR	2003	18:28:37.038	36.3	141.68	33	5.8
24	APR	2003	10:56:21.098	48.76	154.99	43	6.1
29	APR	2003	13:53:17.03	43.71	147.8	62	6
14	MAY	2003	06:03:35.086	18.27	-58.63	41	6.7
26	MAY	2003	09:24:33.04	38.85	141.57	68	7
28	MAY	2003	16:15:18.094	-17.65	66.12	10	6.2
9	JUN	2003	01:52:51.001	24.41	122.02	48	5.8
10	JUN	2003	08:40:30.083	23.52	121.63	44	6
15	JUN	2003	19:24:35.006	51.66	176.83	33	6.4
16	JUN	2003	22:08:02.014	55.49	160	174	6.9
23	JUN	2003	12:12:34.047	51.44	176.78	20	7
30	JUN	2003	00:07:27.066	17.46	-61.14	33	5.7
2	JUL	2003	23:52:26.028	42.32	144.84	23	5.9
12	JUL	2003	23:01:38.00	54.65	-134.47	20	6
15	JUL	2003	20:27:50.053	-2.6	68.38	10	7.6
21	JUL	2003	15:16:31.093	25.98	101.29	10	6
23	JUL	2003	16:38:37.021	-15.59	-13.35	10	5.8
25	JUL	2003	22:13:29.097	38.42	141	6	6.1
26	JUL	2003	23:18:17.096	22.85	92.31	10	5.7
27	JUL	2003	06:25:31.095	47.15	139.25	470	6.8
3	AUG	2003	04:10:50.069	56.11	-153.32	17	5.7
11	AUG	2003	21:22:30.042	12.12	93.53	100	6
21	AUG	2003	23:31:49.014	68.69	-148.04	12	6
31	AUG	2003	23:08:00.026	43.39	132.27	481	6.2
5	SEP	2003	01:23:01.096	5.32	95.9	124	5.9
20	SEP	2003	03:54:50.078	35	140.17	51	5.7
21	SEP	2003	18:16:13.041	19.92	95.67	10	6.9
22	SEP	2003	04:45:36.024	19.78	-70.67	10	6.6
25	SEP	2003	19:50:06.036	41.81	143.91	27	8.3
26	SEP	2003	06:26:57.015	42.16	144.67	33	5.9
26	SEP	2003	20:38:22.01	41.99	144.58	33	6
29	SEP	2003	02:36:53.014	42.45	144.38	25	6.5
8	OCT	2003	09:06:55.034	42.65	144.57	32	6.7
11	OCT	2003	00:08:49.014	41.92	144.36	33	5.9
25	OCT	2003	12:41:35.025	38.4	100.95	10	5.8
28	OCT	2003	21:48:21.001	43.84	147.75	65	6.1
31	OCT	2003	01:06:28.028	37.81	142.62	10	7
1	NOV	2003	13:10:07.066	37.74	143.08	10	5.9
12	NOV	2003	08:26:43.074	33.17	137.07	384	6.4
17	NOV	2003	06:43:06.08	51.15	178.65	33	7.8
3	DEC	2003	14:11:14.002	42.36	144.73	33	5.9
5	DEC	2003	21:26:09.048	55.54	165.78	10	6.7
9	DEC	2003	12:44:01.068	51.33	-179.27	33	6.2
10	DEC	2003	04:38:11.059	23.04	121.36	10	6.8
22	DEC	2003	19:15:56.00	35.71	-121.1	7	6.5
29	DEC	2003	01:30:54.07	42.42	144.61	33	6.1
30	DEC	2003	09:50:44.025	47.05	154.19	33	5.9
16	JAN	2004	18:07:55.066	7.64	-37.7	10	6.2

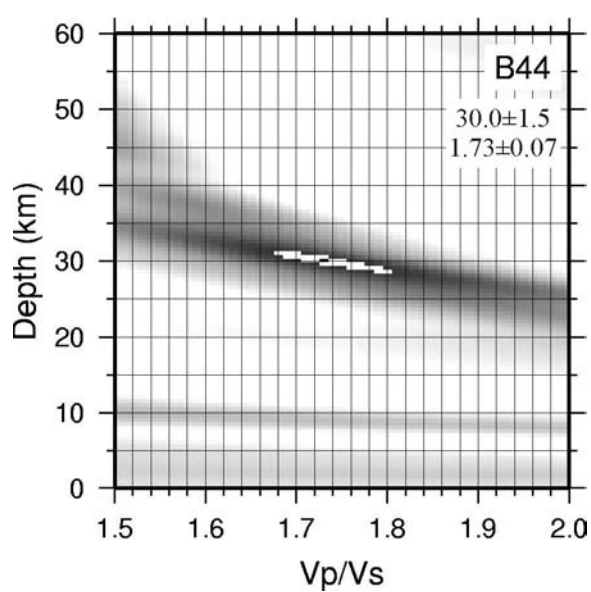
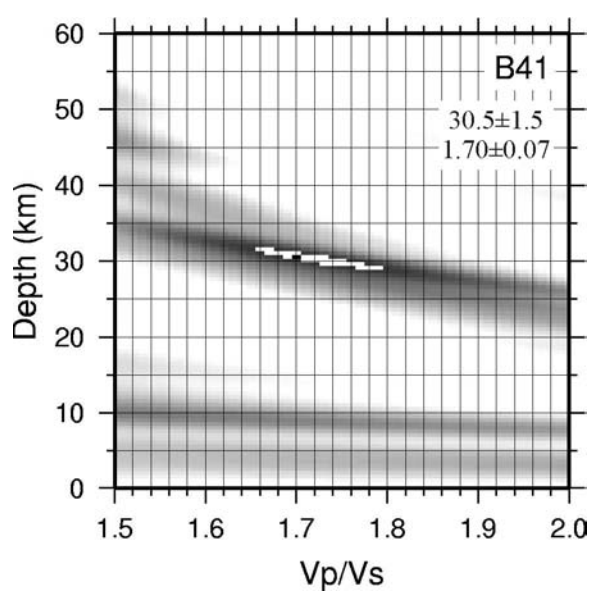
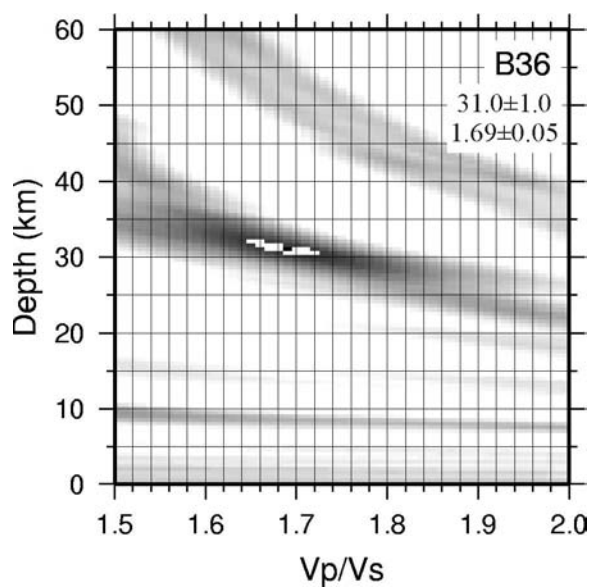
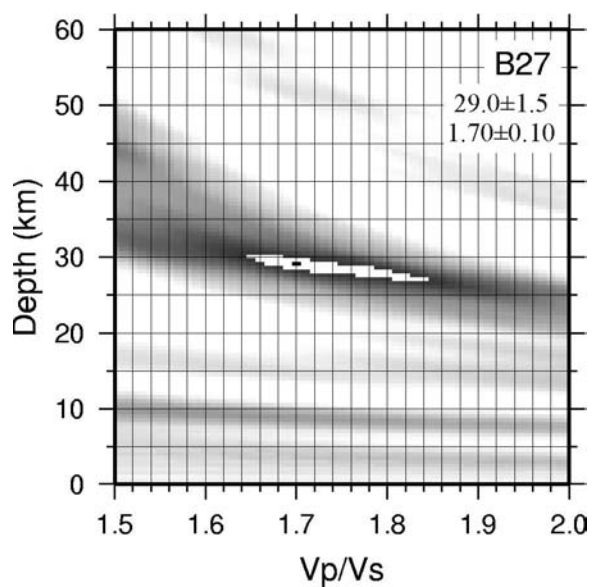
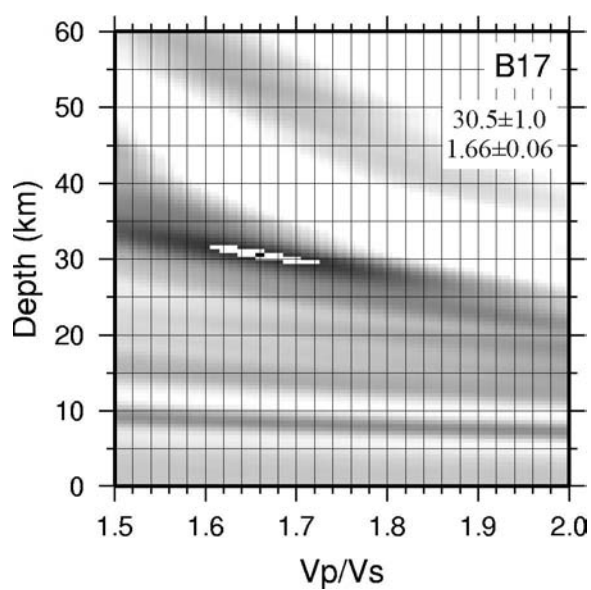
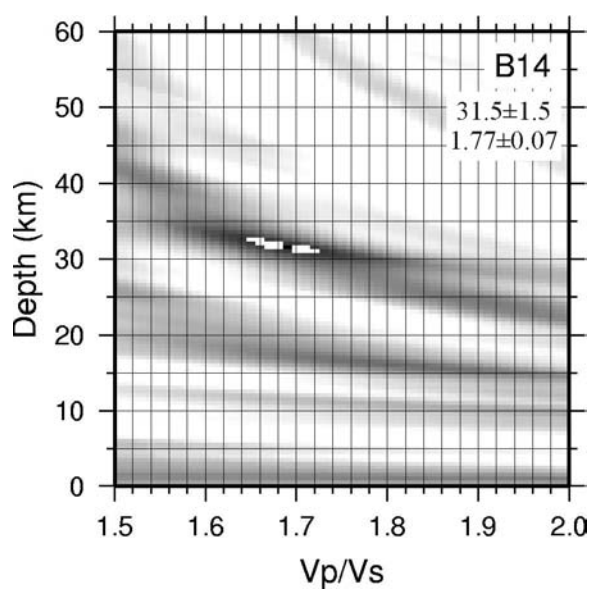
continued on next page

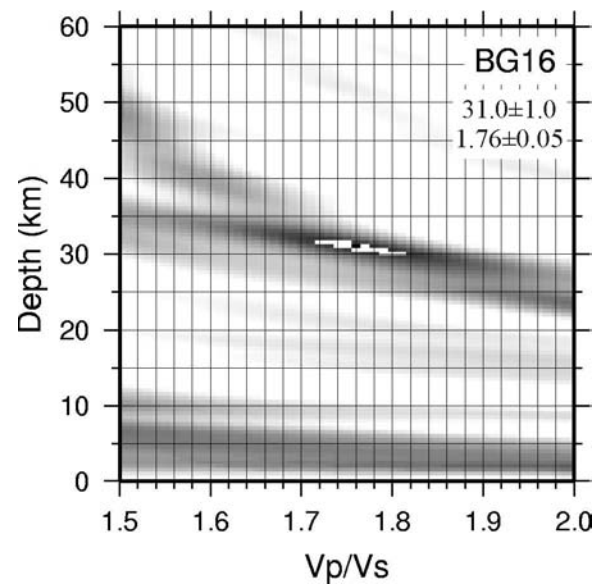
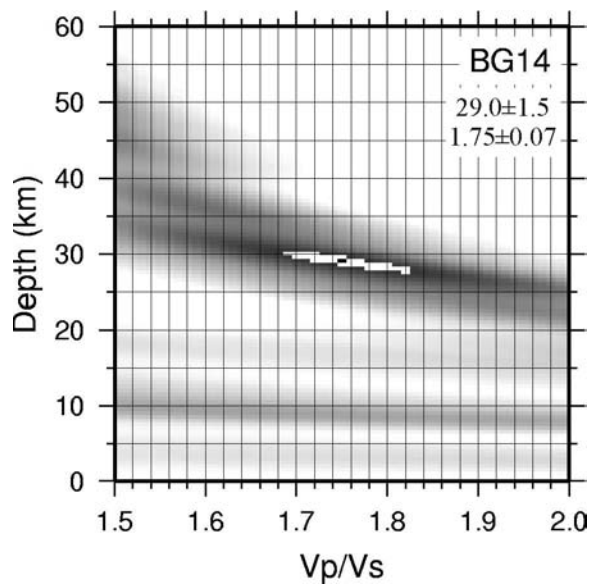
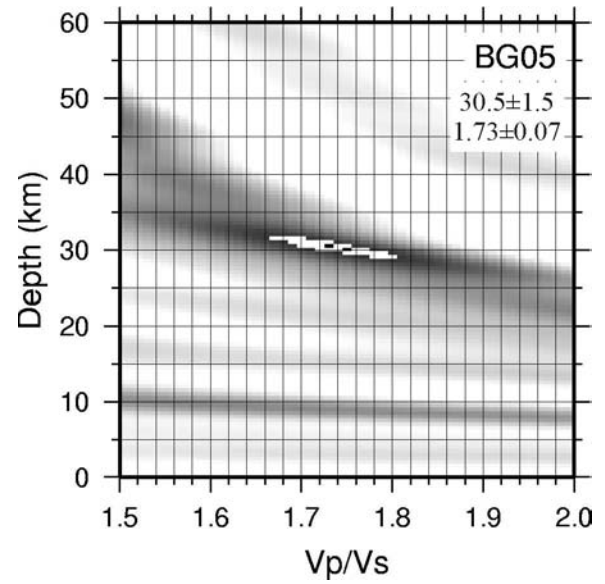
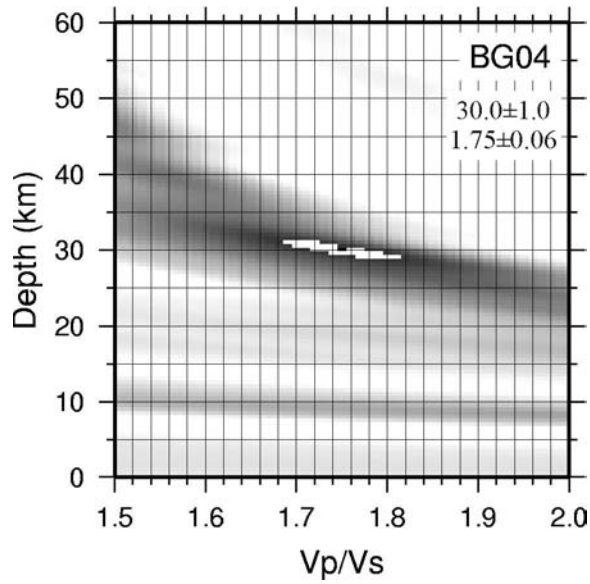
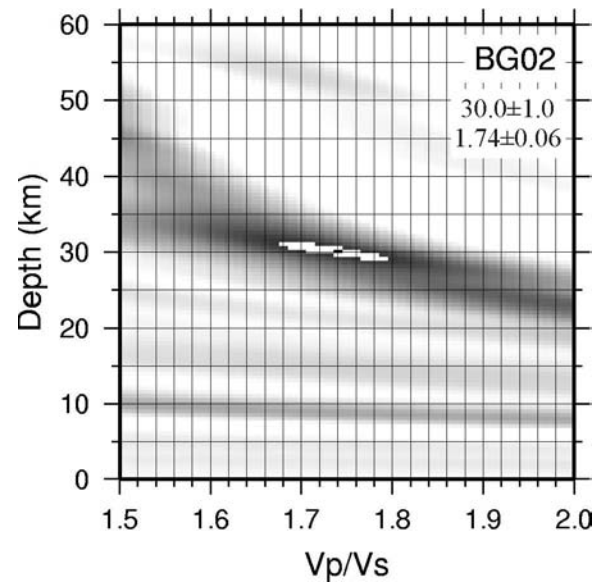
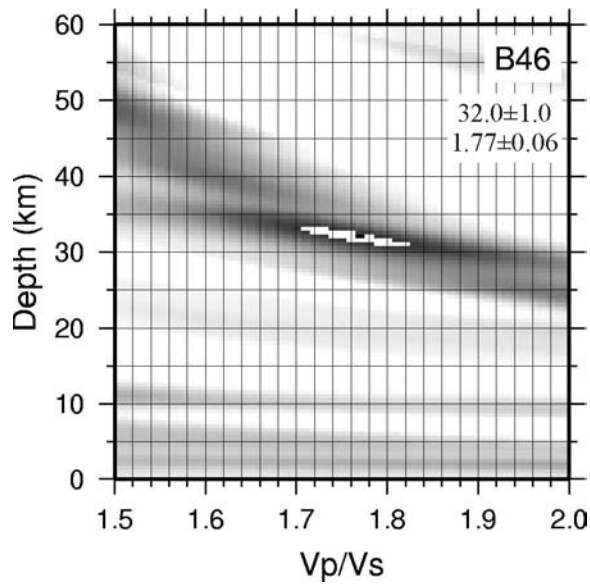
Day	Month	Year	UTM time	Lat [°]	Lon [°]	Depth	Magnitude
8	MAR	2004	23:39:11.034	10.48	-43.92	10	6.1
3	APR	2004	23:02:00.087	36.43	141.01	31	6
11	APR	2004	18:06:12.048	42.92	144.84	41	6.1
14	APR	2004	01:54:09.022	55.23	162.66	51	6.2
8	MAY	2004	08:02:54.022	21.95	121.6	26	5.7
19	MAY	2004	07:04:11.071	22.66	121.5	20	6.2
29	MAY	2004	20:56:09.06	34.25	141.41	16	6.6
1	JUN	2004	20:47:30.043	-9.04	67.25	10	5.7
8	JUN	2004	08:55:52.074	17.51	-83.46	10	5.9
10	JUN	2004	15:19:57.075	55.68	160	188	6.9
28	JUN	2004	09:49:47.00	54.8	-134.25	20	6.8
8	JUL	2004	10:30:49.016	47.2	151.3	128	6.4
15	JUL	2004	12:06:52.04	49.69	-126.86	18	5.9
19	JUL	2004	08:01:49.046	49.62	-126.97	23	6.4
22	JUL	2004	09:45:14.09	26.49	128.89	20	6.1
29	JUL	2004	01:44:06.091	12.45	95	22	5.9
6	AUG	2004	14:35:27.003	12.43	95	23	5.7
7	AUG	2004	09:30:16.094	51.75	-166.31	8	6.3
30	AUG	2004	12:23:21.041	49.54	157.27	10	5.7
1	SEP	2004	02:49:28.06	36.96	141.6	34	5.7
5	SEP	2004	10:07:07.087	33.07	136.64	14	7.2
5	SEP	2004	14:57:18.062	33.19	137.07	10	7.4
5	SEP	2004	20:30:59.081	33.25	136.8	10	5.7
6	SEP	2004	23:29:35.009	33.21	137.23	10	6.7
8	SEP	2004	14:58:25.06	33.14	137.2	19	6.2
9	SEP	2004	16:33:21.081	17.78	-81.55	25	6
13	SEP	2004	03:00:12.075	43.97	151.41	8	6.1
24	SEP	2004	10:34:53.044	0.45	-26.4	10	5.8
2	NOV	2004	10:02:12.082	49.277	-128.772	10	6.7
8	NOV	2004	15:55:01.015	24.104	122.542	29	6.3
28	NOV	2004	18:32:14.013	43.006	145.119	39	7
6	DEC	2004	14:15:11.089	42.9	145.228	35	6.8
26	FEB	2005	12:56:52.062	2.908	95.592	36	6.8
29	MAR	2005	05:16:29.085	2.648	96.581	30	5.9
9	APR	2005	15:16:27.089	56.168	-154.524	14	6
28	APR	2005	14:07:33.07	2.132	96.799	22	6.3
14	JUN	2005	17:10:16.064	51.232	179.406	51	6.8
15	JUN	2005	02:50:53.018	41.301	-125.97	10	7.2
17	JUN	2005	06:21:42.028	40.768	-126.574	10	6.7
9	JUL	2005	23:37:11.014	33.422	140.825	55	5.8
30	AUG	2005	18:10:45.077	38.502	143.169	23	6.2
6	SEP	2005	01:16:02.032	24.082	122.186	32	5.8

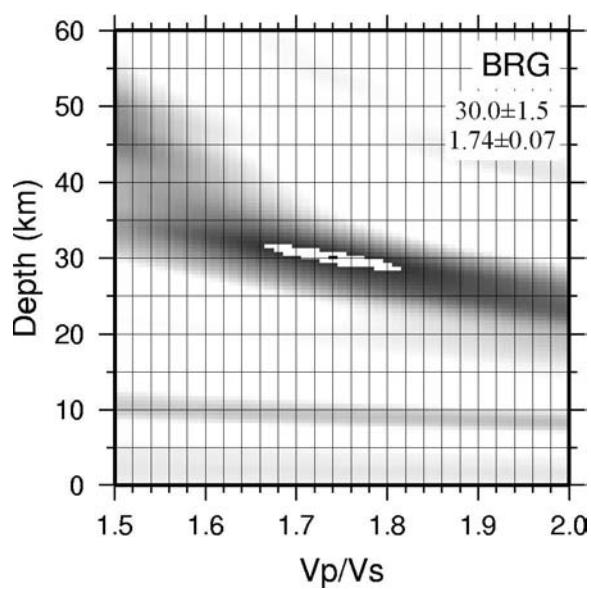
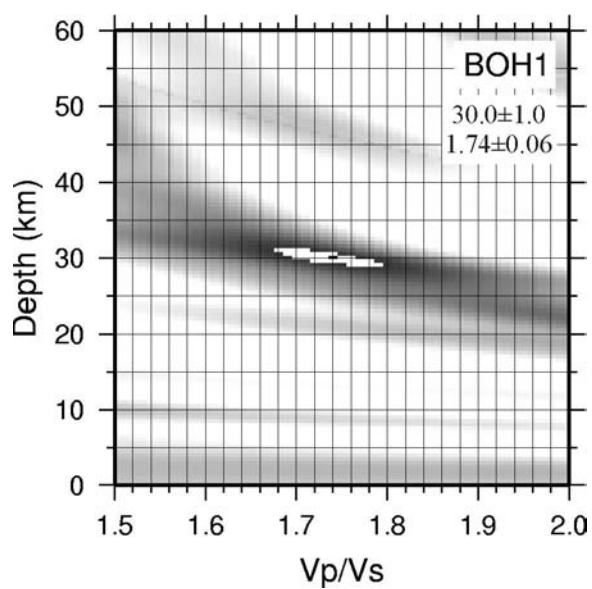
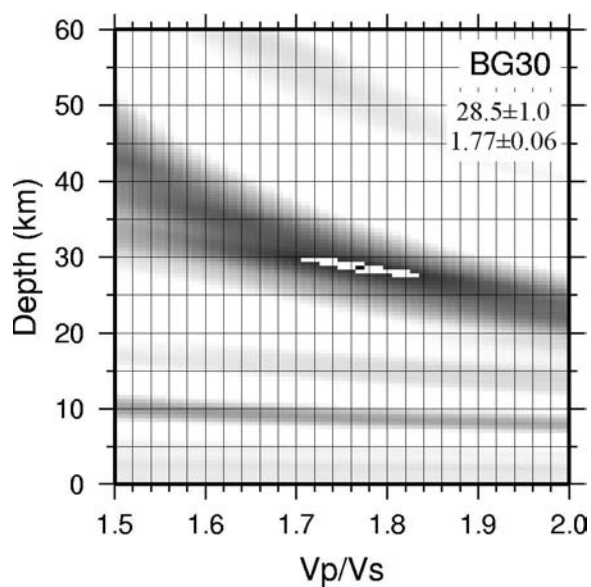
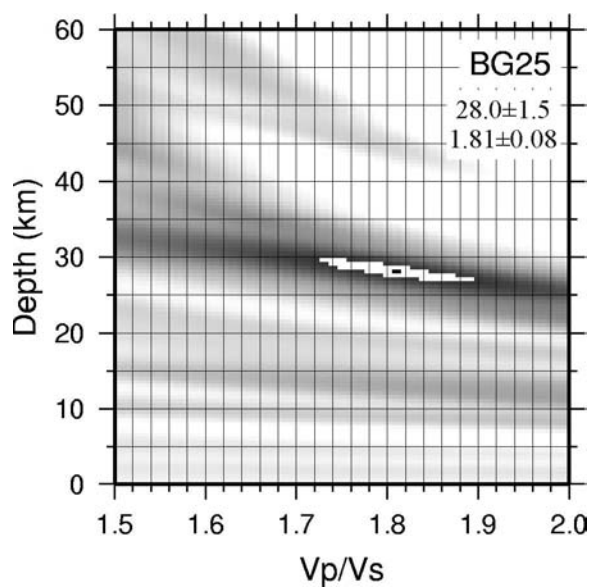
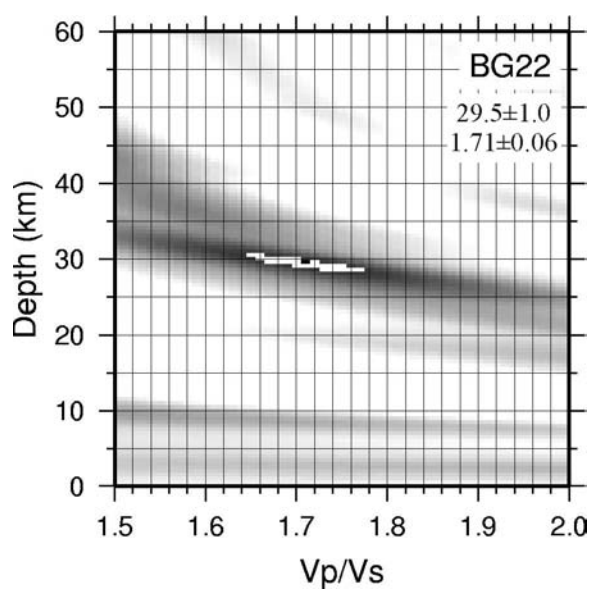
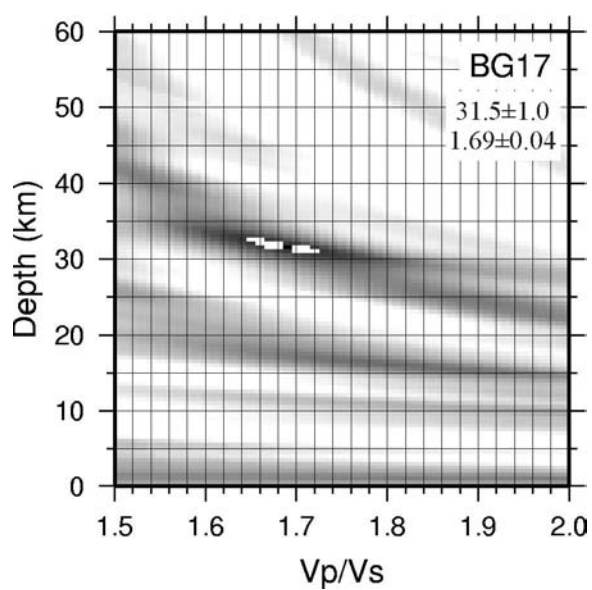
C.1 Moho depths and v_p/v_s ratios obtained by the method of Zhu and Kanamori

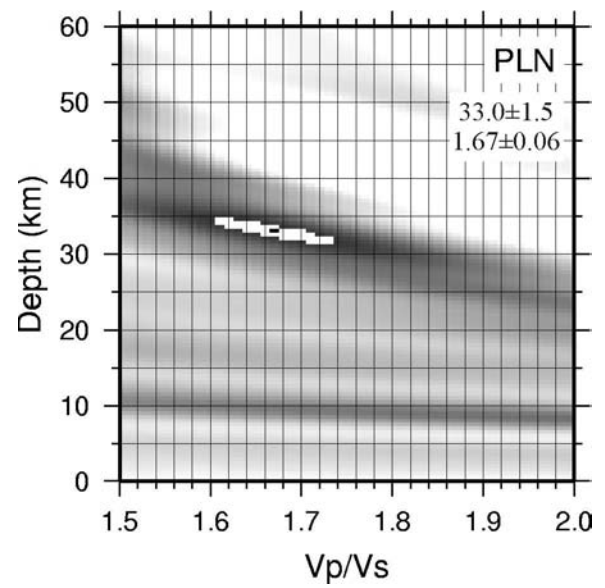
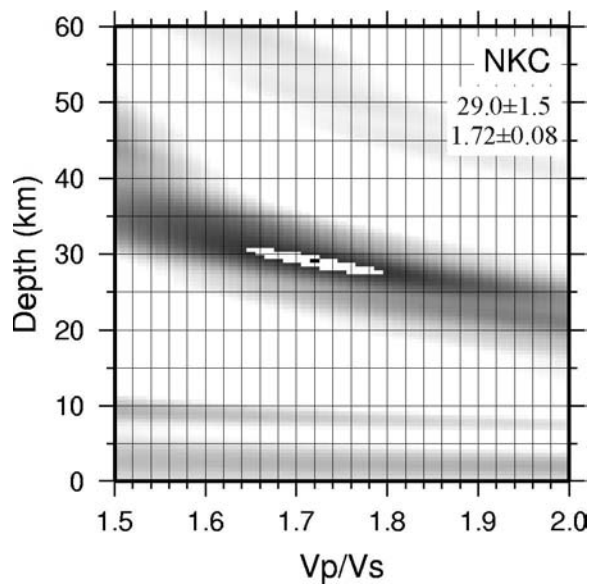
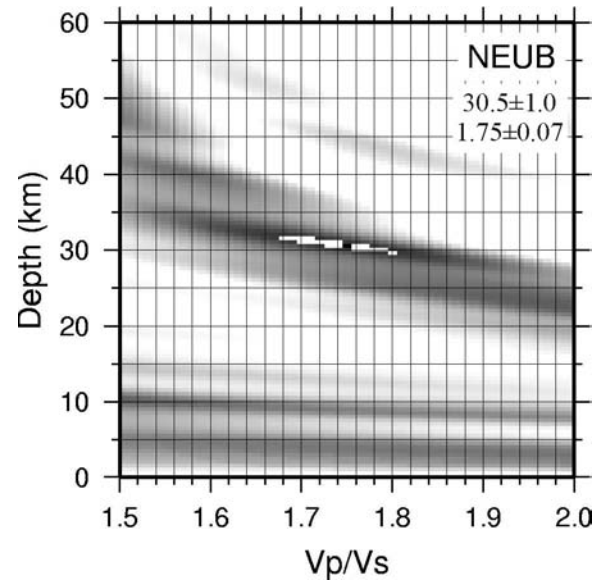
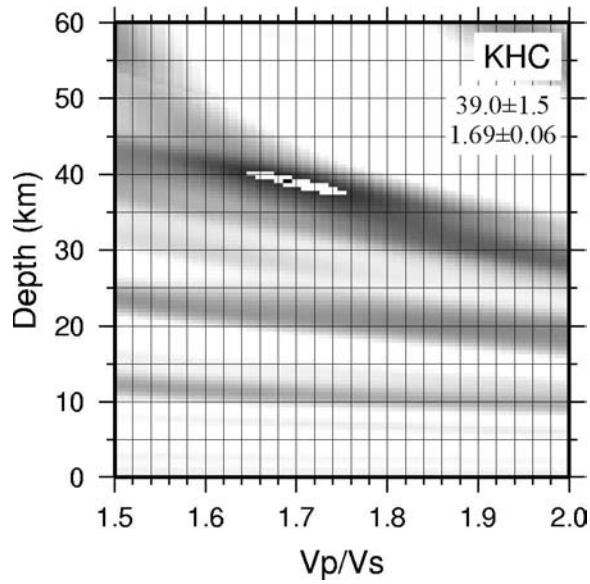
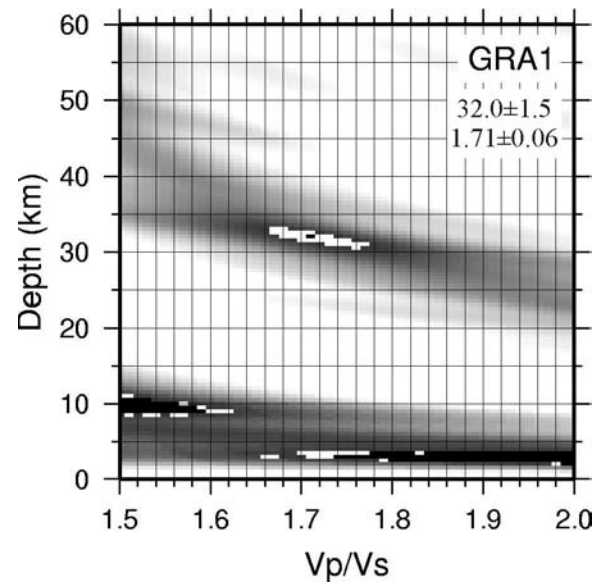
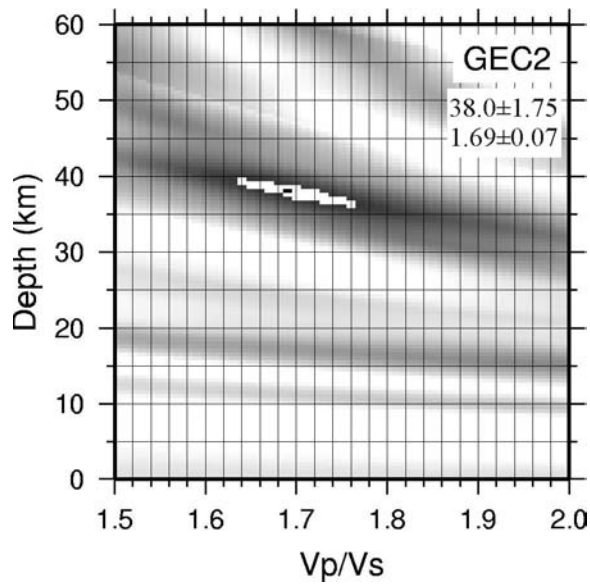
At 34 stations of the BOHEMA experiment with high signal/noise ratio, Moho depth and v_p/v_s ratios were obtained with the grid search method by *Zhu and Kanamori* (2000). The maximum stacked amplitude is marked by a black dot surrounded by a white ellipse. The ellipse marks the area of 95% of the maximum stacked amplitude and was used to estimate the uncertainty of the obtained values.

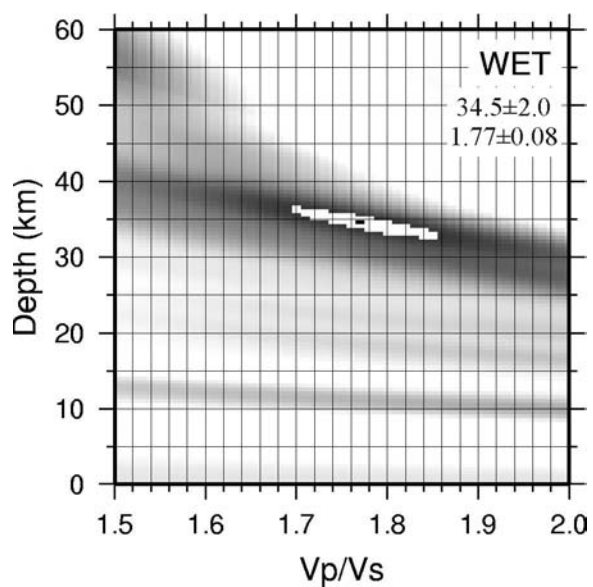
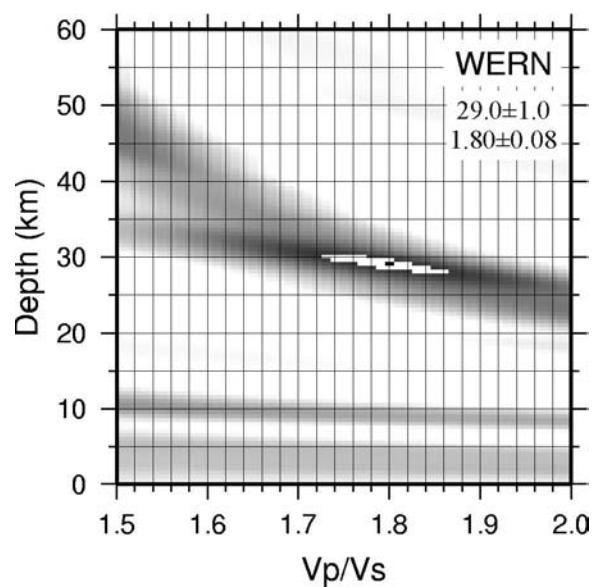
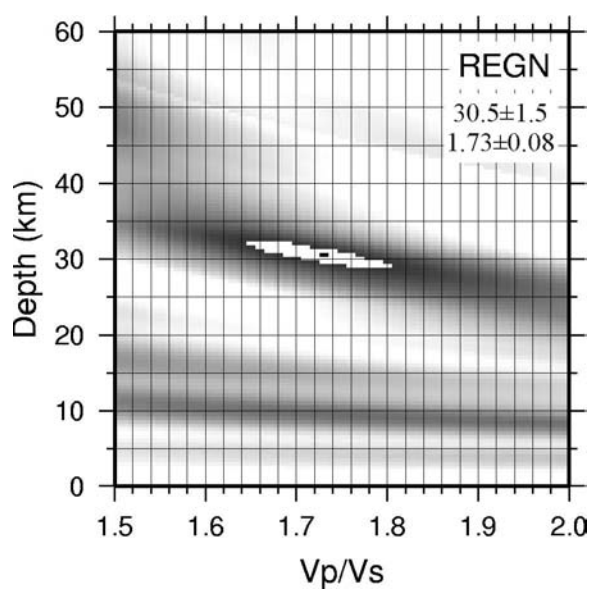
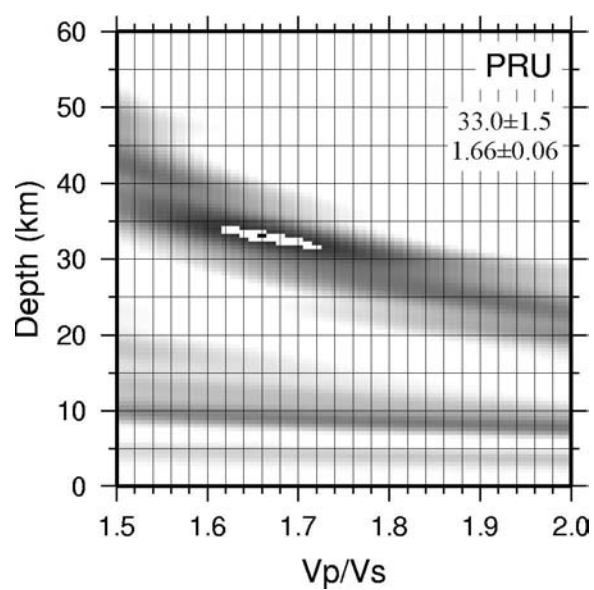












C.2 Moho depths and v_p/v_s ratios obtained from delay times of Moho Ps conversion and crustal multiple PpPs

Comparison of v_p/v_s ratios and Moho depth obtained by two different methods: 1) Zhu and Kanamori method; 2) manual calculation from delay times of Moho *Ps* conversion and multiple reverberation *PpPs*. For both methods, an average crustal *P* wave velocity of 6.3 km/s was assumed. The difference in Moho depth between the two methods is in most cases ± 1 km or less.

Station	method by <i>Zhu and Kanamori (2000)</i>		from delay times of Moho <i>Ps</i> and <i>PpPs</i>	
	v_p/v_s	H [km]	v_p/v_s	H [km]
B09	1.69±0.07	31.5±1.5	1.70	31.1
B11/BM11	1.74±0.07	30.5±1.5	1.72	31.4
B12/BM12	1.73±0.05	36.0±1.5	1.72	36.6
B13/BM13	1.73±0.07	32.5±1.5	1.73	32.7
B14/BM14	1.77±0.07	31.5±1.5	1.78	31.1
B17	1.66±0.06	30.5±1.0	1.65	31.1
B27	1.70±0.10	29.0±1.5	1.72	29.1
B36	1.69±0.05	31.0±1.0	1.65	32.3
B41	1.70±0.07	30.5±1.5	1.71	30.7
B44	1.73±0.07	30.0±1.5	1.71	30.7
B46	1.77±0.06	32.0±1.0	1.75	32.7
BG02	1.74±0.06	30.0±1.0	1.71	31.0
BG04	1.75±0.06	30.0±1.0	1.72	30.4
BG05	1.73±0.07	30.5±1.5	1.72	30.7
BG10	1.77±0.08	30.5±1.5	1.74	31.4
BG14	1.75±0.07	29.0±1.5	1.73	29.5
BG16	1.76±0.05	31.0±1.0	1.74	32.0
BG17	1.69±0.04	31.5±1.0	1.66	32.5
BG22	1.71±0.06	29.5±1.0	1.72	28.8
BG24	1.72±0.07	30.0±1.5	1.71	30.4
BG25	1.81±0.08	28.0±1.5	1.79	28.6
BG30	1.77±0.06	28.5±1.0	1.75	29.1
BOH1	1.74±0.06	30.0±1.0	1.71	30.8
BRG	1.74±0.07	30.0±1.5	1.71	31.0
GEC2	1.69±0.07	38.0±1.75	1.67	39.2
GRA1	1.71±0.06	32.0±1.5	1.69	33.1
KHC	1.69±0.06	39.0±1.5	1.67	40.6
NEUB	1.75±0.07	30.5±1.0	1.72	31.1
NKC	1.72±0.08	29.0±1.5	1.67	30.6
PLN	1.67±0.06	33.0±1.5	1.64	34.2
PRU	1.66±0.06	33.0±1.5	1.64	33.4
REGN	1.73±0.08	30.5±1.5	1.69	31.8
WERN	1.80±0.08	29.0±1.0	1.76	30.2
WET	1.77±0.08	34.5±2.0	1.74	36.0

Erklärung

Hiermit erkläre ich an Eides statt, daß ich die vorliegende Arbeit selbständig angefertigt habe und keine weiteren außer den angegebenen Quellen und Hilfsmitteln verwendet habe.

Potsdam, im Juni 2006

Barbara Heuer

Lebenslauf (Curriculum vitae)

Barbara Heuer

geboren am 11. Mai 1976 in Erfurt

Schulbesuch

1982 – 1991	Polytechnische Oberschule „Theodor Neubauer“ Erfurt
1991 – 1994	„Königin-Luise-Gymnasium“ Erfurt
06/1994	Abitur
09/1994 – 07/1995	Auslandsaufenthalt in Dublin (Irland) als Au-pair

Hochschulstudium

10/1995 – 01/2001	Studium der Geophysik am Institut für Geophysik und Geologie, Universität Leipzig
1999 – 2000	Anfertigung der Diplomarbeit zum Thema: „Untersuchung anomaler ScP/P-Amplitudenverhältnisse in Aufzeichnungen des GRSN“, Betreuer: Prof. Dr. Michael Korn
01/2001	Diplom in Geophysik an der Universität Leipzig

Berufserfahrung

02/2001 – 10/2001	Routineauswertung lokaler, regionaler und teleseismischer Ereignisse am SZGRF Erlangen/BGR
11/2001 – 02/2002	Mitarbeit im DFG-Forschungsvorhaben „Herdmechanik und Seismotektonik der Schwarmbeben in der Region Vogtland/NW-Böhmen“ am SZGRF Erlangen/BGR, Ableitung und Interpretation von Skalierungsfunktionen;
seit 04/2002	Mitarbeit im DFG-Forschungsvorhaben „BOHEMA: Seismische und stoffliche Erkundung von Erdkruste und Erdmantel des Vogtland/NW-Böhmen-Swarmbebengebietes“ (unterbrochen durch Mutterschutz/ Elternzeit 09/2004–05/2005)